

Engineered atomic states for precision interferometry

Thèse de doctorat de l'Université Gottfried Wilhelm Leibniz Universität Hannover et de
l'Université Paris-Saclay préparée à l'Université Paris-Sud

Ecole doctorale n°572 Ondes et Matière (EDOM)
Spécialité de doctorat : Physique Quantique

Thèse présentée et soutenue à Hanovre, le 02 Juillet 2019, par

ROBIN CORGIER

Composition du Jury :

Klemens Hammerer Professeur des Universités, Leibniz Universität Hannover	Président
Christiane Koch Professeure des Universités, Universität Kassel	Rapporteur
Augusto Smerzi Professeur des Universités, Università degli Studi di Firenze	Rapporteur
Jacques Vigué Directeur de Recherche, Université Toulouse III Paul Sabatier	Rapporteur
Olivier Dulieu Directeur de Recherche, Université Paris-Sud & Paris-Saclay	Examineur
Dennis Schlippert Chercheur, Leibniz Universität Hannover	Examineur
Eric Charron Professeur des Universités, Université Paris-Sud & Paris-Saclay	Directeur de thèse
Ernst M. Rasel Professeur des Universités, Leibniz Universität Hannover	Directeur de thèse

ENGINEERED ATOMIC STATES FOR
PRECISION INTERFEROMETRY

Von der QUEST-Leibniz-Forschungsschule der
Gottfried Wilhelm Leibniz Universität Hannover

zur Erlangung des Grades

Doktor der Naturwissenschaften
- Dr. rer. nat. -

et de l'Université Paris-sud & Paris-Saclay
Ecole Doctorale Ondes et Matière

zur Erlangung des Grades

Docteur

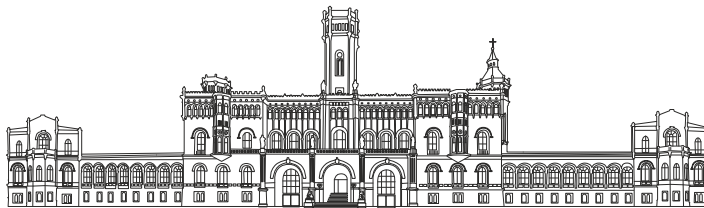
genehmigte Dissertation von

M. Sc. Robin Corgier

geboren am 02.05.1991 in Annecy, France

2019

ENGINEERED ATOMIC STATES FOR PRECISION INTERFEROMETRY



Der QUEST-Leibniz-Forschungsschule der
Gottfried Wilhelm Leibniz Universität Hannover

zur Erlangung des Grades

Doktor der Naturwissenschaften
- Dr. rer. nat. -

genehmigte Dissertation von

M. Sc. Robin Corgier

2019

Referent: Prof. Dr. Christiane Koch

Universität Kassel

Korreferent: Prof. Dr. Augusto Smerzi

Università degli Studi di Firenze

Korreferent: D.R. Jacques Vigué

Université Toulouse III Paul Sabatier

Tag der Disputation: 02.07.2019

ABSTRACT

Modern physics relies on two distinct fundamental theories, General Relativity and Quantum Mechanics. Both describe on one hand macroscopic and cosmological phenomena such as gravitational waves and black holes and on the other hand microscopic phenomena as superfluidity or the spin of particles. The unification of these two theories remains, so far, an unsolved problem. Interestingly, candidate Quantum Gravity theories predict a violation of the principles of General Relativity at different levels. It is, therefore, of a timely interest to detect violations of these principles and determine at which level they occur.

Recent proposals to perform Einstein Equivalence Principle tests suggest a dramatic performance improvement using matter-wave atomic sensors. In this context, the design of the input states with well defined initial conditions is required. A state-of-the-art test of the universality of free fall (UFF) would, for example, require a control of positions and velocities at the level of $1\ \mu\text{m}$ and $1\ \mu\text{m}\cdot\text{s}^{-1}$, respectively. Moreover, size-related systematics constrain the maximum expansion rate possible to the $100\ \mu\text{m}\cdot\text{s}^{-1}$ level. This initial engineering of the input states has to be quite fast, of the order of few hundred ms at maximum, for the experiment's duty cycle to be metrologically-relevant.

In this thesis, fast transport and manipulation protocols of Bose-Einstein condensates (BEC) with an atom chip devices are proposed relying on reverse engineering techniques with shortcut-to-adiabaticity protocols. This technique provides the possibility to engineer transport ramps with specific desired initial and final conditions. The robustness of such an implementation was presented in the context of a realistic experimental configuration. Optimized sequences, involving the characterization of the excited modes of the BEC after transport have been proposed to constrain the size of the BEC to few hundred microns after few seconds with a expansion energy as low as few tens of pK. Such protocols have been successfully transferred to the microgravity Quantus-2 drop tower experiment, to the sounding rocket space BEC mission Maius-1 and to the cold atom laboratory (CAL) on board of the International Space Station.

Moreover, detrimental systematic effects stemming from position and velocity offsets of two clouds of atoms used as test masses in an interferometric measurement motivate a specific engineering of the input states. Optimal Control Theory (OCT) schemes were presented to co-locate and reduce the size oscillations of two thermal clouds of different Rb isotopes in a magnetic trap configuration. This method, implemented at the 10-meter-long atomic fountain at Stanford University in the group of Prof. Mark Kasevich, dramatically improved the starting conditions of the UFF test .

Also on the non-degenerate ensembles side, Optimized sequences, relying on size excitations of a molasses-cooled ensemble, have been proposed to increase the phase-space density by an order of magnitude hinting towards a more efficient subsequent evaporation. In the context of increased sensitivity with BEC matter-wave interferometers, higher atom numbers is of a particular interest. This optimized sequence has been studied in realistic dipole trap configurations.

In the case of degenerate mixtures, the interaction effects were taken into account to find the different ground state configurations of the system in different interaction regimes. A scaling theory was developed to efficiently describe the dynamics of a two-component BEC in time-dependent harmonic traps and compare its outcome to the solution of the mean field Gross-Pitaevskii equation. Based on this, the implementation of a delta-kick collimation stage was proposed to constrain the expansion of the matter-waves to the $100 \mu\text{m.s}^{-1}$ level. The influence of the interaction between the degenerate mixture has been highlighted in the context of matter wave atomic sensors. With all these tools at hand, the initial conditions requirements of a competitive UFF test with state-of-the-art techniques are theoretically met.

La physique moderne repose sur deux théories fondamentales distinctes, la relativité générale et la mécanique quantique. Toutes les deux décrivent d'une part les phénomènes macroscopiques et cosmologiques tels que les ondes gravitationnelles et les trous noirs et d'autre part les phénomènes microscopiques comme la superfluidité ou le spin des particules. L'unification de ces deux théories reste, jusqu'à présent, un problème non résolu. Il est intéressant de noter que les différentes théories de gravité quantique prédisent une violation des principes de la relativité générale à différents niveaux. Il est donc hautement intéressant de détecter les violations de ces principes et de déterminer à quel niveau elles se produisent.

De récentes propositions pour effectuer des tests du principe d'équivalence d'Einstein suggèrent une amélioration spectaculaire des performances en utilisant des capteurs atomiques à ondes de matière. Dans ce contexte, il est nécessaire de concevoir des états d'entrée de l'interferomètre avec des conditions initiales bien définies. Un test de pointe de l'universalité de la chute libre (Universality of Free Fall en anglais (UFF)) nécessiterait, par exemple, un contrôle des positions et des vitesses avec une précision de l'ordre de $1\ \mu\text{m}$ et $1\ \mu\text{m}\cdot\text{s}^{-1}$, respectivement. De plus, les systématiques liées à la taille du paquet d'ondes limitent le taux d'expansion maximum possible à $100\ \mu\text{m}\cdot\text{s}^{-1}$. La création initiale des états d'entrée de l'interféromètre doit être assez rapide, de l'ordre de quelques centaines de ms au maximum, pour que le temps de cycle de l'expérience soit pertinent d'un point de vue métrologique.

Dans cette thèse, des protocoles de transports et de manipulations rapides des condensats de Bose-Einstein (CBE) avec un dispositif à puce atomique sont proposés sur la base de techniques de rétroingénierie avec des protocoles de raccourcis adiabatiques. Cette technique offre la possibilité de concevoir des rampes de transports avec des conditions initiales et finales spécifiques souhaitées. Des séquences optimisées, impliquant la caractérisation des modes excités du CBE après transport ont été proposées pour limiter la taille du CBE à quelques centaines de microns après quelques secondes avec une énergie d'expansion aussi faible que quelques dizaines de pK. De tels protocoles ont été transférés avec succès à l'expérience en microgravité Quantus-2 dans la tour de chute libre à Bremen, à la mission CBE embarqué sur missile Maius-1 et au laboratoire d'atomes froids (CAL) à bord de la Station spatiale internationale.

De plus, les effets systématiques préjudiciables dus aux décalages en positions et en vitesses de deux nuages d'atomes dans une mesure d'interférométrie motivent la création d'états spécifiques. Des protocoles basés sur la théorie du contrôle optimal (TCO) ont été présentés pour co-localiser et réduire les oscillations en taille de deux nuages thermiques de différents isotopes du Rubidium dans une configuration de piège magnétique. Cette méthode, appliquée à une configuration expérimentale réaliste, a amélioré de façon spectaculaire les conditions de départ pour un test de l'universalité de la chute libre dans le cas de la fontaine atomique de 10 mètres de long de l'Université de Stanford dans le groupe du professeur Mark Kasevich.

Des séquences optimisées, s'appuyant sur l'excitation de la taille d'un ensemble d'atomes refroidis par mélasse optique, ont été proposées pour augmenter la densité dans l'espace des phases d'un ordre de grandeur. Dans le cadre de l'augmentation de la sensibilité d'une mesure basée sur la technologie de l'interférométrie à ondes de matière,

un nombre d'atomes plus élevé dans le CBE est particulièrement intéressant.

Dans le cas de mélanges dégénérés, les effets d'interaction ont été pris en compte pour trouver les différentes configurations d'état fondamental du système dans différents régimes d'interaction. Une théorie de lois d'échelle a été développée pour décrire efficacement la dynamique d'un CBE à deux composantes dans des pièges harmoniques dépendant du temps et comparer les résultats obtenus à la résolution de l'équation de Gross-Pitaevskii dans le cadre de la théorie du champ moyen. Sur cette base, la mise en œuvre d'une étape de collimation à l'infini a été proposée pour limiter l'expansion des ondes de matière au niveau de $100 \mu\text{m}\cdot\text{s}^{-1}$. L'influence de l'interaction entre le mélange de deux espèces a été mise en évidence dans le contexte de capteurs atomiques à ondes de matière. Avec tous ces outils théoriques à portée de main, les conditions initiales d'un test compétitif de l'universalité de la chute libre avec les techniques actuelles sont remplies.

Die moderne Physik stützt sich auf zwei verschiedene fundamentale Theorien, die Allgemeine Relativitätstheorie und die Quantenmechanik. Beide beschreiben einerseits makroskopische und kosmologische Phänomene wie Gravitationswellen und Schwarze Löcher und andererseits mikroskopische Phänomene wie Suprafluidität oder den Spin von Teilchen. Die Vereinheitlichung dieser beiden Theorien ist ein bisher ein ungelöstes Problem. Interessanterweise prognostizieren potentielle Kandidaten für Theorien einer Quantengravitation eine Verletzung der Prinzipien der Allgemeinen Relativitätstheorie auf verschiedenen Ebenen. Es ist daher von erheblichem Interesse, Verstöße gegen diese Grundsätze zu entdecken und festzustellen, auf welcher Ebene sie auftreten.

Jüngste Vorschläge versprechen ein signifikantes Potential von Sensoren basierend auf Materiewellen für Tests des Einstein Äquivalenzprinzips. In diesem Zusammenhang ist die Gestaltung der Eingangszustände mit klar definierten Ausgangsbedingungen erforderlich. Ein hochmoderner Test der Universalität des freien Falles (UFF) würde beispielsweise eine Kontrolle der Positionen und Geschwindigkeiten auf dem Niveau von $1\ \mu\text{m}$ und $1\ \mu\text{m}\cdot\text{s}^{-1}$ erfordern. Darüber hinaus schränken Systematiken, die im Bezug zur Größe des atomaren Ensembles stehen, die maximal mögliche Expansionsrate auf das Niveau von $100\ \mu\text{m}\cdot\text{s}^{-1}$ ein. Dieses anfängliche Engineering der Eingangszustände muss recht schnell, maximal in der Größenordnung von wenigen hundert ms, erfolgen, damit die Repetitionsrate des Experiments meteorologisch relevant ist.

In dieser Arbeit werden schnelle Transport- und Manipulationsprotokolle von Bose-Einstein-Kondensaten (BEC) mit Atomchips vorgeschlagen, die sich auf Reverse Engineering Techniken mit Shortcut-to-Adiabaticity-Protokollen stützen. Diese Methode bietet die Möglichkeit, Transportrampen mit spezifisch gewünschten Anfangs- und Endbedingungen zu konstruieren. Die Robustheit einer solchen Implementierung wurde im Rahmen einer realistischen experimentellen Konfiguration dargestellt. Optimierte Sequenzen, welche die Charakterisierung der angeregten Moden des BEC nach dem Transport beinhalten, wurden vorgeschlagen, um die Größe des BEC nach wenigen Sekunden auf wenige hundert Mikrometer mit einer Expansionsenergie von nur wenigen zehn pK zu begrenzen. Solche Protokolle wurden erfolgreich im Fallturmexperiment Quantus-2, in der Höhenforschungsraketen-BEC-Mission Maius-1 und dem Kalte-Atomelabor (CAL) an Bord der Internationalen Raumstation angewandt.

Darüber hinaus erfordern nachteilige systematische Effekte, die sich aus Positions- und Geschwindigkeitsabweichungen zweier Atomwolken ergeben, welche als Testmassen in einer interferometrischen Messung verwendet werden, eine spezifische Realisierung der Eingangszustände. Optimal Control Theory (OCT) Schemata wurden vorgestellt, um die Größenschwankungen von zwei thermischen Wolken verschiedener Rb-Isotope in einer Magnetfallen-Konfiguration zu reduzieren. Diese Methode, die am 10 Meter hohen atomaren Fontäne der Stanford University in der Gruppe von Prof. Mark Kasevich implementiert wurde, verbesserte die Startbedingungen für den UFF-Test signifikant.

Ebenfalls im Kontext nicht-degenerierter Ensembles wurden optimierte Sequenzen vorgeschlagen, die sich auf Größenanregungen eines melassegekühlten Ensembles stützen. Damit kann die Phasenraumdicke um eine Größenordnung zu erhöht werden, was eine effizientere anschließende evaporative Kühlung ermöglicht. Im Zusammenhang mit der erhöhten Empfindlichkeit bei BEC-Materialwellen-Interferometern sind

insbesondere höhere Atomzahlen von Interesse. Diese optimierte Sequenz wurde in realistischen Dipolfallenkonfigurationen untersucht.

Im Falle von degenerierten Gemischen wurden die Interaktionseffekte berücksichtigt, um die unterschiedlichen Grundzustandskonfigurationen des Systems in verschiedenen Interaktionsregimes zu finden. Eine Skalierungstheorie wurde entwickelt, um die Dynamik eines Zweikomponenten-BEC in zeitabhängigen harmonischen Fallen effizient zu beschreiben, und das Ergebnis wurde mit der Lösung der Groß-Pitaevskii-Gleichung verglichen. Darauf aufbauend wurde die Implementierung einer Delta-Kick-Kollimationsstufe vorgeschlagen, um die Ausdehnung der Materiewellen auf die $100 \mu\text{m}\cdot\text{s}^{-1}$ Ebene zu begrenzen. Der Einfluss der Wechselwirkung innerhalb des degenerierten Gemisches wurde im Zusammenhang mit Materiewellen-Atomsensoren aufgezeigt. Mit all diesen Werkzeugen werden die Ausgangsbedingungen für einen wettbewerbsfähigen UFF-Test mit modernsten Techniken theoretisch erfüllt.

ACKNOWLEDGEMENTS

First and foremost, I thank my two first advisors Eric Charron and Ernst M. Rasel for the opportunities they offered to me during my PhD thesis and the joint collaboration between the university in France and Germany. I thank Naceur Gaaloul, my third advisor and the leader of the T-SQUAD team (Theory-Simulation of QUAntum Dynamics) in the group of Ernst M. Rasel I worked in. The unfailing motivation, optimism, enthusiasm and excitement of Eric, Ernst and Naceur have been a source of inspiration throughout my PhD. They were always here for counsel, support and assistance in my work. I owe you what I learned in terms of physics, programming and presentation skills, to name only a few. You always encouraged me to do my best and have been there to push me even further. It has been a privilege for me to work on so many ambitious projects as much for the science, in space or on ground, as the people, under their supervision.

I am very grateful to my referees, Olivier Dulieu, Klemens Hammerer, Christiane Koch, Augusto Smerzi, Dennis Schlippert and Jacques Vigué, for their time, interest and comments on my thesis.

Special thanks go out to David Guéry-Odelin from the University of Toulouse for the knowledge he shared with all over my thesis time, for the one-month internship in his group at the beginning of my time as a doctoral researcher and his excitement to use Shortcut-to-Adiabaticity techniques in a real experimental setup.

I also want to thank Dominique Sugny for teaching me the basics of Optimal Control Theory which has been particularly useful to me.

An other special thank goes to Mark Kasevich from the University of Stanford for the opportunity to join his group for a three-month internship in the 10-meter long fountain experiment team. I enjoyed his motivation to bring Optimal Control Theory protocols to the experiment and I thank his team, Tim Kovachy, Remy Notermans, Peter Asenbaum and Chris Overstreet, for the knowledge and experimental details they shared with me.

I want to deeply thank Osman Atabek, Annie Klisnick, Danielle Dowek, Fabien Gatti and Jennifer Joseph for all their valuable advice, their support and our discussion during the lunch and coffee time. A very valuable advice from Osman I cannot forget to mention is to write one paragraph each day during the PhD thesis time to compile all of them at the end. I deeply thank also Bernard Bourguignon, the director of the Institute, for all his advice and time. I really enjoyed my time in France in this very nice group.

I thank Laurance Pruvost, Marion Jacquy, Bruneau Viaris and Citlali Cabrera for

teaching me the basics of cold atoms during my first internship during my study at the university of Paris-Sud in the Magistère de Physique Fondamentale. I have been extremely lucky to have been a student of Pascal Parneix who provided awesome teaching and put me in contact with Eric for my Master-1 internship which I made partially in France and in Germany with Naceur and Ernst. I liked so much this field so much I never changed to something else. Many thank to Alexandre Gauguet, Jacques V., Boris Décamps, Julien Alibert, Aléa Fortun and Gabriel Condon for deepern my knowledge in the physic of cold atoms and matter-wave atom interferometry during my Master-2 internship in Toulouse and for the good time with them there.

I am very grateful to the members of the *Shadow Theory* team lead by Naceur, and Holger Ahlers, Sina Loriani and Jan-Niclas. Since the beginning of my Phd thesis, they have always made me feel at home. I am also very grateful to the official creation of this group, the T-SQUAD team, and to their new members: Florian Fitzek, Sirine Amri and Annie Pichery. I have been extremely lucky to share the office with Sina, Jan-Niclas and Florian where the working ambiance has always been pleasant, stimulating and inspiring. Thank you for the nice time we shared together at work and beyond. During this collaboration between the university in France and Germany both countries have been the winners of the World Football Championship leading to an excellent ratio of the cotutelle (although France has been much better in 2014 than Germany in 2018).

It is natural and time to say that I am very grateful to all my colleagues in the group of Ernst Rasel who shared their knowledge and time with me about experimental life in general, giving me the possibility to engineer theoretical protocol presented in this thesis. I thank particularly Waldermar Herr, Etienne Wodey, Sebastian Bode, Felix Kösel, Dennis Becker, Maïke Lachmann, Manuel Popp, Stephan Seidel, Henning Albers, Dennis Schlippert and Christian Schubert I deeply interacted with in the case of their respective experiment, Quantus-2, Qport, Maius-1, Atlas and even more over the last past four years. I cannot forget to mention all the valuable discussions, advice and feedback from Sven Abend, Torben Schulze, Klaus Zipfel and Dominika Fim and for sure all the members of the Institut für Quantenoptik not already mentioned. I am very honored to have been part of this big family and I would like to finish with two words: “Denmark Seminar”.

I deeply thank the members of the Cold atom and Ultra cold Atom in Space (CUAS) consortia lead by Nick Bigelow from the University of Rochester for the nice discussions and strategies about experiment sequences on the Cold Atom Lab (CAL) experiment and Jason Williams, Rob Thompson and their team for the awesome interaction to run the proposed sequences.

I am also very grateful for the hard work of the group staff, Katrin Pfennig, Birgit Ohlendorf, Gunhild Faber, Elke Hünitzsch, Anne-Dore Göldner-Pauer, Marie-Claire Paul, Bérangère Ustaze and Nathalie Schwart who have always been available to help out.

To finish I would like to thank all my friends who encourage me to pursue my goal. My family in general and more specifically my father, mother, brother, sister and cats who always supported and encouraged my choices since the beginning and finally to Jessie, my love.

FINANCIAL SUPPORT

DAAD

Deutscher Akademischer Austauschdienst
Office allemand d'échanges universitaires



Université
franco-allemande
Deutsch-Französische
Hochschule

I am grateful to the German Foreign Academic Exchange (DAAD) for partially supporting my research activities in Germany in 2016.

I would like to thank the IP@Leibniz program of the Leibniz University of Hanover for travel grants supporting my stays in France.

I would like to acknowledge the mobility support from the Q-SENSE project, which has received funding from the European Union's Horizon 2020 Research and Innovation Staff Exchange (RISE) Horizon 2020 program under Grant Agreement Number 691156 to support my stay at Stanford during my 3-month research stay in 2018.

Additional mobility funds were thankfully made available through the bilateral exchange project PHC-Procope giving me the possibility to travel to France during my PhD time.

Many thanks to the Université Franco-Allemande for the support to invite my committee board the day of my defense.

TABLE OF CONTENTS

	Page
1 Introduction	1
1.1 The theory of everything	1
1.1.1 General relativity and Quantum theory	1
1.1.2 Einstein Equivalence Principle tests (EEP)	2
1.2 Matter-wave interferometers	5
1.3 Cold atoms and Bose-Einstein condensates	7
1.3.1 A brief history of cold atoms	7
1.3.2 The different regimes	10
1.3.3 BEC interferometry	12
1.4 Objectives of the thesis	13
1.5 Thesis outline	14
2 Optimized manipulation of a single-species condensate	17
2.1 Introduction	18
2.2 Scheme and atom chip model	20
2.2.1 Scheme	20
2.2.2 Chip model	21
2.3 Theoretical model	22
2.3.1 Semi-classical approach	23
2.3.2 Reverse engineering protocols	28
2.4 Theoretical Results	30
2.4.1 Control of the BEC position dynamics	30
2.4.2 Robustness of the STA protocol	33
2.4.3 Dynamics of the atomic cloud size	35
2.4.4 Collective excitations and optimization of the expansion dynamics	38
2.5 Micro-gravity experimental implementation	43

TABLE OF CONTENTS

2.5.1	The Quantus 2 drop tower experiment	43
2.5.2	The MAIUS-1 sounding rocket mission	45
2.6	Conclusion and outlook	48
3	Optimized manipulation of thermal ensembles	51
3.1	Theoretical tools	52
3.1.1	Optimal Control Theory	52
3.1.2	Model of a thermal ensemble of N particles	59
3.2	Applications	63
3.2.1	Dual-source input state optimization	63
3.2.2	Thermal cloud phase-space density optimization by atomic lensing	83
3.3	Conclusion and outlook	95
4	Optimized manipulation of a degenerate bosonic mixture	97
4.1	Introduction	98
4.2	A dual-species Gross-Pitaevskii approach	100
4.3	The different ground state structures	101
4.3.1	The Thomas-Fermi (TF) approximation	101
4.3.2	Study in the case of two domains in the TF approximation	106
4.3.3	Study in the case of three domains in the TF approximation	108
4.4	Dynamics	108
4.4.1	The time-dependent coupled Gross-Pitaevskii equations in spherical coordinates	109
4.4.2	Scaling approach for a two-component BEC	110
4.5	Results	113
4.5.1	Ground state comparison between TF and GPE	114
4.5.2	Comparison between the TDCGPE and the generalized scaling approach	119
4.5.3	Application to dual-species twin atomic lensing to the pico-Kelvin level	124
4.6	Conclusion	129
5	Conclusion and perspectives	131
A	Numerical simulation of the linear Schrödinger Equation	137
	Bibliography	141

INTRODUCTION

Contents

1.1	The theory of everything	1
1.1.1	General relativity and Quantum theory	1
1.1.2	Einstein Equivalence Principle tests (EEP)	2
1.2	Matter-wave interferometers	5
1.3	Cold atoms and Bose-Einstein condensates	7
1.3.1	A brief history of cold atoms	7
1.3.2	The different regimes	10
1.3.3	BEC interferometry	12
1.4	Objectives of the thesis	13
1.5	Thesis outline	14

1.1 The theory of everything**1.1.1 General relativity and Quantum theory**

Modern physics was born at the beginning of the last century, when observations of the nature of light changed the conception of our world. Fifty years earlier, considered as the culmination of classical physics, Maxwell's equations seemed to reflect all the

properties of light described initially by Huyghens, Young and Fresnel. The behaviour of light that seemed to have been well understood at the end of the 19th century was then called into question by some observations. The frequency distribution of the light emitted by a heated black body, the photoelectric effect and the discrete nature of the spectra absorbed or emitted by a gas could not be explained. Our understanding of today's world in physics is the result of two fundamental theories developed at the beginning of the 20th century. The introduction of the idea that the speed of light does not depend on the observer and by admitting a maximum speed of propagation for all information gave the basis of the theory of relativity. Extended to the description of the effects of gravitation, the theory of general relativity [1–3] describes macroscopic phenomena and gives a new conception of space and time as well as of our entire universe. The unification of the two classical theories of light, treated first in a purely corpuscular way by Newton who interpreted light as a flow of particles and secondly as a wave, led to the idea of the duality of light and paved the way for quantum theory [4–6]. The notions of particles and waves, which cannot be dissociated, provide a thorough understanding of the microscopic effects induced by weak, strong and electromagnetic interactions. Both fundamental theories, General Relativity and quantum mechanics were initiated by the work of A. Einstein [7–10] and were tested several times in their respective fields, without showing any deviation. On the one hand, quantum theory explains phenomena such as the laser effect, superconductivity, the tunnel effect, and the existence of spin, to mention just a few. These effects led to everyday powerful applications such as lasers, transistors, computers, medical imaging by magnetic resonance and atomic clocks, for instance. On the other hand, the mathematical formalism of general relativity predicts and explains phenomena such as gravitational waves, the effect of gravitation on time and is the basis for the current understanding of black holes. Well known practical everyday-life instruments, based on the Global Positioning System (GPS), benefit from both theoretical approaches. Quantum physics is involved in the definition of time through atomic clocks and general relativity is involved in signal triangulation.

1.1.2 Einstein Equivalence Principle tests (EEP)

Up to now, the unification of these two models, by incorporating the effects of gravitation into the quantum world, remains an unresolved problem. So far, general quantum gravity theories [11], unifying all non-gravitational interactions with gravity, like the string theory or the quantum loop theory, predict a violation of the fundamental principles of general relativity synthesized by the Einstein Equivalence Principle (EEP), at some

particular scale [11, 12]. It is consequently of fundamental importance to search for a possible violation of the pillars of general relativity [13].

The EEP test consists in three different parts, and a violation of one of these three tests directly implies a violation of the two others:

- The Local Lorentz Invariance (LLI) stipulates that the result of any non-gravitational experiment performed in a freely falling frame has to be independent of the velocity and the orientation of this frame.

In 1881, before the discovery of the theory of general relativity, A. Michelson and E. Morley conducted an experiment aimed at detecting the existence of the aether [14], a supposed material support of the vibrations of an electromagnetic wave such as light. With a series of measurements of the speed of light in two orthogonal directions [15], A. Michelson and E. Morley were aiming for a difference. The negative result brought them to reconsider the existence of the aether. Tests of the isotropy of space [16, 17], time-dilation [18, 19] and anisotropy of light propagation [20–22] have been carried out. The last test did not show any evidence of a possible violation with an accuracy at the level of $\Delta c/c = 10^{-17}$ [23].

- The Local Position Invariance (LPI) stipulates that such an experiment depends neither on the position where the experiment is carried out, nor when this one is done.

General relativity predicts that a set of different clocks in different gravitational fields, because of their different speeds and their different positions, tick at slightly different rates. The measurement of the red shift is a consequence of this phenomena. A clock on Earth ticks slower than a clock on the Moon. Two clocks located initially at the same position, *i.e.* in the same gravitational potential, ticking at the same rate, ν and then transported in different gravitational potential, with a difference ΔU , show a frequency difference $\Delta \nu$ such as

$$\frac{\Delta \nu}{\nu} = \frac{\Delta U}{c^2}. \quad (1.1)$$

In 1980, a test of general relativity with the measurement of the frequency of two hydrogen masers, one on ground and the other one in space, at a distance of 10 000 km, showed an agreement with theory with an accuracy of $7 \cdot 10^{-5}$ [24]. More recently, on ground, a comparison of data taken over eight years between various hydrogen masers and the frequencies of three separate Cesium fountain clocks

and one of Rubidium at SYRTE have been reported in [25]. The Local position invariance coefficients have been measured to a precision of up to parts in 10^{-11} with respect to the cosmic microwave background rest frame.

- The Universality of Free Fall (UFF), also called weak equivalence principle (WEP), stipulates that the trajectories of test masses only depend on their initial positions and velocities. This test does not depend on the constitution (protons or neutrons for instance), forms, charges (positive, neutral or negative) or spins (up or down) of the test masses.

High-precision measurements, based on fundamentally different classical and quantum tests, have been performed and include ground and space experiments. The difference in acceleration of two test bodies yield to defined the so-called “Eötvös ratio” given by

$$\eta = 2 \frac{a_1 - a_2}{a_1 + a_2}, \quad (1.2)$$

where a_1 and a_2 are the accelerations of the two masses. One example of test is the torsion balance [26–28]. This experiment is based on the measurement of the torsion of two test masses attached to a rigid and mass-less frame with a relative accuracy at the level of 10^{-13} in the Eötvös coefficient [29–31]. A second example is the lunar laser telemetry experiment [32–34]. This test measures the distance between the moon and the earth and gives an information on the free fall toward the sun of these two celestial bodies with a relative accuracy at the level of 10^{-13} in the Eötvös coefficient [35].

The MICROSCOPE mission [36] takes advantages of the very quiet environment that space can offer and holds the state-of-the-art in inaccuracy of the UFF test. This experiment, performed with material test masses of different compositions (titanium and platinum) freely falling in the same orbit around the Earth, measures the force required to maintain in equilibrium the two test masses. In this experiment, the relative acceleration has been measured with an accuracy at the level of level of $\delta(Ti, Pt) = [-1 \pm 9(stat) \pm 9(syst)] \cdot 10^{-15}$ (1σ statistical uncertainty) [36].

Recent proposals were made to test the UUF with matter-wave atom interferometers with an inaccuracy around 10^{-15} . The principle of such tests relies on the measurement of the phase shift due to the different accelerations of two isotopes in free fall, either on ground in tall fountains [37–40], or in space within the STE-QUEST - satellite Space-Time Explorer and QUantum Equivalence principle Space

Test - candidate mission [41, 42] for example. In both cases, the aim is to maximize the free fall time. **To measure such a violation of the UFF at the femto-level in the Eötvös ratio, one has to define the differential position and velocity of the two isotopes at a level better than 1 nm and $1 \text{ nm}\cdot\text{s}^{-1}$, respectively [40]. Recent proposals [43] relax these requirements to a level of $1 \mu\text{m}$ and $1 \mu\text{m}\cdot\text{s}^{-1}$ [37, 44]. Finding manipulation protocols at this level of control of the atomic samples constitutes one of the main motivations of this thesis.**

1.2 Matter-wave interferometers

Matter-wave atom interferometers are based on the diffraction of atoms generated by light pulses. In the 90's fringes have been observed by the diffraction of Helium atoms in a Young's double slit geometry [45]. At that time, atom interferometers had been set up and operated by various groups [46–51] and they have since become a common technique in physics laboratories.

The principle of the matter-wave interferometer can be explained in a very simple way in the context of a two-level atom. An atom initially in a ground level, $|a\rangle$, is placed in a quantum superposition between two levels, $|a\rangle$ and $|b\rangle$, and follows different paths. The paths are then brought back together and give rise to interferences indicating the different phase accumulated along the different paths influenced by the different forces acting on the atomic wave packet.

The high sensitivity of matter-wave interferometers has been widely used for fundamental physics tests and has been used so far to measure the fine structure constant [52–55], the gravitational constant [56–58] and topological phases [59–63]. Atomic properties such as the electric polarizability [64–66] and the atom and neutron neutrality [67, 68] have been tested. Ambitious proposals proposed matter-wave atom interferometers to test general relativity and to detect the gravitational waves [69–76], which were detected in 2016 for the first time with the laser interferometer LIGO [77]. Einstein Equivalence Principle tests have been performed and tested the Local Lorentz Invariance [78] and the Universality of Free Fall [38, 39, 79–84]. Atom interferometers technology have been so far developed to measure inertial forces such as in a gravimeter [85–91], gradiometer [56, 89, 92, 93] and gyroscope [94–102]. Miniaturized and portable payloads have already been developed [103–107] and commercialized [108–110]. With the development of quantum entanglement [62, 63, 111–116] and quantum squeezing [117, 118],

Quantum Metrology [119–121] promises to develop measurement techniques with a better precision than within a classical framework.

One of the most common atom interferometry schemes relies on the Mach-Zehnder type configuration [122]. In optics, a coherent polarized laser beam is separated with a beam-splitter, reflected with mirrors and then recombined with a beam-splitter to finally interfere. With matter-waves [49], the wave function of an atom is split in a coherent superposition of two distinct states, $|a\rangle$ and $|b\rangle$, retro-reflected and then superimposed to interfere. In this case the different steps are driven by laser pulses instead of optics elements. The two states are coupled by a two-photon transition undergoing so-called Rabi oscillations [122].

In the example of a gravity acceleration measurement with a Mach-Zehnder scheme, as shown in Fig. 1.1, the initial wave function $|\psi\rangle = |a\rangle$ is equally split between the two states with a $\pi/2$ -pulse and extra momentum is transferred to one part of the superposition. The two states, $|a, p\rangle$ and $|b, p + \delta p\rangle$ follow different paths and after a time duration T , a π -pulse is applied to deflect the matter-wave beams. The two new states, $|a, p + \delta p\rangle$ and $|b, p\rangle$ continue to evolve and are recombined after another time duration T , when a final $\pi/2$ pulse is applied and the two paths are brought back at each of the two ports of the interferometer. At first order, the phase difference accumulated is proportional to the gravity acceleration experienced by the atoms, g , the effective wave number, $k_{eff} = \delta p/\hbar$, and to the square of the total time spent in the interferometer, T_i

$$\Delta\phi = k_{eff} g T_i^2. \quad (1.3)$$

Tests of the Universality of Free Fall involve differential acceleration measurements of two test masses. This goal can be pursued either with identical atoms in different internal states [83, 123, 124] or isotopes like ^{87}Rb and ^{85}Rb [37, 39, 125], or with different atoms, ^{87}Rb and K [38, 41, 42, 81, 126] or ^{87}Rb and Yb [40], for instance. In this case the sensitivity of the differential acceleration of an atom interferometer [126, 127] is given by

$$\Delta a = \sqrt{\frac{2t_c}{N}} \frac{1}{C k_{eff} T_i^2}, \quad (1.4)$$

where t_c denotes the cycle time of the experiment. The final precision of the atom interferometer is indeed increased by averaging over many cycles. N represents the number of atoms which participate to the measurement. In the shot noise limit the sensitivity scales as $1/\sqrt{N}$. An increase of the total atom number is then beneficial to the measurement. C is the contrast of the measurement varying between 0 and 1. $k_{eff} T_i^2$

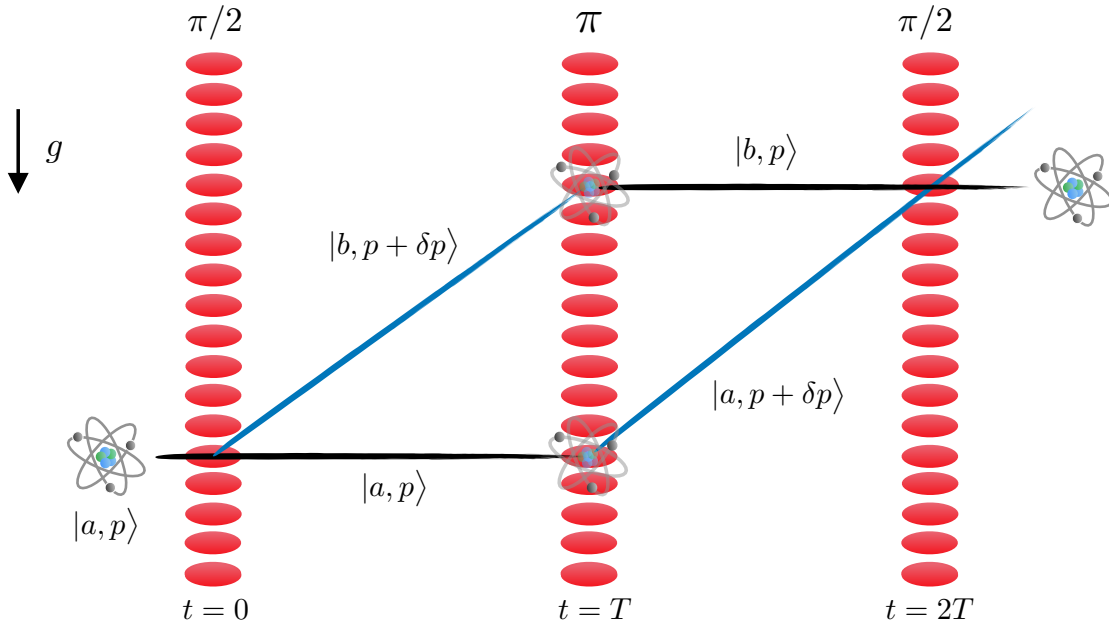


Figure 1.1: Mach-Zehnder type atom interferometer. The different pulses, $\pi/2$ at time 0, π at time T and $\pi/2$ at time $2T$ split, mirror and recombine the two paths. The time interaction with the light defines the phase of the Rabi oscillation between the states $|a\rangle$ and $|b\rangle$. The trajectory of the two path shown are in the ideal case $g=0$.

is proportional to the interferometer area. An increase of this total quantity yields an increase of the area covered and in the information achieved by the different arms of the two interferometer, and thus benefits to the sensitivity.

The maximum drift time of an atom interferometer is limited by the atom optics in use but also by the temperature and density regime of the atomic ensembles. Cold atoms and Bose-Einstein condensates are two interesting candidates featuring low expansion rates, which allows to observe them for relatively long times (few ms to several seconds).

1.3 Cold atoms and Bose-Einstein condensates

1.3.1 A brief history of cold atoms

Since the mid-1980s, atomic physics has undergone spectacular developments thanks to experiments in which small clouds of atoms are immobilized, suspended in vacuum, and cooled to temperatures of only a few billionths of a degree above absolute zero [128–132].

These developments have allowed to probe phenomena related to the most intimate laws of quantum physics [133].

Those experiments are mainly based on laser technology and largely benefit from the advent of this technology over the past 60 years, leading to an incredible development in many fields of physics, including cold atom physics through atom-light interactions. The laser, literally a light amplifier based on stimulated emission, was developed after the maser (in the microwave domain) invented by J. P. Gordon, H. J. Zeiger, and C. H. Townes in 1953 [134]. The first laser was made in 1960 by T. H. Maiman [135] based on the theoretical work of C. H. Townes and A. L. Schawlow [136]. One of the most exciting technologies combining quantum mechanics, cold atomic samples and laser physics is certainly the atomic clock used for an accurate definition of time [137, 138].

Experimentally, cooling and trapping atomic samples requires specific sequences we are going to introduce in a non extensive way thanks to the model of a two level atom and more specifically for the Rubidium-87 isotope, largely considered in this thesis. In typical experiments, a beam of atoms emerges from an oven with a velocity of about 300 m.s^{-1} at room temperature¹. The beam of atoms passes through a Zeeman slower, where a laser in resonance with the atomic transition propagates in the direction opposite to the atomic flux. An atom travelling initially at a velocity v undergoes cycles of absorption of counter-propagating photons and isotropic spontaneous emissions, thus yielding to a deceleration process. In a Zeeman slower an inhomogeneous magnetic field compensates the Doppler effect and avoids, after a few cycles only, an off-resonance between the atoms and the laser. In the case of an atom of ^{87}Rb of mass $m=1.45 \cdot 10^{-27} \text{ kg}$ with a laser characterized by the wavelength $\lambda = 780 \text{ nm}$, at each cycle the atom has its speed decreased by the recoil velocity, $v_R = h/(m\lambda) \simeq 6 \text{ mm.s}^{-1}$, corresponding to a cooling of approximately 100 nK . It takes typically 3 ms over 1 m to slow down an atom from 300 m.s^{-1} to 10 m.s^{-1} , equivalent to a temperature of 0.3 K . Other methods involve a chirp to accommodate the laser frequency to the Doppler effect.

The next step commonly used to cool atomic samples has been proposed by A. Ashkin in 1970 [140]. At a temperature close to 1 K , the atomic sample is cold enough to be trapped in a magneto-optical-trap (MOT) [141–149] where the atoms can be cooled further down thanks to the radiation pressure. The cooling principle is based again on the Doppler effect and on pairs of counter-propagating resonant beams red-detuned from the atomic transition, *i.e.* for $\delta = (\omega_L - \omega_0) < 0$, where ω_L is the light frequency and

¹At thermal equilibrium the atom distribution follows Boltzmann's statistics, with a temperature T such that $3k_B T = m \langle v \rangle^2$ [139].

ω_0 is the atomic resonance frequency. An atom moving with a velocity v is most likely subject to absorb an up-coming photon due to the resonance condition $\omega_L + kv \approx \omega_0$, where $k = 2\pi/\lambda$, than to absorb a photon from the co-propagating beam, for which the resonance condition is not fulfilled since then $\omega_L - kv < \omega_0$. The atom undergoes again cycles of photon absorption and isotropic spontaneous emission. This technique is referred to as the molasses cooling technique. It is important to note that an atom initially at rest has the same probability to absorb a photon from both directions, limiting therefore the cooling temperature. In 1985 S. Chu and A. Ashkin reported the cooling of a Sodium gas at a temperature of $T = 240 \mu\text{K}$ [150], corresponding approximately to the quantum limit of the transition used, with $k_B T \simeq h\Gamma/2$, where $1/\Gamma$ is the life time of the excited state. In comparison, in the case of ^{87}Rb , the Doppler cooling limit is $140 \mu\text{K}$. In addition, the optical molasses only provides an average force but does not trap atoms. After some cycles of absorption and emission, due to their erratic trajectories, atoms are finally ejected from the molasses environment. The MOT configuration takes advantages of an inhomogeneous magnetic field, inducing an extra energy level splitting. The absorption of photons depends now on the position of the atoms in space. The combination of molasses beams with a magnetic trap leads an atom to feel the sum of both a dissipative - cooling effect - and a restoring - trapping effect - force.

Some years after, subsequent studies have shown that temperatures below the Doppler limit and beyond theoretical models derived at that time can be accessed. In 1988, the group of W. D. Phillips reported the measurement of a temperature of $43 \pm 20 \mu\text{K}$, significantly below the Doppler cooling limit with a gas of Sodium [151]. This effect is nowadays referred as sub-Doppler cooling. One can more particularly cite the Sisyphus cooling scheme, where a degenerate atomic ground state is split by the presence of an electromagnetic field. In an optical molasses the interference of the two lasers leads to a standing wave, where the potential energy seen by an atom is modulated. Optical pumping gives the possibility to create cycles where an atom with non-zero velocity climbs the periodic potential hill and is then pumped to the bottom of the hill each half period of the standing wave. At each cycle the atom loses energy until not being able to climb the hill anymore. For ^{87}Rb , sub-Doppler cooling gives the possibility to cool an atomic ensemble to a few μK . In 2000, the group of S. Chu demonstrated the possibility to cool neutral atoms thanks to 3D-sideband cooling. They demonstrated this principle with a sample of $3 \cdot 10^8$ Cesium atoms cooled and spin polarized in 10 ms. They observed at minimum a 2D temperature of 210 nK [152]. For the developments of methods for cooling and trapping atoms with lasers, Steven Chu, Claude Cohen-Tannoudji and William D.

Phillips were awarded the 1997 Nobel Prize in Physics [128–130].

In 1924 with the collaboration of S. N. Bose, A. Einstein described the statistical distribution of identical particles with an integer spin, today referred as bosons [153]. Below a critical temperature a significant fraction of bosons occupy the lowest atomic quantum state of the system. At this stage, these atoms share the same phase and behave the same way to create a macroscopic coherent quantum state, the Bose-Einstein condensate. Experimentally, this stage is reached using the so-called “evaporative cooling” technique. It consists in decreasing the trap depth U of the external potential, where an atomic ensemble is confined at the temperature T , keeping constant the dimensionless ratio $U/(k_B T)$. At each step of the evaporative cooling process, the atoms with the highest energy “evaporate”, *i.e.* are ejected from the trap. After re-thermalization the atomic ensemble reaches a new equilibrium temperature $T' < T$ and the trap depth is decreased again. Typically, at the cost of decreasing by three orders of magnitude the initial atom number, the cloud enters the quantum degenerate regime. This condensation phenomenon was first observed in 1995 [154] at the University of Colorado, Boulder in the NIST-JILA laboratory by the team of E. Cornell and C. Wieman with a gas of Rubidium 87 cooled down to 170 nK. Shortly afterward W. Ketterle at MIT showed important properties of Bose-Einstein condensates with Sodium 23.

In 2001, for their achievements E. Cornell, C. Wieman, and W. Ketterle received the Nobel Prize in Physics [132, 155]. In the simplest case of ultracold temperatures, the condensed state can be described by the non-linear Schrödinger equation also known as the Gross-Pitaevskii equation.

1.3.2 The different regimes

In the case of a trapped atomic gas, different regimes can be identified depending on the gas density, n , and on the temperature T as shown in the Fig. 1.2. Within the gas, two characteristic distances are in competition, the average distance between the particles, $d \sim n^{-1/3}$, and the spatial extension of the atomic translational wave packet estimated with the thermal de Broglie wavelength

$$\lambda_{\text{dB}} = \sqrt{\frac{2\pi\hbar^2}{mk_B T}}, \quad (1.5)$$

where m is the mass of the atom. In the case of high temperatures, $d \gg \lambda_{\text{dB}}$, and the atomic ensemble can be described by distinguishable point-like particles [156] interacting through elastic collisions and described within the classical kinetic theory based on Boltz-

mann's equation [157]. Within this description, different regimes can be distinguished by the quantification of the collision rate. A direct comparison between the average distance between the particles and the mean free path of the atoms

$$\lambda_{\text{mfp}} = \frac{1}{\sqrt{2}n\sigma}, \quad (1.6)$$

where σ is the elastic scattering cross section, draws two limits. On one hand the regime where $\lambda_{\text{mfp}} \gg d$ is described as the collision-less regime. On the other hand the case $\lambda_{\text{mfp}} \ll d$ is described by hydrodynamics fluid laws where the particles undergo a large number of collisions such that local equilibrium is rapidly established [158–160].

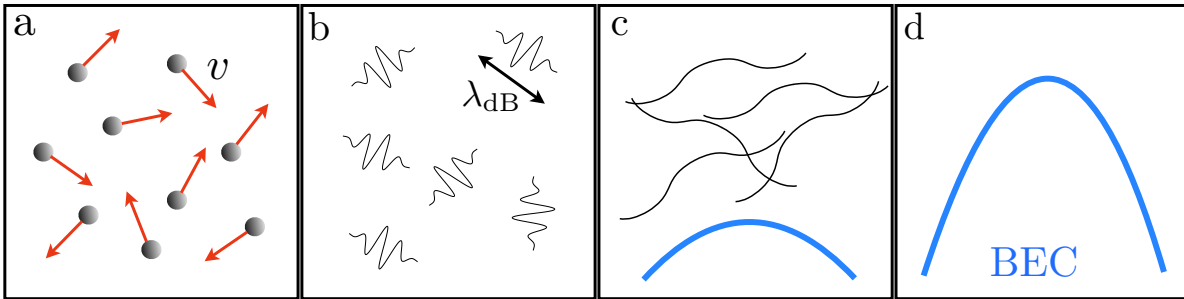


Figure 1.2: Bose-Einstein condensation. (a) High temperatures. The classical gas is described with the kinetic theory. (b) Low temperature. The wave nature of the particles appears, each particle is described by a wave function with a characteristic spatial extension given by λ_{dB} . (c) Critical temperature $T = T_C$. The wave-packets overlap and start to form a macroscopic quantum state. (d) Zero temperature. Formation of the macroscopic quantum state: The Bose-Einstein condensate. In the mean field approximation each atom of the condensate behaves similarly and shares a global phase. This figure is adapted from [156].

By cooling the atomic ensemble, the de Broglie wavelength and therefore the extension of the wave packet of each atom increases. When the ensemble is cooled to the point where λ_{dB} is comparable to inter-atomic separation d , the atomic wave packets start to overlap and the atoms start to become indistinguishable. In physics, the de Broglie's relation $\lambda = h/p$ asserts that all matter has an associated wave, and can exhibit wave-like behavior, the wave-particle duality [161]. The de Broglie thermal wavelength can therefore be interpreted as the position uncertainty associated with the momentum distribution. Cooling further down the atomic ensemble leads to the creation of a macroscopic quantum states. In the case of bosonic ensemble, the critical temperature is given by

$$T_c = \left(\frac{n}{\zeta(3/2)} \right)^{2/3} \frac{h^2}{2\pi k_B}, \quad (1.7)$$

where n denotes the bosons density, ζ the zêta function of Riemann, h the Planck constant and k_B the Boltzmann constant.

1.3.3 BEC interferometry

While the phase accumulated between the two paths of an atom interferometer is proportional to the time spent in the interferometer T_i and to the total effective wave number k_{eff} , two main strategies show up to increase the sensitivity of the measurement: (i) the increase of the momentum transfer [162–164] and (ii) the increase of the time spent in the interferometer [83, 165–168]. The two strategies come with different challenges. On one hand, large momentum transfer requires high laser powers to be sufficiently detuned and suppress spontaneous emission during the momentum transfer. On the other hand, the increase of the interferometer time up to seconds requires very low expansion temperatures of the cloud, an experimental setup of several meters long or microgravity operation. Only few experiments today meet these constrains [39, 40, 165, 169–171] and motivate the need of a microgravity environment such as a drop tower [168, 172], a zero-g parabolic flight [173], a sounding rocket [174], the International Space Station [175] or a satellite space mission [41], as shown in Fig. 1.3.



Figure 1.3: Different micro-gravity environments. From left to right, the Bremen drop tower experiment, the zero-g-Airbus A310, the launch of the Maius-1 sounding rocket, the International space station (ISS) and the CAL experiment. The different pictures were respectively taken from [174–180]

Recent proposals to test foundations of physics propose Bose-Einstein condensates as sources of atom interferometry sensors [41, 181]. Due to its narrower velocity distribution and smaller size compared to thermal ensembles, Bose-Einstein condensates offer the possibility to improve the efficiency of a beam splitter and thus to increase the contrast

of the matter wave interferometer [182]. Moreover, the compact size of a BEC initially and through the expansion decreases the systematic effects resulting from spatially dependent wave-front aberrations when the different laser-pulses are applied [106, 183–185]. This last effect is a leading systematic while testing the EEP. To give an order of magnitude, competitive UFF tests at the $\eta = 10^{-15}$ limit the expansion rate of the used atomic ensembles to $100 \mu\text{m}\cdot\text{s}^{-1}$. The delta-kick collimation (DKC) technique allows to efficiently slow down the expansion of atomic clouds [186, 187]. **Adapting schemes relying on DKC to realistic cases and to dual-species BEC sources is another motivation of this thesis.**

The mean field energy of BECs is a challenge while using them in the metrology field. For long-time free-space interferometers, however, this energy is dissipated in few tens of seconds. BEC machines with high repetition rates (10^5 condensed atoms/s), as demonstrated in the QUANTUS project [168], for instance, allow for a metrologically-significant use of a transportable BEC experiment.

1.4 Objectives of the thesis

A violation of the UFF is detected by a non-zero differential acceleration of the different test masses. A differential mismatch in position, velocities and temperature expansion rate between the two test masses lead to gravity-gradients coupling systematics and wave-front aberrations effects. These effects are the leading systematics to date in realized or projected UFF tests. It is therefore crucial to carefully engineer the atomic source initial conditions.

More precisely, performing a quantum test of the UFF on ground with an accuracy at the level of $\eta = 10^{-15}$ [40] relies on the possibility to define the differential position and velocity of the two test masses at a level better than $1 \mu\text{m}$ and $1 \mu\text{m}\cdot\text{s}^{-1}$, respectively [37, 43, 44]. Moreover, the expansion rates of the two clouds have to not exceed $100 \mu\text{m}\cdot\text{s}^{-1}$, equivalent to an expansion energy of 70 pK. Last but not least, the duty cycle of the experiment is typically constrained to a maximum of 10 s, speaking for a fast implementation despite the challenging requirements.

In this thesis, the aim is to tackle these objectives in the most realistic way possible. In most of the cases, a direct successful comparison between the proposed theoretical methods and experimental results was taking place. Different schemes were found mainly realize the following objectives:

1. **Controlled transports of a BECs over large distances in realistic experi-**

mental configurations. This is performed with Shortcut-to-adiabaticity (STA) protocols giving the possibility to engineer transport ramps thanks to the reverse engineering technique with specific desired final positions in time frames dramatically faster than what an adiabatic transformation would require. These protocols have been implemented in the microgravity atom chip-based experiment Quantus-2 where the transport of a BEC mm away from the chip surface was successful in 100 ms time and with a residual oscillation of few $\mu\text{m}\cdot\text{s}^{-1}$. Comparable transport and manipulation protocols were developed and implemented within of the first space BEC experiment realized in 2017 on board of the MAIUS sounding rocket.

2. **Control of the expansion velocity of a single atomic species with the Delta-kick-collimation (DKC) technique.** Optimized sequences, involving the characterization of the excited modes of the BEC after transport are proposed such that the size of the BEC is constrained to few hundred of microns after few seconds with a expansion energy as low as few tens of pK.
3. **The generalization of points (1) and (2) to the simultaneous manipulation of two species.** Optimal Control theory (OCT) protocols are developed to tackle the case of a non interacting mixture of two thermal clouds. The results of it were successfully put in practice in the Stanford 10-m fountain. A study of the collimation of an interacting BEC mixture where the interaction between the two species can be controlled with Feshbach resonances is done.

1.5 Thesis outline

My doctoral work started during the summer of 2015. At that time the Quantus-2 drop tower experiment required theoretical support to control the dynamics of the produced Bose-Einstein condensates. In parallel, the Maius sounding rocket mission entered its calibration phase.

- In this context, chapter 2 summarizes studies of the magnetic transport of a BEC away from an atom chip surface. Due to the proximity of the atoms to the chip surface, high magnetic field gradients makes it possible to create a BEC of 10^5 atoms within 1 s [168]. Close to the chip, nevertheless, the proximity of the BEC to the surface in high trap frequencies is far from being favorable for an interferometry sequence. It is then required to transport the BEC in a lower trap frequency

configuration and in a lower noise environment. In this chapter we introduce the reverse engineering technique to engineer Shortcut-to-adiabaticity transport ramps. The transport is then analyzed with a semi-classical approach and the Gross-Pitaevskii equation is used to describe the evolution of the wave-function and its excitations. Experimental results of the Quantus-2 drop tower experiment and Maius-1 sounding rocket are discussed in this chapter.

In a later phase of my PhD, I have been invited to join the team of M. Kasevich for a three-month research stay at Stanford. During this exchange, the development of OCT protocols and an N -particle simulation tool was done.

- Chapter 3 starts with a description of the Optimal Control Theory and of the aforementioned N -particle simulation tool. These theoretical approaches are then applied in the context of two applications. The first one is the transport of two non-interacting thermal ensembles in the case of the experiment at Stanford. Optimized sequences are then proposed for their specific experimental setup. The second application proposes a new sequence to increase the phase space density of an atomic ensemble. The aim of this study is to highlight the possibility to reach Bose-Einstein condensation with higher atom numbers. The idea is currently adapted to be tested in an experimental setup in Hanover.

Motivated by the different competitive UFF tests proposals, the rest of my doctoral research has been dedicated to the generalization of the previous concepts to the study of a two-component quantum fluid.

- In chapter 4 different ground state configurations of a bosonic degenerate mixture are presented. A study of the dynamics is then conducted with a comparison between a semi-classical approach and the simulation using Gross-Pitaevskii equations. The last section of this chapter proposes a sequence of twin atomic lenses to significantly reduce the expansion temperature of the two species in interaction and the control of the shape of the two condensates is discussed in the context of precise measurements.

A last chapter finally summarizes the results of the thesis and highlights some perspectives of future studies.

OPTIMIZED MANIPULATION OF A SINGLE-SPECIES CONDENSATE

Contents

2.1	Introduction	18
2.2	Scheme and atom chip model	20
2.2.1	Scheme	20
2.2.2	Chip model	21
2.3	Theoretical model	22
2.3.1	Semi-classical approach	23
2.3.2	Reverse engineering protocols	28
2.4	Theoretical Results	30
2.4.1	Control of the BEC position dynamics	30
2.4.2	Robustness of the STA protocol	33
2.4.3	Dynamics of the atomic cloud size	35
2.4.4	Collective excitations and optimization of the expansion dynamics	38
2.5	Micro-gravity experimental implementation	43
2.5.1	The Quantus 2 drop tower experiment	43
2.5.2	The MAIUS-1 sounding rocket mission	45
2.6	Conclusion and outlook	48

In this chapter, I present a detailed theoretical analysis of the implementation of shortcut-to-adiabaticity protocols for the fast transport of neutral atoms with atom chips. The objective is to engineer transport ramps with durations not exceeding a few hundred milliseconds to provide metrologically-relevant input states for an atomic sensor. Aided by numerical simulations of the classical and quantum dynamics, I study the behavior of a Bose-Einstein condensate in an atom chip setup with realistic anharmonic trapping. A realistic atom chip model is described in section 2.2. Details on the implementation of fast and controlled transports over large distances of several millimeters, *i.e.* distances 1000 times larger than the size of the atomic cloud, are presented. A subsequent optimized release and collimation step demonstrates the capability of the transport method to generate ensembles of quantum gases with expansion speeds in the pico-Kelvin regime. The performance of this procedure is analyzed in terms of collective excitations reflected in residual center of mass and size oscillations of the condensate. I further evaluate the robustness of the protocol against experimental imperfections. The theory is developed in section 2.3 and the results are shown in section 2.4. In section 2.5, I present the results of the STA protocols obtained by the experimental team of the Quantus 2 drop-tower experiment where my contribution to this work was to deliver a current control STA sequence to transport the BEC over a millimeter within 150 ms. As part of the MAIUS-1 sounding rocket project I also present the results of the experimental Maius 1 team where my contribution consisted in interpreting the observed data with simulations of the BEC dynamics. A significant part of the results presented in this chapter has been the subject of recent papers [174, 188, 189], for which I was a co-author.

2.1 Introduction

Recent proposals for the implementation of fundamental tests of the foundations of physics assume Bose-Einstein condensates (BEC) [190, 191] as sources of atom interferometry sensors [40, 42, 125, 181]. In this context, atom chip devices have allowed to build transportable BEC machines with high repetition rates, as demonstrated within the Quantus project for instance [168, 172]. The proximity of the atoms to the chip surface is, however, limiting the optical access and the available interferometry time necessary for precision measurements. This justifies the need of well-designed BEC transport protocols in order to perform long-baseline, and thus precise, atom interferometry measurements.

The controlled transport of atoms is a key ingredient in many experimental platforms dedicated to quantum engineering. Neutral atoms have been transported as thermal atomic clouds [192–194], condensates [195, 196], or individually [197, 198], using magnetic or optical traps. Transport of ions with electromagnetic traps has also been achieved recently [199, 200]. In all those experimental realizations, the transport was performed in 1D. When solving the transport problem, it is tempting to first consider the most trivial solution: the *adiabatic* transport. Yet, besides the fact that the adiabatic solution is far from optimal, it is usually not possible to implement it due to typical experimental constraints. Close to an atom chip surface for example, fluctuations of the chip currents constitute an important source of heating for the atoms, which can lead ultimately to the destruction of the BEC. A nearly adiabatic, and therefore slow, transport is consequently unpractical in most cases. Pioneering theoretical work on fast transport was reported in [201] and shortcut-to-adiabaticity (STA) protocols were proposed [202] to implement fast, non-adiabatic transport with well defined boundary conditions. Such a reduction of the time overhead can be promising as well for scalable quantum information processing in certain architectures [203, 204]. On the theoretical side, the protocols that have been proposed relied either on optimal control [205, 206], counterdiabatic driving [207, 208] or reverse engineering [209] and the validity of a variety of such fast transport protocols for BECs was established beyond the mean-field regime [210, 211]. Besides the transport in harmonic traps, the transport in the presence of anharmonicities [212–214] or the issues related to robustness have been extensively discussed [215]. Experimentally, it is worth noting that STA transport protocols were successfully implemented for BECs [216] and for trapped ions in phase space [217].

The optimization proposed here is found using a reverse engineering method applied to a simplified one-dimensional approximation of the system’s classical equations of motion. This solution is then tested numerically in a full three-dimensional quantum calculation using a time-dependent mean-field approach [218, 219]. Our results are then analyzed in terms of residual center-of-mass and size oscillations of the condensate density distribution in the final trap, at the end of the transport. We then propose to implement a subsequent holding step whose duration is precisely controlled in order to minimize the expansion rate of the BEC in directions where a delta-kick collimation (DKC) procedure [165, 167, 186, 187] is not efficient. This DKC step towards the pK regime is necessary for atom interferometry experiments lasting several seconds. The conclusion of this chapter is that, with the conjugation of (i) a controlled transport, (ii) a controlled holding time, and (iii) a well-designed final DKC step, it is possible to

displace BECs by millimeters and to reach expansion speeds in the pK regime. Indeed, the practical implementation we are discussing here leads to an optimal final expansion temperature of 2.2 pK.

The outline of the chapter is as follows: in section 2.2 we describe the architecture of the atom chip and of the magnetic bias field creating the time-dependent potential for the atoms, with strong confinement in two dimensions. We also give the values of currents, bias field, and wire sizes that realize this time-dependent trap. In section 2.3 we present the theoretical models we are using and their associated numerical implementations, as well as the reverse engineering technique we have adopted. In section 2.4 we give the results of our numerical investigations on the performance of the controlled transport and expansion of the condensate. We also discuss here the robustness of the proposed protocol. Conclusions and prospective views are given in the final section 2.6.

2.2 Scheme and atom chip model

2.2.1 Scheme

In this section we introduce the atom chip model and the trapping potential used in the present study. Atom chips designed for the manipulation of neutral atoms are insulating substrates with conducting micro-structures such as metal wires [195, 220, 221]. The wire geometry design can easily be adapted for a particular application [222]. DC wire currents generate inhomogeneous magnetic fields which can be used to trap atoms near the chip surface where high magnetic field gradients produce high trap frequencies and enable fast evaporation. This allows high-flux BEC creation of typically 10^5 atoms/s [168].

We consider here the case of a Z-shaped chip configuration [223], as shown in Fig. 2.1, in the presence of a time-dependent homogeneous magnetic bias field $B_{bias}(t)$. If the bias field varies slowly, the spins of the atoms remain adiabatically aligned with the total magnetic field. In the weak field approximation and in the absence of gravity, the trapping potential can be expressed as

$$V(\mathbf{R}, t) = m_F g_F \mu_B B(\mathbf{R}, t), \quad (2.1)$$

where μ_B is the Bohr magneton, g_F is the Landé factor, m_F is the azimuthal quantum number, and $B(\mathbf{R}, t)$ is the total magnetic field. The three-dimensional spatial position is denoted by $\mathbf{R} \equiv (X, Y, Z)$. As shown in Ref. [192], a temporal variation of the magnetic

field can be used to transport the atoms. Our goal here is to design and test a fast transportation scheme for a realistic setup. We show how the implementation of such a scheme is feasible by specializing our discussion to the hyperfine state $|F = 2, m_F = 2\rangle$ of the ground $5S_{1/2}$ state of ^{87}Rb as a study case. This hyperfine state is a low-field seeking state with $g_F = +1/2$ [224].

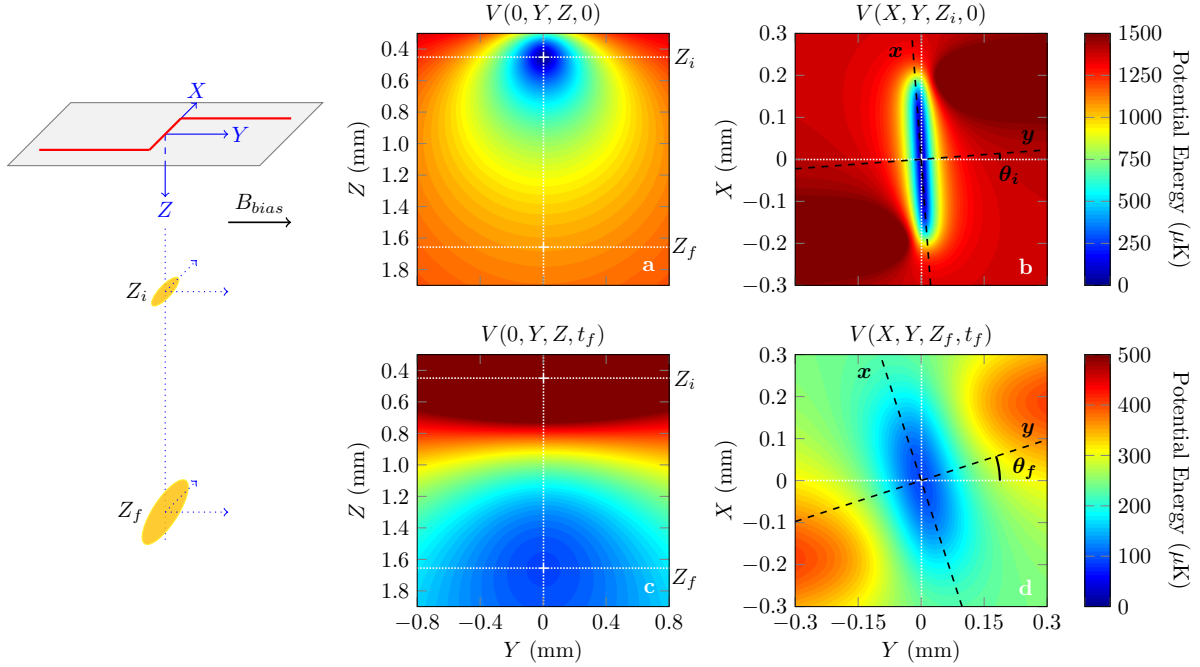


Figure 2.1: *Left panel*: Schematic representation of the chip configuration and of the displacement of the BEC. *Other panels*: (a) and (b) show two cuts of the initial trapping potential $V(\mathbf{R}, 0)$ in the (YZ) and (XY) planes, respectively. (c) and (d) show similar cuts of the trapping potential $V(\mathbf{R}, t_f)$ at the end of the transport procedure corresponding to the time $t = t_f$. The dashed black lines in panels (b) and (d) serve to illustrate the tilt angle $\theta(t)$ of the principal axis x and y of the trap in the (XY) plane. The associated energy color scales are given on the right side, in μK .

2.2.2 Chip model

The Z-shaped wire is represented schematically on the left side of Fig. 2.1. In a first approximation the wires are considered as infinitely thin. The two wires aligned along the Y-axis are 16 mm long. The wire along X measures 4 mm. They carry a DC current $I_w = 5 \text{ A}$. The magnetic bias field $B_{bias}(t)$ points along Y and its magnitude varies between $B_{bias}(0) = 21.5 \text{ G}$ (initially) and $B_{bias}(t_f) = 4.5 \text{ G}$ (at the end of the displacement). These parameters are close to those used in the Quantus experiment [168] and we used

the Biot and Savart law to develop an analytic model of the Z-chip. The approximation of infinitely thin wires leads to errors in the magnetic field calculation very close to the atom chip, where the finite size of the atom chip wires can play a role. In such configurations finite element calculations have to be considered [225], but it is not the case in our setup.

Slices of the initial trapping potential $V(\mathbf{R}, 0)$ at time $t = 0$ in the (YZ) and (XY) planes are shown in panels (a) and (b) of Fig. 2.1, respectively. As shown in the left panel of Fig. 2.1, Z denotes the distance to the chip surface. The atoms are initially trapped at a distance $Z_i \approx 0.45$ mm from the chip surface directly under the origin of the axes. The shape of the trap seen in panel (a) shows a strong confinement in the Y and Z directions with similar trap frequencies $\nu_Y(0)$ and $\nu_Z(0)$. On the contrary, the cigar shape seen in panel (b) reveals that $\nu_X(0) \ll \nu_Y(0) \approx \nu_Z(0)$. The initial trap is thus characterized by a strong two dimensional confinement in the Y and Z directions. The initial potential shows a small tilt angle $\theta(0) = \theta_i \approx 1.53$ deg in the (XY) plane. In Fig. 2.1, the positions of the initial and final potential minima are marked by a white '+' sign. The trapping potential $V(\mathbf{R}, t_f)$ obtained at the end of the transport ($t = t_f$) is shown in panels (c) and (d) of Fig. 2.1. At this time the minimum of the potential is located at a distance $Z_f \approx 1.65$ mm from the chip surface and is again centered in the (XY) plane. The BEC transport takes place over a total distance $Z_f - Z_i \approx 1.2$ mm. This distance is much larger than the typical size of the BEC, of a few μm . The comparison of panels (a) and (c), and of panels (b) and (d) shows that during the transport the depth of the trap along Y and Z decreases a lot while remaining of the same order of magnitude along X . Thus, at t_f the aspect ratio is not as large as initially, and $\nu_X(t_f) < \nu_Y(t_f) \approx \nu_Z(t_f)$. The tilt of the potential has increased to $\theta(t_f) = \theta_f \approx 12.5$ deg. In order to calculate the three eigenfrequencies of the rotated trap, one can diagonalize the Hessian matrix associated to the potential [226]. This allows to rotate the coordinate system by the tilt angle $\theta(t)$, and to define the new coordinates $\mathbf{r} \equiv (x, y, z)$, with $z = Z$, associated with the three eigen-axes of the trap at any time t . The rotated axes x and y are shown as black dotted lines in Figs. 2.1b and 2.1d.

2.3 Theoretical model

In the harmonic approximation the trapping potential generated by the chip can be written as

$$V(\mathbf{r}, t) = \frac{1}{2}m [\omega_x^2(t)x^2 + \omega_y^2(t)y^2 + \omega_z^2(t)(z - z_t)^2], \quad (2.2)$$

where z_t denotes the position of the minimum of the trap along the z -axis at time t and $\omega_\alpha(t) = 2\pi \cdot \nu_\alpha(t)$ for $\alpha = x, y$ or z . For a more precise description of the trap, the lowest order anharmonic term (cubic) along z should be included, yielding the anharmonic potential

$$V_\alpha(\mathbf{r}, t) = V(\mathbf{r}, t) + \frac{1}{3} m \omega_z^2(t) \frac{(z - z_t)^3}{L_3(t)}, \quad (2.3)$$

where $L_3(t)$ determines the characteristic length associated with this third order anharmonic term. For typical chip geometries as reported in Ref. [168], the cubic term is by far the largest correction to the harmonic order.

Fig. 2.2 shows the different trap parameters used in this study such as the position of the minimum of the trap along the z -axis, z_t (panel a), the trapping frequencies ν_x , ν_y and ν_z (panel b), the parameter L_3 (panel c), and the tilt angle θ (panel d). z_t is shown as a function of the experimentally tunable parameter B_{bias} while all other parameters are shown as a function of z_t for the sake of simplicity. In table 2.1, we give the coefficients of the different forms of Padé fits (2.4) used for these quantities.

$$f(t) = \frac{A_0 + A_1 B_{bias}(t) + A_2 B_{bias}^2(t)}{1 + C_1 B_{bias}(t) + C_2 B_{bias}^2(t)}, \quad (2.4a)$$

$$g(t) = \frac{1}{2\pi} \sqrt{\frac{A_0 + A_1 z_t(t) + A_2 z_t^2(t)}{1 + C_1 z_t(t) + C_2 z_t^2(t)}}, \quad (2.4b)$$

$$h(t) = \frac{A_0 + A_1 z_t(t) + A_2 z_t^2(t)}{1 + C_1 z_t(t) + C_2 z_t^2(t)}, \quad (2.4c)$$

$$i(t) = \frac{A_0 + A_1 z_t(t) + A_2 z_t^2(t) + A_3 z_t^3(t)}{1 + C_1 z_t(t) + C_2 z_t^2(t)}. \quad (2.4d)$$

2.3.1 Semi-classical approach

It is well known that, if the potential remains (to a good approximation) harmonic at all time, the average position of the condensate follows Newton's classical equation of motion according to the Ehrenfest theorem [228]. Since the potential minimum in the X - and Y -directions remains at the origin, the instantaneous position of the center-of-mass of the BEC will fulfill $X_\alpha(t) = Y_\alpha(t) = 0 = x_\alpha(t) = y_\alpha(t)$ during the entire propagation. Along z , in the harmonic approximation and in the absence of gravity, the center-of-mass position $Z_\alpha(t) = z_\alpha(t)$ simply follows

$$\ddot{z}_\alpha(t) + \omega_z^2(t)(z_\alpha(t) - z_t) = 0. \quad (2.5)$$

		Fitting Coefficients					
Quantity	Form	A_0	A_1	A_2	A_3	C_1	C_2
v_x	$f(t)$	-3.2354	44066	$2.1609 \cdot 10^6$	–	1061.0	$7.8991 \cdot 10^5$
v_y		1.1455	$3.8222 \cdot 10^4$	$4.8131 \cdot 10^7$	–	-340.38	$4.9526 \cdot 10^4$
θ		28.915	$-2.4456 \cdot 10^4$	$5.1197 \cdot 10^6$	–	1992.0	$-8.4329 \cdot 10^5$
v_z	$g(t)$	$1.4008 \cdot 10^6$	$-6.5543 \cdot 10^8$	–	–	$-4.5229 \cdot 10^4$	$5.5027 \cdot 10^6$
L_3^{-1}	$h(t)$	$4.1633 \cdot 10^4$	$-1.2821 \cdot 10^7$	–	–	$-1.7284 \cdot 10^4$	$6.4326 \cdot 10^6$
B_{bias}	$i(t)$	$1.7253 \cdot 10^5$	$1.5058 \cdot 10^7$	$-5.1633 \cdot 10^{10}$	$1.6122 \cdot 10^{13}$	$1.7553 \cdot 10^{11}$	$-1.2814 \cdot 10^{12}$

Table 2.1: Parameters used for the simulations of the atom chip.

In practice, to take into account the eventual influence of anharmonicities we consider that the classical transport trajectory $z_a(t)$ is a solution of the anharmonic equation

$$\ddot{z}_a(t) + \omega_z^2(t)(z_a(t) - z_t) \left(1 + \frac{z_a(t) - z_t}{L_3(t)} \right) = 0, \quad (2.6)$$

in agreement with Eq. (2.3).

The collective excitations, also named size dynamics of the condensate, are treated using a semi-classical approach. This approach is described in [229–231] and we just give here the main steps of the calculation. We start from an atomic density distribution given initially (at time $t = 0$) by the Thomas-Fermi approximation[231]. This approximation consist on neglecting the kinetic term of the time independent Gross-Pitaevskii equation,

$$\mu \psi(\vec{r}, 0) = \left[-\frac{\hbar^2}{2m} \vec{\nabla}_{\vec{r}}^2 + U(\vec{r}, 0) + Ng|\psi(\vec{r}, 0)|^2 \right] \psi(\vec{r}, 0), \quad (2.7)$$

with μ the chemical potential, U the external potential, m the mass of the atom and g is related to the s-wave scattering length of ^{87}Rb , a , by the relation

$$g = \frac{4\pi\hbar^2 a}{m}. \quad (2.8)$$

The classical density of the cloud is then expressed in the Thomas-Fermi approximation as:

$$\rho(\vec{r}, 0) = N|\psi(\vec{r}, 0)|^2 = \begin{cases} \frac{\mu - U(\vec{r}, 0)}{g} & \text{if } U(\vec{r}, 0) \leq \mu \\ 0 & \text{otherwise,} \end{cases} \quad (2.9)$$

where the chemical potential μ is found by the normalization condition

$$\iiint \rho(\vec{r}, 0) d\vec{r} = N. \quad (2.10)$$

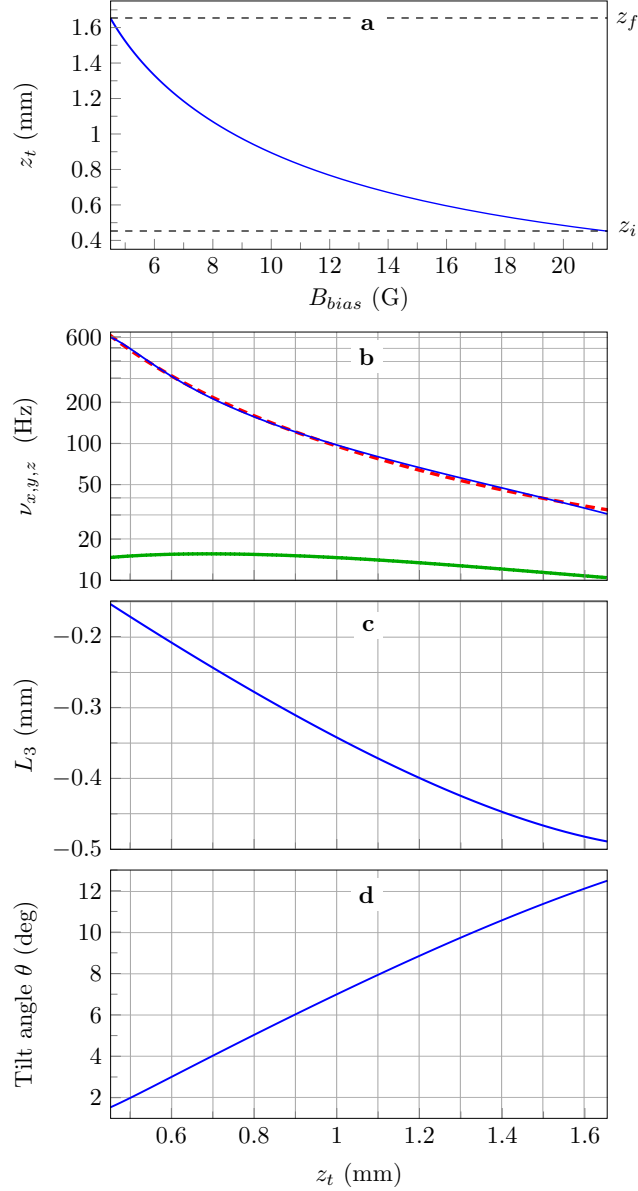


Figure 2.2: (a) Position z_t (in mm) of the minimum of the trap with respect to the chip surface (z -direction) as a function of the magnetic bias field B_{bias} (in G). Note that $B_{bias} = 21.5$ G at time $t = 0$ and that $B_{bias} = 4.5$ G at the end of the displacement (time $t = t_f$). The two horizontal dashed lines mark the values of the initial and final trap-to-chip distances z_i and z_f , respectively. (b) Trapping frequencies ν_x (thick green line), ν_y (dashed red line) and ν_z (thin blue line) in Hz (log scale) as a function of z_t (in mm). (c) Anharmonic coefficient L_3 (in mm) as a function of z_t (in mm). (d) Tilt angle θ (in degrees) as a function of z_t (in mm). For the simulations presented later in the chapter, we use accurate analytical fits of the quantities plotted here using second- or (when necessary) third-order Padé approximants [227].

In the case of an external harmonic trap this yields

$$\mu = \frac{\hbar\bar{\omega}(0)}{2} \left(15Na \sqrt{\frac{m\bar{\omega}(0)}{\hbar}} \right)^{2/5}, \quad (2.11)$$

where $\bar{\omega}(0) = [\omega_x(0)\omega_y(0)\omega_z(0)]^{1/3}$ is the geometric mean of the three oscillator frequencies. The sizes of the initial BEC along the directions x , y and z are characterized by the lengths $R_x(0)$, $R_y(0)$ and $R_z(0)$ given by

$$R_\alpha(0) = a_{osc} \left(\frac{15Na}{a_{osc}} \right)^{1/5} \frac{\bar{\omega}(0)}{\omega_\alpha(0)} \quad \text{for } \alpha \in \{x, y, z\}, \quad (2.12)$$

with $a_{osc} = [\hbar/(m\bar{\omega}(0))]^{1/2}$ the average quantum-mechanical length scale of the 3D harmonic oscillator.

We now introduce the classical force seen by each atom of the BEC as a sum of the gradient of the external potential confining the cloud and the gradient of the mean field interaction describing the repulsion force within the condensate

$$\vec{F}(\vec{r}, t) = -\vec{\nabla} [U(\vec{r}, t) + g\rho(\vec{r}, t)]. \quad (2.13)$$

In the case of a harmonic trap, in the TF approximation the parabolic shape of the cloud remains unaltered and the cloud just experiences a dilatation or a compression, which can be described by three scaling coefficients, $\lambda_\alpha(t)$. The size and shape evolution of the cloud is then given by the set of equations

$$R_\alpha(t) = \lambda_\alpha(t) R_\alpha(0), \quad (2.14)$$

and

$$\rho(\vec{r}, t) = \frac{\rho(\vec{r}', 0)}{\lambda_x(t)\lambda_y(t)\lambda_z(t)}. \quad (2.15)$$

In this expression the coordinates \vec{r} and \vec{r}' are defined as

$$\vec{r} = x\vec{u}_x + y\vec{u}_y + z\vec{u}_z \quad \text{and} \quad \vec{r}' = \frac{x}{\lambda_x(t)}\vec{u}_x + \frac{y}{\lambda_y(t)}\vec{u}_y + \frac{z}{\lambda_z(t)}\vec{u}_z. \quad (2.16)$$

Finally, Newton's law applied to the size dynamics yields

$$\ddot{\lambda}_\alpha(t) + \omega_\alpha^2(t)\lambda_\alpha(t) = \frac{\omega_\alpha^2(0)}{\lambda_\alpha(t)\lambda_x(t)\lambda_y(t)\lambda_z(t)}. \quad (2.17)$$

These ‘‘scaling laws’’ assume that the BEC keeps its parabolic shape at all time and that the condensate follows adiabatically the rotation of the trap in the (XY) plane. The

right hand side of Eq.2.17 describes the coupling of the three directions through the mean field term of the GPE equation and explains why the size evolution couples the three directions in the general case. Knowing the parabolic shape of the wave function, these three typical sizes $R_\alpha(t)$ can be related to the three widths $\Delta\alpha(t)$ (*i.e.* the standard deviations in the directions $\alpha = x, y$ and z) of the BEC wave function. After calculation we find

$$\Delta\alpha(t) = \frac{R_\alpha(t)}{\sqrt{7}}. \quad (2.18)$$

Numerically, we also evaluate these three widths $\Delta x(t)$, $\Delta y(t)$ and $\Delta z(t)$ from the solution of the time-dependent Gross-Pitaevskii equation.

2.3.1.1 Collective excitation modes.

We use the scaling approach Eq. (2.17) to describe the characteristic size excitations of the BEC which arise in the final trap at the end of the transport protocol, due to the fast anisotropic trap decompression over the transport. These excitations can be described as a sum of different collective modes with different amplitudes [229, 230, 232–237].

The first low lying collective excitation modes of a BEC in a cigar shape potential are well known [232]. They can be easily described if we approximate the atom chip trapping potential at time t_f by

$$V(\mathbf{r}, t_f) \approx \frac{1}{2} m \omega_\perp^2 (\eta^2 x^2 + r_\perp^2), \quad (2.19)$$

where $r_\perp = \sqrt{y^2 + z^2}$ and $\omega_\perp = \omega_y(t_f) \approx \omega_z(t_f)$. The trap aspect ratio is denoted here by $\eta = \omega_x(t_f)/\omega_\perp$. For a low degree of excitation, these modes form a basis of six possible excitations, as depicted schematically in Fig. 2.3.

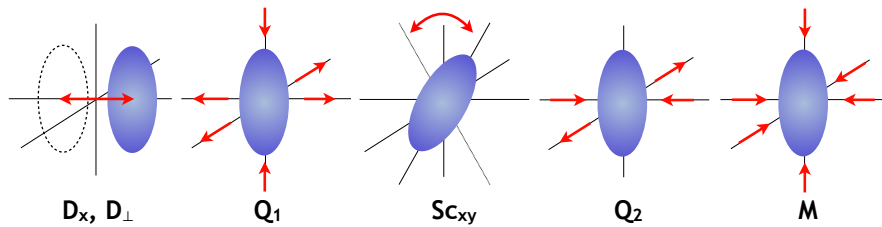


Figure 2.3: Schematic representation of the excitation dynamics of the condensate for the first lowest excitation modes. From left to right: the dipole oscillations D_x and D_\perp , the first quadrupole mode Q_1 , the scissors mode $S_{c_{xy}}$, the second quadrupole mode Q_2 , and the monopole mode M .

These modes are associated with specific, characteristic frequencies [232]

$$\omega_{D_x} = \eta \omega_{\perp} = \omega_x(t_f), \quad (2.20a)$$

$$\omega_{D_{\perp}} = \omega_{\perp}, \quad (2.20b)$$

$$\omega_{Q_1} = [2 + 3\eta^2/2 + \delta/2]^{1/2} \omega_{\perp}, \quad (2.20c)$$

$$\omega_{Q_2} = \sqrt{2} \omega_{\perp}, \quad (2.20d)$$

$$\omega_{Sc_{xy}} = [1 + \eta^2]^{1/2} \omega_{\perp}, \quad (2.20e)$$

$$\omega_M = [2 + 3\eta^2/2 - \delta/2]^{1/2} \omega_{\perp} \quad (2.20f)$$

where $\delta = [9\eta^4 - 16\eta^2 + 16]^{1/2}$. The dipole modes D_{\perp} and D_x show a classical oscillation of the center of mass of the condensate at the trap frequencies $\omega_{D_{\perp}} = \omega_{\perp}$ and $\omega_{D_x} = \eta \omega_{\perp} = \omega_x(t_f)$, respectively. The first quadrupole mode Q_1 shows a simultaneous expansion of the two strong axes, while the weak axis is compressed. In the second quadrupole mode, Q_2 , the weak axis does not oscillate and the size oscillations are only present along the two strong axes. The scissors mode Sc_{xy} shows the effect of the trap rotation about the direction of transport, and the monopole mode M , also called breathing mode, shows an alternating compression and expansion of the condensate in the three directions in phase.

2.3.2 Reverse engineering protocols

We present here the method of reverse engineering, used to find a perturbation-free transport of the center of mass of the BEC [238, 239] within a shortcut-to-adiabaticity (STA) approach. This reverse engineering protocol works as follows: We set the classical trajectory of the atoms, $z_a(t)$, according to fixed boundary conditions, which have to be fulfilled experimentally to ensure an optimized transport, *i.e.* initially and finally the center of mass has to be at rest, at the position of the minimum of the trap. This leads to the following boundary conditions

$$z_a(0) = z_i \quad \dot{z}_a(0) = 0 \quad \ddot{z}_a(0) = 0, \quad (2.21)$$

$$z_a(t_f) = z_f \quad \dot{z}_a(t_f) = 0 \quad \ddot{z}_a(t_f) = 0, \quad (2.22)$$

where z_i and z_f denote the initial and final positions, respectively. To account for experimental constraints, we also wish the trap to be at rest initially and finally. We therefore impose

$$z_t(0) = z_i \quad \dot{z}_t(0) = 0 \quad \ddot{z}_t(0) = 0, \quad (2.23)$$

$$z_t(t_f) = z_f \quad \dot{z}_t(t_f) = 0 \quad \ddot{z}_t(t_f) = 0. \quad (2.24)$$

The conditions on the second derivatives of the positions are imposed to enforce smooth magnetic field changes. Inserting these last six constraints in Newton's equations Eq. (2.5) or Eq. (2.6) shows that they are equivalent to the additional four constraints

$$z_a^{(3)}(0) = 0 \qquad z_a^{(4)}(0) = 0, \qquad (2.25)$$

$$z_a^{(3)}(t_f) = 0 \qquad z_a^{(4)}(t_f) = 0, \qquad (2.26)$$

where the exponent (n) denotes the n^{th} time derivative. These four extra boundary conditions Eq. (2.25) - Eq. (2.26) can be seen as additional robustness constraints against oscillations of the center of mass of the BEC in the final trap. The simplest polynomial solution to the ten boundary conditions is the polynomial function of order nine

$$z_a(t) = z_i + (z_f - z_i) [126 u^5 - 420 u^6 + 540 u^7 - 315 u^8 + 70 u^9], \qquad (2.27)$$

where $u = u(t)$ denotes the rescaled time t/t_f . The second derivative of the polynomial function Eq. (2.27) presents a sine-like variation due to the presence of an acceleration stage followed by a deceleration step. This suggests a non-trivial Ansatz for $z_a(t)$ in the form

$$z_a(t) = z_i + \left(\frac{z_f - z_i}{12\pi} \right) [6v - 8 \sin(v) + \sin(2v)], \qquad (2.28)$$

whose second derivative presents a similar sine-like shape, and where

$$v = v(t) = 2\pi \left(\frac{1 + a u + b u^2}{1 + a + b} \right) \frac{t}{t_f}, \qquad (2.29)$$

is a 'chirped' function of time. The constants a and b act here as two additional control parameters, making this solution more powerful than the simple polynomial one¹. These parameters can be optimized to limit the impact of the anharmonic term in Eq. (2.3) in order to recover a BEC at rest after the transport. Note that, according to Eq. (2.6), to limit the anharmonic effects, one has to fulfill the following criterium

$$\chi(t) = \left| \frac{z_a(t) - z_t}{L_3(t)} \right| \ll 1, \quad \forall t. \qquad (2.30)$$

The elaborate form Eq. (2.28) of $z_a(t)$ is used in Sec. 2.4 with $a = -1.37$ and $b = 0.780$. With such parameters the maximum value reached by $\chi(t)$ during the transport is 0.03 while it reaches 0.09 without any chirp (*i.e.* for $a = b = 0$). Once $z_a(t)$ is defined, one can extract the time evolution of the minimum of the trap, $z_t(t)$, using Eq. (2.5) in

¹In the case of the polynomial ansatz one can increase the degree of the polynomial function to add some tunable control parameter such as the control of the position, velocity or acceleration of the particle at $t_f/2$ for example.

combination with the fit of the angular trap frequency along the z -axis, see Eq. (2.4b). Thanks to this simple but accurate form chosen for the fit of ω_z it is easy to infer the evolution of the minimum of the trap $z_t(t)$ as a function of $z_a(t)$ and its derivatives, by solving analytically the simple second order polynomial equation

$$(C_2\ddot{z}_a - A_1)z_t^2 + (A_1z_a + C_1\dot{z}_a - A_0)z_t + (\ddot{z}_a + A_0z_a) = 0. \quad (2.31)$$

Technically, since the trap minimum position $z_t(t)$ is related to $B_{bias}(t)$ unambiguously, see Eq. (2.4d), a straightforward experimental implementation of such protocols can easily be implemented in a real experiment.

It can be noted that the reverse engineering protocol is not limited to harmonic traps. Out of Eq. (2.4b), Eq. (2.4c) and Eq. (2.6), it is possible to infer a trajectory for the trap minimum $z_t(t)$ dealing with the real trap configuration. As before the form of the fits describe accurately the behavior of the angular trap frequency and of the cubic term L_3 and this gives the possibility to infer the evolution of the minimum of the trap $z_t(t)$ as a function of $z_a(t)$ and its derivatives, by solving analytically a simple fourth order polynomial equation. In the rest of the study we concentrate on the case where the reverse engineering technique is used to design a transport ramp in a pure harmonic trap configuration and we study the detrimental effects of the anharmonicities of the trap.

2.4 Theoretical Results

The results of the transport protocol realized with the atom chip arrangement described in the preceding sections are presented for a total displacement duration of 75 ms. The consequences of this manipulation are evaluated for the position of the wave packet center, denoted as the “classical” degree of freedom, as well as for the size dynamics of the BEC.

2.4.1 Control of the BEC position dynamics

In Figure 2.4(a), the atomic cloud position is shown during and after the implementation of the STA protocol in the cases of a chip trap assumed to be harmonic (thin solid blue line) and more realistically including the cubic term of Eq. (2.3) (dashed red line). In both cases, the classical solution of Newton’s equation is indistinguishable from the average position of the wave packet solution of the Gross-Pitaevskii equation. The position of the

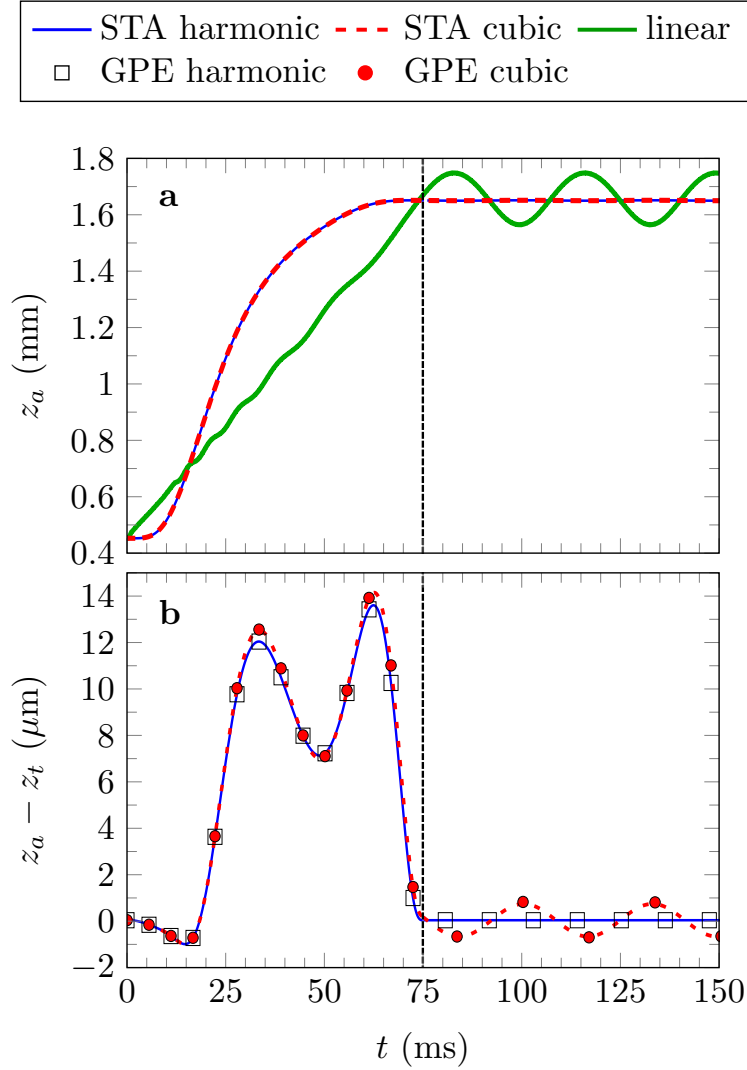


Figure 2.4: BEC position during and after the STA transport ramp. The vertical dashed line signals the end of the transport time and the beginning of the in-trap oscillations. The upper plot (a) depicts the evolution of the position expectation value z_a of the BEC as a function of time in the case of a linear ramp (solid green), the harmonic trap case (thin blue curve) and the case with a cubic term (dashed red line). The lower graph (b) shows the deviation from the trap position z_t for better visibility of the STA ramp results. The Gross-Pitaevskii solutions computed by my colleague S. Amri are indicated at chosen times by the empty squares (harmonic case) and the plain circles (cubic term included) symbols. In the latter case, the non-adiabatic transport is reflected in residual oscillations of the wave packet in the final trap. Their amplitude is, however, remarkably low ($0.7 \mu\text{m}$).

atomic cloud during the transport is plotted in the left part of the figure. The dashed vertical line signals the end of the displacement and the beginning of a holding period

in the final trap. The upper panel (a) of the graph shows the appropriateness of the transport ramp to guide the atoms over more than 1.2 mm with no noticeable residual center of mass oscillations. To be more convinced that the STA ramp works out thanks to the careful optimization described in the previous section and not because the transport time is long enough to approach the adiabatic limit, we also plot the classical solution for the same displacement time but with a linear ramp (green solid line). The contrast with the optimized solutions is clear, with large residual oscillations with an amplitude of the order of $100 \mu\text{m}$ after $t_f = 75 \text{ ms}$. This clearly shows that the chosen ramp duration is far from the adiabatic time scale, which would trivially bring the atoms at rest in the final trap.

The STA ramp devised in this case allows for the position of the atomic cloud to deviate from the trap position during the transport. This becomes visible in Fig. 2.4(b), which shows the offset $[z_a(t) - z_t]$ between the position of the BEC and the time-dependent trap center. In this graph, the Gross-Pitaevskii solutions are indicated at chosen times by empty black squares (harmonic potential) and by plain red circles (cubic term included). For the chosen ramp time, the maximum offset is about $14 \mu\text{m}$. This relatively large offset is responsible for limiting the quality of the transport, as quantified by the amplitude of residual oscillations in the anharmonic case (dashed red line and circles). Indeed, the harmonic solution found for the BEC trajectory by solving Eq. (2.5) becomes less appropriate the more the atoms explore trap anharmonicities which show up when leaving the trap center. This effect is clearly noticed when comparing the holding trap oscillations in Fig. 2.4(b) between the harmonic case (no visible residual oscillations) and the one with a cubic term, which shows an oscillation amplitude of about $0.7 \mu\text{m}$ around the trap center. It is interesting to note that the chirp introduced in Eq. (2.29) drastically reduces the residual oscillations of the BEC. Indeed, the oscillation amplitude would reach approximately $6 \mu\text{m}$ with $a = b = 0$. Similarly, with no chirp, the same oscillation amplitude of $0.7 \mu\text{m}$ would require a ramp time $t_f > 300 \text{ ms}$. The quantum mechanical solution found by computing the average position of the BEC wave function rigorously lies on the Newtonian trajectory in both cases. This was predictable in the harmonic case since it is a consequence of Ehrenfest's theorem applied to our problem. Indeed the non-linear term in the GPE equation play a role only for the size of the wave-packet but doesn't change the mean position of this one in the case a pure harmonic trap. One can also notice that the quantum mechanical solutions are following here the Newtonian trajectory in the anharmonic case. This is because the anharmonic effect is small for such a transport time of 75 ms and the quantum correction from the Ehrenfest theorem

is negligible.

In order to quantitatively assess the magnitude of the anharmonic term during the transport, we plot in Fig. 2.5(a) the maximum offset to the trap center reached by the BEC as a function of the ramp time t_f . The solid curve is again corresponding to the Newton's equation solution and the red dots are depicting the Gross-Pitaevskii solution. As expected, short ramps lead to atomic positions departing further from the trap center in both the classical and quantum case since the adiabaticity criterion is less respected. The larger this spatial offset is, the higher the magnitude of the cubic term in Eq. (2.3) is, the worse the harmonic trap-based reverse engineering for the chip trap trajectory is, and the larger the final residual oscillations are. This is perfectly visible when analyzing Fig. 2.5(b) giving the magnitude of the cubic term (in percent) relative to the one of the harmonic term. As a consequence, the residual oscillation amplitudes shown in Fig. 2.5(c) are larger for shorter ramp times, as expected.

In all cases, the quantum solution is in a good agreement with the classical one, leading to the conclusion that regarding the position of the wave packets, BECs can here be safely treated as classical point-like particles. As a result, knowing the maximum oscillation amplitude tolerated in an experiment, one can implement our treatment to find the fastest transport ramp.

2.4.2 Robustness of the STA protocol

To assess the practical feasibility of the proposed fast BEC transport, it is necessary to estimate the impact of small experimental imperfections. The present robustness study, therefore, characterizes the residual oscillation amplitude induced by ramp timing errors, denoted here by δt_f , and offsets δB_{bias} in the time-dependent magnetic bias field applied to drive the chip trap. Both noise sources are considered independent.

Considering the more complete case where cubic potential terms are present, we use Newton's equations Eq. (2.6), where ω_z , z_t and L_3 are implicit functions of $B_{bias}(t)$. The average position of the condensate can be written as

$$z_a(t) = z_a^0(t) + \epsilon_z(t), \quad (2.32)$$

where $z_a^0(t)$ denotes the unperturbed trajectory. A lowest order perturbative treatment applied to Newton's equation Eq. (2.6) yields

$$\ddot{\epsilon}_z + \omega_z^2(t)(\epsilon_z - \delta z_t) + \delta \omega_z^2(z_a^0 - z_t) + \frac{\omega_z^2(t)}{L_3(t)}(z_a^0 - z_t)^2 = 0, \quad (2.33)$$

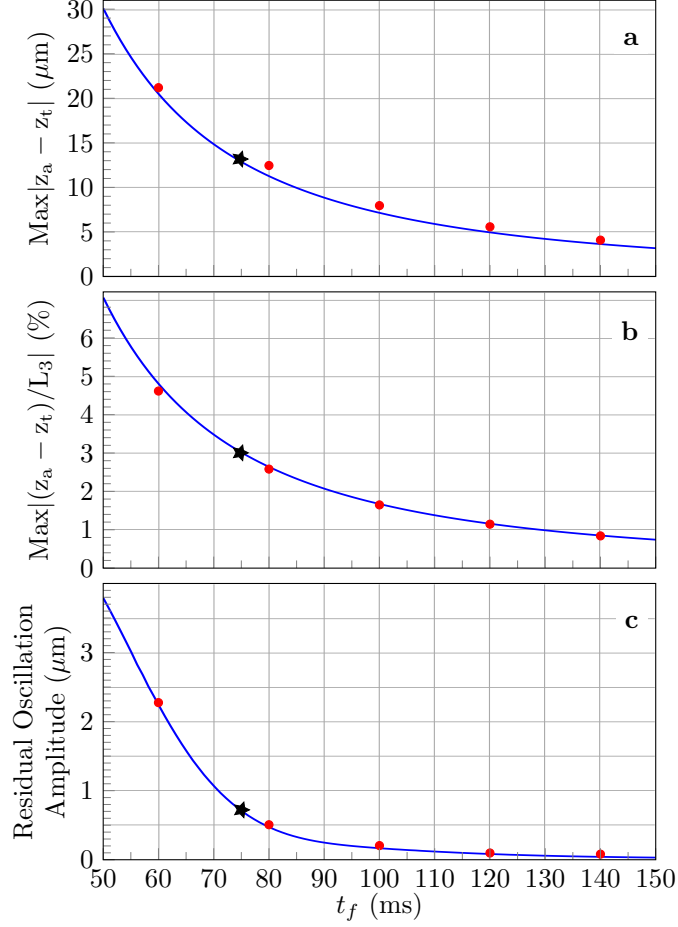


Figure 2.5: Offset to adiabaticity and its impact on the transport as a function of ramp times. The maximum distance reached by the atomic cloud relative to the trap center is plotted in (a), the anharmonicity (cubic potential term) magnitude in percents of the harmonic potential term is depicted in (b) and the consecutive amplitude of the residual oscillations is shown in (c). The longer the transport duration, the more the system tends to the adiabatic limit, the smaller these oscillations caused by the cubic term. The Newtonian trajectories (solid blue curves) agree very well with the full GP solutions (red dots). The black star marks the ramp time $t_f = 75$ ms used in this study.

where δz_t and $\delta \omega_z$ denote first order perturbations to the trap position and to the trap frequency, respectively. In the following, we solve Eq. (2.33) for the harmonic (*i.e.* $L_3 \rightarrow \infty$) and anharmonic trapping cases.

Figure Fig. 2.6 shows the residual oscillation amplitude as a function of the perturbations δB_{bias} in panel (a) and δt_f in panel (b). This figure confirms the robustness of our transport method. Indeed, for typical δB_{bias} of the order of $\delta B_{bias} = 1$ mG of control error in the bias field only leads to an offset of about $0.5 \mu\text{m}$ in the final position of the

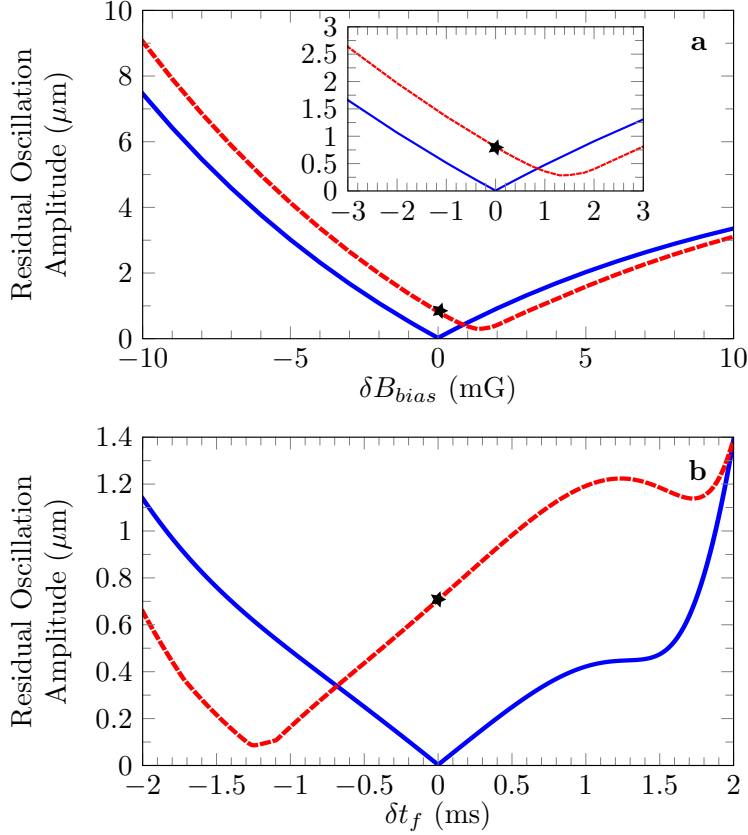


Figure 2.6: Residual oscillation amplitude of the BEC in the final trap as a function of a magnetic field offset (a) or timing errors in the applied ramp (b). Both harmonic (solid blue curve) and anharmonic (dashed red curve) cases are considered. For typical state-of-the-art cold atom experiments, the level of control should be sufficient to ensure errors smaller than $1 \mu\text{m}$. The black stars mark the results obtained for a ramp time $t_f = 75$ ms taking into account the anharmonicities of the potential in the case where both t_f and B_{bias} are perfectly controlled.

BEC. Moreover, the same order of infidelity in the final position of the BEC requires ramp timing errors better than 1 ms, a limit which is easily matched experimentally. Both limits are therefore considered to be safely within state-of-the-art capabilities of standard cold-atom laboratories.

2.4.3 Dynamics of the atomic cloud size

In this section, the time-dependent spatial density distribution of the transported BEC is considered. By applying a similar treatment as reported in [238, 239] but in the context of important trap decompression in non-harmonic trap, it is possible to suppress residual

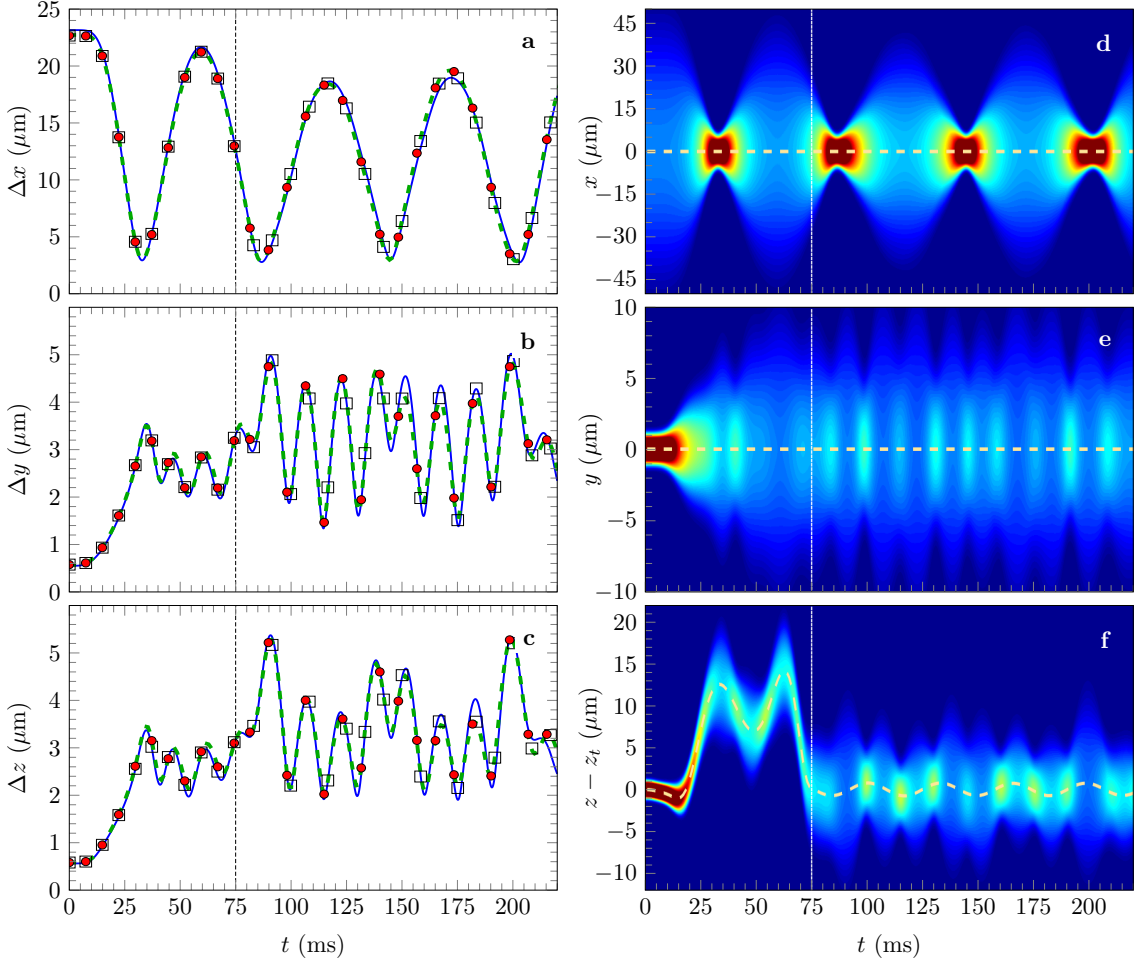


Figure 2.7: Size dynamics of the BEC wave packet. In the left panels (a), (b) and (c), the standard deviations of the spatial density distributions are calculated for the time-dependent condensate wave function for the three principal axes. The solid blue curve is the solution of the scaling approach, the empty black circles are found by solving the Gross-Pitaevskii equation in the harmonic case and the red circles correspond to the more realistic case of the anharmonic trapping potential. The dashed green line is the most complete case including anharmonicities and trap rotation during the transport. The right column shows the averaged probability densities along x (graph d), y (graph e) and z (graph f) calculated by solving the Gross-Pitaevskii equation for the anharmonic case with trap rotation, revealing the collective oscillations connecting the three directions. The dark red regions are associated with density maxima and the dark blue regions correspond to low atomic densities. The last plot (f) is shifted with respect to the trap position z_t . The dashed white lines show the expected BEC position in the three directions as a function of time. The vertical dashed lines mark the end of the transport ($t_f = 75$ ms) and the beginning of the holding period.

holding trap oscillations of the wave packet center as well as size excitations after the transport. This is achieved, however, at the cost of a long transport time. In this chapter, we would like to highlight the potential of atom chip-generated STA protocols in the metrological context, *i.e.* with fast enough transport to allow for short duty cycles.

The gallery in Fig. 2.7 shows typical BEC wave packet size oscillations occurring during and after the transport ramp considered in the last section. An adiabatic or long enough transport would bring the BEC to its ground state in the final holding trap, reflected in trivial flat lines starting at 75 ms for the three sizes of the left panel. We observe instead a breathing of the wave packet in the three space directions with the largest amplitude occurring in the weak frequency axis x . Although the transport is performed in our simulations solely in the z direction, we clearly witness a size oscillation of the atomic wave packet in the two other directions due to the mean-field interactions connecting all spatial directions.

The left panel of Fig. 2.7 illustrates the results of simulations based on the scaling approach (harmonic approximation, solid blue curve) on one hand and on a numerical solution of the Gross-Pitaevskii equation in the harmonic case (black empty squares) on the other. The influence of the anharmonicities and the anharmonicities with the rotation during the transport in the Gross-Pitaevskii equation is shown with the solid red circles and the dashed green line respectively. These Gross-Pitaevskii simulations were performed by my colleague S. Amri.

Qualitatively, the four configurations show a similar behavior. The numerical results being similar with and without the cubic term suggests that our trade-off ramp time versus anharmonicities magnitude, previously made for the atomic cloud center, is conclusive regarding BEC size dynamics as well. This is one of the main results of this study since it demonstrates the benign effect of anharmonicities in typical atom chip traps even with fast STA non-adiabatic transports.

The right panel of Fig. 2.7 is a density plot complementing the left part with the density probability distribution during the transport and for 150 ms of holding time. The quasi-cylindrical symmetry of the trap is reflected in the collective excitation modes observed. Indeed, the strongly trapped directions y and z are subject to in phase size oscillations. The size along the weak axis x is subject to larger-amplitude size oscillations since the trapping frequency is weak along this axis. The excited modes responsible for these oscillations will be identified by the quantitative study of next section.

2.4.4 Collective excitations and optimization of the expansion dynamics

2.4.4.1 Collective excitations in the holding trap

To gain insight into the impact of the transport speed on the collective excitation of the BEC in the final trap, we plot in Figs. 2.8(a) and 2.8(c) the extracted BEC size oscillations resulting from the ramp of Eq. (2.28) for a total transport time of 75 ms and 750 ms, respectively. In order to compare to analytical results, we consider a cylindrical symmetry suggested by Fig. 2.2(b) where v_y is chosen to be strictly equal to v_z . We plot the sizes normalized to the ones at the end of the transport in the directions x (solid blue line) and y or z (dashed red line) as a function of the holding time $t_{hold} = (t - t_f)$ in the final trap.

In both cases, the final holding time is chosen to be 500 ms and one easily notices the complex shape of the residual size oscillations for the fast ramp compared to the slower one, where a simple periodic evolution of the size of the BEC is obtained. This difference occurs due to the rapid variation of the trap aspect ratio in the fast ramp. Indeed, in the transport of Fig. 2.8(a), the aspect ratio (ω_x/ω_\perp) varies by one order of magnitude in 10 ms only, when a similar variation happens in 100 ms for the slow transport of Fig. 2.8(c).

In Fig. 2.8(b) and (d) we plot the Fourier transforms of the Thomas Fermi radii $R_x(t)$ and $R_y(t)$ in Log scale, as a function of the oscillation mode frequency ν for the two cases mentioned previously of $t_f = 75$ ms and 750 ms. These graphs reveal the main collective modes and their harmonics present in the holding trap after the end of the transport. The vertical dashed lines in these plots denote the analytically found collective excitation frequencies according to the treatment described in Sec. 2.3 and reported in [232]. This treatment is an approximation in the case of small perturbations. It is clearly not valid for the faster transport reported here in the case of a 75 ms ramp. It is, nevertheless, a useful indicator to identify the excitation modes presenting the largest magnitude.

The slow ramp is characterized by the presence of a single quadrupole mode Q_1 explaining the simple periodicity of the size oscillation behavior, with the two strong axes in phase and the weak axis out of phase. Note that the oscillation magnitude is, in this case, quite negligible, the size departing only by about 1% from the one at the end of the transport. The fast transport ramp is, however, exciting several collective modes explaining the more complex size oscillation periodicity and the larger amplitude variation to about $\pm 70\%$ change relative to the final transport size in the weak axis x .

This analysis is useful on many levels. The predominance of the quadrupole Q_1 mode, suggests, for example, the optimization we discuss in the next section. By taking

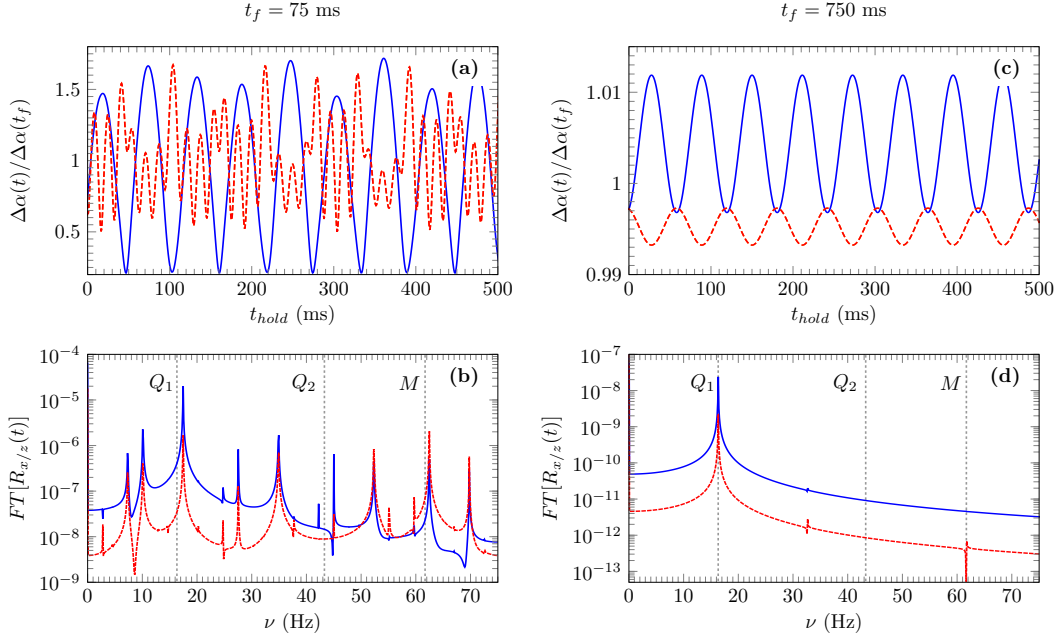


Figure 2.8: *Upper panel*: Size excitation dynamics after the transport of the BEC as a function of the holding time $t_{hold} = (t - t_f)$ in the final trap. Two realizations of the same ramp are considered: a fast transport with $t_f = 75$ ms (left column) and a slow transport with $t_f = 750$ ms (right column). *Lower panel*: Fourier transform of the Thomas-Fermi radii $R_x(t)$ and $R_y(t)$ of the BEC in Log scale as a function of the mode frequency ν . For both panels, the solid blue curves are used for the weak axis x and the dashed red ones for the two strong axes y and z . The vertical dashed lines in (b) and (d) correspond to the three low-lying excitations modes Q_1 , Q_2 and M calculated following the treatment of Ref. [232].

advantage of the symmetry of certain modes, one can also imagine, in further studies, designing a transport protocol forbidding or enhancing them.

2.4.4.2 Optimization of the expansion dynamics

The designed quantum states studied in this chapter would serve as an input of a precision atom interferometry experiment [240]. In such measurements, it is beneficial to work with the slowest cloud expansion possible since this increases the maximum interferometry time available, with an impact on the density threshold for detection and hence, on the sensitivity of the atomic sensor [241]. Moreover, long free evolution times of several seconds are beneficial for micro-gravity [41, 167, 173, 175, 242, 243] and atomic fountain experiments [39, 40, 125]. To largely reduce the expansion rate of the atomic samples, the delta-kick collimation (DKC) technique [165, 167, 186, 187] is commonly

applied. It consists in re-trapping an expanding cloud of atoms for a brief duration in order to align its phase-space density distribution along the position coordinate axis, therefore minimizing its momentum distribution width in preparation for a further expansion. This is in analogy with the collimating effect of a lens in optics and DKC is often referred to as an atomic lens. The principle and the analogy with optics is shown in Fig. 2.9. It is worth noticing that the phase-space density is conserved in such a process which does therefore not achieve a cooling in the sense of reducing the phase-space density. This method was successfully implemented and led to record long observation times of several seconds [165, 244].

If the trap is anisotropic, as the quasi-cylindrical case considered in this section, the lensing effect is different in every direction and would typically be negligible in the weak frequency axis when the two others are well collimated. To overcome this problem, we take advantage of the collective excitations described in the preceding section to release the BEC at a well-defined time, *soon after* a maximum size amplitude of the weak trapping direction such that the subsequent expansion velocity is naturally reduced. This timing is chosen such that the kinetic energy associated with the natural re-compression of the cloud is quickly balanced by the repulsive mean-field interaction energy which naturally leads to an expansion of the cloud in this direction. In our case the strategy is therefore to choose the appropriate timing of the holding time to collimate the BEC along the weak-axis [186] and then to apply a second delta-kick after letting the BEC expand along the two strong axis.

To illustrate this optimization, we consider in this section the case of a transport from $z_i \simeq 0.45$ mm to $z_f \simeq 1.35$ mm in 75 ms. This transport is realized with the chip DC current $I_w = 5$ A and a bias magnetic field which varies between $B_{bias}(0) = 21.6$ G (initially) and $B_{bias}(t_f) = 5.9$ G (at the end of the displacement). The final trap is characterized by the frequencies $\nu_x = 12.5$ Hz, $\nu_y = 50$ Hz and $\nu_z = 49.5$ Hz. This is realized following the reverse engineering technique described in Sec. 2.3. The final trap is used to hold the atoms after the end of the transport. The result of this optimization is shown in Fig. 2.10(a) where the blue curves show the variation of the size of the released BEC in the x -direction for three different holding times of 29.4, 31.4 and 33.4 ms. A natural choice is to consider the switch-off time of 31.4 ms leading to a collimated subsequent free expansion. Indeed, a holding time slightly below leads to an immediate fast increase of the condensate size (see the dash-dotted blue line in Fig. 2.10(a)) while a holding time slightly above leads to a transient compression of the BEC (see the dashed blue line in Fig. 2.10(a)) soon followed by a very fast expansion.

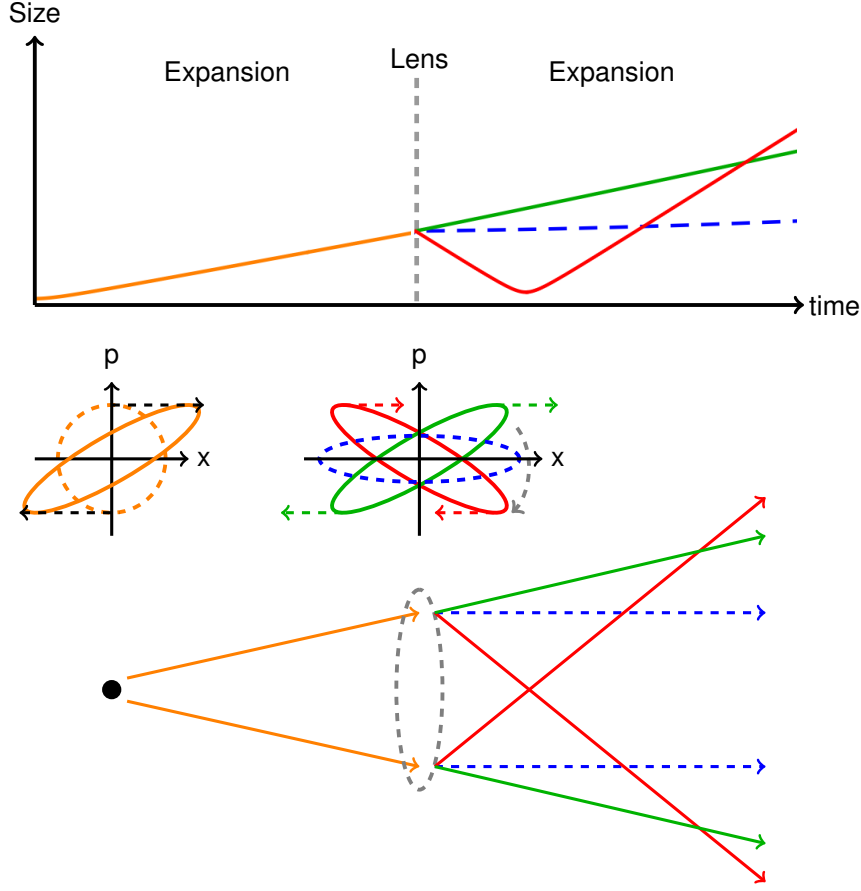


Figure 2.9: Principle of the pulsed delta-kick collimation (DKC) technique. Representation of the size and phase space evolution of the cloud as a function of the time for different lens duration, *i.e.* the time the atom are re-trapped, in analogy with optics. The effect of the initial free expansion is shown in orange. The blue dashed line depicts the configuration where the cloud is collimated at the end of the lens, *i.e.* aligned with the spatial axis in the phase space representation. The green and red curves show the effect of the lens when this one is too short in time, *i.e.* for a divergent lens, or too long in time, *i.e.* for a convergent lens, respectively, compared to the collimated configuration in blue.

Following the intermediate and optimal choice $t_{hold} = 31.4$ ms, after 100 ms of free expansion the mean field interaction energy is almost entirely in the form of kinetic energy and an atomic lens (DKC pulse) can be applied. It is realized by switching-on a cylindrical trap of frequencies $\nu_x = 1.7$ Hz and $\nu_y = \nu_z = 7.2$ Hz for $\Delta t_{lens} = 4.84$ ms, created with a DC current of intensity $I_w = 0.1$ A and a magnetic bias field of $B_{bias} = 0.12$ G, leaving the trap minimum at $z_f = 1.35$ mm. The collimation effect is dramatic in the y and z -directions (red dashed line and green dash-dotted line in Fig. 2.10(b)). The expansion observed after the application of the DKC pulse corresponds to an average

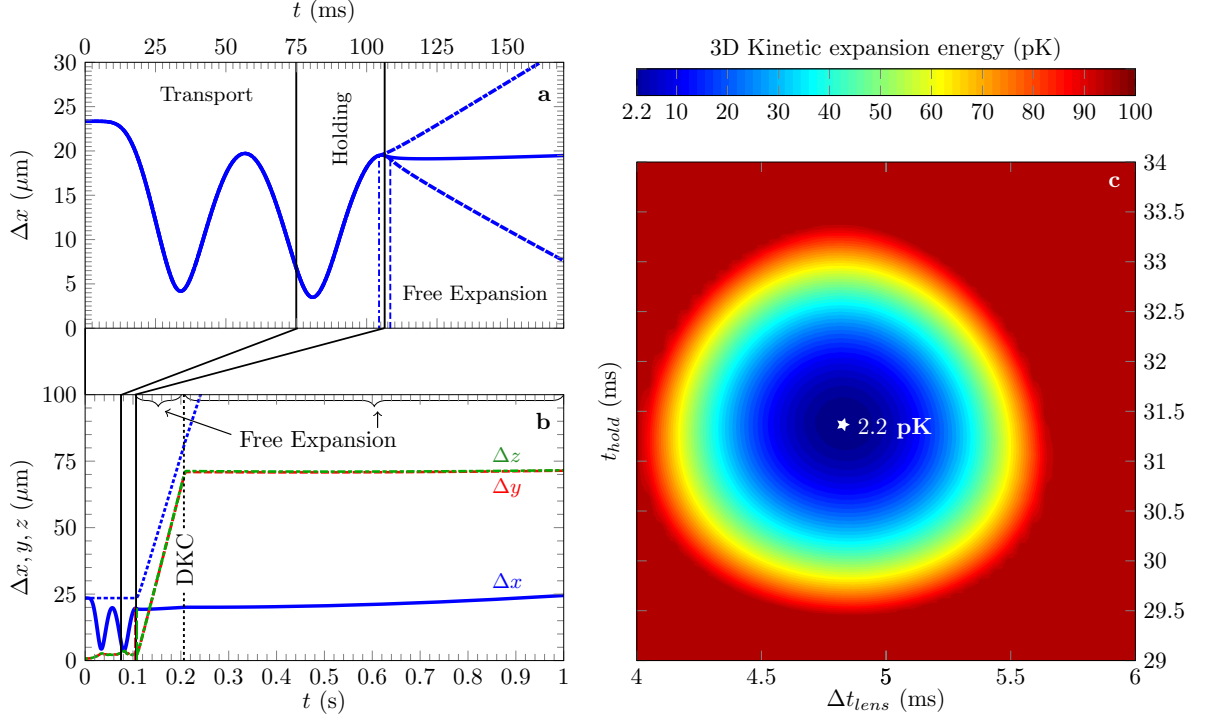


Figure 2.10: Transport, holding, release and magnetic lensing of a BEC to pK expansion velocities. Panel (a): Effect of the release timing from the holding trap in the weak trapping direction x . The choices of 29.4 ms (dash-dotted blue curve), 31.4 ms (solid blue curve) or 33.4 ms (dashed blue curve) illustrate different expansion behaviors (diverging, collimated and focused, respectively). This timing has a little effect on the released size dynamics of the two strong axes y and z , not shown here for the sake of clarity. Panel (b): Full sequence with transport, holding, release and delta-kick collimation leading to an average, over the three spatial directions, expansion rate at the pK level. The naturally collimated case of panel (a) is chosen (solid blue line). A free expansion of 100 ms is necessary before applying the DKC pulse lasting for 4.84 ms in a $\{1.7, 7.2, 7.2\}$ Hz trap. This pulse has a negligible effect on the x -axis expansion due to the weak frequency in this direction, but it collimates well the atomic cloud in the y and z directions (dashed red line and dash-dotted green line). The resulting expansion speeds are $22.2 \mu\text{m/s}$ (5.2 pK), $8.7 \mu\text{m/s}$ (0.8 pK) and $8.2 \mu\text{m/s}$ (0.7 pK) in the x , y and z -directions, respectively. This amounts to a global expansion temperature of 2.2 pK only. Without the collective excitations (*i.e.* for an adiabatic transport in the x direction, thin blue dotted curve representing Δx as a function of time), the collimation performance is much worse, leading to a global expansion temperature of 555 pK. Panel (c): Optimal parameters search by scanning the holding and lens durations. The white star marks the optimal values leading to an expansion temperature of 2.2 pK shown in (b).

speed in the three spatial directions of about $25.3 \mu\text{m/s}$, equivalent to a temperature of 2.2 pK.

In analogy with the common definition of temperature in Maxwell-Boltzmann statistics [139], we define the expansion temperature by

$$\frac{3}{2}k_B T = \frac{m}{2} \left[\left(\frac{d\Delta x}{dt} \right)^2 + \left(\frac{d\Delta y}{dt} \right)^2 + \left(\frac{d\Delta z}{dt} \right)^2 \right], \quad (2.34)$$

in 3D and by

$$\frac{1}{2}k_B T = \frac{m}{2} \left(\frac{d\Delta \alpha}{dt} \right)^2, \quad (2.35)$$

in 1D, where $\alpha = \{x, y, z\}$.

Fig. 2.10(c) finally shows the robustness of the procedure in case of timing errors for the holding time t_{hold} and for the lens duration Δt_{lens} . With timing errors as large as 0.5 ms the expansion temperature remains below 20 pK. This demonstrates the marginal influence of relatively large timing errors for the 3D collimation effect proposed here.

To illustrate the importance of taking advantage of the collective oscillations, we plot in the same figure the virtual case of an adiabatic transport in the x -direction (thin dotted blue line). If one applies a mere adiabatic decompression as suggested by this latter curve, the expansion temperature would be much larger, higher than 550 pK, even if we consider very well collimated y and z -directions, the x -direction being hardly affected by the magnetic lens. It is therefore crucial to control the release timing of the BEC in order to implement low-velocity expansions.

2.5 Micro-gravity experimental implementation

In this section 2.5, I present an overview of some experimental results of the QUANTUS collaboration (acronym from the German consortium name: Quanten Gase unter Schwerelosigkeit). Some additional results can be found in Refs. [84, 167, 168, 172, 174, 242, 245–249]. This cold atom space-oriented research is a collaboration between the Physics Institutes from the University of Hanover, Ulm, Hamburg, Bremen (ZARM), Humboldt and the Max-Planck Institute in Garching supported by the German Space Agency (DLR) [243]. My contribution was to deliver STA ramps to the Quantus 2 microgravity drop tower experiment based in Bremen [244, 250–252], and to propose a theoretical interpretation of the measured data of the Maius 1 sounding-rocket mission [174].

2.5.1 The Quantus 2 drop tower experiment

The Quantus 2 drop tower experiment is based in Bremen in the facility of the Center of Applied Space Technology and Microgravity (Germ: Zentrum für angewandte Raum-

fahrttechnologie und Mikrogravitation (ZARM)). The microgravity-based experiment can be either dropped from the top or catapulted from the bottom of the 145 meter height tower. The available micro-gravity free fall experimental time is approximately 4.5 s in the dropped configuration, or 9 s in the catapulted configuration.

The apparatus is based on a multilayer atom chip technology [168, 192, 220, 221, 244]. A realistic atom chip model, based on finite element calculations has been developed by the Quantus 2 team and accurately calibrated based on ground and micro-gravity experimental measurements [253].

A BEC of Rubidium 87 is created close to the atom chip surface at approximately $200 \mu\text{m}$ within 1 s [168] in a $2\pi \cdot (25 ; 565 ; 570)$ Hz trap. Experimentally, to circumvent the problems of the very large initial mean-field energy and of the atomic loss close to the chip surface caused by the current fluctuations [254], a transport away from the atom chip surface is required. Adiabatic solutions are excluded due to the limited amount of micro-gravity time. A fast transport of the cloud is then required.

STA protocols I theoretically investigated were implemented ramping down the bias magnetic field, thus transporting the BEC away from the chip surface in a shallower trap configuration of frequencies $2\pi \cdot (10 ; 28 ; 25)$ Hz, at approximately 1.5 mm from the chip. The protocol was pretty successful leading to residual oscillations of the BEC center of mass at an amplitude as low as $4 \mu\text{m}$. At this position even though the mean field energy is reduced by a least an order of magnitude, the remaining mean field interaction energy brings the BEC to expand with an expansion temperature of some nK.

At the end of the transport a subsequent magnetic lens is applied after 80 ms of free expansion to reduce the temperature expansion to below 100 pK in 3D and BECs have been observed with some 10^5 atoms after 2.7 s of free expansion time giving the possibility in the future to perform interferometry sequences during this time. A detailed description of these experimental results can be found in the chapter 6 “Magnetic Lensing in Microgravity”, of the PhD thesis of J. Rudolph [244], in the chapter 6 “Magnetic lensing of the condensate” in the PhD thesis of C. Grzeschik [251] and in the chapter “Center of mass motion” in the PhD thesis of T. Sternke [252].

The possibility to reduce the expansion temperature of the cloud to such record low temperatures relies on small residual COM excitation of the BEC at the final position where detrimental center-of-mass motions limit the efficiency of the magnetic lens. The post-transport ramp is followed by a holding time sequence used principally to collimate the weak axis while the magnetic lens collimates the two strong axis, as explained in section 2.4.4.2. In this setup, a robust STA ramp has been engineered to transport the

BEC over 1.3 mm within 150 ms. The figure Fig. 2.11 shows the results of the center-of-mass oscillation of the BEC in the final trap, $\omega = 2\pi \cdot 25$ Hz emphasizes by a Time of Flight (TOF) of 80 ms (red circle) fitted with a sinusoidal function (blue). The data have been taken by W. Herr, C. Deppner, M. Cornelius and P. Stromberger. The amplitude oscillation of the BEC position of approximately $50 \mu\text{m}$ after 80 ms TOF correspond approximately to $4 \mu\text{m}$ of residual position amplitude oscillation in the final trap.

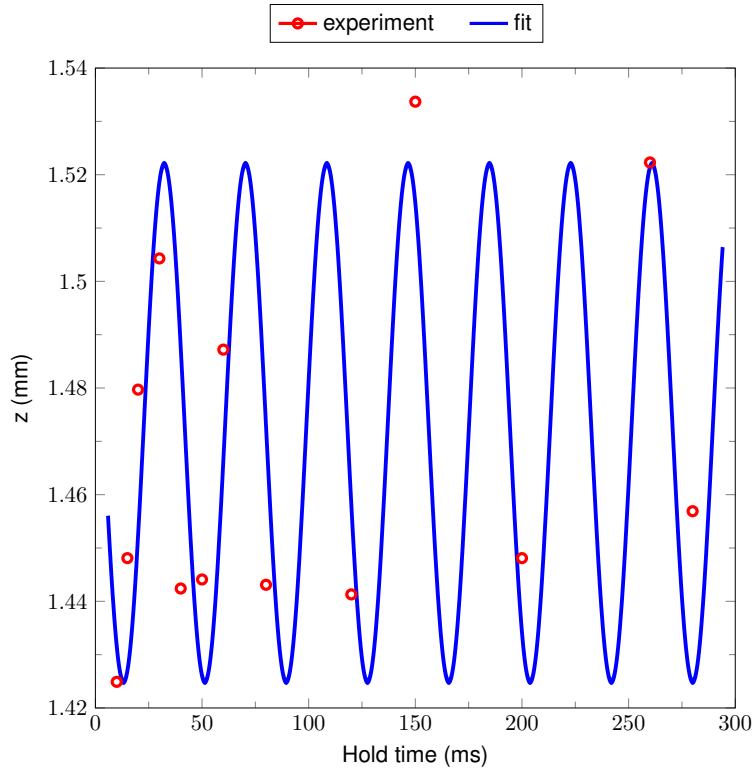


Figure 2.11: Result of the center-of-mass motion after the STA ramp in the Quantus-2 experiment. The experimental data are shown after 80 ms TOF at different time in the final trap (red circles) and fitted with a sinusoidal fit function. The amplitude oscillation of the BEC position of approximately $50 \mu\text{m}$ after 80 ms TOF correspond approximately to $4 \mu\text{m}$ of residual position amplitude oscillation in the final trap.

2.5.2 The MAIUS-1 sounding rocket mission

On 23 January 2017, as part of the sounding-rocket mission MAIUS-1, 110 experiments central to matter-wave interferometry have been realized in space [174]. At 3:30 AM the first man-made Bose-Einstein condensate in space has been observed. The experimental apparatus description can be found in [174, 255]. The results shown in this section were

measured by D. Becker, M. D. Lachmann, S. T. Seidel, H. Ahlers, A. N. Dinkelaker, J. Grosse, O. Hellmig, H. Müntinga, V. Schkolnik, T. Wendrich, A. Wenzlawski, B. Weps, T. Franz, D. Lüdtke, M. Popp, M. Erbe, A. Kohfeldt, H. Duncker, A. Kubelka-Lange and M. Krutzik, who have designed, built and tested the apparatus. D. Becker, M. D. Lachmann, S. T. Seidel evaluated the data.

My contribution to this work [174] consists in the interpretation of the analyzed data supported by simulations based on Newton's equation and on the scaling approach, previously described in section 2.3.1.

In Fig. 2.12, a part of the analyzed experimental results obtained in space and so far published in [174] are presented. In the same context than described before, the BEC of Rubidium 87 created close to the atom chip at some hundred of microns from the chip surface is displaced at a millimeter distance away over a 50 ms transport duration with a sigmoidal current ramp. In panel (a) we show the position along the z -direction and with respect to the chip surface, of the BEC imaged after 50 ms of free expansion for different holding times in the final trap. In panel (b), we present the BEC position without any holding after the transport for different free expansion times in different Zeeman states of the $F = 2$ manifold ($m_F = 0$ grey triangles and $m_F = 2$ black and green circles). Despite the strong effect of preparation and transport on the motion of the BEC, the trajectories of the center of mass of the BEC demonstrate only a small scatter in the experimental data for different Zeeman states of the $F = 2$ manifold as shown on panel (b). In general it is convenient to transfer the atoms to the state $m_F = 0$ to avoid detrimental effects, such as residual acceleration, in the presence of residual magnetic field. The green points of panel (a), observed after 50 ms of release are reported on panel (b). The purple dashed line represents a correlated sinusoidal (panel a) and linear (panel b) fit of the position of the BEC for different holding and free expansion times at the end of the 50 ms transport. The purple-shaded area indicates the 95% confidence level with respect to the numerical simulations, which used the expected atomic-chip potential. The data presented here have been measured over a total time of two minutes, when the sounding rocket was travelling over a hundred of kilometers in space. As shown by the purple dashed line the center-of-mass motion (COMM) of the BEC away from the chip after release, panel (b), is almost identical for the different Zeeman states, showing a nice reproducibility of the COMM.

Panels (c) and (d) show the corresponding Thomas-Fermi radii for different holding times and free expansion times of the BEC in the different m_F states. Each data point has been re-normalized with respect to its detected atom number. The blue and red colors

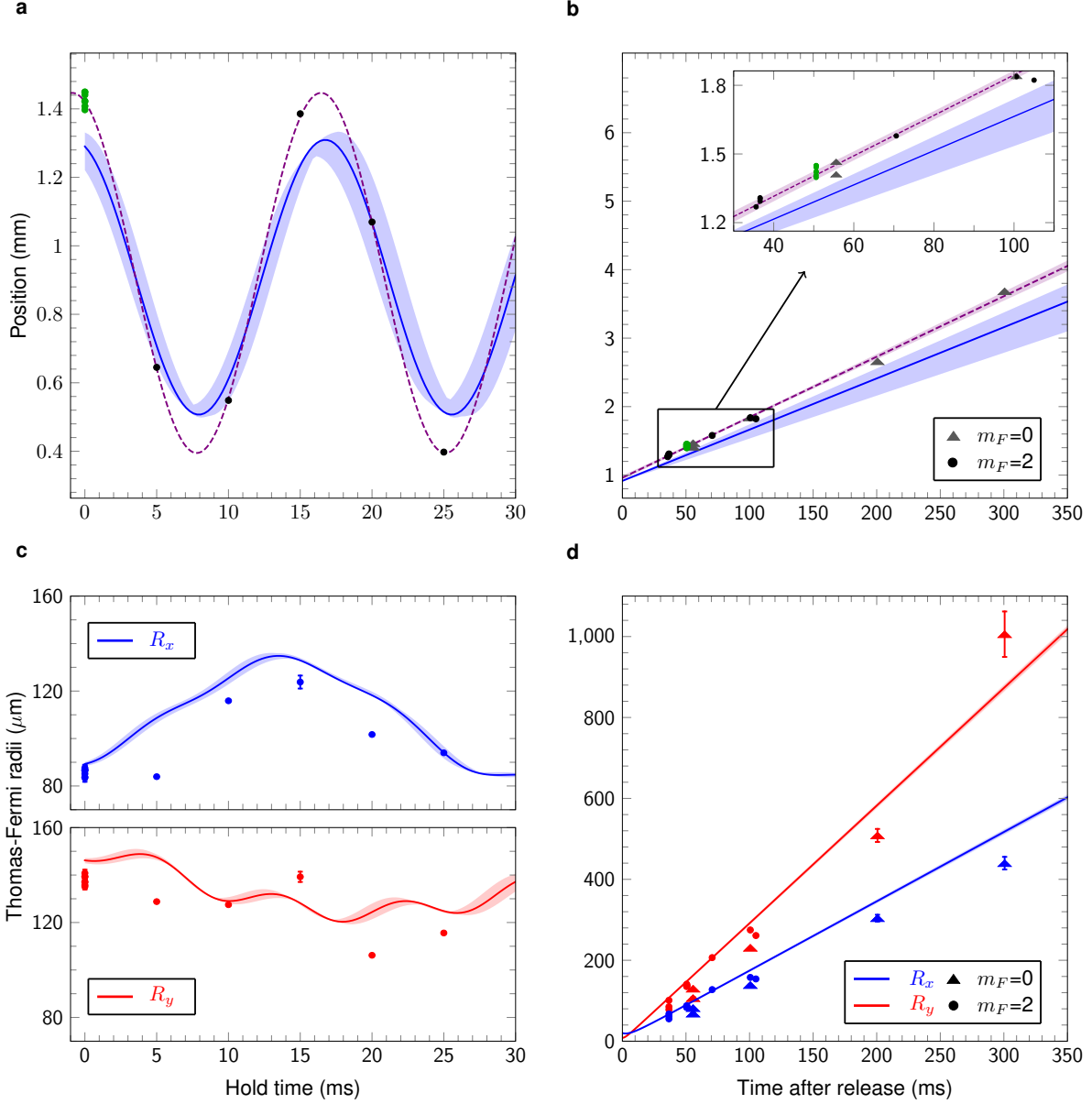


Figure 2.12: Result of the COMM and size evolution of the Maius-1 sounding rocket [174]: Evolution of the BEC after its transport away from the atom chip in different m_F states. Panels (a) and (c): Position and Thomas-Fermi radii of the BEC after 50 ms of free expansion time for different holding times. Panels (b) and (c): Position and Thomas-Fermi radii of the BEC for different free evolution times without any holding.

indicate the two different axis of the camera. The error bars indicate the uncertainties of the fit of the BECs' images. More information can be found in [174].

The realistic atom chip model developed by the Quantus 2 team has been fully adapted and accurately calibrated to the Maius 1 experimental setup. The model includes the

current-carrying wire structures and coil configurations. In each panel the blue (red) lines and blue (red) shaded areas show the theoretical behavior I could predict for the BEC. The lines denote the expected behavior based on the expected currents in the different multi-layers of the atom chip and coils used to perform the different experiments. The shaded area has been theoretically calculated using the atom chip model and simulates the expected impact of the circuitry. The different current values are reasonably modified (a few percents) according to the expected batteries and current driver performance of the experimental payload during the flight around the expected ones.

The simulated behavior of the position of the BEC in panel (a) and (b) agree well with the experimental data points and differ only by a slight underestimation of the oscillation amplitude corresponding to a slight velocity offset. This offset may result in the limited knowledge of the current driver behavior when the trap is switched off. This step has been considered infinitely fast in the simulation. The complicated shape oscillation of the BEC in the final trap shown in panel (c) is reflected by the theory. The tiny shaded area in panels (c) and (d) lead to the conclusion that the shape evolution of the BEC is not a consequence of current noise fluctuations but a consequence of the trap decompression, consequence itself of the transport as described in section 2.4.3. This result is confirmed in panel (d). The reduction of the mean field energy by an order of magnitude at the end of the transport brings the BEC to expand to about a 1 millimeter total size after 300 ms, corresponding to a few nK for the expansion temperature.

2.6 Conclusion and outlook

While BEC creation on atom chips was demonstrated with competitive high-flux of 10^5 BEC atoms/second as a source of metrology-oriented experiments [168], the necessary displacement of the atoms far from the chip surface constrained the use of this technique due to the long times needed to bring atoms at desired positions without detrimental center of mass and size excitations. In this chapter, we demonstrated a shortcut-to-adiabaticity set of protocols based on reverse engineering that solves this speed issue. This proposal includes characteristic mean-field interactions in non-harmonic traps and their coupled effects in the three spatial dimensions even for a 1D transport of a degenerate bosonic gas in the case of fast and big trap decompression. To illustrate the appropriateness of our theoretical proposal, we considered the commonly used Z-chip wire geometry combined with a bias homogeneous magnetic field. The study is carried out considering atom-chip-characteristic cubic anharmonic terms in the rotating trapping

potentials which manipulate the atoms. Although the STA protocols are inspired by harmonic traps and Newton's equations, the validity of our recipe is supported by solving a scaling approach and mean field equations for interacting BEC ensembles. With the help of analytical and numerical models, we were able to engineer fast atomic transport ramps in few tens of ms and to carry a trade-off study between speed and accepted residual excitations at the target position imposed by non-ideal realistic trap profiles. This trade-off showed the benign effect of typical atom chip anharmonicities on the transport speeds. For the sake of experimental implementation, the efficiency of this proposal was tested against typical deviations in the main control parameters (magnetic field and timing errors) showing an excellent degree of robustness. Landmark effects of BEC physics as collective excitations were considered and analyzed. The results of this latter investigation revealed the benign character of collective excitations compared to the single particle approach on one hand, and the potential for optimization one could benefit from by using these collective excitations on the other.

Combining all the aforementioned tools, this theoretical study, applied to the Quantus-2 experiment, exhibited the possibility to precisely transport an atom-chip-generated BEC for several mm with a μm control level. Delta-kick atom chip collimation prepares this ensemble in a regime of a pK expansion rate thanks to the collective excitations acquired during the transport ramp. Similar temperatures have been achieved in the experiment where the real trap configuration allowed an expansion temperature of only a few tens of pK [244]. This highly controlled BEC source concept required only a few hundreds of ms (about 300 ms) when implemented in a state-of-the-art atom chip BEC machine [168, 242]. These specifications make of the proposed arrangement an exquisite and novel source concept to feed a highly precise atom interferometer. This would allow to unfold the already promising potential (mobility, autonomy and low power consumption) of atom chip-based atomic sensors in the metrology field [256]. Further directions would involve the implementation of optimal control theory tools [205, 206, 257] to consider arbitrary potential profiles and even faster manipulations while allowing for larger intermediate excitations.

The methods developed in this chapter and published in Ref. [188] are also directly applicable for optimizing the manipulation of cold atomic ensembles in optical dipole traps. One should also note the possibility to generate "painted potentials" [258] with these traps, which is of a particular interest as a future complementary control tool in shortcut-to-adiabaticity protocols, as discussed explicitly in Ref. [259] for the combined transport and expansion of BECs.

OPTIMIZED MANIPULATION OF THERMAL ENSEMBLES

Contents

3.1	Theoretical tools	52
3.1.1	Optimal Control Theory	52
3.1.2	Model of a thermal ensemble of N particles	59
3.2	Applications	63
3.2.1	Dual-source input state optimization	63
3.2.2	Thermal cloud phase-space density optimization by atomic lens- ing	83
3.3	Conclusion and outlook	95

In this chapter two problems of a timely significance for precision measurements involving the transport and manipulation of thermal ensembles are treated. The first one is the dual-transport of a laser-cooled mixture of two species with different masses starting at different kinematic conditions. The study case considered is the isotopes pair of rubidium: (^{87}Rb and ^{85}Rb). Indeed, the position and velocity offsets of the two clouds of atoms when used in an interferometric measurement couple with various residual gradients and forces leading to important systematics as highlighted in the general introduction of the thesis. This problem was the subject of a 3-month internship I had in the group of Prof. Mark Kasevich (Stanford University) and more precisely at the 10-meter atomic fountain experiment. The long-term goal of this experiment is to

perform tests of the Einstein Equivalence Principle to an unprecedented level of accuracy. For this purpose, the control of the position and velocity of the two-species sample at the end of the transport is crucial [260–262]. Moreover, an optimization of the expansion energy of the two species at the end of the transport protocol is performed.

The second problem consists in enhancing the phase-space density of thermal clouds before evaporation. Indeed, the number of atoms in a BEC relies on the starting number of particles in the initial thermal ensemble. Since the inaccuracy of an interferometric phase measurement involving a BEC is proportional to the inverse of the square root of the atom number [263], this number being low directly impacts the performance of an experiment. Over the recent years within the QUANTUS project [167, 168], increasing the initially trapped atoms number by one order of magnitude led to the same enhancement factor for the condensed particle numbers. Motivated by this scaling, we propose to combine here the traditional optical molasses technique with a "delta-kick" collimation stage of the pre-evaporated cloud to enhance the phase space density by one order of magnitude.

Besides an N -particle modelling of the thermal ensembles, Optimal Control Theory (OCT) protocols are performed in this study. Both methods are presented in the next section before applying them to the two problems introduced above.

3.1 Theoretical tools

3.1.1 Optimal Control Theory

The aim of optimal control theory is to bring a dynamical system from one state to another, while minimizing a cost functional¹. The modern version of OCT was born with the Pontryagin's Maximum Principle (PMP) in the late 1950s [264, 265]. Originally applied to problems of space dynamics, OCT is nowadays a key tool to study a large spectrum of applications in both classical [265, 266] and quantum physics [267–270]. In the Pontryagin formulation, solving an optimal control problem is equivalent to finding extremal trajectories which are solutions of a generalized Hamiltonian system. These trajectories satisfy the maximization condition of the PMP as well as specific boundary conditions [265–267]. The implementation of the PMP is far from being trivial and numerical control algorithms have been developed to approximate the optimal solution [271]. Among others, we can mention the GRAPE (GRAdient Ascent Pulse

¹In literature, the different cost functionals are also known as total payoff functional, running payoff functional and terminal payoff functional.

Engineering) and Krotov algorithms both gradient-based [266, 271–273], which are nowadays standard tools in physics. OCT has been applied with success to quantum systems since the 1980s in domains extending from molecular physics and nuclear magnetic resonance to quantum information science and atom interferometry [274–280]. The application of OCT to BEC dynamics has also been explored in different contexts. Using the Gross-Pitaevskii equation, the optimal coherent manipulation of a BEC has been investigated in a series of studies [206, 275, 281–284]. The transport of cold atoms has also been optimized for simple models in combination with invariant-based inverse methods [174, 215, 285, 286].

To introduce the technique, we will highlight the different steps of the OCT protocol in the next sections to solve the transport of two classical particles in a 1D trap. Subsequently, OCT will be used to solve the problem of a dual-species input atom interferometer in the real trap configuration specific to the 10-meter long tower at Stanford in the group of Mark Kasevich [37, 125, 165, 287, 288].

3.1.1.1 1D Transport

We begin our discussion by considering the control of the dynamics of two particles in harmonic traps whose minimum positions and trap frequencies are adjustable by a time-dependent control parameter, $c(t)$. The dynamic is described by Newton's equations

$$\ddot{z}_1(t) + \omega_1^2[c(t)](z_1(t) - z_{sag,1}[c(t)]) = 0, \quad (3.1a)$$

$$\ddot{z}_2(t) + \omega_2^2[c(t)](z_2(t) - z_{sag,2}[c(t)]) = 0, \quad (3.1b)$$

where the trap minima are $z_{sag,1/2}$ and the trap frequencies are $\omega_{1/2}$ for species 1 and 2, respectively. In this study, we limit ourselves to the case of a single control parameter $c(t)$ common to both species. While more than one control parameter can be used to optimize a situation in an experiment, it is simpler to rely only on one.

For a given time evolution of the control parameter, Eq. (3.1) describes the trajectory of the particles, $z_1(t)$ and $z_2(t)$. Depending on the evolution of the control parameter, the system may react very differently. In practice, the value of the control parameter can be chosen at each time t , which leads to an infinite number of hidden control variables. This approach of imposing the evolution of the control parameter is the opposite of reverse engineering, which imposes the trajectory of the particle and searches for the associated evolution of the control parameter.

We first rewrite the two second-order differential equations Eq. (3.1) as four first order coupled differential equations

$$\dot{\mathcal{X}}(t) = \begin{pmatrix} \dot{x}_1(t) \\ \dot{x}_2(t) \\ \dot{x}_3(t) \\ \dot{x}_4(t) \end{pmatrix} = \begin{pmatrix} x_2(t) \\ -\omega_1^2[c(t)](x_1(t) - z_{sag,1}[c(t)]) \\ x_4(t) \\ -\omega_2^2[c(t)](x_3(t) - z_{sag,2}[c(t)]) \end{pmatrix}, \quad (3.2)$$

where

$$\vec{\mathcal{X}}(t) = \begin{pmatrix} x_1(t) \\ x_2(t) \\ x_3(t) \\ x_4(t) \end{pmatrix} \equiv \begin{pmatrix} z_1(t) \\ \dot{z}_1(t) \\ z_2(t) \\ \dot{z}_2(t) \end{pmatrix}. \quad (3.3)$$

In the following, without loss of generality, we impose the particles to be at rest at $t = 0$, the initial conditions being

$$\vec{\mathcal{X}}(0) = \begin{pmatrix} z_{i,1} \\ 0 \\ z_{i,2} \\ 0 \end{pmatrix} = \begin{pmatrix} z_{sag,1}[c(0)] \\ 0 \\ z_{sag,2}[c(0)] \\ 0 \end{pmatrix} \quad (3.4)$$

and

$$\dot{\vec{\mathcal{X}}}(0) = \begin{pmatrix} 0 \\ 0 \\ 0 \\ 0 \end{pmatrix}. \quad (3.5)$$

We want to achieve a new state of equilibrium at the end of the transport protocol, defined by the final boundary conditions

$$\vec{\mathcal{X}}(t_f) = \begin{pmatrix} z_{f,1} \\ 0 \\ z_{f,2} \\ 0 \end{pmatrix} = \begin{pmatrix} z_{sag,1}[c(t_f)] \\ 0 \\ z_{sag,2}[c(t_f)] \\ 0 \end{pmatrix} \quad (3.6)$$

and

$$\dot{\vec{\mathcal{X}}}(t_f) = \begin{pmatrix} 0 \\ 0 \\ 0 \\ 0 \end{pmatrix}. \quad (3.7)$$

3.1.1.2 Cost functional

The purpose of the OCT protocol is to minimize a cost functional J_{tot} defined by the sum of a terminal cost, J_{ter} , and a current cost, J_{run} . The terminal cost is designed to ensure that the final state is the desired state, which in our case is the final equilibrium state imposed by minimizing the total energy at the end of transport for both species. The running cost can be designed to optimize the transformation of the system in time. It can be used to find the minimum time of a process or to account for certain experimental constraints. In our case, in order to imitate the design of the STA ramp (see section 2.3.2), we chose to derive the case where the running cost limits the transient excitation of the two particles in the trap. The different cost functionals chosen are as follows

$$J_{tot} = J_{ter} + \int_0^{t_f} J_{run} dt, \quad (3.8a)$$

$$J_{ter} = \frac{1}{2} \omega_1^2 [c(t_f)] \left(x_1(t_f) - z_{sag,1} [c(t_f)] \right)^2 + \frac{1}{2} x_2^2(t_f) + \frac{1}{2} \omega_2^2 [c(t_f)] \left(x_3(t_f) - z_{sag,2} [c(t_f)] \right)^2 + \frac{1}{2} x_4^2(t_f), \quad (3.8b)$$

$$J_{run} = \frac{w_r}{2t_f} \left(\omega_1^2 [c(t)] \left(x_1(t) - z_{sag,1} [c(t)] \right)^2 + \omega_2^2 [c(t)] \left(x_3(t) - z_{sag,2} [c(t)] \right)^2 \right), \quad (3.8c)$$

where w_r represents the weight of the running cost in relation to the weight of the terminal cost equal to 1. In this parametrization, the OCT protocol gives more importance to optimize the terminal cost function when $w_r \ll 1$, or the running cost, when $w_r \gg 1$.

The objective of the cost functional could also be to optimize the total duration of the process, for example. In this case, the following cost function could be added

$$J'_{run} = \frac{w_{r2}}{t_f}. \quad (3.9)$$

In principle, there is no limit to the number of running cost functionals one can use.

3.1.1.3 The Pontryagin Hamiltonian

We now introduce the appropriate Pontryagin Hamiltonian of the system. The Pontryagin Hamiltonian [265, 266], \mathcal{H}_p , is by definition given by

$$\mathcal{H}_p = \vec{\mathcal{P}} \cdot \dot{\vec{\mathcal{X}}} - J_{run}, \quad (3.10)$$

where $\vec{\mathcal{P}}$ is the adjoint state, also called the generalized momentum. If $\vec{\mathcal{P}}$ is written as

$$\vec{\mathcal{P}}(t) = \begin{pmatrix} p_1(t) \\ p_2(t) \\ p_3(t) \\ p_4(t) \end{pmatrix}, \quad (3.11)$$

the Pontryagin Hamiltonian reads as

$$\begin{aligned} \mathcal{H}_p &= p_1(t)x_2(t) - p_2(t)\omega_1^2[c(t)](x_1 - z_{sag,1}[c(t)]) \\ &+ p_3(t)x_4(t) - p_4(t)\omega_2^2[c(t)](x_3 - z_{sag,2}[c(t)]) \\ &- \frac{w_r}{2t_f} \left(\omega_1^2[c(t)](x_1(t) - z_{sag,1}[c(t)])^2 + \omega_2^2[c(t)](x_3(t) - z_{sag,2}[c(t)])^2 \right). \end{aligned} \quad (3.12)$$

The theory behind the PMP is complex and will not be described here for the sake of simplicity. The details of this theory can be found in [264, 265]. Here, we simply extract the main ingredients necessary for the present optimization scheme. The evolution of the adjoint state is given by the coupled differential equations

$$\dot{\vec{\mathcal{P}}}(t) = \begin{pmatrix} \dot{p}_1(t) \\ \dot{p}_2(t) \\ \dot{p}_3(t) \\ \dot{p}_4(t) \end{pmatrix} = \begin{pmatrix} -\frac{\partial \mathcal{H}_p}{\partial x_1} \\ -\frac{\partial \mathcal{H}_p}{\partial x_2} \\ -\frac{\partial \mathcal{H}_p}{\partial x_3} \\ -\frac{\partial \mathcal{H}_p}{\partial x_4} \end{pmatrix} = \begin{pmatrix} p_2(t)\omega_1^2[c(t)] + \frac{w_r}{t_f}\omega_1[c(t)]^2(x_1(t) - z_{sag,1}[c(t)]) \\ -p_1(t) \\ p_4(t)\omega_2^2[c(t)] + \frac{w_r}{t_f}\omega_2[c(t)]^2(x_3(t) - z_{sag,2}[c(t)]) \\ -p_3(t) \end{pmatrix}, \quad (3.13)$$

where the boundary condition of the adjoint state at t_f reads as

$$\vec{\mathcal{P}}(t_f) = \begin{pmatrix} p_1(t_f) \\ p_2(t_f) \\ p_3(t_f) \\ p_4(t_f) \end{pmatrix} = \begin{pmatrix} \left(-\frac{\partial J_{ter}}{\partial x_1} \right)_{t=t_f} \\ \left(-\frac{\partial J_{ter}}{\partial x_2} \right)_{t=t_f} \\ \left(-\frac{\partial J_{ter}}{\partial x_3} \right)_{t=t_f} \\ \left(-\frac{\partial J_{ter}}{\partial x_4} \right)_{t=t_f} \end{pmatrix} = \begin{pmatrix} -\omega_1^2[c(t_f)](x_1(t_f) - z_{sag,1}[c(t_f)]) \\ -x_2(t_f) \\ -\omega_2^2[c(t_f)](x_3(t_f) - z_{sag,2}[c(t_f)]) \\ -x_4(t_f) \end{pmatrix}. \quad (3.14)$$

Note that the Pontryagin Hamiltonian Eq. (3.12) and the evolution equation of the adjoint state Eq. (3.13) depend on the running cost and only the boundary condition Eq. (3.14) of the adjoint state depends on the terminal cost function.

3.1.1.4 Optimal control algorithm

I use a first-order standard gradient algorithm that is adapted to the control problem under consideration. The optimization procedure is given by the following steps:

- (i) First we choose an arbitrary initial control ramp $c(t)$, such as a linear ramp $c(t) = t/t_f$ for instance ;
- (ii) We then deduce the trap dynamics by calculating the two trap motions $z_{sag,1/2}(t)$ and the two trap frequencies $\omega_{1/2}(t)$;
- (iii) Using the Verlet method [289], we then solve Eq. (3.2) to simulate the dynamics of the particles from the initial time $t = 0$ to the final time $t = t_f$;
- (iv) We calculate the adjoint state $\vec{\mathcal{P}}(t_f)$ at the end of the transport using Eq. (3.14) and we propagate $\vec{\mathcal{P}}(t)$ backward in time until $t = 0$ using Eq. (3.13) ;
- (v) Finally, we add a first order correction to the control ramp by replacing the control function $c(t)$ by $c(t) + \delta_c(t)$, where the correction is $\delta_c(t) = \epsilon (\partial \mathcal{H}_p / \partial c)$, ϵ being a small positive constant.

At each iteration the procedure brings the final state closer to the target state and the procedure repeats until convergence is achieved.

3.1.1.5 Experimental considerations

Experiments can be limited by the rate of change of a given control parameter, such as a magnetic field for example. We bypass this problem by ensuring a smooth and more robust variation of the control parameter at initial and final times where the first and second derivative are imposed to be zero. For this we choose to impose

$$c(t) = c_0 + (c_f - c_0) \left[10 \left(\frac{u(t)}{u_f - u_0} \right)^3 - 15 \left(\frac{u(t) - u_0}{u_f - u_0} \right)^4 + 6 \left(\frac{u(t) - u_0}{u_f - u_0} \right)^5 \right] \quad (3.15)$$

where $u(t)$, the new control parameter, is a continuous function of time, starting at time $t = 0$ with $u_0 = u(0)$ and ending at time $t = t_f$ with $u_f = u(t_f)$. This definition naturally imposes the following boundary conditions for the control parameter

$$\begin{aligned} c(0) &= c_0 & c(t_f) &= c_f \\ \dot{c}(0) &= 0 & \text{and} & \dot{c}(t_f) = 0 \\ \ddot{c}(0) &= 0 & & \ddot{c}(t_f) = 0 \end{aligned} \quad (3.16)$$

Note that a consequence of these boundary conditions imposed on $c(t)$ is that similar relationships apply to all trap parameters such as trap positions $z_{\text{tag},1/2}$ and trap frequencies $\omega_{1/2}$. The optimization procedure we have adopted therefore uses the function $u(t)$, from which we can calculate the optimal control parameter using Eq. (3.15). In section 3.1.1.4, the control function, $u(t)$, is replaced by $u(t) + \delta_u(t)$, where the correction is

$$\delta_u(t) = \epsilon \left(\frac{\partial \mathcal{H}_p}{\partial c} \right) \times \left(\frac{\partial c}{\partial u} \right). \quad (3.17)$$

It can be notice that other flexible approaches have been introduced in the literature to circumvent this problem [206]

3.1.1.6 Comparison between STA and OCT

As indicated in section 2.3.2, the STA protocol is based on the reverse engineering technique. In this approach, the trajectory $z(t)$ is chosen, based on the knowledge of a boundary condition that this trajectory has to fulfill. In the equation $m\ddot{z} = F(z, \dot{z}, t; c)$, the only remaining unknown function is then the control parameter $c(t)$, and the reverse engineering technique extracts its evolution from the imposed trajectory. It is therefore important to understand that the key point of this technique is the ability to solve this equation, either analytically or numerically. In the general case, we need at least the same number of independent control parameters (currents, powers, voltages) as functions to be controlled (trajectory, size, energy). Mathematically, this corresponds to solving n equations with n unknowns. In the case of the control of two independent particles with a single control parameter, only specific configurations would provide the possibility to use the reverse engineering technique to design a transport for both species.

Unfortunately, this is not always the case experimentally. In a recent publication [257], we proposed OCT to solve the transport of a BEC from an initial ground state configuration to another. While STA techniques are able to solve the classical trajectory of the BEC, it is nevertheless difficult to control the BEC's shape oscillations using STA in the case of a single control parameter. On the other hand, in cases where there are many control parameters, although it may be possible in theory to express the different quantities of interest according to independent control parameters and vice versa, it may remain difficult to experimentally assess the impact of each control parameter. A good example to consider is the case of experiments on atom chips, where the number of possible wires and structures results in a large space of tunable parameters. Note that to overcome uncertainty problems during characterization measurements, robustness techniques have also been developed [215].

3.1.2 Model of a thermal ensemble of N particles

The aim of this section is to provide theoretical tools to describe the dynamics of a gas of N particles at temperature T where the average distance between the particles is greater than the size of the wave packet characterized by the de Broglie wavelength (see section 1.3.2). Within this approach, each particle is considered as "billiard balls"[156].

3.1.2.1 Properties of a thermal cloud

In the classical thermodynamic equilibrium where atoms can be considered as point particles, a thermal cloud is described by the Maxwell Boltzmann's distribution. In the case of a harmonic trap at time $t = 0$, the spatial and velocity density distributions are Gaussian, following

$$n_0(\mathbf{r}) = \frac{\exp\left(-\sum_{i=1}^3 \frac{r_i^2}{2\sigma_{r_i}^2(0)}\right)}{(2\pi)^{3/2} \prod_{i=1}^3 \sigma_{r_i}(0)}, \quad (3.18a)$$

$$\tilde{n}_0(\mathbf{v}) = \frac{\exp\left(-\sum_{i=1}^3 \frac{v_i^2}{2\sigma_{v_i}^2(0)}\right)}{(2\pi)^{3/2} \prod_{i=1}^3 \sigma_{v_i}(0)}, \quad (3.18b)$$

where $(r_1, r_2, r_3) \equiv (x, y, z)$ and $(v_1, v_2, v_3) \equiv (v_x, v_y, v_z)$. These distributions are characterized by the spatial and velocity widths

$$\sigma_{r_i}(0) = \sqrt{\frac{k_B T}{m\omega_i^2}} \quad \text{and} \quad \sigma_{v_i}(0) = \sqrt{\frac{k_B T}{m}}, \quad (3.19)$$

where T denotes the temperature of the cloud, k_B is the Boltzmann constant, m is the mass of the atom and ω_i is the frequency of the trap in the direction $i \in \{x, y, z\}$. It can be seen that the velocity distribution is always isotropic while the isotropy or anisotropy of the spatial distribution depends on the angular trap frequencies. We note $d_0(\mathbf{r}, \mathbf{v})$ the total density probability in phase space

$$d_0(\mathbf{r}, \mathbf{v}) = n_0(\mathbf{r}) \times \tilde{n}_0(\mathbf{v}), \quad (3.20)$$

which represents the probability to find a particle at position \mathbf{r} with a velocity \mathbf{v} .

3.1.2.2 Scaling approach

As described in [159, 290], in the case of a pure harmonic trap, the phase space dynamics of a cloud can be described by the set of coupled differential equations

$$\ddot{b}_i(t) + \omega_i^2(t) b_i(t) - \omega_i^2(0) \frac{\theta_i(t)}{b_i(t)} + \xi \left(\frac{\theta_i(t)}{b_i(t)} - \frac{1}{b_i(t) \prod_j b_j(t)} \right) \omega_i^2(0) = 0, \quad (3.21a)$$

$$\dot{\theta}_i(t) + 2 \frac{\dot{b}_i(t)}{b_i(t)} \theta_i(t) + \frac{1}{\tau(t)} \left(\theta_i(t) - \frac{1}{3} \sum_j \theta_j(t) \right) = 0, \quad (3.21b)$$

where the scaling parameter $b_i(t)$ denotes the dilation factor of the cloud and where $\theta_i(t)$ is an effective temperature in the i^{th} direction. The variable $\omega_i(t)$ refers to the tunable external angular trap frequency while $\omega_i(0)$ refers to its initial value, with which the cloud has been created initially at equilibrium. This set of equations takes into account two effects, first the mean-field interaction through

$$\xi = \frac{E_{mf}}{E_{mf} + k_B T}, \quad (3.22)$$

where E_{mf} is the mean-field interaction energy and T the temperature of the cloud. It also takes collision effects into account through

$$\tau(t) = \tau_0 \times \left(\prod_j b_j(t) \right) \times \left(\frac{1}{3} \sum_k \theta_k(t) \right), \quad (3.23)$$

where τ_0 is the average time of collision at equilibrium. The mean-field energy E_{mf} [160] is defined as

$$E_{mf} = \frac{4\pi\hbar^2 a N n_0(0)}{\sqrt{2} m}, \quad (3.24)$$

where a is the s-wave scattering length, N the total atom number, m the atomic mass and $n_0(0)$ the central initial density of the 3D distribution. The average time between collisions at equilibrium $\tau_0 = 5/(4\gamma)$ [159] is defined by the classical collision rate at the cloud center γ , where

$$\gamma = \frac{2}{\sqrt{2\pi}} N n_0(0) \sigma_s \sqrt{\frac{k_B T}{m}}. \quad (3.25)$$

In this last expression $\sigma_s = 4\pi a^2$ is the scattering cross section for identical bosons.

The time evolution of the characteristic spatial and velocity widths of the phase space density are described by the scaling laws

$$\sigma_{r_i}(t) = \sigma_{r_i}(0) \times b_i(t), \quad (3.26a)$$

$$\sigma_{v_i}(t) = \sqrt{\sigma_{v_i}^2(0) \times \theta_i(t) + \sigma_{r_i}^2(0) \times \dot{b}_i^2(t)} \quad (3.26b)$$

In the collision-less regime we can neglect the mean-field interactions, yielding to $\xi \rightarrow 0$ and $\tau_0 \rightarrow \infty$. We can then simplify the set of coupled differential equations Eq. (3.21) which become

$$\ddot{b}_i(t) + \omega_i^2(t) b_i(t) = \frac{\omega_i^2(0)}{b_i^3(t)}, \quad (3.27a)$$

$$\theta_i(t) = \frac{1}{b_i^2(t)}. \quad (3.27b)$$

It is also interesting to note that in the case of an isotropic trap the set of equations Eq. (3.21) can be simplified and rewritten as

$$\ddot{b}_i(t) + \omega_i^2(t) b_i(t) = \omega_i^2(0) \left(\frac{1-\xi}{b_i^3(t)} + \frac{\xi}{b_i(t) \prod_j b_j(t)} \right), \quad (3.28a)$$

$$\theta_i(t) = \frac{1}{b_i^2(t)}, \quad (3.28b)$$

which holds for a thermal gas in all collisional regimes.

3.1.2.3 N -particle representation of a thermal cloud

In the collision-less case, another numerical approach based on the evolution of N classical particles can be considered. The evolution of each particle is described by Newton's law

$$m\ddot{\mathbf{r}} = -\vec{\nabla}U_{ext}, \quad (3.29)$$

where U_{ext} denotes the external potential. Each particle starts with a specific initial condition $\{\mathbf{r}(0), \mathbf{v}(0)\}$, and is associated with a weight given by the probability distribution $d_0[\mathbf{r}(0), \mathbf{v}(0)]$. Numerically, these initial conditions can be defined on a uniform grid along the three directions $r_i \in \{x, y, z\}$, both for the position and velocity, following

$$r_{i,m}(0) = r_{i,min} + (m-1) \times \delta r_i \quad \text{for } m \in \{1, \dots, M\}, \quad (3.30)$$

$$v_{i,p}(0) = v_{i,min} + (p-1) \times \delta v_i \quad \text{for } p \in \{1, \dots, P\}, \quad (3.31)$$

where $\delta r_i = (r_{i,max} - r_{i,min})/(M-1)$ and $\delta v_i = (v_{i,max} - v_{i,min})/(P-1)$ are the step sizes of the spatial and velocity grids. Here, $r_{i,min/max}$ ($v_{i,min/max}$) are the minimum and maximum positions (velocities) in the direction $r_i \in \{x, y, z\}$. M (P) is the number of position (velocity) grid points.

In order to avoid the result of the simulation to be affected by the sampling method as shown in Fig. 3.1(a), we randomize the initial position and velocity of each particle

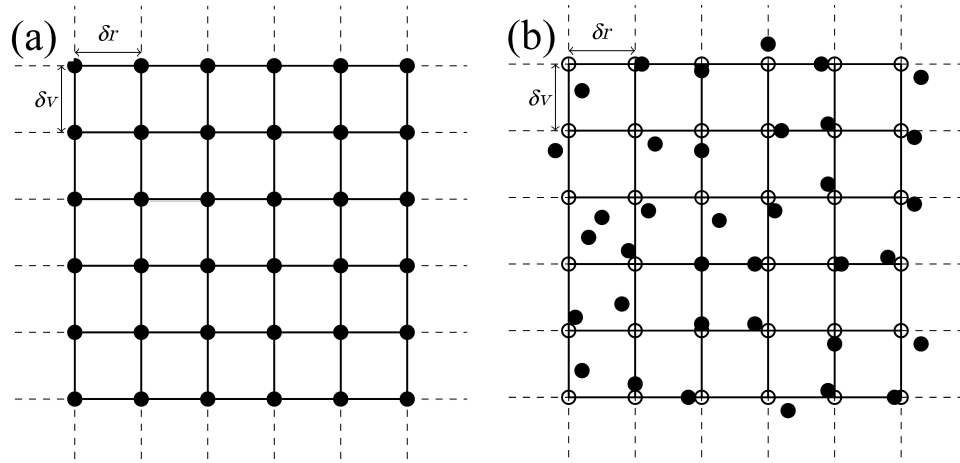


Figure 3.1: (a) Left: Biased sampling. The black points denote the position of each particle in phase space. They are equally distributed along the spatial and velocity axis. (b) Right: Randomized sampling. The black points denote the randomized position of each particle in phase space. They are non-equally distributed along the spatial and velocity axis. The empty black circles denote the previous biased configuration of Panel (a).

as shown in Fig. 3.1(b). To this end, we introduce random parameters which sample the initial coordinates around a uniform distribution.

Initially if the grids are not well chosen, with too large grids for instance, the biased sampling technique can propagate particles with a zero total density probability and the effective number of particles useful for the simulation is not optimized. A more efficient way to simulate the dynamics of the particles is to randomly select each particle according to the weight of its total density probability distribution. In this configuration, a hypothetical particle with a zero total density probability cannot be chosen and all particles contribute to the simulation. The algorithm procedure adopted follows the steps below:

- (i) Choose a particle in phase space : $\{r_{i,m}, v_{i,p}\}$.
- (ii) Solve the ODE for the trajectory of the particle at each time steps with initial conditions $\{r_0, v_0\} = \{r_{i,m}, v_{i,p}\}$. At time t , the particle in phase space has the coordinates $\{r_{i,m}(t), v_{i,p}(t)\}$.
- (iii) Reconstruction of the phase space density at each time step t . The initial particle at position $\{r_0, v_0\}$ with the weight $d_0(r_0, v_0)$ is then at position $\{r_t, v_t\}$ with the weight $d_t(r_t, v_t) = d_0(r_0, v_0)$.

3.2 Applications

3.2.1 Dual-source input state optimization

The aim of the Stanford experiment is to test the Universality of Free Fall (UFF) with two isotopes of Rubidium, ^{87}Rb and ^{85}Rb [37, 125, 261, 262]. Other groups pursue this goal with different atoms, ^{87}Rb and K [38, 41, 81], ^{87}Rb and Yb [40] or with identical atoms in different internal states [83, 124]. For all these cases, the initial co-location of the two test masses must be insured at a high level. Recently, the Stanford group suppressed the relative phase shifts associated with non-constant gravity gradients coupling to initial position and velocity offset to below 10^{-13} in the gravity gradient systematic errors with the Frequency Shift Gravity Gradient (FSGG) compensation method [37], an idea initially proposed in Ref. [43]. This technique was also successfully applied in the group of G. M. Tino [44]. For competitive UFF tests at 10^{-15} , however, the co-location uncertainty must be at the level of the μm and the differential velocities offset at the $\mu\text{m}\cdot\text{s}^{-1}$ level. This motivates the treatment developed below to prepare the dual-source in a UFF test-compatible initial state.

3.2.1.1 Experimental configuration

The complete experimental setup has already been described in various PhD theses such as Refs. [261, 262, 291]. For the sake of simplicity we only present in Fig. 3.2 a scheme of the experimental realization.

The device is defined by a vertically oriented quadrupole trap characterized by a quadrupole gradient $\nabla B = A$, and by two pairs of horizontal coils to create a rotating bias magnetic field B_0 , leading to a time-orbiting potential (TOP) trap designated by V_{TOP} . The potential associated with the TOP magnetic field B_{TOP} is given by

$$V_{TOP} = \vec{\mu} \cdot \vec{B}_{TOP}, \quad (3.32)$$

where $\vec{\mu}$ is the magnetic dipole moment of the atom given by the product of the Zeeman sublevel number, m_F , the Landé factor g_F , and the Bohr magneton μ_B , with $\mu = m_F g_F \mu_B$. We assume that the magnetic dipole remains aligned with the rotating magnetic field and therefore

$$V_{TOP} = \mu B_{TOP}. \quad (3.33)$$

The total TOP trap [292] created by the sum of the bias magnetic field B_0 and the quadrupole magnetic field $B_{quad} = A\sqrt{\rho^2 + 4z^2}$ has a cylindrical shape, where the two

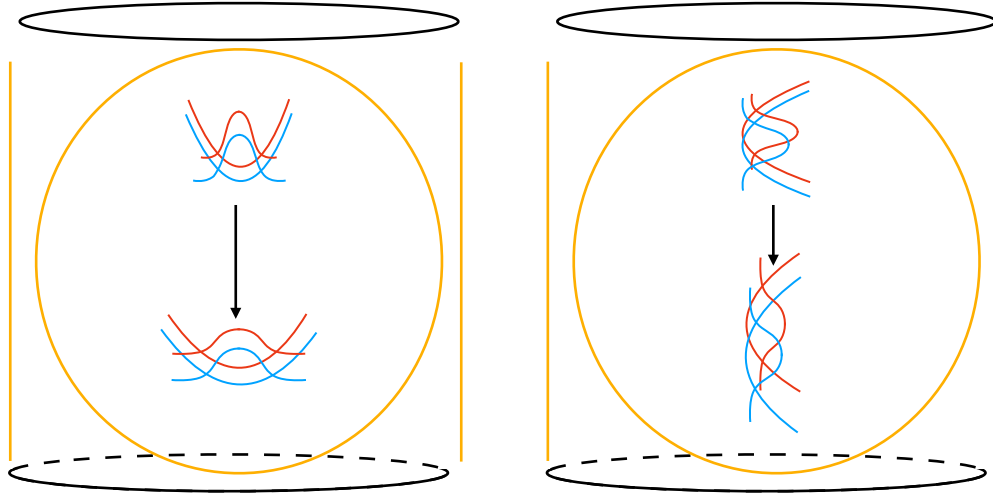


Figure 3.2: Stanford bottom of fountain setup. The black circle denotes the vertically oriented quadrupole trap responsible for the quadrupole gradient $\nabla B = A$. The orange lines and circle denote the two sets of horizontal coil pairs responsible for the rotating bias magnetic field B_0 . In both graphs the upper trap denotes the initial trap along the radial direction (left panel) and vertical direction (right panel). The two clouds of ^{87}Rb (in blue) and ^{85}Rb (in red) are depicted in their initial trap configuration ($A = 10.3 \text{ G}\cdot\text{cm}^{-1}$ and $B_0 = 1.2 \text{ G}$, top) and in their final configuration ($A = 10.3 \text{ G}\cdot\text{cm}^{-1}$ and $B_0 = 6.9 \text{ G}$, bottom). While the bias field B_0 increases, both clouds fall along the direction of gravity (black arrow) and the trap frequencies decrease.

characteristic directions are indicated by the variables ρ for the radial direction and by z for the vertical direction. In a pure quadrupole trap, the minimum of the trap is at zero magnetic field and consequently Majorana spin flips [293] occur, causing atomic losses. To avoid this problem, a bias magnetic field is switched on, leading to a minimum trap translation of B_0/A position where the atoms would be ejected from the trap. The direction of the bias magnetic field is rotated and applied in a non-adiabatic manner such that the atoms are trapped in a non-zero magnetic field. Atoms passing through the so-called circle-of-death at $r_{death} = B_0/A$ are then ejected out of the trap. In 1995, in the group of E. Cornell, this setup led to the creation of the first BEC [154].

The experiment sequence begins with the creation of a cold Rubidium cloud, where ^{87}Rb is prepared in $|F = 2, m_F = 2\rangle$ ($g_F = 1/2$) and ^{85}Rb is prepared in $|F = 3, m_F = 3\rangle$ ($g_F = 1/3$) at a temperature of few micro-Kelvin (we choose $T=1 \mu\text{K}$ for the simulation), in a fixed trap defined by a quadrupole gradient of 10.3 cm/G ($\pm 5\%$) and an adjustable bias rotating field of 1.2 G . While maintaining the quadrupole gradient constant, the rotating bias magnetic field is tuned, from 1.2 G to 6.9 G to transport (only along the vertical axis)

the two clouds in lower trap frequencies. This decompression induces a size oscillation of the atomic clouds, which will be used later for the DKC technique to optimize the launch in a blue detuned lattice. The next steps, which are not discussed here, are the launch in the 10 meter long tube in a vertical blue detuned lattice, the DKC technique with a vertical dipole trap, the interferometry sequence and the detection at the bottom of the tower. The details of the sequences can be found in [262]. However, the following case study will be limited to the transport and shape optimization of the two species prior to the vertical launch.

3.2.1.2 Trap configuration

It can be shown that the total TOP magnetic field is given by

$$B_{TOP} = \frac{1}{2\pi} \sqrt{B_0^2 + B_{quad}^2} \int_0^{2\pi} \sqrt{1 + \beta \cos(\tau)} d\tau, \quad (3.34a)$$

$$= \frac{1}{\pi} \sqrt{B_0^2 + B_{quad}^2} \left[\sqrt{1 - \beta} E\left(\frac{-2\beta}{1 - \beta}\right) + \sqrt{1 + \beta} E\left(\frac{2\beta}{1 + \beta}\right) \right], \quad (3.34b)$$

where

$$\beta = \frac{2AB_0\rho}{B_0^2 + B_{quad}^2}, \quad (3.35)$$

and E indicates the complete elliptic integral. More details can be found in [262, 292, 294, 295].

In the experimental configuration, changing the control parameter B_0 ² only induces a classical motion of the atoms along the vertical direction and maintains the classical radial degrees of freedom unchanged. In parallel with the classical motion, the change of the control parameter induces a cloud size excitation in both directions. In the following, the classical trajectory of each cloud is described by the evolution of an equivalent classical particle whose position is given by the average position of the cloud

$$\langle z \rangle = \int_{-\infty}^{\infty} z n_0(z) dz. \quad (3.36)$$

At the position $\rho = 0$ the total TOP magnetic field reads

$$B_{TOP} \Big|_{\rho=0} = \sqrt{B_0^2 + 4A^2 z^2}, \quad (3.37)$$

leading, in the presence of gravity, to the total potential given by

$$V_{TOP}(z) \Big|_{\rho=0} = \mu \sqrt{B_0^2 + 4A^2 z^2} + m g z. \quad (3.38)$$

²Here we consider the case where the parameter is not changed adiabatically

The classical motion in the trap is given by the Newton's law

$$m\ddot{z}\Big|_{\rho=0} = -\frac{4\mu A^2 z}{\sqrt{B_0^2 + 4A^2 z^2}} - mg. \quad (3.39)$$

A Taylor expansion close to the minimum of the potential gives valuable information such as the expression of the position of the minimum of the trap, z_{sag} , the frequency of the trap, ω_z , and the characteristic cubic length L_3 defined by

$$V_{TOP}(z) = V_{TOP}(z_{sag}) + \frac{(z - z_{sag})^2}{2} \left(\frac{d^2 V_{TOP}}{dz^2} \right)_{z_{sag}} + \frac{(z - z_{sag})^3}{6} \left(\frac{d^3 V_{TOP}}{dz^3} \right)_{z_{sag}} \quad (3.40a)$$

$$= V_{TOP}(z_{sag}) + \frac{1}{2} m \omega_z^2 \left(1 + \frac{z - z_{sag}}{L_3} \right) (z - z_{sag})^2, \quad (3.40b)$$

The different quantities are given by

$$z_{sag}[B_0] = \frac{mgB_0}{2A\sqrt{4A^2\mu^2 - m^2g^2}}, \quad (3.41a)$$

$$\omega_z[B_0] = \frac{(4A^2\mu^2 - m^2g^2)^{3/4}}{\mu\sqrt{2AB_0m}}, \quad (3.41b)$$

$$L_3[B_0] = \frac{\sqrt{4A^2\mu^2 - m^2g^2}}{18AB_0gm} \left(B_0^2 + \frac{m^2g^2B_0^2}{4A^2\mu^2 - m^2g^2} \right). \quad (3.41c)$$

Note that in the general case, the mass-dependence of the gravitational sag, z_{sag} , leads to a displacement of the trap minima for different species. The term $(z - z_{sag})/L_3$ denotes the strength of the cubic term and serves to quantify the limit of the harmonic trap approximation. If the amplitude oscillation, $z - z_{sag}$, also also referred to as offset in the following, is small enough, *i.e.* for

$$|z - z_{sag}| \ll L_3, \quad (3.42)$$

the trajectory of the particle is limited to the harmonic part of the trap and can be described by the equation

$$\ddot{z} + \omega_z^2[B_0] (z - z_{sag}[B_0]) = 0, \quad (3.43)$$

If the strength of the cubic term is not negligible, the trajectory of the particle is governed by

$$\ddot{z} = -\frac{4\mu A^2}{m\sqrt{B_0^2 + 4A^2 z^2}} z - g. \quad (3.44)$$

The initial and final configurations of the trap are shown along the vertical axis in Fig. 3.3a and Fig. 3.3b, respectively. The blue and red lines indicate the trap seen by ^{87}Rb and ^{85}Rb , respectively. Following the same color code, the curved dashed lines show the harmonic approximation and the positions of the minima of the two traps are highlighted by the vertical dashed lines. Experimentally, the motion of the cloud is very limited along the radial direction, and since the trap is harmonic over a wide range, as shown in Fig. 3.4, we limit the Taylor expansion to the second order. Along this axis, the motion of the cloud is described by Newton's equation

$$\ddot{\rho} + \omega_{\rho}^2[B_0] \rho = 0, \quad (3.45)$$

where ω_{ρ} denotes the radial angular trap frequency

$$\omega_{\rho}[B_0] = \frac{(4A^2\mu^2 - m^2g^2)^{1/4} (4A^2\mu^2 + m^2g^2)^{1/2}}{4\mu\sqrt{mAB_0}}. \quad (3.46)$$

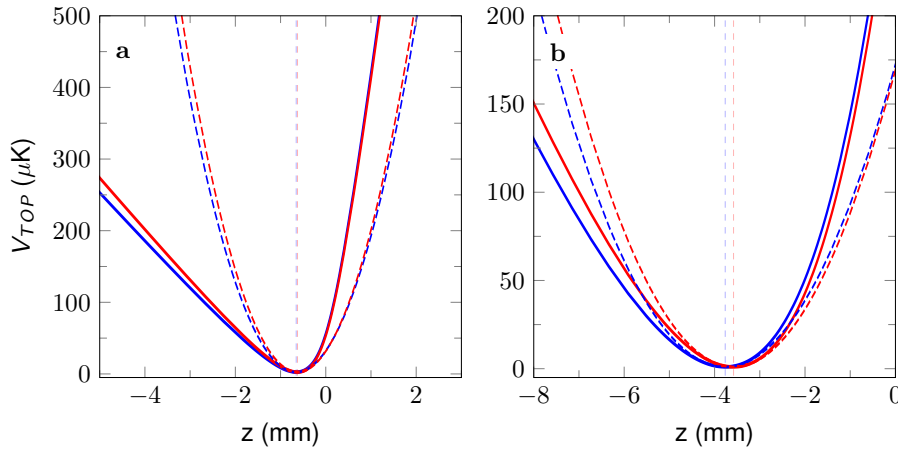


Figure 3.3: Representation of the two traps along the vertical direction at the initial (a) and final position (b). The blue and red lines denote the trap seen by ^{87}Rb and ^{85}Rb , respectively. Following the same color code the harmonic approximation of both traps at both positions are shown in dashed lines. The positions of the minima of the traps are highlighted by vertical dashed lines.

Finally, Fig. 3.5 shows the evolution of the trap frequencies in both directions for both species as a function of the bias magnetic field. The change of the control parameter B_0 leads to a trap decompression. In Refs. [188, 291] this effect is used to reduce the cloud's kinetic expansion which will be further discussed in section 3.2.1.4.

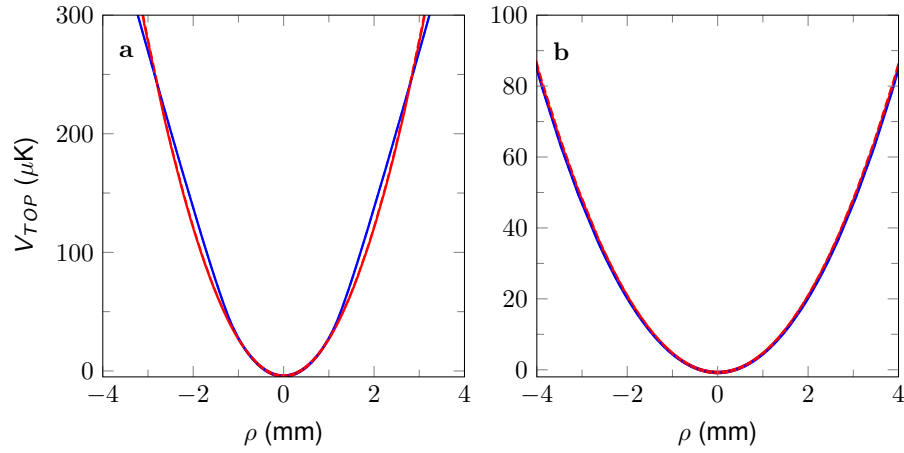


Figure 3.4: Representation of the two traps along the radial direction at the initial position (a) and final position (b). The blue and red lines denote the trap seen by ^{87}Rb and ^{85}Rb , respectively. Following the same color code the harmonic approximations are shown as superimposed dashed lines. Both traps are centered at $\rho = 0$.

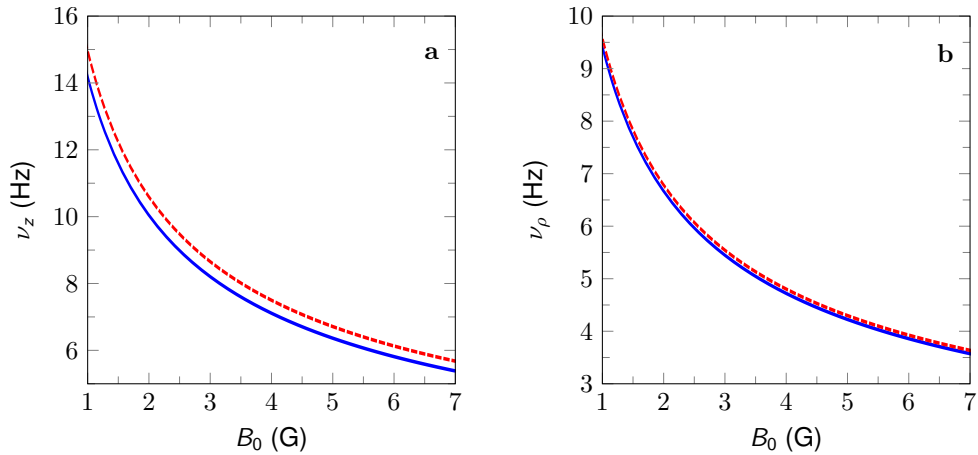


Figure 3.5: Evolution of the trap frequencies as a function of the bias magnetic field along the vertical direction in panel (a) and along the radial direction in panel (b). The blue line is for ^{87}Rb and the red dashed line for ^{85}Rb .

3.2.1.3 Optimal transport in the harmonic trap approximation

The OCT technique introduced in section 3.1.1 is now applied to study the vertical transport of two classical particles of different mass in the harmonic trap approximation. To this end, we fix the total duration of the transport to 150 ms and compare the results of different protocols, where the weight of the running cost function w_r takes the values: 0, 10^{-3} , 10^{-2} and 10^{-1} . The case $w_r = 0$ denotes a protocol where nothing is done to limit

the transient energy of the system. Fig. 3.6 shows the OCT results for different classical particles trajectories, z_{87Rb} in blue and z_{85Rb} in red, together with the minima z_{sag} of their corresponding trap potentials (dashed). The impact of the transient excitation is shown in the left panel of Fig. 3.7. As expected, the offset between the particle position and the trap minimum decreases for large values of w_r . In the panels a, b and c of Fig. 3.7 we compare the offset with a fixed value of w_r (straight lines) to $w_r = 0$ (dashed lines). Without optimization of the transient energy, the maximum offset reaches -1.2 mm while for $w_r = 10^{-1}$ the maximum offset has been divided by 2. To validate that the harmonic approximation hold for the different protocols, it is necessary to compare the offset to the cubic length of the trap given in Eq. (3.41c). The right panel of Fig. 3.7 shows that even though the oscillation amplitude is reduced, the harmonic criterion Eq. (3.42) is not fulfilled.

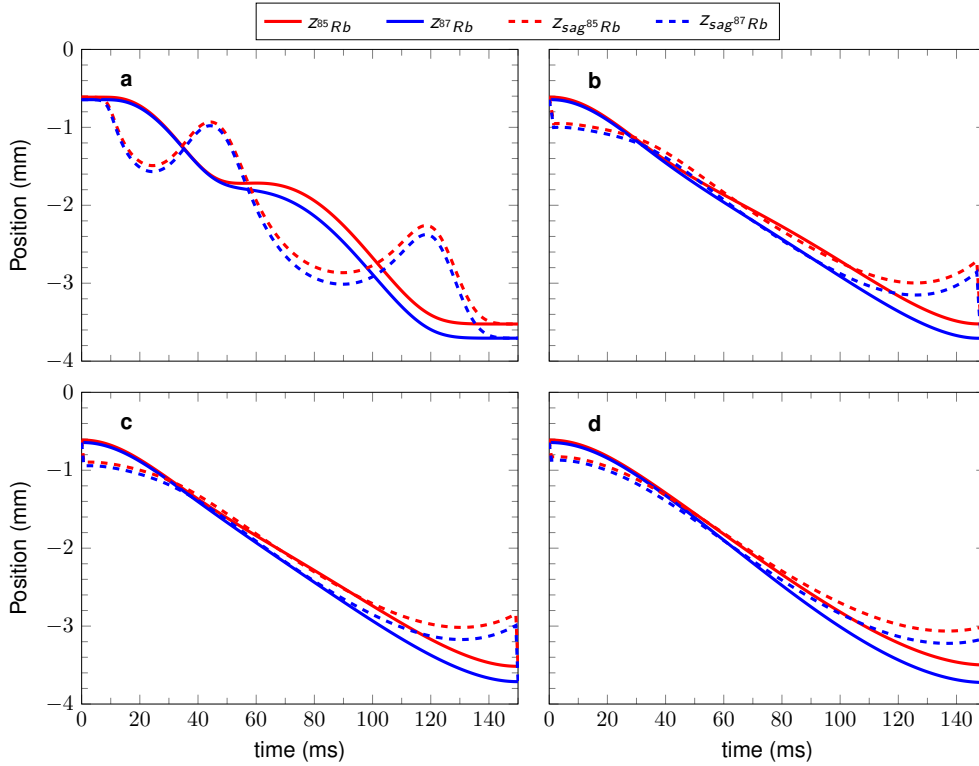


Figure 3.6: Result of the OCT protocol for the transport in 150 ms of the two species. The evolution of the two particles is shown in colored solid lines as well as their corresponding trap minima in dashed colored lines, for different weights of the running cost function: (a) $w_r = 0$, (b) $w_r = 10^{-3}$, (c) $w_r = 10^{-2}$, (d) $w_r = 10^{-1}$. The larger the values of w_r are, the smaller the offset between the particle position and the trap position of each particle is.

To solve this problem, it would be natural to increase the weight of the running

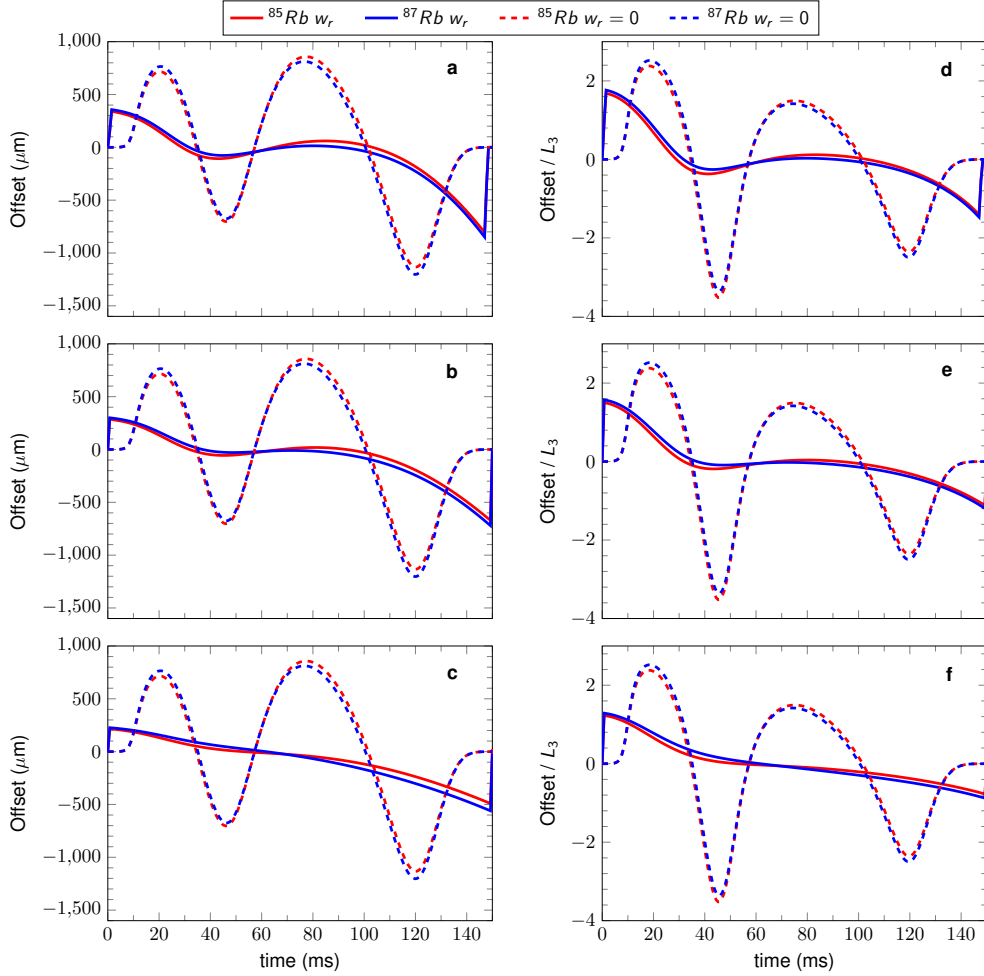


Figure 3.7: Result of the OCT protocol for the offset and the strength of the cubic term. The left column shows the offset between the position of each particle to its corresponding trap minimum for a 150 ms transport with different weights of the running cost function. The offset is shown in colored straight lines and compared to an OCT protocol without optimization of the offset ($w_r = 0$), shown as dashed colored lines. The right column depicts the strength of the cubic term for the corresponding transport. (a-d) $w_r = 10^{-3}$, (b-e) $w_r = 10^{-2}$, (c-f) $w_r = 10^{-1}$. With increasing value of w_r , the offset, and with that the strength of the cubic term, is decreasing.

cost function. Figures Fig. 3.8 and Fig. 3.9, respectively, represent the position and velocity offsets of the two particles at the end of the transport as a function of the OCT iteration steps. For $w_r = 10^{-3}$, in panel (a), the offset in position is less than $\pm 1 \mu\text{m}$ with a velocity offset less than $7 \mu\text{m/s}$, while for $w_r = 10^{-1}$, in panel (c), the position offset is approximately $\pm 25 \mu\text{m}$ for the two species with a final velocity offset of -0.17 mm/s (for ^{87}Rb) and -0.48 mm/s (for ^{85}Rb). We can see here that the increase of the weight, w_r ,

unfortunately leads to a final state out of equilibrium because the OCT algorithm then prioritizes the minimization of the transient excitation energy, while missing the final target state at $t=150\text{ms}$.

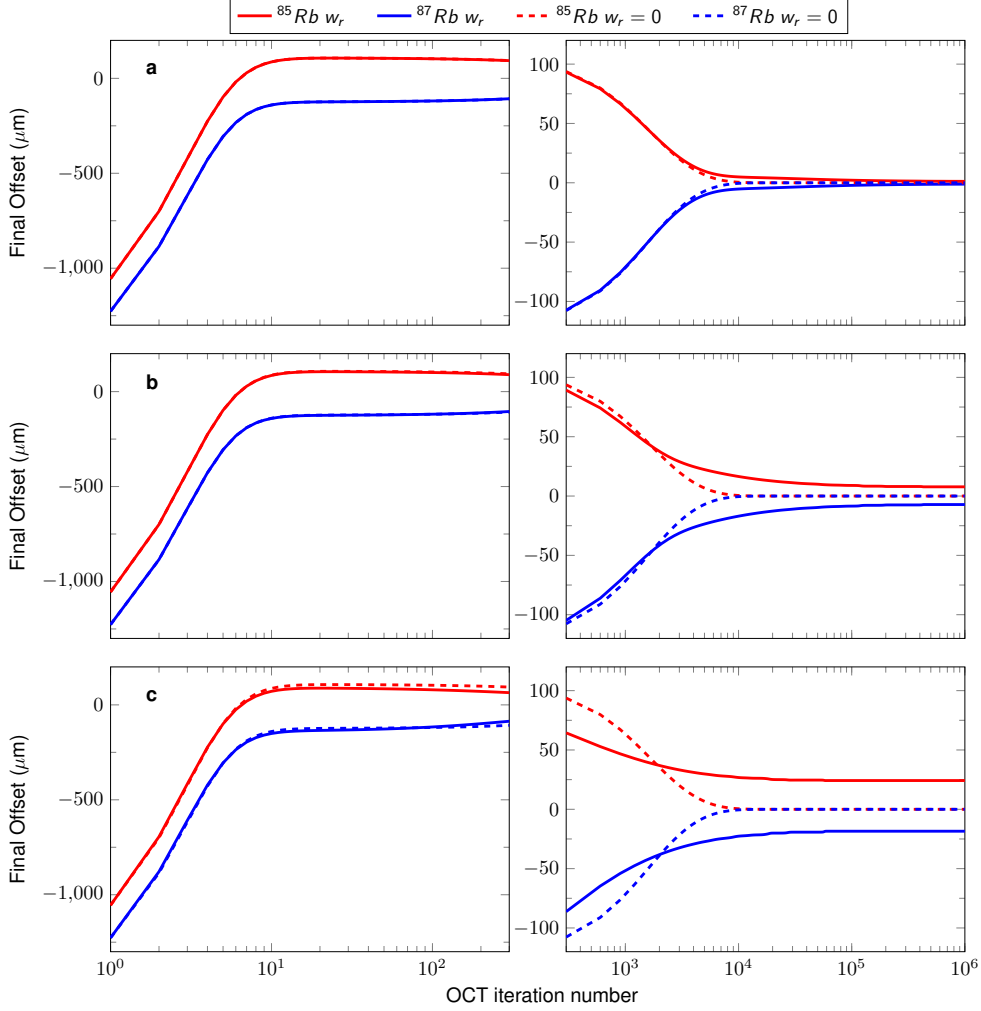


Figure 3.8: Influence of the weight of the running cost function on the final position offsets as a function of the number of OCT iterations. In colored straight lines: (a) $w_r = 10^{-3}$, (b) $w_r = 10^{-2}$, (c) $w_r = 10^{-1}$. The dashed colored lines depict the case where $w_r = 0$. The same quantities are shown in the left and right panels, but with different scales. The increase of the weight, w_r , leads the OCT algorithm to miss the final equilibrium states, the particles are displaced from their corresponding trap minimum.

Increasing the weight of the running cost function has another detrimental impact. Experimentally, one has to take into account the maximum switch on/off time of the control parameter for the implementation of such protocols. In Fig. 3.10 we show the different evolutions of the optimal control parameter B_0 for the different values of w_r .

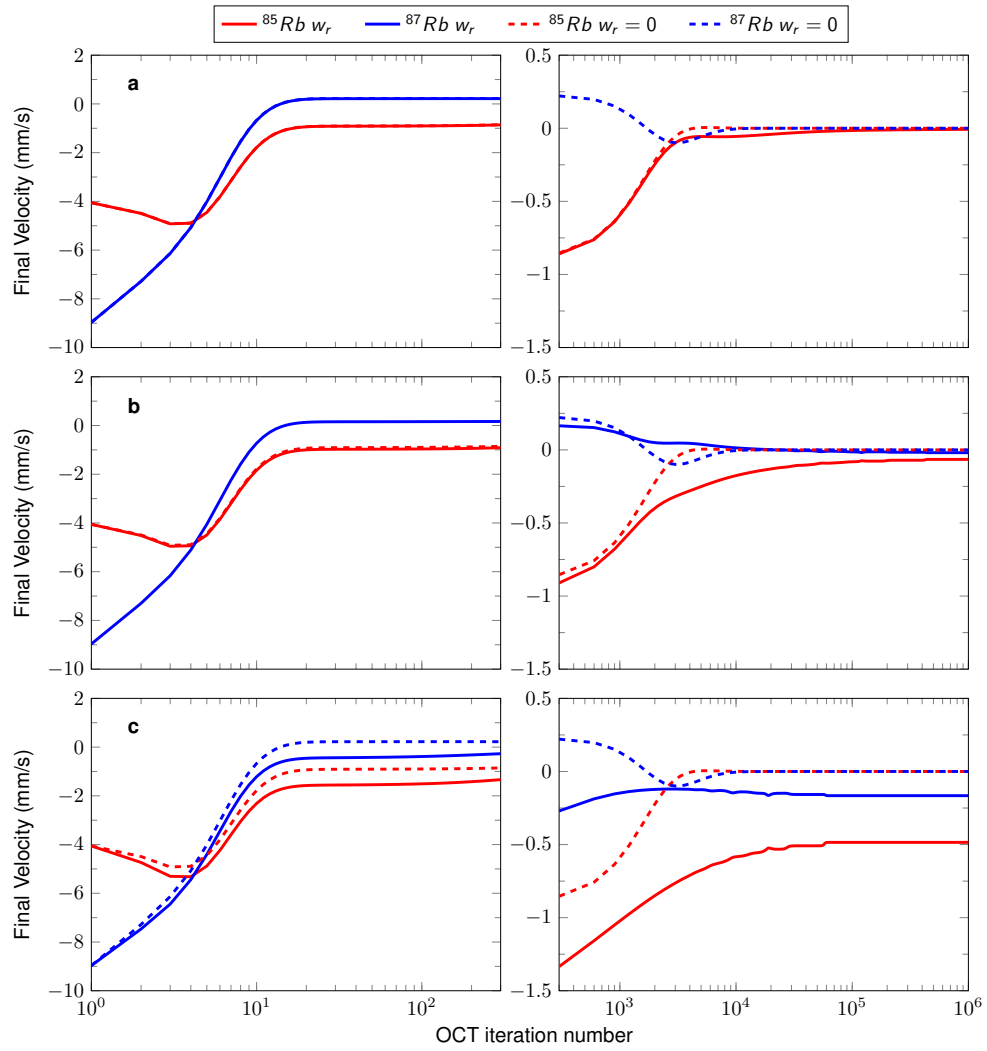


Figure 3.9: Influence of the weight of the running cost function on the final velocity as a function of the OCT iteration number. In colored straight lines: (a) $w_r = 10^{-3}$, (b) $w_r = 10^{-2}$, (c) $w_r = 10^{-1}$. The dashed colored lines depict the case where $w_r = 0$. The same quantities are shown in the left and right panels, but with different scales. The increase of the weight, w_r , leads the OCT algorithm to miss the final equilibrium states, the final velocities of the two particles are non-zero.

The optimization of the transient energy causes a sudden change of the control parameter at the beginning and at the end of the protocol. Similar effects have been shown in [296]. Due to experimental limitations, such sudden changes are detrimental and have to be avoided to insure the robustness of the ramp³.

A solution to limit the transient excitation energy and to avoid a sudden change in

³The rate change of a magnetic field depends on the experimental setup

the control parameter B_0 is to increase the total ramp time. We excluded this solution because of the increase of cycle time of the experiment. The fact that it is impossible to find a smooth ramp for the control parameter in time within the harmonic criterion within a 150 ms ramp implies the necessity of designing OCT protocols in the real trap configuration and is the subject of the next section.

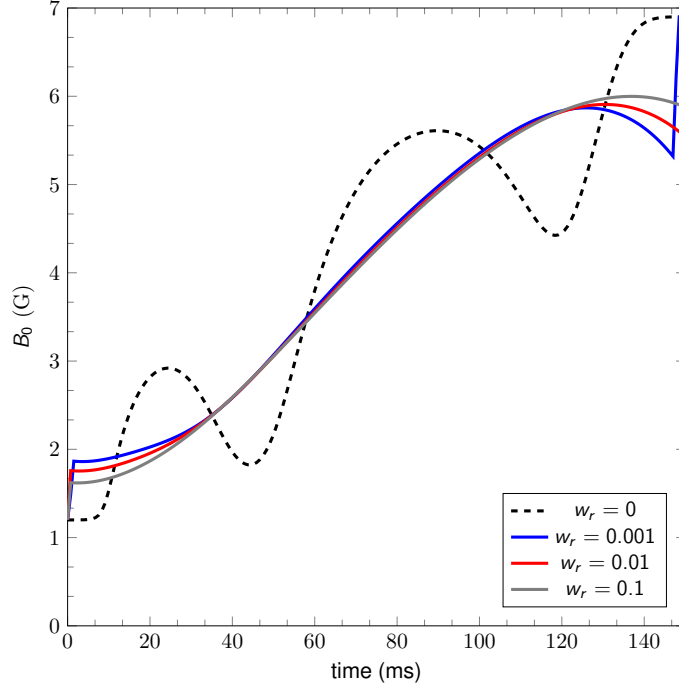


Figure 3.10: Time evolution of the control parameter $B_0(t)$ for the different weights w_r of the running cost function. The increase of the weigh, w_r , leads to fast change of the control parameter.

3.2.1.4 Optimal transport in the real trap configuration

In the actual trap configuration, it is necessary to rewrite the different equations of the OCT protocol derived in section 3.1.1. The dynamics of the two particles along the vertical axis are given by

$$\ddot{z}_1 = -\frac{4\mu_1 A^2 z_1}{m_1 \sqrt{B_0^2 + 4A^2 z_1^2}} - g, \quad (3.47a)$$

$$\ddot{z}_2 = -\frac{4\mu_2 A^2 z_2}{m_2 \sqrt{B_0^2 + 4A^2 z_2^2}} - g. \quad (3.47b)$$

In the previous section, the OCT protocols had to restrain the offset such that the harmonic approximation is feasible. However, in the following, we take the actual trap configuration into account, such that the only target of the OCT protocol is the minimization of the final energy of the classical system by bringing the two particles at rest in their respective trap minimum. The cost function then reads as

$$J_{tot} = J_{ter} = \frac{\mu_1}{m_1} \sqrt{B_0^2 + 4A^2 x_1^2} + g x_1 + \frac{1}{2} x_2^2 + \frac{\mu_2}{m_2} \sqrt{B_0^2 + 4A^2 x_3^2} + g x_3 + \frac{1}{2} x_4^2. \quad (3.48)$$

The Pontryagin Hamiltonian, $\mathcal{H}_p = \vec{\mathcal{P}} \cdot \dot{\mathcal{X}}$, is then

$$\begin{aligned} \mathcal{H}_p = & p_1 x_2 - \frac{1}{m_1} \frac{4\mu_1 A^2}{\sqrt{B_0^2 + 4A^2 x_1^2}} x_1 p_2 - g p_2 \\ & + p_3 x_4 - \frac{1}{m_2} \frac{4\mu_2 A^2}{\sqrt{B_0^2 + 4A^2 x_3^2}} x_3 p_4 - g p_4, \end{aligned} \quad (3.49)$$

where the evolution of the adjoint state is given by

$$\dot{\vec{\mathcal{P}}}(t) = \begin{pmatrix} \dot{p}_1(t) \\ \dot{p}_2(t) \\ \dot{p}_3(t) \\ \dot{p}_4(t) \end{pmatrix} = \begin{pmatrix} -\frac{\partial \mathcal{H}_p}{\partial x_1} \\ -\frac{\partial \mathcal{H}_p}{\partial x_2} \\ -\frac{\partial \mathcal{H}_p}{\partial x_3} \\ -\frac{\partial \mathcal{H}_p}{\partial x_4} \end{pmatrix} = \begin{pmatrix} \frac{4\mu_1 A^2 B_0^2}{m_1 (B_0^2 + 4A^2 x_1^2)^{3/2}} p_2(t) \\ -p_1(t) \\ \frac{4\mu_2 A^2 B_0^2}{m_2 (B_0^2 + 4A^2 x_3^2)^{3/2}} p_4(t) \\ -p_3(t) \end{pmatrix}, \quad (3.50)$$

with the following boundary condition at t_f

$$\vec{\mathcal{P}}(t_f) = \begin{pmatrix} p_1(t_f) \\ p_2(t_f) \\ p_3(t_f) \\ p_4(t_f) \end{pmatrix} = - \begin{pmatrix} \left(\frac{\partial J_{ter}}{\partial x_1} \right)_{t=t_f} \\ \left(\frac{\partial J_{ter}}{\partial x_2} \right)_{t=t_f} \\ \left(\frac{\partial J_{ter}}{\partial x_3} \right)_{t=t_f} \\ \left(\frac{\partial J_{ter}}{\partial x_4} \right)_{t=t_f} \end{pmatrix} = \begin{pmatrix} -\frac{4\mu_1 A^2}{m_1 \sqrt{B_0^2 + 4A^2 x_1^2(t_f)}} x_1(t_f) - g \\ -x_2(t_f) \\ -\frac{4\mu_2 A^2}{m_2 \sqrt{B_0^2 + 4A^2 x_3^2(t_f)}} x_3(t_f) - g \\ -x_4(t_f) \end{pmatrix}. \quad (3.51)$$

Out of Eqs. (3.4), (3.47), (3.50), (3.51) and the OCT protocol steps discussed in section 3.1.1.4 one can find the optimized evolution of the control parameter $B_0(t)$ for the real trap configuration.

3.2.1.5 Classical trajectories

We are now interested in the impact of the OCT protocol in the realistic trap configuration case for different total times. Fig. 3.11 shows the evolution of the control parameter $B_0(t)$ for different final times of the ramp. The black dashed line shows the evolution of the control parameter for a final time of 1 s typical for an adiabatic dynamics. It is compared to three transport times, $t_f = 200$ ms (red curve), $t_f = 150$ ms (blue curve) and $t_f = 100$ ms (gray curve). The decrease of the duration of the transport ramp results in an increase in the transient kinetic energy, and results in an oscillation of the control parameter whose number of oscillations and the amplitude depend on the duration of the ramp.

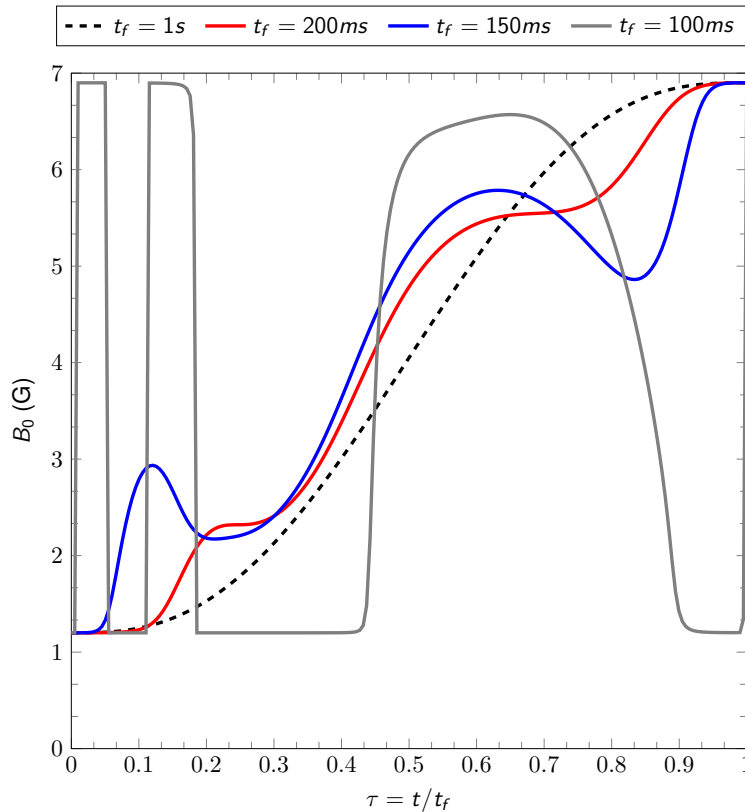


Figure 3.11: Time evolution of the control parameter $B_0(t)$ for different transport durations. The horizontal time axis is rescaled to one using $\tau = t/t_f$. The black dashed line represents a transport in 1 s, a typical time associated with an adiabatic dynamics. The reduction of the total time of the ramp leads to fast oscillation of the control parameter. Longer ramps lead to smooth evolution of the control parameter. The apparent complexity of the ramp increases with fast ramps.

It can be noted that the fastest the ramp is the more abrupt is the change of the control parameter. The impact of the non-harmonic part of the trap on the change of the

control parameter is highlighted by the difference between the black dashed curve of Figure 3.10 and the blue solid curved of Figure 3.11 where both control ramp have been calculated for a transport time of 150 ms. The solution find out with the OCT protocol is very similar but the amplitude oscillation is modified, in a non predictable way, to compensate for the non-harmonic trap behavior shown in Figure 3.3.

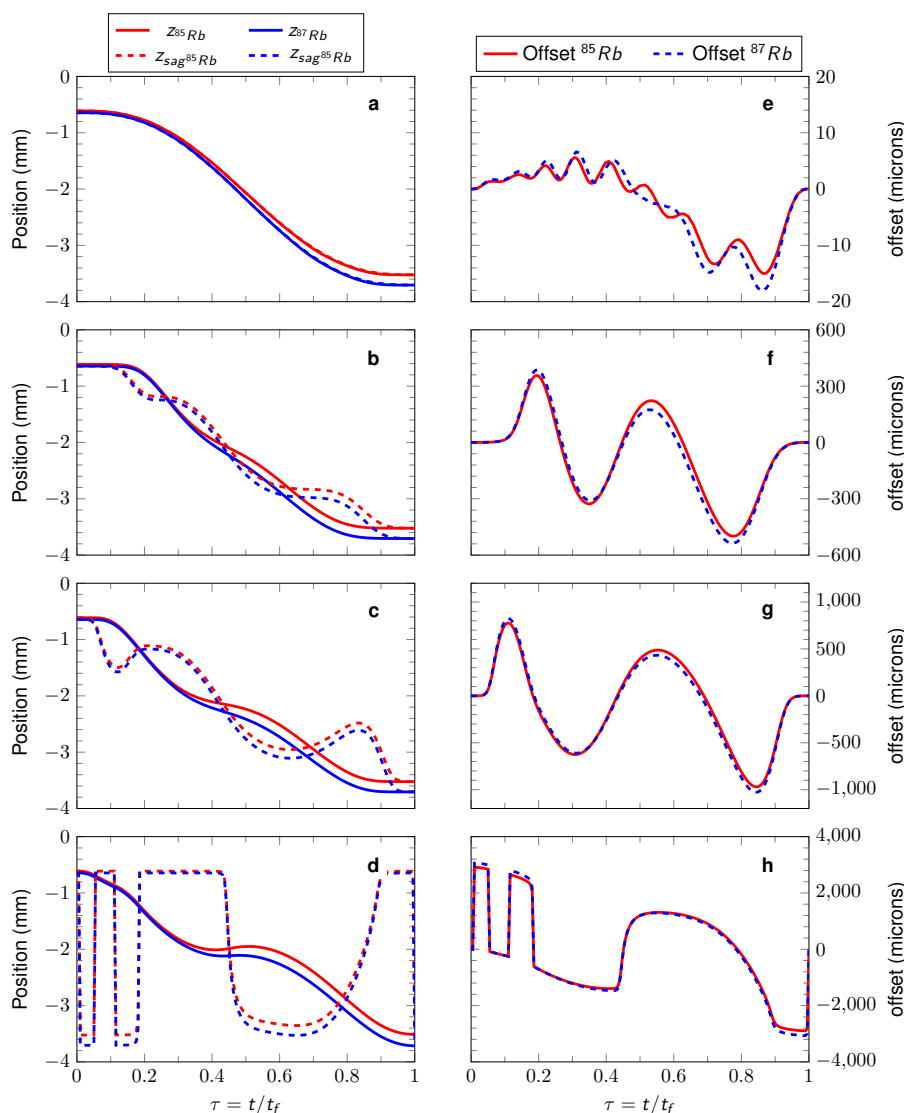


Figure 3.12: Result of the OCT protocol for the transport of two particles in the real trap. Panels (a-d): Position of the two particles in solid lines and their corresponding trap trajectories in dashed lines. Panels (e-h): Offset between the position of the particle and the trap minimum. The transport times are (a,e): $t_f = 1$ s, (b,f): $t_f = 200$ ms, (c,g): $t_f = 150$ ms, (d,h): $t_f = 100$ ms. In the same way than for the figure Fig. 3.11, fast ramps lead to an increase of the offset and the number of oscillation in the trap.

Figure 3.12 shows the impact of the different ramp duration on the trajectory of the particles. The left column shows the trajectories of the particles in solid colored lines and in dashed colored lines the corresponding trajectories of the trap minima. The right panel represents the offset between the positions of the particles and the minimum of the corresponding trap. For all cases, the OCT protocol brings the two particles from their initial position to their final position at rest. A comparison between Fig. 3.12 panel (c) and Fig. 3.6 panel (a) gives a quantitative idea of the impact of the anharmonic term. In both cases the transport is performed in 150 ms with $w_r = 0$.

3.2.1.6 Size excitations

Depending on the transport duration, the two thermal clouds do not follow the same trajectory. The phase space evolution, described with a N -particles simulation, can be optimized by modifying the final time of the ramp. In this section I study the impact of the final time of the ramp on the final phase space distribution⁴. Fig. 3.13 and Fig. 3.14 show the distributions in phase space of the two thermal clouds along the vertical direction denotes by z and the radial direction denotes by ρ , for different final times of the protocol and at different times of the transport, $\tau = t/t_f = 0, 0.25, 0.5, 0.75$ and 1. In each panel the horizontal axis represents the velocity in mm/s and the vertical axis represents the position in mm denotes by z and ρ for simplicity. The horizontal dashed lines represent the initial and final positions of the two clouds while the vertical dashed line represents the zero velocity axis. In Fig. 3.13 the two initial positions are different but are not distinguishable since $\Delta z_{sag}(0) = 33 \mu\text{m}$. They are distinguishable at the end of the transport, with $\Delta z_{sag}(t_f) = 188 \mu\text{m}$. Along the radial direction, in Fig. 3.14, the clouds are collocated at the same position and the change of the control parameter only rotates the ellipsoid in phase space.

Due to the increase of the transient energy for fast ramps and to the non-harmonic shape of the trap, cloud size expansions are maximized for fast transports. This can be understood by looking at the trap (see Fig. 3.3), where the gradient of the potential is smaller on the left side and stronger on the right side. For large offsets (see the right panel Fig. 3.12), the clouds are collocated at positions where, on average, the confinement is weaker and therefore the clouds expand more, compared to cases where the clouds move near the minimum of the trap.

The strategy used to maximize the cloud launch efficiency in the optical lattice is therefore not only to bring the clouds at rest, but also to align the longest (shortest)

⁴OCT protocol is applied for different final time of the ramp as shown before.

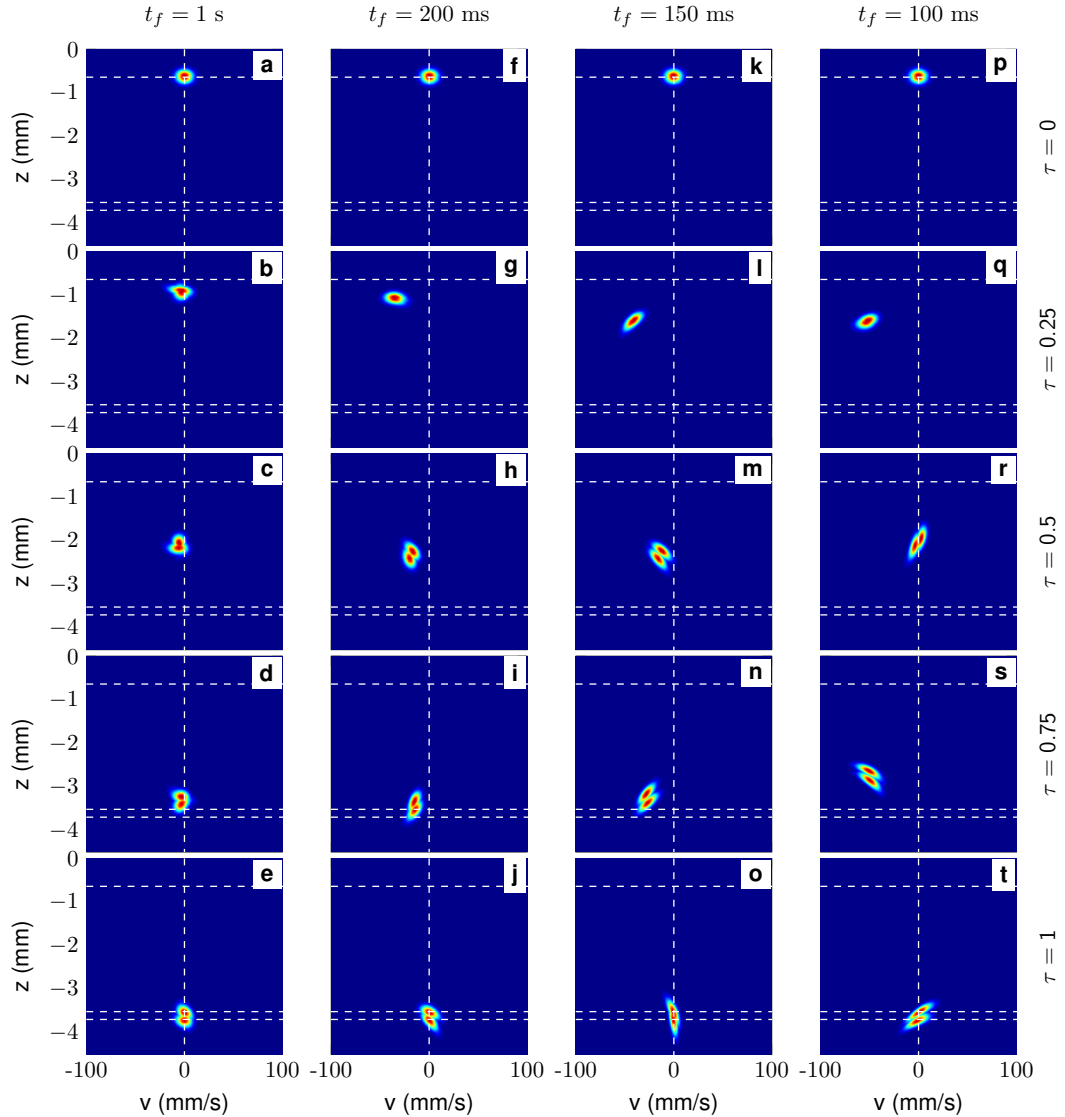


Figure 3.13: Evolution of the distribution of the two thermal ensembles in phase space along the vertical axis z for different total durations of the protocol at different moments in time. In each plot, the vertical axis is the position z and the horizontal axis is the velocity v_z . From left to right, the results correspond to different values of t_f and from top to bottom to different values of $\tau = t/t_f$. (a-e): $t_f = 1$ s, (f-j): $t_f = 200$ ms, (k-o): $t_f = 150$ ms, (p-t): $t_f = 100$ ms. The first line corresponding to $\tau = 0$ shows the initial distribution. The second to fourth lines represent the evolution of the two densities at 25%, 50% and 75% of the total time of the transport. The last line corresponding to $\tau = 1$ shows the final distribution. In each panel the two horizontal top lines denote the initial average position of the two clouds (not distinguishable) and the two bottom horizontal lines highlight the final target positions of the two clouds. The vertical dashed line represents the zero velocity axis.

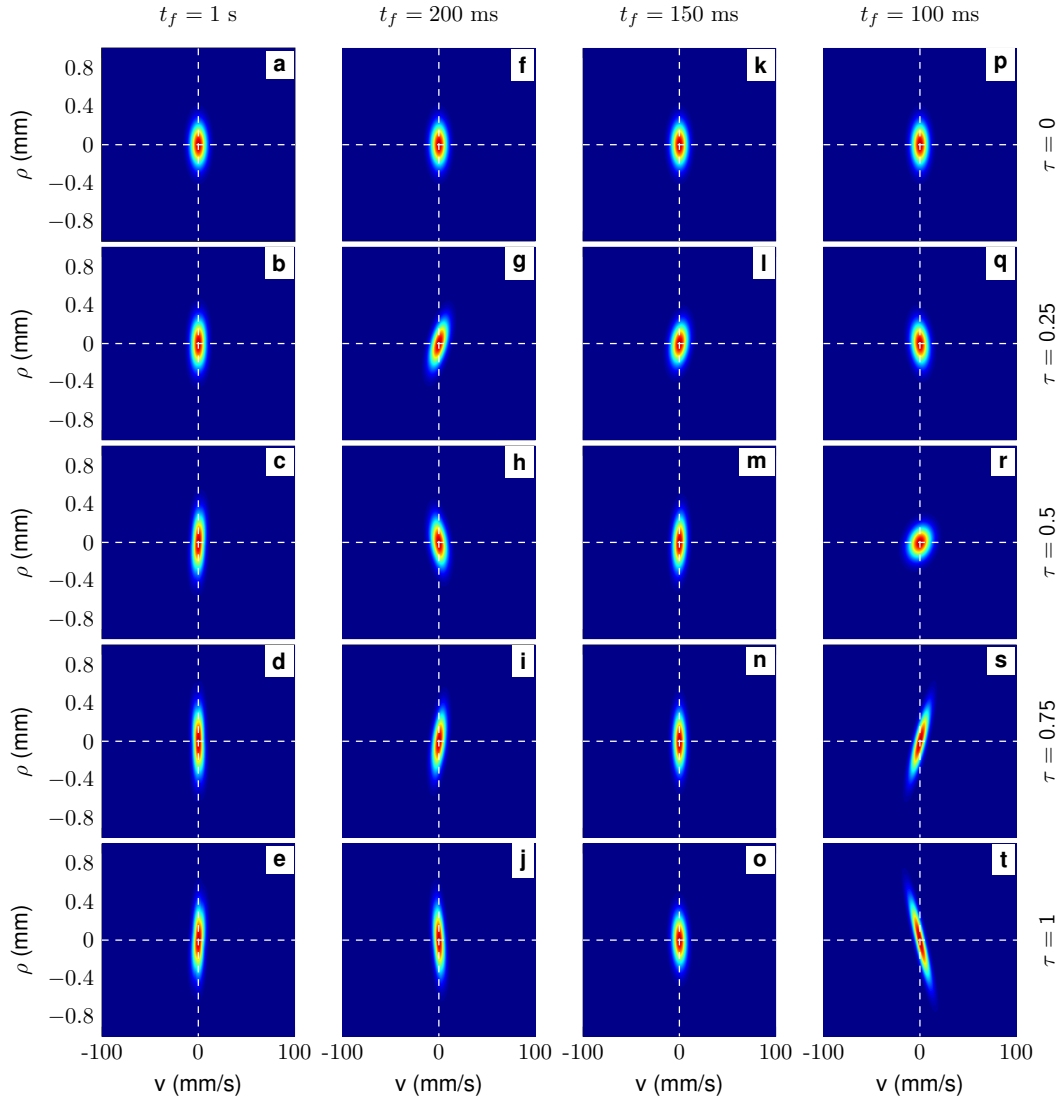


Figure 3.14: Evolution of the distribution of the two thermal ensembles in phase space along the radial axis ρ for different total duration of the protocol at different moments in time. In each plot, the vertical axis is the position ρ and the horizontal axis is the velocity v_ρ . From left to right, the results correspond to different values of t_f and from top to bottom to different values of $\tau = t/t_f$. (a-e): $t_f = 1$ s, (f-j): $t_f = 200$ ms, (k-o): $t_f = 150$ ms, (p-t): $t_f = 100$ ms. The first line corresponding to $\tau = 0$ shows the initial distribution. The second to fourth lines represent the evolution of the two densities at 25%, 50% and 75% of the total time of the transport. The last line corresponding to $\tau = 1$ shows the final distribution. In each panel the horizontal dashed lines denote the initial and final average positions of the two clouds (identical) and the vertical dashed line represents the zero velocity axis.

ellipsoid axis in phase space along the spatial (zero-velocity) axis at the end of the transport in order to minimize the expansion rate of the clouds. Experimentally, after launching the two clouds into the optical lattice, it is possible to apply a dipole trap acting mainly along the radial direction. More details about this process can be found in [165].

In this configuration, we want the transport to minimize the expansion rates of the clouds along the z and ρ axis in order to avoid atomic losses in the dipole trap, where the size is limited to a few mm at a time when the clouds have spread during some tens of ms. Fig. 3.15 shows the final characteristic sizes $\sigma_{z/\rho}(t_f)$ and $\sigma_{v_{z/\rho}}(t_f)$ of the two thermal ensembles as a function of the final time t_f . The left panel is for the vertical direction z and the right panel for the radial direction ρ . The first row is for the position and the second row for the velocity.

For the total duration $t_f = 140$ ms, the velocity distribution along z reaches a minimum for both species, with $\sigma_{v_z} \simeq 2.4$ mm/s, equivalent to a 1D temperature expansion⁵ of 59 nK for both species. Along the radial direction the expansion velocity of the clouds are then limited to $\sigma_{v_\rho} \simeq 4.6$ mm/s and 4.7 mm/s for ^{87}Rb and ^{85}Rb , respectively, equivalent to expansion temperatures of 225 nK and 234 nK for these two species. The resulting expansion temperatures in 3D are $T = 170$ nK and 176 nK for ^{87}Rb and ^{85}Rb , respectively. This can be compared to the case of a transport performed in 100 ms, where the expansion velocity is maximum along the vertical direction, with $\sigma_{v_z} = 7.5$ mm/s for ^{87}Rb and $\sigma_{v_z} = 8$ mm/s for ^{85}Rb , equivalent to 1D expansion temperatures of 595 nK and 657 nK, respectively. In the radial direction we obtain for $t_f = 100$ ms the sizes $\sigma_{v_\rho} = 6.4$ mm/s for ^{87}Rb and $\sigma_{v_\rho} = 6.8$ mm/s for ^{85}Rb , equivalent to 1D expansion temperatures of 431 nK and 477 nK, respectively. The resulting temperatures in 3D would then be $T = 486$ nK and $T = 537$ nK for ^{87}Rb and ^{85}Rb , respectively.

These results have to be compared with the initial temperature of the system, $T = 1\ \mu\text{K}$. In the case of the final duration $t_f = 140$ ms, the expansion temperature of the two species is reduced by a factor 6.

Beyond this reduction of the expansion temperature of the two species, the great advantage of the OCT protocol is to engineer a ramp aimed at optimizing the final quantum state of the two species at their final position before the launch in the 10-meter tower with the help of an optical lattice. In the context where one of the limitations to the accuracy of the atom interferometer is the initial conditions, OCT is an interesting tool to increase the robustness of the state preparation. In the future, other boundary

⁵The temperature is calculated in 1D according to $k_B T = m \sigma_v^2$ [139].

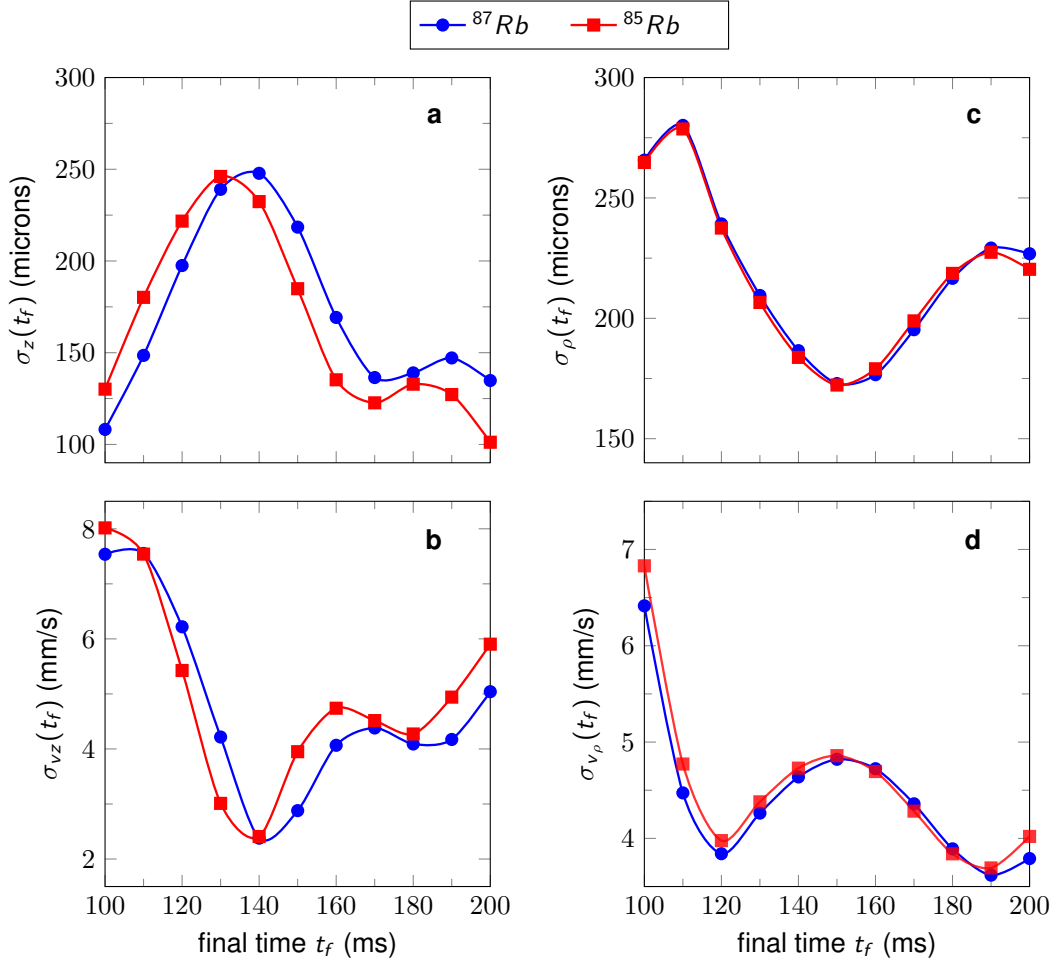


Figure 3.15: Characteristic sizes $\sigma_{z/\rho}(t_f)$ and $\sigma_{v_{z/\rho}}(t_f)$ of the two thermal ensembles as a function of the ramp time t_f . The numerical simulation results are depicted by the squares and circles for different final times of the OCT ramp. The different curves are the result of a spline interpolation. The blue and red colors stand for ^{87}Rb and ^{85}Rb , respectively.

conditions could also be implemented. To optimize the launch of the two species in the optical lattice it could be required that both species end up with a specific final velocity. The objective would be first to be in resonance with the upper lattice and thus avoid atomic losses. In a second time, since the two species do not feel the same acceleration at the launch, a well chosen final differential velocity could compensate this effect and lead to identical trajectories. It is of particular interest in the context of testing the Universality of Free Fall where gravity gradient between to test masses induced a differential acceleration [37]. In the future OCT offers the possibility to design a ramp to target the desired phase space distributions in addition to the classical requirement

as already demonstrated theoretically in the case of the transport of a Bose-Einstein condensate away from an atom chip surface [257]. Within the framework of multiples initial states preparation OCT is a key tools to engineer robust sequences.

3.2.1.7 Conclusion

In summary, I have presented a detailed implementation of OCT protocols to solve the problem of the transport of two non-interacting species, first in the case of a pure harmonic trap configuration, where the impact of the running cost function has been shown, and then in a real trap configuration. To increase the duty cycle of the experiment, short transport ramps are required and the real trap configuration has to be considered. Based on a N -particle simulation, I highlighted the possibility to design the phase space distribution in real experimental configurations. In the context of engineering optimized input state for precision measurements, OCT protocols is a key tool. Indeed, in the case of realistic traps, I have demonstrated (i) the possibility to bring two independent atomic ensembles at rest in their corresponding trap minimum, $\Delta z_X = z_X - z_{sag,X} < 1\mu\text{m}$ $X = \{^{85}\text{Rb}, ^{87}\text{Rb}\}$, distant by $\Delta z_{sag} = z_{sag,87} - z_{sag,85}$, without residual classical velocities, $\dot{z}_X < 1\mu\text{m}\cdot\text{s}^{-1}$, $X = \{^{85}\text{Rb}, ^{87}\text{Rb}\}$ and (ii) the possibility to reduce the temperature expansion of the two clouds from $T = 1\mu\text{K}$ to approximately $T = 170\text{ nK}$. In the past, without the implementation of OCT ramp, the Stanford team achieved an expansion temperature of a ^{87}Rb BEC as low as 50 pK in 2D [165]. The implementation of OCT could bring the possibility to decrease even further this expansion temperature by the optimization of the third axis dynamics. A specific change of the control parameter, calculated with the OCT algorithm, would for example emphasize the Q_1 excitation mode, particularly useful to collimate two different axis as described in chapter 2.

The impossibility to design protocols limiting the classical transient energy and to constrain the center-of-mass of the two clouds close to their respective trap minimum for fast ramps led to necessity of considering the real trap configuration. This situation is usually avoided as much as possible because anharmonicities directly impact the collimation of the atomic ensembles, collimation required for long time atom interferometry. The result of the OCT ramp with a total time of 140 ms shows the possibility to enhance the interferometry time available by decreasing the expansion temperature by a factor of 6. Even if the impact of the anharmonicities is higher than for longer ramps, the collimation effect is maximized for this particular ramp time.

3.2.2 Thermal cloud phase-space density optimization by atomic lensing

Usual methods to increase the phase space density (PSD) of an atomic cloud rely on a reduction of its temperature, *i.e.* the kinetic energy of the system. Magnetic optical trapping combined with optical molasses allow for dramatic cooling of cold atomic samples. In this section, we explore the possibility to increase the PSD even further by shrinking the size of the molasses-cooled ensemble. The idea proposed here is to engineer sequences combining cooling⁶ with focusing of the cloud sizes. In the context of precise measurements with Bose-Einstein condensates, an increase of the initial phase-space density of the gas before evaporative cooling leads to an increase of the atom number in the BEC and therefore to a better sensitivity of the interferometer.

3.2.2.1 Principle

We consider a cloud of $N = 10^7$ atoms of Rubidium-87 initially at rest in a spherical trap close to the recoil limit temperature $T = 2\mu\text{K}$. The purpose of this study is to increase the phase space density of the cloud by implementing the specific sequence shown in Fig. 3.16.

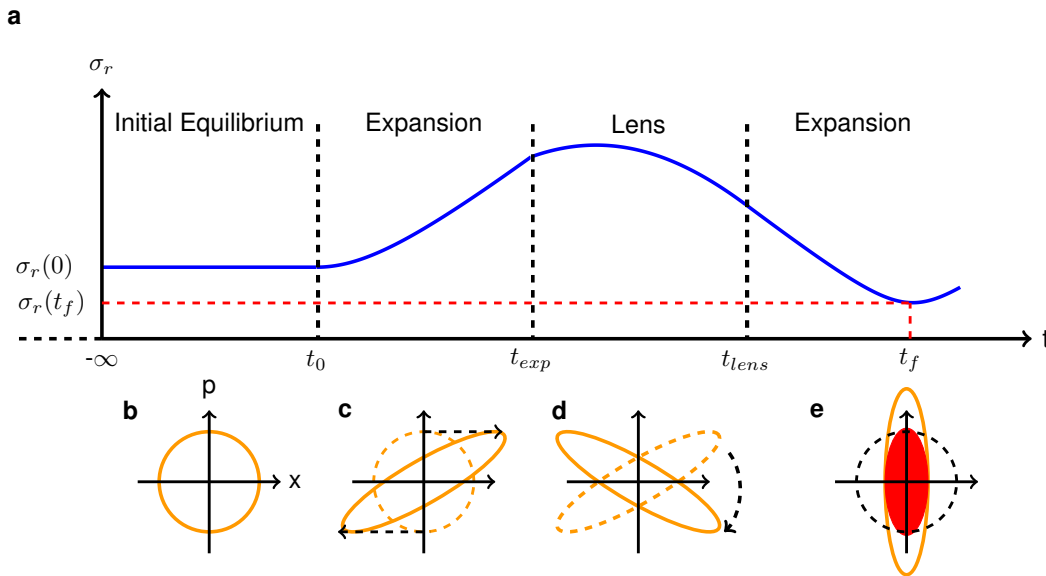


Figure 3.16: Diagram of principle for the atomic lensing effect. (a) Trapping and expansion sequence. (b-e) Corresponding phase space dynamics.

⁶Here the term cooling refers to the technique of Doppler cooling and Sub-Doppler cooling introduced in the first chapter.

The blue curve in panel (a) shows the evolution of the characteristic spatial size of the cloud $\sigma_r(t)$ in a 3D isotropic trap for different trapping configurations separated with vertical dashed lines. Initially, the cloud is at equilibrium in the trap with an initial size $\sigma_r(0)$, at time $t = t_0$. The trap is then switched off and the cloud expands until $t = t_{exp}$, when the trap is switched on again. In this trap, the cloud is out of equilibrium and its size oscillates. At a specific time, denoted by t_{lens} , the trap is switched off again. The time t_{lens} is chosen such that $\dot{\sigma}_r(t_{lens}) < 0$, to spatially compress the cloud and reach a minimum size at time $t = t_f$. This step is called “lens” in analogy with classical optics where a beam can be focused to a specific position after a converging lens. At this time, highlighted with a red horizontal dashed line, the cloud is focused, and its spatial extension, denoted by $\sigma_r(t_f)$, is smaller than the initial one $\sigma_r(0)$.

We show in panels (b-e) the characteristic phase space evolution of the cloud during the different steps. The cloud, initially at rest, is represented by a circle in panel (b). The same circular shape is represented in dashed lines on the two panels (c) and (e). During the free expansion, an atom starting initially at a position r_0 with a momentum p_0 moves freely in the direction given by the sign of p_0 , resulting in an elongation of the distribution, leading to the ellipsoid shape shown in panel (c). The trap is then switched on again and the atoms oscillate in the trap. For harmonic traps, the ellipsoid simply rotates in phase space, as shown in panel (d). For an adequate timing, $t = t_f$, one obtains an alignment of the longest axis of the ellipsoid with the momentum axis, as shown in panel (e). At this stage, the cooling techniques are applied [151, 152] in order to reduce the cloud temperature to its initial value and to recover the same momentum width than in (b), $\sigma_p(t_f) = \sigma_p(0)$. In the case where the cooling is fast enough (ellipsoid shape hardly changed), the cloud phase-space density, features a smaller spatial extension, $\sigma_r(t_f) < \sigma_r(0)$ for the same momentum width: its phase space density has increased. This situation is represented by the red filled ellipsoid in panel (e). The maximum gain in phase space density is then given by the ratio of the initial volume to the final volume of the cloud

$$G_{max} = \frac{\sigma_r^3(0)}{\sigma_r^3(t_f)}. \quad (3.52)$$

One could repeat this step multiple times until saturation of this gain.

The optimization of the phase space density is first semi-analytically studied in the case of a harmonic truncated trap and then validated in the case of a realistic Gaussian (dipole) trap, where the effects of anharmonicities is present. In both cases we discuss the impact of the sequence on atomic losses to asses the overall efficiency of the method.

The total gain is then rewritten as

$$G = \mathcal{P} \cdot G_{max}, \quad (3.53)$$

where \mathcal{P} denotes the fraction of atoms kept during the process.

3.2.2.2 Truncated harmonic trap approximation

In an optical trap, the dipole potential

$$U_{dip}(r) = U_0 \cdot I(r). \quad (3.54)$$

is proportional to the intensity $I(r)$ of the laser field, with a proportionality factor U_0 which depends on the optical properties of the atom [224]. The intensity

$$I(r) = \frac{2P}{\pi w_0^2} \exp\left[-\frac{2r^2}{w_0^2}\right] \quad (3.55)$$

is a function of the waist w_0 and of the power P of the laser beam. The proportionality factor for alkaline atoms illuminated by an off-resonant laser reads

$$U_0 = -\frac{\pi c^2}{2} \left[\frac{2\Gamma_{D_2}}{\omega_{D_2}^3} \left(\frac{1}{\omega_{D_2} - \omega_L} + \frac{1}{\omega_{D_2} + \omega_L} \right) + \frac{\Gamma_{D_1}}{\omega_{D_1}^3} \left(\frac{1}{\omega_{D_1} - \omega_L} + \frac{1}{\omega_{D_1} + \omega_L} \right) \right] \quad (3.56)$$

and depends on the natural line widths (FWHM) Γ_{D_1} and Γ_{D_2} of the D_1 and D_2 lines of Rubidium-87[224]. $\hbar\omega_{D_1}$ and $\hbar\omega_{D_2}$ denote the corresponding transition energies and $\hbar\omega_L$ denotes the photon energy addressed by the laser and characterized by its wavelength $\lambda_L = 2\pi c/\omega_L$, where c denotes the speed of light in the vacuum.

We first approximate this trapping potential by a truncated harmonic trap characterized by the trap depth

$$U_{depth} = -\frac{2U_0P}{\pi w_0^2}, \quad (3.57)$$

the trap frequency

$$\omega_0 = \sqrt{-\frac{8U_0P}{m\pi w_0^4}}, \quad (3.58)$$

and the truncation radius

$$r_R = \sqrt{\frac{2U_{depth}}{m\omega_0^2}}. \quad (3.59)$$

The Fig. 3.17 represents the real trap potential (blue solid line) and its truncated harmonic approximation (red dashed line). For this study we set the laser properties to

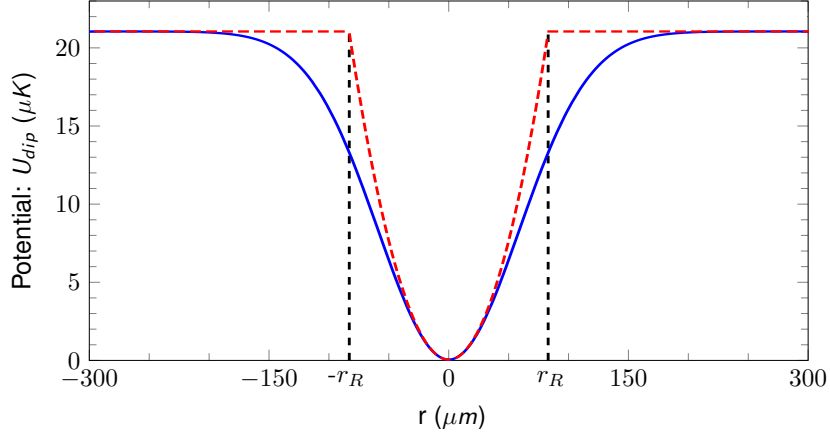


Figure 3.17: Trap configuration: The dipole trap is represented in blue. The red dashed line shows the harmonic trap truncated for $|r| > r_R$. This truncation radius is highlighted with two vertical black dashed lines. See text for the laser parameters.

$P = 3$ W, $w_0 = 117.6$ μm and $\lambda_L = 1064$ nm. In this configuration, the truncated harmonic trap has a depth of 21 μK , a trap frequency of 122.4 Hz and a truncated radius of $r_R = 83$ μm . The initial characteristic spatial width is $\sigma_r(0) = 18.1$ μm . For a purely harmonic trap, the characteristic spatial size evolution of the cloud is described by Eq. (3.21), which, in the case of an isotropic trap, can be rewritten as shown in section 3.1.2.2 with $\sigma_r(t) = \sigma_r(0) \cdot b(t)$. The scaling coefficient $b(t)$ follows

$$\ddot{b}(t) + \omega^2(t) b(t) = \frac{\omega_0^2}{b^3(t)} \quad (3.60)$$

if $\xi \ll 1$, *i.e.* in the case where the mean-field energy E_{mf} is negligible compared to the thermal energy $k_B T$ of the cloud, as shown in Eq. (3.22). If this is not the case, the scaling coefficient $b(t)$ will follow

$$\ddot{b}(t) + \omega^2(t) b(t) = \omega_0^2 \left(\frac{1 - \xi}{b^3(t)} + \frac{\xi}{b^4(t)} \right), \quad (3.61)$$

where $\xi = E_{mf} / (E_{mf} + k_B T)$.

In both cases the variable $\omega(t)$ is the frequency of the trap at time t , using the convention that $\omega(t) = 0$ if the trap is off. In this expression we have also used ω_0 for the initial trapping frequency. The initial boundary conditions are as follows: $b(0) = 1$ and $\dot{b}(0) = 0$. For the parameters chosen above, we estimate $E_{mf} = 28.5$ nK and $\xi = 0.007$ justifying safely neglecting the mean-field term.

In Fig. 3.18 we show the optimized evolution of the cloud characteristic size $\sigma_r(t)$ for two iterations of the optimization sequence following the steps describe in Figure 3.16.

The lens duration is optimized such as the cloud focused with a size smaller than its initial one at $t = 0$ after the lens have been turn off. In panel (a) we focus our attention on the first iteration⁷, where the blue and red dashed lines show the evolution of $\sigma_r(t)$, described respectively by Eqs. (3.61) and (3.60). The cloud, initially at rest, is released at $t = 0$ and expands to twice its initial size, indicated by the gray horizontal dashed line. At $t = 2.25$ ms the potential is on again for $\Delta t_{lens} = 2.40$ ms, as highlighted by the orange colored area. At $t = 4.66$ ms the trap is switched off and the cloud is focused at $t_{f,1} = 4.84$ ms. This first focusing time is highlighted by the black vertical line. At the focus point the cloud size is $\sigma_r(t_{f,1}) = 8.4 \mu\text{m}$ and the spatial gain defined in Eq. (3.52) is $G_{max} = 10$. If nothing is done the cloud continues to expand, as shown by the dash-dotted lines. It can be noted that the increase of the mean-field energy of approximately 10% seen during this procedure does not lead to any discrepancy between the results obtained from Eqs. (3.61) and (3.60).

To simplify the problem, we first assume the possibility of an instantaneous cooling of the cloud leading to a new immediate thermal equilibrium. This instantaneous cooling assumption leads to a discontinuity of the velocity distribution at the end of the cooling step, at time $t = t_f^+$, while the spatial distribution remains unchanged. The new characteristic sizes are given by

$$\sigma_r(t_f^+) = \sigma_r(t_f), \quad (3.62a)$$

$$\sigma_v(t_f^+) = \sigma_v(0), \quad (3.62b)$$

where, at time t_f^+ , the spatial width in the new equilibrium situation can be written as

$$\sigma_r(t_f^+) = \frac{\sigma_r(0)}{G} = \sqrt{\frac{k_B T}{m G^2 \omega_0^2}} = \sqrt{\frac{k_B T}{m \omega_f^2}}. \quad (3.63)$$

This situation is analogous to a cloud held in a trap with a larger effective trap frequency, $\omega_f = G \omega$. After cooling, for $t > t_f^+$, the evolution of the cloud is described by

$$\sigma_r(t) = \sigma_r(t_f^+) \cdot b(t), \quad (3.64a)$$

$$\sigma_v(t) = \sqrt{\frac{\sigma_v^2(0)}{b^2(t)} + \sigma_r^2(t_f^+) \cdot \dot{b}^2(t)}, \quad (3.64b)$$

where $b(t)$ is given by Eq. (3.60) or Eq. (3.61), according to the value of ξ . The boundary conditions at $t = t_f^+$ read as $b(t_f^+) = 1$ and $\dot{b}(t_f^+) = 0$.

⁷Here iteration denotes one step of the process leading to a smaller cloud at the focused point

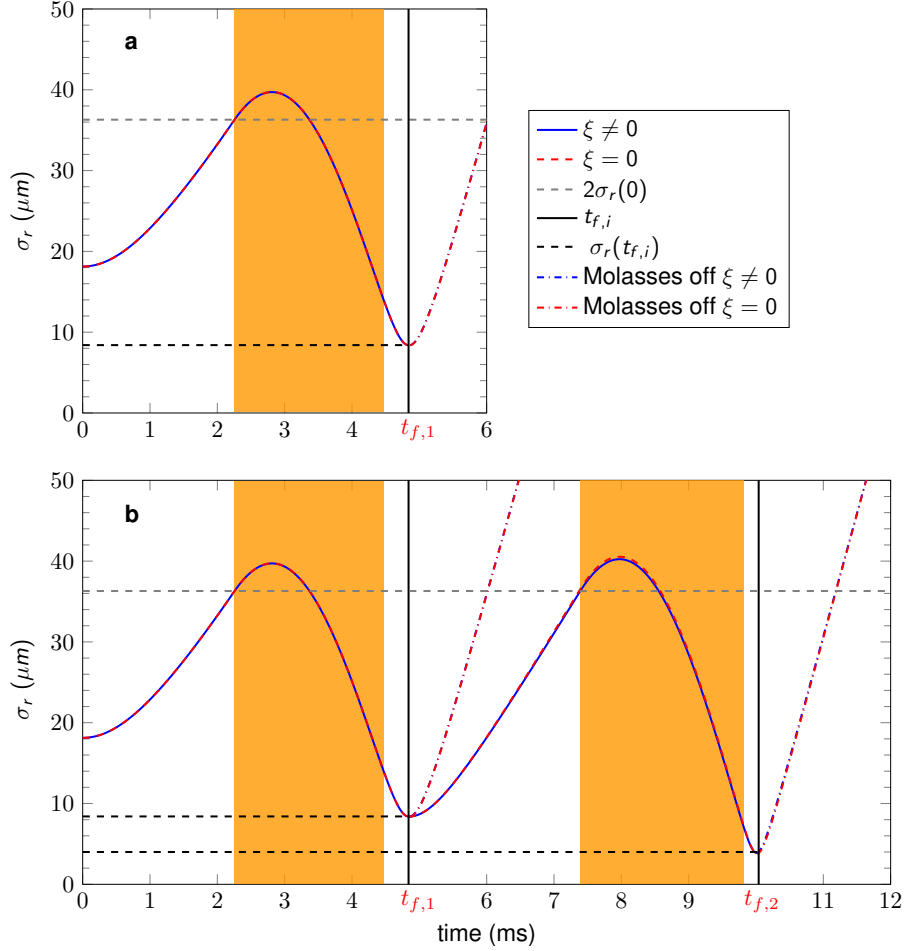


Figure 3.18: Optimization of the phase space density for 10^7 atoms supposing an instantaneous cooling at the different focus points. Panel (a): The initial cloud is released and left to expand to twice its initial size. The lens duration is optimized such as the cloud focused at $t_{f,1}$ with a size smaller than its initial one at $t = 0$ after the lens have been turn off represented by the horizontal dashed line. The blue (red) line shows the case where the mean-field energy is neglected (is not neglected) and where the dynamic is described by Eq.3.60 (Eq.3.61). The blue and red dashed curves show the dynamic of the size if the atomic ensemble is not cooled to its initial temperature at $t_{f,1}$. Panel b: The proceed is reiterated to focus the cloud to a smaller size at $t_{f,2}$. For low atom number the contribution of the mean-field energy can be neglected.

Panel (b) shows the situation where at the end of the first iteration we repeat the lensing procedure. After the instantaneous cooling, the mean-field energy is $E_{mf} = 0.29 \mu\text{K}$ and $\xi = 0.0066$. The cloud at $t = t_{f,1}$ starts at rest and expands until twice its initial size. At $t = 7.38$ ms the trap is on again for $\Delta t_{lens} = 2.43$ ms, leading to a second focusing at time $t_{f,2} = 10$ ms, with $\sigma_r(t_{f,2}) = 4.1 \mu\text{m}$. At this stage a new equilibrium situation

leads to $E_{mf} = 2.5 \mu\text{K}$ and $\xi = 0.38$. It can be noted that after the first focus point a very small discrepancy between the size evolutions described by Eq. (3.60) and Eq. (3.61). The difference is caused by the increase of the mean-field energy at the end of the first iteration.

Qualitatively, due to the repulsion between atoms, if we repeat the optimization sequence, one can expect the interaction between atoms to increase at the focus point, leading to a different behavior where the exact focus point is shifted in time and the gain at the exact focus point is limited compared to the case where $\xi \ll 1$. To amplify this effect, in Fig. 3.19 we show the exact same sequence as described above with 10^8 atoms instead of 10^7 . Initially $E_{mf} = 0.28 \mu\text{K}$ and $\xi = 6.6 \cdot 10^{-3}$. At $t = t_{f,1}$, $E_{mf} = 2.9 \mu\text{K}$ and $\xi = 0.42$. At $t = t_{f,2}$, $E_{mf} = 24.5 \mu\text{K}$ and $\xi = 0.86$. For the rest of the chapter the number of atom is fixed to $N=10^7$.

Due to the expansion of the cloud and the limited size of the trap, atomic losses must be taken into account when the trap is switched on. In our case

$$\mathcal{P} = \frac{1}{\mathcal{Q}} \int_0^{r_R} 4 \pi r^2 dr \frac{1}{2} m \omega^2 r^2 \frac{\exp\left[-\frac{r^2}{2 \sigma_r^2(t_{exp})}\right]}{(2\pi \sigma_r^2(t_{exp}))^{3/2}}, \quad (3.65)$$

where

$$\mathcal{Q} = \int_0^\infty 4 \pi r^2 dr \frac{1}{2} m \omega^2 r^2 \frac{\exp\left[-\frac{r^2}{2 \sigma_r^2(t_{exp})}\right]}{(2\pi \sigma_r^2(t_{exp}))^{3/2}}, \quad (3.66)$$

and only $\mathcal{P} = 81\%$ of the atoms in the cloud are trapped. This leads to a total gain at the end of the first iteration, $t = t_{f,1}$, of $G_1 = 0.81 \cdot \left(\frac{18.1}{8.4}\right)^3 \approx 8$ and at the end of the second iteration, $t = t_{f,2}$, to $G_2 = 0.81^2 \cdot \left(\frac{18.1}{4.1}\right)^3 \approx 56$. The gain is, therefore, still significant also after counting the atoms dropping out of the truncated trap.

The approach described so far assumes some approximations: (i) The cloud is assumed to keep its Gaussian shape at each step of the manipulation with an harmonic potential. (ii) The cooling of the cloud at the focus point was assumed to be instantaneous. In order to deliver a realistic recipe, we depart from the first approximation in section 3.2.2.3, where the evolution of the particles is described by an N -particle simulation (arbitrary shape) in a Gaussian dipole trap. The second approximation is a key point of the proposal to increase the density in phase space. Indeed, if the cooling takes too long to bring the atoms back to the initial temperature of $2 \mu\text{K}$, the efficiency of the sequences is worse. In the following, we discuss the impact of cooling time on the maximum gain.

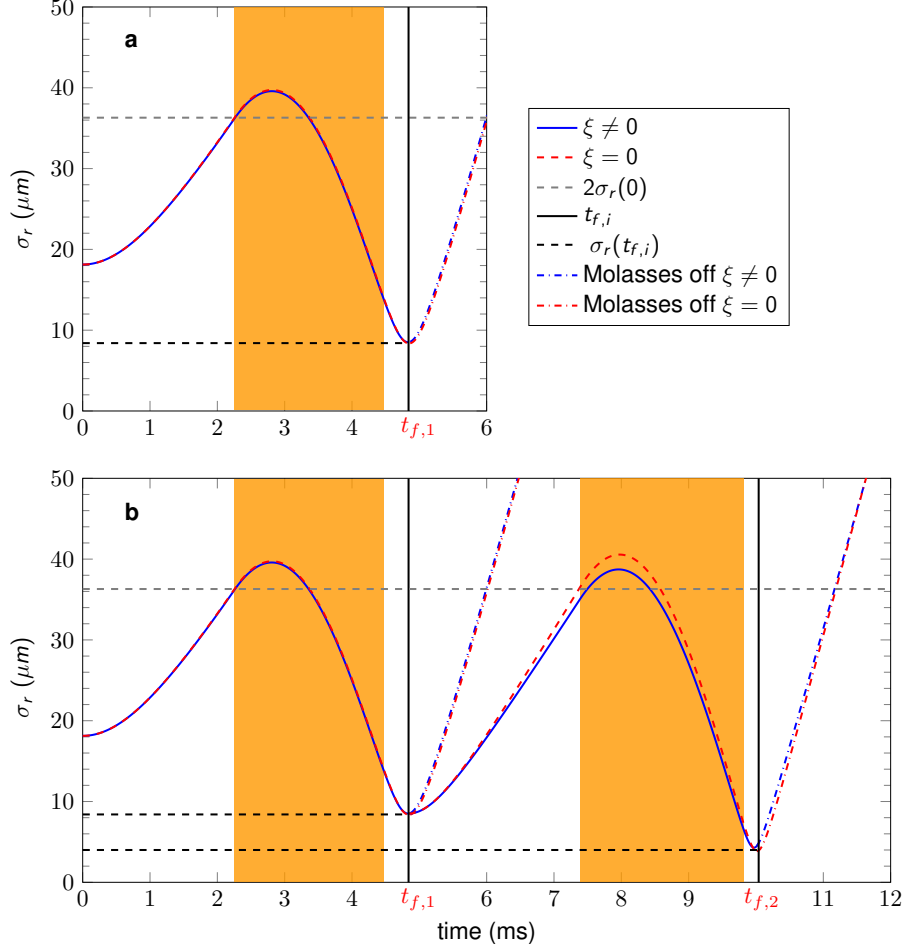


Figure 3.19: Optimization of the phase space density for 10^8 atoms supposing an instantaneous cooling at the different focus points. Panel (a): The initial cloud is released and left to expand to twice its initial size. The lens duration is optimized such as the cloud focused at $t_{f,1}$ with a size smaller than its initial one at $t = 0$ after the lens have been turn off represented by the horizontal dashed line. The blue (red) line shows the case where the mean-field energy is neglected (is not neglected) and where the dynamic is described by Eq.3.60 (Eq.3.61). The blue and red dashed curves show the dynamic of the size if the atomic ensemble is not cooled to its initial temperature at $t_{f,1}$. Panel b: The proceed is reiterated to focus the cloud to a smaller size at $t_{f,2}$. In the case of higher atom number it is not possible to neglect the mean-field term of Eq.3.61.

In Fig. 3.20, we show the evolution of the total gain, G_{max} , as a function of the lens duration, t_{lens} , and of the free expansion time after the lens, t_{exp} , for the first iteration of the technique presented in Fig. 3.18.

In this figure, we neglect the atomic losses at recapture, and the maximum gain is therefore $G_{max} = 10$. The blue color denotes cases where $G_{max} < 1$. The three vertical

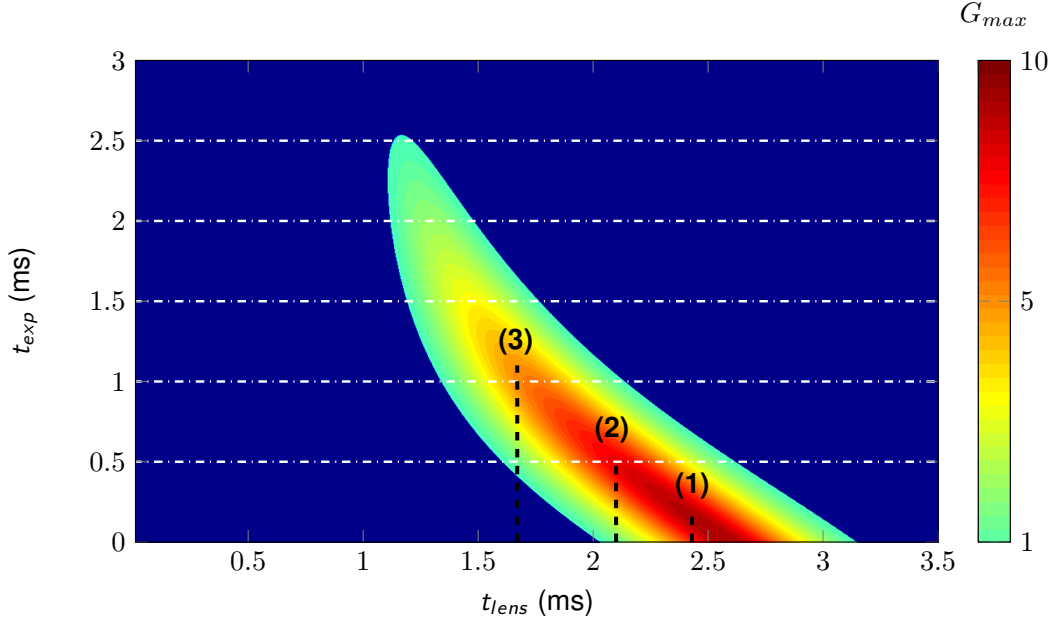


Figure 3.20: Evolution of the maximum gain as a function of the lens duration and of the post lens expansion time. The total atom number is fixed to $N=10^7$.

black dashed lines indicate respectively three cases of lens duration and of post-lens expansion time: $(t_{lens}, t_{exp}) = (2.43, 0.18)$ ms case (1) ; $(2.1, 0.5)$ ms case (2) and $(1.67, 1.1)$ ms case (3). For these three cases, the maximum gain is respectively 10, 8 and 5 when cooling is instantaneous. The large area covered when going from case (1) to case (3) proves the robustness of the proposed lensing technique for reaching high phase space density gains, with $G_{max} > 5$.

The time used to cool down the atomic ensemble impacts the size of the cloud. It can be expected that for a rapid cooling, even if not instantaneous, the size evolution is well described by the previous equations *i.e.* the gain should be similar to the one predicted here with an instantaneous cooling. Fast cooling should therefore give the possibility to increase the phase-space density by an order of magnitude, as depicted by case (1). After reaching a minimum, the cloud size continues to increase and in the case of a very long cooling time the gain could finally be lower than 1. To allow for an increase of the cooling time without losing too much in terms of phase-space density, the case number (3) highlights the possibility to start the cooling process just at the end of the lensing step during the expansion time. In this case the cooling process could take more than 1 ms to recover the initial temperature with a phase-space density 5 times higher than initially.

3.2.2.3 Dipole trap

We now take into account a realistic configuration of the trap. The potential is given by the Eq. (3.54). Instead of the simplified truncated harmonic potential, we now simulate the dynamics of $N = 10^7$ atoms in a realistic dipole trap following the method described in 3.1.2.3.

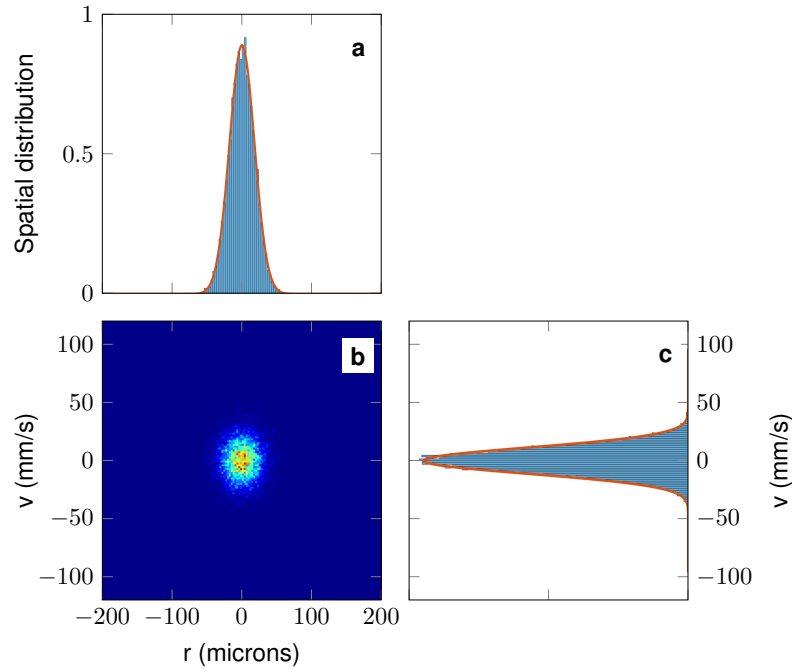


Figure 3.21: Initial phase space density in a dipole trap. The phase space is represented by the N -particle simulation panel (b). The corresponding spatial and velocity distributions are respectively on panels (a) and (c) in blue. The red curves show the Gaussian distributions calculated in the case of a purely harmonic trap as a comparison to the ideal case.

In Fig. 3.21 we show the initial phase space density distribution (panel b) of the N particles, along with the corresponding spatial and velocity distributions, respectively on panels (a) and (c). The cloud, released at time $t = 0$, expands and Fig. 3.22 shows the phase space distribution at $t = t_{exp}$. The two integrated spatial and velocity distributions are shown again on panels (a) and (c). Here the red curves show the Gaussian distributions calculated with Eq. (3.18) and Eq. (3.27) in the presence of a purely harmonic trap. It can be noted that the spatial distribution of Fig. 3.22 is broader than in Fig. 3.21 while the velocity distribution remains identical, reflecting the free expansion of the cloud. The effect of the realistic trap is only seen when it is restarted. Due to the extension of the cloud, some atoms see at this point the effect of the anharmonic part of the trap.

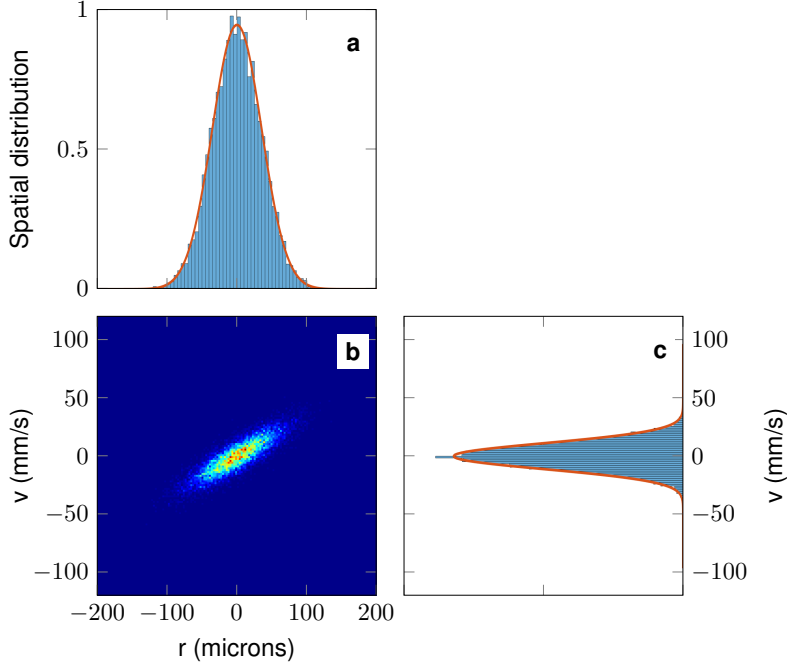


Figure 3.22: Phase space distribution at $t = t_{exp}$ after release from the dipole trap. The phase space is represented by the N -particle simulation panel (b). The corresponding spatial and velocity distributions are respectively on panels (a) and (c) in blue. The red curves show the Gaussian distributions calculated in the case of a purely harmonic trap as a comparison to the ideal case.

The Fig. 3.23 shows the situation at the end of the lens calculated in a purely harmonic trap in panels (a-c), and in the dipole trap in panels (d-f). In the panels (a,c,e,f), the red line represents the Gaussian spatial and velocity distributions calculated in the case of purely harmonic trap. We can see the impact of the real trap in phase space by comparing panel (d) with panel (b). Two curved tails are now present at the edge of the expected ellipsoidal distribution. These tails can be qualitatively explained by the different frequencies of the local harmonic traps perceived by each atom in the distribution: The atoms constrained at the minimum of the trap perceive the harmonic frequency ω_0 and behave as in a purely harmonic trap. All the other atoms oscillate in a trap where the frequency is a function of position. Over time, all the atoms in the non-harmonic part of the trap dephase from the central part, leading to the tails seen in panel (d).

In the realistic trap configuration, due to the limited expansion of the cloud, with $\max(\sigma_r) \simeq 2\sigma_r(0)$, no atoms are lost because of the expansion phase. To characterize the performance decrease due to the anharmonicities, we now calculate the overlap of the

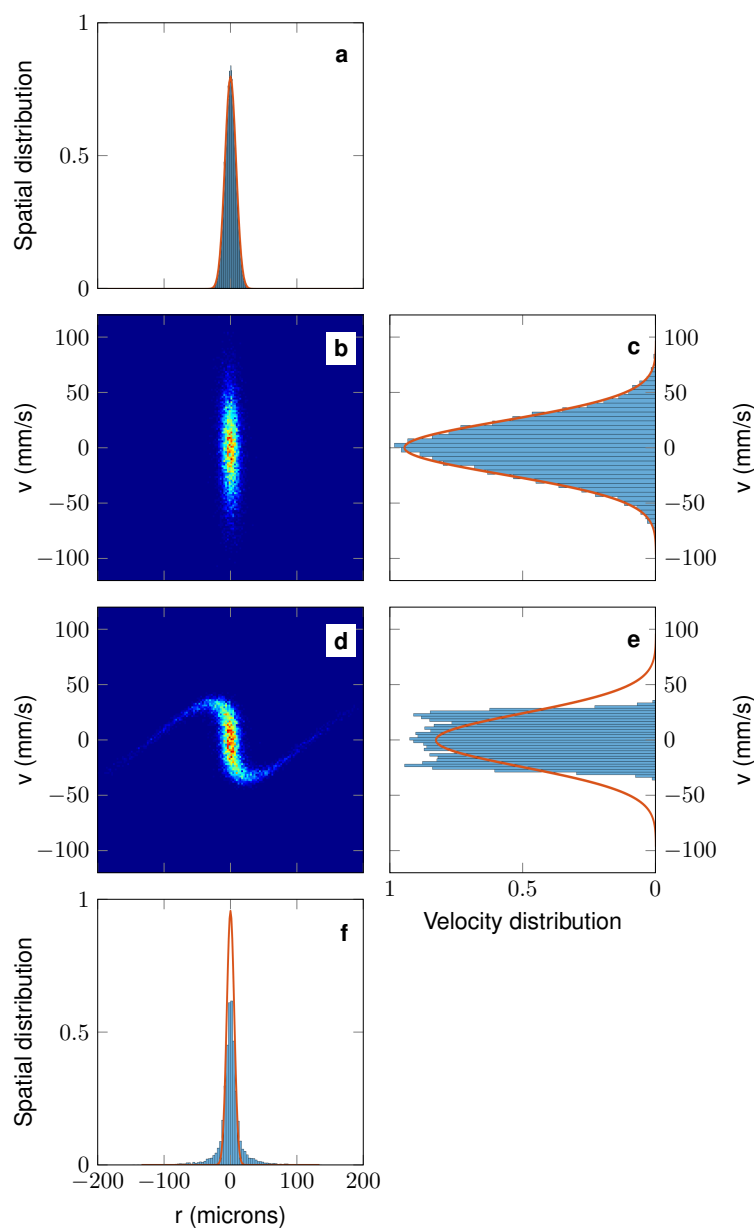


Figure 3.23: Phase space distribution at $t = t_{lens}$. The panel (a,b,c) show the configuration of an ideal harmonic trap for the lens. The phase space is represented by the N -particle simulation panel (b). The corresponding spatial and velocity distributions are respectively on panels (a) and (c) in blue. The red curves show the Gaussian distributions calculated in the case of a purely harmonic trap as a comparison to the ideal case. The panel (d,e,f) show the configuration of a dipole trap for the lens. The phase space is represented by the N -particle simulation panel (d). The corresponding spatial and velocity distributions are respectively on panels (e) and (f) in blue. The red curves show the Gaussian distributions calculated in the case of a purely harmonic trap as a comparison to the ideal case.

spatial distribution in the pure harmonic case, denoted by $G(r)$ and shown as a red line in panel (f), to the realistic trap distribution one, denoted by $D(r)$ and represented in blue in panel (f). The percentage of atoms in the non-harmonic part of the dipole trap at the end of the lensing step is then

$$\mathcal{L} = 1 - \int_{-\infty}^{\infty} \left(G(r) D(r) \right)^{1/2} dr, \quad (3.67)$$

where $(G(r) D(r))^{1/2}$ denotes the cross distribution. The modified total gain is given by

$$G = (1 - \mathcal{L}) \cdot G_{max}. \quad (3.68)$$

Strictly speaking these atoms are not physically lost in the process, they are still in the trap but due to their different behavior they are not focused. For the specific configuration shown in Fig. 3.23 the percentage of unfocused atoms is $\mathcal{L} = 10\%$. The modified possible gain at the focus point is then only slightly degraded to $G = 9$.

3.2.2.4 Conclusion

To sum up this section, I have presented a sequence to increase the phase-space density of an atomic sample. This possibility relies on rapid cooling processes at the focus point in a few ms. In the case the cooling process take 1 ms, the phase space density is 5 times higher than initially. This is the current state-of-the-art in the field [152]. The results of the phase-space density gain have been shown in a harmonic truncated trap and in a more realistic case of a dipole trap configuration including anharmonicities. In both cases, atomic losses were taken into account together with an assessment of the impact of the cooling duration. In addition, the sequence described here is not limited to initial high cloud densities where the efficiency of the molasses cooling technique is limited but would work as well in the case of lower atom numbers with larger cloud sizes leading to an even more realistic experimental configurations.

3.3 Conclusion and outlook

In this chapter, two ways to improve the initial configurations of future atom interferometry sources are proposed. A description of the theory tools was done with OCT protocols based on Pontryagin's Hamiltonians with a gradient method and an N -particle model based on Newton's equation. The first application showed how OCT protocols can help prepare dual-source atom interferometer input states with well defined positions and

velocities. Indeed, the initial positions, velocities and expansion temperatures have to fulfill drastic requirements. This approach is illustrated in the case of a state-of-the-art dual-species atom interferometer, the 10-meter fountain experiment of Stanford. As discussed already, a possible extension of this work can be done to launch efficiently the two species in the tower and limit atomic losses coming with the final conditions.

Also in the context of precision measurements, the second application tackled the enhancement of the number of pre-evaporated atoms in a matter-wave interferometer. Based on a semi-analytical approach and supported with a N -particle simulation, this application paves the way to an increase in phase-space density of a cold gas in the case of a truncated harmonic trap and then in a realistic dipole trap configuration. At first order, one can estimate that an increase of one order of magnitude in the condensed atom number is achievable. Such a significant increase of the atom number is important for the sensitivity of interferometry measurements.

OPTIMIZED MANIPULATION OF A DEGENERATE BOSONIC MIXTURE

Contents

4.1	Introduction	98
4.2	A dual-species Gross-Pitaevskii approach	100
4.3	The different ground state structures	101
4.3.1	The Thomas-Fermi (TF) approximation	101
4.3.2	Study in the case of two domains in the TF approximation . . .	106
4.3.3	Study in the case of three domains in the TF approximation . .	108
4.4	Dynamics	108
4.4.1	The time-dependent coupled Gross-Pitaevskii equations in spher- ical coordinates	109
4.4.2	Scaling approach for a two-component BEC	110
4.5	Results	113
4.5.1	Ground state comparison between TF and GPE	114
4.5.2	Comparison between the TDCGPE and the generalized scaling approach	119
4.5.3	Application to dual-species twin atomic lensing to the pico- Kelvin level	124

In the previous chapters, we described manipulation protocols of single-species Bose-Einstein condensates where a single macroscopic quantum state is occupied by identical bosonic particles, as well as some solutions to the transport of non-interacting pairs of thermal ensembles. In each case, we have shown the possibility of controlling and reducing the expansion rates of the different ensembles. In this chapter, we focus on bosonic mutually interacting BEC mixtures and how to collimate both of them with the delta-kick collimation technique. We first describe the ground state structure of the mixture in section 4.3, to solve later in section 4.4 its dynamics. Finally, we show, in section 4.5, how to simultaneously engineer the expansion rates of the two species by tuning the interactions between the two components of the mixture.

4.1 Introduction

Two-component quantum fluids have long been known to exhibit rich physical properties that are not accessible in single-component physics and have been the subject of extensive studies over the past two decades [297–309]. Phase transitions and different phase mixtures in multi-component systems are of great importance in various fields of physics but also in chemistry and biology. Thanks to the simplicity of their theoretical description, unlike other complex chemical and biological systems, dilute multi-component Bose-Einstein condensates are an ideal candidate for studying these phenomena. Shortly after the creation of the first Bose-Einstein condensate, these studies were pioneered by the experimental work carried out in JILA [310, 311] and MIT [312]. With the support of theoretical studies, these experimental works have shown a wide range of interesting physical effects such as the topological properties of different ground and excited states [313–315], phase separations [303, 316–319], phase transitions and symmetry breaking [304, 305], low-lying excitations [302] and collective oscillations [320, 321], stability properties [306], Josephson-type oscillations [307, 322], spin superfluidity [323–329] and spin supercurrent [330, 331] and this list is far from being exhaustive.

Degenerate mixtures, including interactions between bosons, between fermions and between bosons and fermions, are now produced in many laboratories worldwide using different hyperfine states of the same atomic species [310, 320] or of different isotopes of the same species such as ^3He - ^4He [332], ^6Li - ^7Li [333, 334], ^{85}Rb - ^{87}Rb [335], ^{84}Sr - ^{87}Sr [336], ^{168}Yb - ^{174}Yb [337], ^{86}Sr - ^{87}Sr [338] or different elements such as ^{41}K - ^{87}Rb [329,

339–341], ^{23}Na - ^{40}K [342], ^{40}K - ^{87}Rb [343], ^6Li - ^{23}Na [344], ^6Li - ^{87}Rb [345], ^6Li - ^{40}K [346], ^{87}Rb - ^{133}Cs [347, 348], ^6Li - ^{133}Cs [349], ^{84}Sr - ^{87}Rb [350], ^{39}K - ^{87}Rb [351], ^{23}Na - ^{87}Rb [352], ^6Li - ^{174}Yb [353], ^{23}Na - ^{39}K [354], ^{166}Er - ^{164}Dy [355].

In such systems, theoretical predictions require the knowledge of the different intra-species and inter-species scattering lengths. The knowledge of the inter-species scattering length is of particular interest for the understanding of the miscibility of interpenetrating quantum fluids. It should also be noticed that it is sometimes possible and practical to tune the different scattering lengths via an external magnetic field near a Feshbach resonance [335, 354, 356]. This tunable parameter gives the possibility to study phase transitions and symmetry breaking and is used later in this chapter to engineer optimized dual-species atomic states for precision interferometry.

In spite of the high number of characteristic parameters (three scattering lengths, two different atom numbers, different trap characteristics, etc.), two-component mixtures could be classified in two general categories [297, 298, 316]. The first class includes situations where the two centers of the wave packets spatially overlap respecting the symmetry of the trap. In the literature this class of system is referred as “miscible systems”. The second class contains only situations where the two components do not overlap and where the density distributions of the two components spontaneously break the symmetry of the trap. This class is referred as “immiscible systems”. In literature, the miscible-immiscible criteria and the possibility of switching from one class to another by changing the s-wave scattering length as well as the number of atoms have been theoretically described using two-component GPE numerical simulations and compared to semi-analytical models calculated in the Thomas-Fermi approximation. In the latter case, in the same manner than for a single component, the Thomas-Fermi approximation leads to neglecting the initial kinetic energy of both components [316].

Throughout this chapter, we focus on an ultra-cold pure bosonic mixture of ^{41}K and ^{87}Rb described by a two-component BEC at zero temperature in the miscible regime. We assume that the different scattering lengths are real and that the interactions, described within the limit of contact interactions, conserve the number of atoms of each species *i.e.* there is no atomic loss. We will first describe typical ground state properties in situations where the two species either may coexist together in some regions of space *i.e.* overlapped or remain separated from each other in other regions [335]. In this analysis we compare the results of the dual-species Gross-Pitaevskii equation to the Thomas-Fermi approximation derived in section 4.3.1. We then propose an extension of the scaling approach [229, 230] to describe the dynamics of a dual-species bosonic

Bose-Einstein condensate and we compare this approximation with the results of a numerical simulation of coupled Gross-Pitaevskii equations.

The main result of the chapter is the possibility to control the expansion rate of this two-component superfluids to an expansion temperature lower than 50 pK. Such a low expansion energy is a prerequisite for an EEP test with an accuracy below 10^{-15} [41].

4.2 A dual-species Gross-Pitaevskii approach

In the general case of a two-component BEC in interaction, the dynamics is described by the time-dependent coupled Gross-Pitaevskii equations

$$i\hbar\partial_t\psi_1(\vec{r},t) = \left[-\frac{\hbar^2}{2m_1}\vec{\nabla}_{\vec{r}}^2 + U_1(\vec{r},t) + N_1g_{11}|\psi_1(\vec{r},t)|^2 + N_2g_{12}|\psi_2(\vec{r},t)|^2 \right] \psi_1(\vec{r},t), \quad (4.1a)$$

$$i\hbar\partial_t\psi_2(\vec{r},t) = \left[-\frac{\hbar^2}{2m_2}\vec{\nabla}_{\vec{r}}^2 + U_2(\vec{r},t) + N_2g_{22}|\psi_2(\vec{r},t)|^2 + N_1g_{12}|\psi_1(\vec{r},t)|^2 \right] \psi_2(\vec{r},t), \quad (4.1b)$$

where $\psi_i(\vec{r},t)$ with $i \in \{1,2\}$ denotes the wave function of the species number i . The constants g_{ij} are related to the respective scattering lengths, a_{11} , a_{12} and a_{22} by the relation

$$g_{i,j} = \frac{2\pi\hbar^2 a_{ij}}{m_{ij}} \quad \text{with} \quad m_{ij} = \frac{m_i m_j}{m_i + m_j}. \quad (4.2)$$

N_i and $U_i(\vec{r},t)$ are the number of atoms and the external potential of the species i , respectively. The last terms of Eq. (4.1a) and Eq. (4.1b) describe the coupling between the two components. The normalization condition for each wave function is given by

$$\iiint |\psi_i(\vec{r},t)|^2 d\vec{r} = 1, \quad i \in \{1,2\}. \quad (4.3)$$

In the same way as for a single species component [231], the stationary solutions, $\psi_1(\vec{r},0)$ and $\psi_2(\vec{r},0)$, are given by

$$\psi_1(\vec{r},t) = \psi_1(\vec{r},0) \exp\left[-i \frac{\mu_1 t}{\hbar}\right], \quad (4.4a)$$

$$\psi_2(\vec{r},t) = \psi_2(\vec{r},0) \exp\left[-i \frac{\mu_2 t}{\hbar}\right], \quad (4.4b)$$

where μ_i is the chemical potential of species i . The time independent coupled Gross-Pitaevskii equations are then written as

$$\left[-\frac{\hbar^2}{2m_1}\vec{\nabla}_{\vec{r}}^2 + U_1(\vec{r},0) + N_1g_{11}|\psi_1(\vec{r},0)|^2 + N_2g_{12}|\psi_2(\vec{r},0)|^2 - \mu_1 \right] \psi_1(\vec{r},0) = 0, \quad (4.5a)$$

$$\left[-\frac{\hbar^2}{2m_2}\vec{\nabla}_{\vec{r}}^2 + U_2(\vec{r},0) + N_2g_{22}|\psi_2(\vec{r},0)|^2 + N_1g_{12}|\psi_1(\vec{r},0)|^2 - \mu_2 \right] \psi_2(\vec{r},0) = 0. \quad (4.5b)$$

4.3 The different ground state structures

4.3.1 The Thomas-Fermi (TF) approximation

4.3.1.1 General case

In the same way as for a single atomic species, in the TF approximation, the impact of the kinetic term of each species is neglected in Eq. (4.5a) and Eq. (4.5b). From this approximation, we can rewrite the previous set of differential equations as two linear coupled equations for the two density profiles $|\psi_1(\vec{r}, 0)|^2$ and $|\psi_2(\vec{r}, 0)|^2$ as

$$\mu_1 = U_1(\vec{r}, 0) + N_1 g_{11} |\psi_1(\vec{r}, 0)|^2 + N_2 g_{12} |\psi_2(\vec{r}, 0)|^2, \quad (4.6a)$$

$$\mu_2 = U_2(\vec{r}, 0) + N_2 g_{22} |\psi_2(\vec{r}, 0)|^2 + N_1 g_{12} |\psi_1(\vec{r}, 0)|^2. \quad (4.6b)$$

In the case of a uniform potential and homogeneous gases, *i.e.* for $|\psi_i(\vec{r}, 0)|^2$ being constant, the miscibility criteria of the two condensates is given by the conditions [231, 308]

$$g_{11} > 0, \quad g_{22} > 0 \quad \text{and} \quad g_{11}g_{22} > g_{12}^2, \quad (4.7)$$

where the first two conditions describe the stability of each species in a single atomic species problem and the last condition forces the two species to overlap over the extent of the uniform trap.

We illustrate in Fig. 4.1 the behavior of a mixture of two components, observed for example in [335] with the two isotopes ^{85}Rb and ^{87}Rb , when the inter-species scattering length is adjusted using a Feshbach resonance and we explain the results observed by arguments based on repelling or attractive forces. For that, we define the quantity

$$\Delta = g_{11}g_{22} - g_{12}^2. \quad (4.8)$$

In the first case shown in panel (a), $\Delta < 0$ and $g_{12} < 0$, which means that atoms of different species attract each other more than they repel atoms of the same species. In the same way as for a single species problem where the constant $g_{ii} < 0$, the miscible mixture of superfluids is unstable and collapses.

For smaller values of $|g_{12}|$, such that $g_{12}^2 < g_{11} \cdot g_{22}$ and then $\Delta > 0$, at least one of the two single species interaction constants is dominant and the two superfluids overlap in some region of space, as shown in panel (b). In this particular situation, g_{12} can be either positive or negative. For a larger and positive value of g_{12} , Δ becomes negative again and atoms of different species repel each other more than they repel atoms of the same species, leading to a phase separation. The two superfluids no longer overlap. In

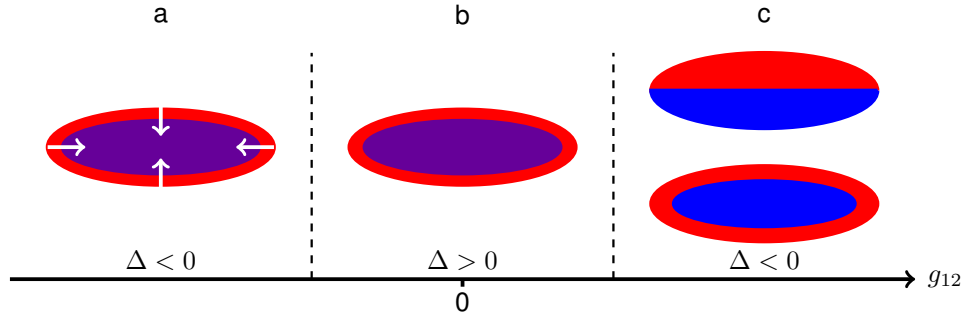


Figure 4.1: Illustration of the behavior of a mixture of bosons when the inter-species scattering length, a_{12} , is tuned from negative to positive values.

this configuration one can find the two possible cases: The first one is when one species is surrounding the other thus keeping the symmetry of the system and the second in an immiscible case with the two species sitting side by side, thus breaking the symmetry of the trap, as shown in panel (c).

4.3.1.2 Miscible case: general set of equations

In the following, we focus on the case described by the conditions of Eq. (4.7), and therefore we have $\Delta > 0$. The purpose of this section is to derive a set of equations describing the density distribution of each species in the different regions of space. We introduce the notion of “domain” to distinguish the different regions and configurations. A domain is by definition a region of space where either the two BECs overlap or where only one BEC is present. Using Eq. (4.6a) and Eq. (4.6b) one can express the two atomic densities as

$$|\psi_1(\vec{r}, 0)|^2 = \frac{g_{22}[\mu_1 - U_1(\vec{r}, 0)] - g_{12}[\mu_2 - U_2(\vec{r}, 0)]}{N_1(g_{11}g_{22} - g_{12}^2)} \times \Theta \left[\frac{g_{22}[\mu_1 - U_1(\vec{r}, 0)] - g_{12}[\mu_2 - U_2(\vec{r}, 0)]}{N_1(g_{11}g_{22} - g_{12}^2)} \right], \quad (4.9a)$$

$$|\psi_2(\vec{r}, 0)|^2 = \frac{g_{11}[\mu_2 - U_2(\vec{r}, 0)] - g_{12}[\mu_1 - U_1(\vec{r}, 0)]}{N_2(g_{11}g_{22} - g_{12}^2)} \times \Theta \left[\frac{g_{11}[\mu_2 - U_2(\vec{r}, 0)] - g_{12}[\mu_1 - U_1(\vec{r}, 0)]}{N_2(g_{11}g_{22} - g_{12}^2)} \right], \quad (4.9b)$$

where $\Theta[x]$ is the Heaviside function. We are interested in how the shape of these density functions can be described in cases characterized by two or three domains of existence. These two situations are represented schematically in Fig. 4.3 and Fig. 4.2 where, for convenience, we illustrate the two configurations in 1D.

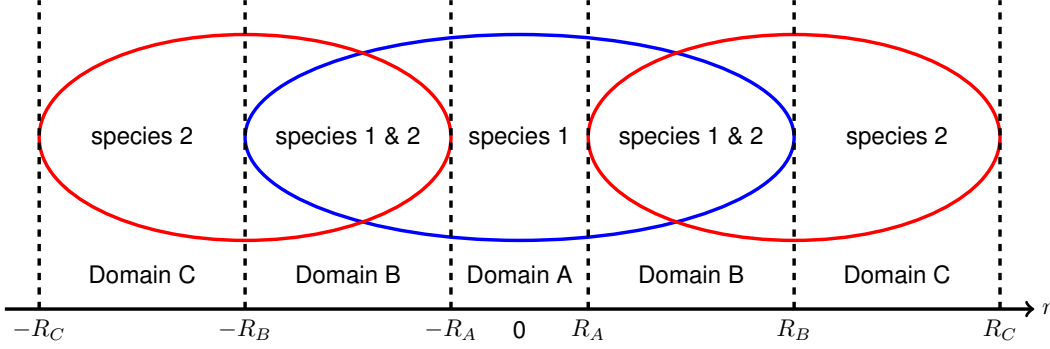


Figure 4.2: Schematic representation of the two-species BEC configuration when three different domains, labeled as domains C, B and A, can be defined.

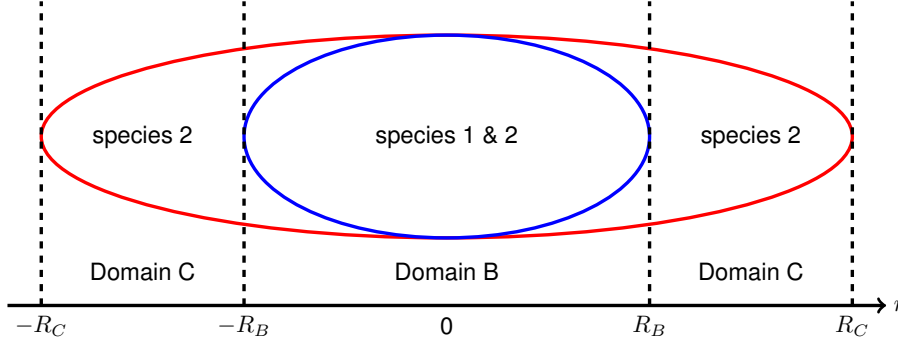


Figure 4.3: Schematic representation of the two-species BEC configuration when two different domains, labeled as domains C and B, can be defined.

In the case of three domains, a single species is present in the center, labelled as domain A. This domain is surrounded by a region where the two species overlap. This overlapping region is domain B. It is surrounded by a region where only the second species is present: this is domain C. In the following, we choose to note species 1 the species present in domain A and species 2 the one present in domain C. In this configuration the density of species 2 in domain A and the density of species 1 in domain C is zero. The different domains are delimited by the separation radii R_A , R_B and R_C .

In the case of two domains, we can see from Eq. (4.7) and Eq. (4.9) that the only possible domains are domains B and C. The first species is therefore always in the presence of the second one (domain B), while the second species has also its own domain of existence (domain C).

In regions where only one species is present, the density distribution is given by the

single species component

$$|\psi_i(\vec{r}, 0)|^2 = \frac{\mu_i}{N_i g_{ii}} \left[1 - \frac{U_i(\vec{r}, 0)}{\mu_i} \right] \times \Theta \left[1 - \frac{U_i(\vec{r}, 0)}{\mu_i} \right]. \quad (4.10)$$

According to the previous notation, the density distribution of species i with $i \in \{1, 2\}$ in domain X with $X \in \{A, B, C\}$ at position \vec{r} reads as

- In domain A:

$$\begin{cases} n_1^A(\vec{r}) = N_1 |\psi_1(\vec{r}, 0)|^2 = \frac{\mu_1}{g_{11}} \left[1 - \frac{U_1(\vec{r}, 0)}{\mu_1} \right], \\ n_2^A(\vec{r}) = N_2 |\psi_2(\vec{r}, 0)|^2 = 0. \end{cases} \quad (4.11)$$

- In domain B:

$$\begin{cases} n_1^B(\vec{r}) = N_1 |\psi_1(\vec{r}, 0)|^2 = \frac{g_{22}[\mu_1 - U_1(\vec{r}, 0)] - g_{12}[\mu_2 - U_2(\vec{r}, 0)]}{g_{11}g_{22} - g_{12}^2}, \\ n_2^B(\vec{r}) = N_2 |\psi_2(\vec{r}, 0)|^2 = \frac{g_{11}[\mu_2 - U_2(\vec{r}, 0)] - g_{12}[\mu_1 - U_1(\vec{r}, 0)]}{g_{11}g_{22} - g_{12}^2}. \end{cases} \quad (4.12)$$

- In domain C:

$$\begin{cases} n_1^C(\vec{r}) = N_1 |\psi_1(\vec{r}, 0)|^2 = 0, \\ n_2^C(\vec{r}) = N_2 |\psi_2(\vec{r}, 0)|^2 = \frac{\mu_2}{g_{22}} \left[1 - \frac{U_2(\vec{r}, 0)}{\mu_2} \right]. \end{cases} \quad (4.13)$$

The different radii R_X which marks the separation between the different domains are defined by the cancellation of the density distributions, and read in Cartesian coordinates as

$$n_2^B(R_{A,x}, R_{A,y}, R_{A,z}) = 0, \quad (4.14a)$$

$$n_1^B(R_{B,x}, R_{B,y}, R_{B,z}) = 0, \quad (4.14b)$$

$$n_2^C(R_{C,x}, R_{C,y}, R_{C,z}) = 0, \quad (4.14c)$$

and in the case of isotropic traps in Spherical coordinates¹ as

$$n_2^B(R_A) = 0, \quad (4.15a)$$

$$n_1^B(R_B) = 0, \quad (4.15b)$$

$$n_2^C(R_C) = 0. \quad (4.15c)$$

¹The two angular variables, θ and ψ , have been dropped out for simplicity, i.e. $n_2^B(R_A) \equiv n_2^B(R_A, \theta, \psi)$.

In the same way as for single species, the chemical potential is expressed thanks to the normalization conditions

$$N_1 = \int_{V_A} n_1^A(\vec{r}) d\vec{r} + \int_{V_B} n_1^B(\vec{r}) d\vec{r} + \int_{V_C} n_1^C(\vec{r}) d\vec{r} = f(\mu_1, \mu_2), \quad (4.16a)$$

$$N_2 = \int_{V_A} n_2^A(\vec{r}) d\vec{r} + \int_{V_B} n_2^B(\vec{r}) d\vec{r} + \int_{V_C} n_2^C(\vec{r}) d\vec{r} = g(\mu_1, \mu_2), \quad (4.16b)$$

where $\int_{V_X} n_i^X(\vec{r}) d\vec{r}$ represents the integral of species density i in domain X .

4.3.1.3 The harmonic trap approximation

We are now interested in the particular case of harmonic external traps. Without losing generality, the traps are considered isotropic for reasons of simplicity and we introduce two coefficients, γ_1 and γ_2 , to express the two external potentials according to a hypothetical mass m_0 and frequency ω_0 , with

$$m_1\omega_1^2 = \gamma_1 m_0\omega_0^2, \quad (4.17a)$$

$$m_2\omega_2^2 = \gamma_2 m_0\omega_0^2. \quad (4.17b)$$

The objective of this section is to highlight the different density distributions in each domain as well as the expressions of the different separation radii that are of particular interest for the rest of the chapter. In the following the different densities read as

- In domain A:

$$\begin{cases} n_1^A(r) &= \frac{\mu_1}{g_{11}} \left[1 - \frac{\gamma_1}{\mu_1} \left(\frac{m_0\omega_0^2}{2} \right) r^2 \right], \\ n_2^A(r) &= 0, \end{cases} \quad (4.18)$$

- In domain B:

$$\begin{cases} n_1^B(r) &= \frac{g_{22}\mu_1 - g_{12}\mu_2}{g_{11}g_{22} - g_{12}^2} \left[1 - \frac{\gamma_1 g_{22} - \gamma_2 g_{12}}{g_{22}\mu_1 - g_{12}\mu_2} \left(\frac{m_0\omega_0^2}{2} \right) r^2 \right], \\ n_2^B(r) &= \frac{g_{11}\mu_2 - g_{12}\mu_1}{g_{11}g_{22} - g_{12}^2} \left[1 - \frac{\gamma_2 g_{11} - \gamma_1 g_{12}}{g_{11}\mu_2 - g_{12}\mu_1} \left(\frac{m_0\omega_0^2}{2} \right) r^2 \right], \end{cases} \quad (4.19)$$

- In domain C:

$$\begin{cases} n_1^C(r) &= 0, \\ n_2^C(r) &= \frac{\mu_2}{g_{22}} \left[1 - \frac{\gamma_2}{\mu_2} \left(\frac{m_0\omega_0^2}{2} \right) r^2 \right], \end{cases} \quad (4.20)$$

where the domain separations are defined by

$$R_A^2 = \frac{g_{11}\mu_2 - g_{12}\mu_1}{g_{11}\gamma_2 - g_{12}\gamma_1} \left(\frac{2}{m_0\omega_0^2} \right), \quad (4.21a)$$

$$R_B^2 = \frac{g_{22}\mu_1 - g_{12}\mu_2}{g_{22}\gamma_1 - g_{12}\gamma_2} \left(\frac{2}{m_0\omega_0^2} \right), \quad (4.21b)$$

$$R_C^2 = \frac{\mu_2}{\gamma_2} \left(\frac{2}{m_0\omega_0^2} \right). \quad (4.21c)$$

In the case of only two domains, the densities of the two species are described by Eq. (4.19) and Eq. (4.20), delimited by the radii given in Eq. (4.21b) and Eq. (4.21c). In each case, the shape of each density distribution is a succession of parabolic branches, with curvatures depending on the different trap parameters in each domain, γ_1 and γ_2 , on the different chemical potentials, μ_1 and μ_2 , and on the three scattering lengths.

4.3.2 Study in the case of two domains in the TF approximation

We first concentrate on the case of two domains, for which an analytical expression of the chemical potentials μ_1 and μ_2 can be found.

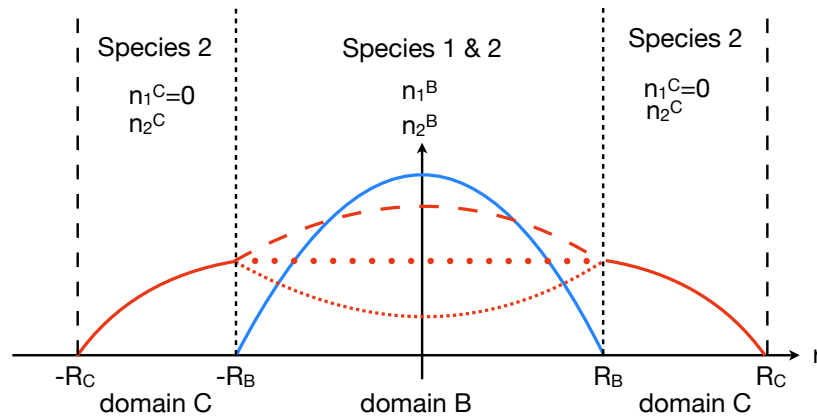


Figure 4.4: Schematic representation of the atomic density distributions in the case of two domains. The blue and red curves show respectively the density profiles of the first and second species in their respective domains.

4.3.2.1 Curvature of the densities

The curvatures of the density profiles are given by the second spatial derivative of the density distributions. In domains B and C they are given by

$$\Delta n_1^B = -\frac{\gamma_1 g_{22}}{g_{11} g_{22} - g_{12}^2} \left(1 - \frac{g_{12} \gamma_2}{g_{22} \gamma_1} \right) m_0 \omega_0^2, \quad (4.22a)$$

$$\Delta n_2^B = -\frac{\gamma_2 g_{11}}{g_{11} g_{22} - g_{12}^2} \left(1 - \frac{g_{12} \gamma_1}{g_{11} \gamma_2} \right) m_0 \omega_0^2, \quad (4.22b)$$

$$\Delta n_2^C = -\frac{\gamma_2}{g_{22}} m_0 \omega_0^2. \quad (4.22c)$$

In the Fig. 4.4 we show the different possible curvatures of the density profiles of each species. The curvature of the first species profile is negative in domain B with the condition $g_{12} \gamma_2 < g_{22} \gamma_1$, while the curvature of the second species in this region depends on the ratio $\chi_B = (g_{12} \gamma_1) / (g_{11} \gamma_2)$: If $\chi_B < 1$ this curvature is negative, represented by the dashed red line ; If $\chi_B > 1$ this curvature is positive, represented by the thin dotted red line ; If $\chi_B = 0$ there is no curvature, represented by the thick dotted red line. In domain C, the only species present is the second species with a negative curvature, and we recover the expected inverse parabola of the single component case.

4.3.2.2 Chemical potentials and atoms numbers

Thanks to the normalization condition given by Eq. (4.16a) and Eq. (4.16b) the total atom number for both species can be written as

$$N_1 = \frac{8\pi}{15} \left(\frac{2}{m_0 \omega_0^2} \right)^{3/2} \frac{1}{g_{11}} \left[\frac{1}{1 - \frac{g_{12}^2}{g_{11} g_{22}}} \frac{\left(\mu_1 - \frac{g_{12}}{g_{22}} \mu_2 \right)^{5/2}}{\left(\gamma_1 - \frac{g_{12}}{g_{22}} \gamma_2 \right)^{3/2}} \right], \quad (4.23a)$$

$$N_2 = \frac{8\pi}{15} \left(\frac{2}{m_0 \omega_0^2} \right)^{3/2} \frac{1}{g_{22}} \left[\frac{\mu_2^{5/2}}{\gamma_2^{3/2}} - \frac{g_{12}}{g_{11}} \frac{1}{1 - \frac{g_{12}^2}{g_{11} g_{22}}} \frac{\left(\mu_1 - \frac{g_{12}}{g_{22}} \mu_2 \right)^{5/2}}{\left(\gamma_1 - \frac{g_{12}}{g_{22}} \gamma_2 \right)^{3/2}} \right], \quad (4.23b)$$

These equations can be inverted to find analytical expressions for the chemical potentials

$$\mu_1 = \frac{g_{12}}{g_{22}}\mu_2 + \left[\frac{15}{8\pi} N_1 g_{11} \left(1 - \frac{g_{12}^2}{g_{11}g_{22}} \right) \left(\frac{m_0\omega_0^2}{2} \right)^{3/2} \left(\gamma_1 - \frac{g_{12}}{g_{22}} \gamma_2 \right)^{3/2} \right]^{2/5}, \quad (4.24a)$$

$$\mu_2 = \left[\frac{15}{8\pi} \left(N_2 g_{22} + N_1 g_{12} \right) \left(\frac{m_0\omega_0^2}{2} \right)^{3/2} \gamma_2^{3/2} \right]^{2/5}. \quad (4.24b)$$

4.3.3 Study in the case of three domains in the TF approximation

The case of three domains can be treated similarly, but it is no longer possible to find an analytical expression of the chemical potentials μ_1 and μ_2 . The curvatures in domains A, B and C are given by

$$\Delta n_1^A = -\frac{\gamma_1}{g_{11}} m_0 \omega_0^2, \quad (4.25a)$$

$$\Delta n_1^B = -\frac{\gamma_1 g_{22}}{g_{11}g_{22} - g_{12}^2} \left(1 - \frac{g_{12}}{g_{22}} \frac{\gamma_2}{\gamma_1} \right) m_0 \omega_0^2, \quad (4.25b)$$

$$\Delta n_2^B = -\frac{\gamma_2 g_{11}}{g_{11}g_{22} - g_{12}^2} \left(1 - \frac{g_{12}}{g_{11}} \frac{\gamma_1}{\gamma_2} \right) m_0 \omega_0^2, \quad (4.25c)$$

$$\Delta n_2^C = -\frac{\gamma_2}{g_{22}} m_0 \omega_0^2. \quad (4.25d)$$

As shown in Fig. 4.5, in the regions where only one of the two species is present, the curvature of the density profile is negative. In the overlapping regions, depending on the value of the coefficients $(g_{22}\gamma_1 - g_{12}\gamma_2)$ and $(g_{11}\gamma_2 - g_{12}\gamma_1)$ the density curvatures for species 1 and 2 may be negative or positive.

4.4 Dynamics

In this section, we focus on the dynamics of the bosonic BEC mixtures whose ground states were calculated in the previous sections. Their mean-field dynamics is first described by the time-dependent coupled Gross-Pitaevskii equations and later by the Thomas-Fermi approximation, both being ultimately compared. For the sake of simplicity, we limit the problems to harmonic isotropic traps. We first introduce the scaling

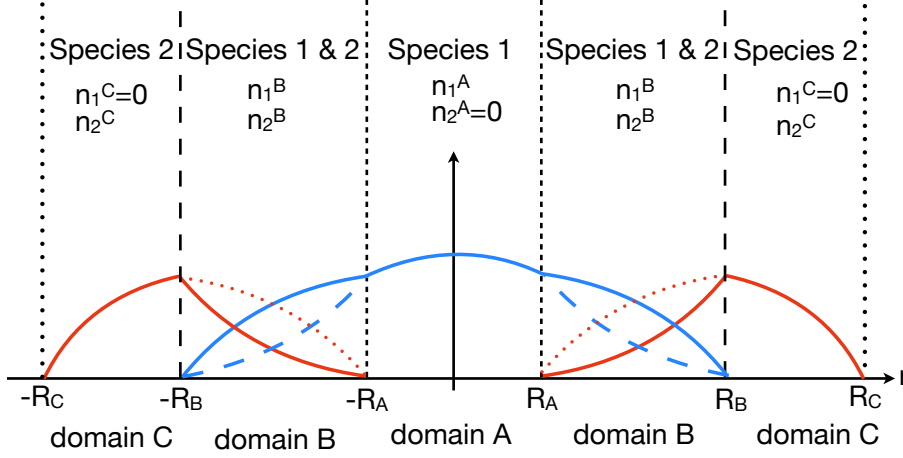


Figure 4.5: Schematic representation of the atomic density distributions in the case of three domains. The blue and red curves show respectively the density profiles of the first and second species in their respective domains.

approach [229, 230] in spherical coordinates for one species and in a second step, we propose an extension of this scaling approach for a dual-species bosonic BEC.

4.4.1 The time-dependent coupled Gross-Pitaevskii equations in spherical coordinates

4.4.1.1 Case of a single species

In the case of a single species BEC, the time-dependent Gross-Pitaevskii equation (TDGPE) reads as

$$i\hbar\partial_t\psi(\vec{r},t) = \left[-\frac{\hbar^2}{2m}\nabla_{\vec{r}}^2 + U(\vec{r},t) + Ng|\psi(\vec{r},t)|^2 \right] \psi(\vec{r},t), \quad (4.26)$$

where the kinetic operator ∇^2 is defined as

$$\nabla_{\vec{r}}^2 = \partial_{xx} + \partial_{yy} + \partial_{zz} \quad (4.27)$$

in Cartesian coordinates and as

$$\nabla_{\vec{r}}^2 = \partial_{rr} + \frac{2}{r}\partial_r + \frac{1}{r^2\sin\theta} \left[\partial_{\theta}(\sin\theta\partial_{\theta}) + \frac{1}{\sin\theta}\partial_{\phi\phi} \right] \quad (4.28)$$

in spherical coordinates. Here r represents the radial coordinate and (θ, ϕ) are the usual angular coordinates. Writing the wave function as a product of radial and angular parts

$$\psi(\vec{r},t) = R(r,t) \cdot Y_{l,m}(\theta, \phi), \quad (4.29)$$

where in the particular case of a pure spherical trap, $Y_{l,m}(\theta, \phi) = Y_{0,0} = 1/\sqrt{4\pi}$, the TDGPE can be simplified to

$$i\hbar\partial_t R(r, t) = \left[-\frac{\hbar^2}{2m} \left(\partial_{rr} + \frac{2}{r} \partial_r \right) + U(r, t) + \frac{Ng}{4\pi} |R(r, t)|^2 \right] R(r, t). \quad (4.30)$$

To simplify the expression of the kinetic term, the following transformation is introduced

$$\chi(r, t) = r \cdot R(r, t). \quad (4.31)$$

The TDGPE then becomes

$$i\hbar\partial_t \chi(r, t) = \left[-\frac{\hbar^2}{2m} \partial_{rr} + U(r, t) + \frac{Ng}{4\pi r^2} |\chi(r, t)|^2 \right] \chi(r, t). \quad (4.32)$$

The normalization condition is given by

$$\int_0^\infty r^2 dr \int_0^\pi \sin\theta d\theta \int_0^{2\pi} |\psi(\vec{r}, t)|^2 d\phi = \int_0^\infty r^2 |R(r, t)|^2 dr = \int_0^\infty |\chi(r, t)|^2 dr = 1. \quad (4.33)$$

4.4.1.2 The case of a dual-species BEC

In the case of a dual-species BEC, in spherical coordinates and in an isotropic harmonic trap, the time-dependent coupled Gross-Pitaevskii equations (TDCGPE) read as

$$i\hbar\partial_t \chi_1(r, t) = \left[-\frac{\hbar^2}{2m_1} \partial_{rr} + U_1(r, t) + \frac{N_1 g_{11}}{4\pi r^2} |\chi_1(r, t)|^2 + \frac{N_2 g_{12}}{4\pi r^2} |\chi_2(r, t)|^2 \right] \chi_1(r, t), \quad (4.34a)$$

$$i\hbar\partial_t \chi_2(r, t) = \left[-\frac{\hbar^2}{2m_2} \partial_{rr} + U_2(r, t) + \frac{N_2 g_{22}}{4\pi r^2} |\chi_2(r, t)|^2 + \frac{N_1 g_{12}}{4\pi r^2} |\chi_1(r, t)|^2 \right] \chi_2(r, t). \quad (4.34b)$$

4.4.2 Scaling approach for a two-component BEC

In this section, inspired by the derivation of the scaling approach described in [229, 230] for a single species, we propose a generalization of the method for a two-component superfluid system. For the sake of generality, this approach is derived in Cartesian coordinates.

4.4.2.1 Derivation of the scaling approach in the overlapping region

As shown in section 4.3, in the TF approximation the density distribution of each species has a parabolic shape in each domain, with a positive or negative curvature in the overlapping region. In the same way as for a single species, we introduce the force seen by the particles of each species

$$\vec{F}_1(\vec{r}, t) = -\vec{\nabla} \left(U_1(\vec{r}, t) + N_1 g_{11} n_1^D(\vec{r}, t) + N_2 g_{12} n_2^D(\vec{r}, t) \right), \quad (4.35a)$$

$$\vec{F}_2(\vec{r}, t) = -\vec{\nabla} \left(U_2(\vec{r}, t) + N_2 g_{22} n_2^D(\vec{r}, t) + N_1 g_{12} n_1^D(\vec{r}, t) \right). \quad (4.35b)$$

The time-dependent spatial density of the two species are given by

$$n_1^D(\vec{r}, t) = \frac{n_1^D(\vec{r}', 0)}{\lambda_{1,x}^D(t) \lambda_{1,y}^D(t) \lambda_{1,z}^D(t)}, \quad (4.36a)$$

$$n_2^D(\vec{r}, t) = \frac{n_2^D(\vec{r}', 0)}{\lambda_{2,x}^D(t) \lambda_{2,y}^D(t) \lambda_{2,z}^D(t)}. \quad (4.36b)$$

In this expression the coordinates \vec{r} and \vec{r}' are defined as

$$\vec{r} = x \vec{u}_x + y \vec{u}_y + z \vec{u}_z \quad \text{and} \quad \vec{r}' = \frac{x}{\lambda_{1,x}^D(t)} \vec{u}_x + \frac{y}{\lambda_{1,y}^D(t)} \vec{u}_y + \frac{z}{\lambda_{1,z}^D(t)} \vec{u}_z. \quad (4.37)$$

The dimensionless scaling coefficients $\lambda_{i,j}^D(t)$ with $i \in \{1, 2\}$ and $j \in \{x, y, z\}$ describe the expansion of the species i in the direction j . The exponent D denotes the presence of a dual-species condensate. From EqEq. (4.9a) and Eq. (4.9b), the initial spatial densities in the domain where the two species are present are given by

$$n_1^D(\vec{r}, 0) = \frac{g_{22} [\mu_1 - U_1(\vec{r}, 0)] - g_{12} [\mu_2 - U_2(\vec{r}, 0)]}{N_1 (g_{11} g_{22} - g_{12}^2)}, \quad (4.38a)$$

$$n_2^D(\vec{r}, 0) = \frac{g_{11} [\mu_2 - U_2(\vec{r}, 0)] - g_{12} [\mu_1 - U_1(\vec{r}, 0)]}{N_2 (g_{11} g_{22} - g_{12}^2)}. \quad (4.38b)$$

The equilibrium condition at time $t = 0$ gives $\vec{F}_1(\vec{r}, 0) = \vec{F}_2(\vec{r}, t) = \vec{0}$. In the case of an external harmonic trap,

$$U_1(\vec{r}, t) = \frac{1}{2} m_1 \left(\omega_{1,x}^2(t) x^2 + \omega_{1,y}^2(t) y^2 + \omega_{1,z}^2(t) z^2 \right), \quad (4.39a)$$

$$U_2(\vec{r}, t) = \frac{1}{2} m_2 \left(\omega_{2,x}^2(t) x^2 + \omega_{2,y}^2(t) y^2 + \omega_{2,z}^2(t) z^2 \right), \quad (4.39b)$$

the projection along the direction $j \in \{x, y, z\}$ of the force acting on species i is given by

$$\begin{aligned} F_{i,j}(r_j, t) = & -m_i \omega_{i,j}^2(t) r_j \\ & + \left[\frac{g_{ii}}{\lambda_{i,x}^D(t) \lambda_{i,y}^D(t) \lambda_{i,z}^D(t)} \left\{ \frac{g_{i'i'} m_i \omega_{i,j}^2(0) - g_{12} m_{i'} \omega_{i',j}^2(0)}{(g_{11} g_{22} - g_{12}^2) (\lambda_{i,j}^D(t))^2} \right\} \right] r_j \\ & + \left[\frac{g_{12}}{\lambda_{i',x}^D(t) \lambda_{i',y}^D(t) \lambda_{i',z}^D(t)} \left\{ \frac{g_{ii} m_{i'} \omega_{i',j}^2(0) - g_{12} m_i \omega_{i,j}^2(0)}{(g_{11} g_{22} - g_{12}^2) (\lambda_{i',j}^D(t))^2} \right\} \right] r_j \end{aligned} \quad (4.40)$$

where $i' = 2$ when $i = 1$ and $i' = 1$ when $i = 2$, and where $r_j \equiv x, y, z$. Newton's law applied in the overlapping region implies

$$\begin{aligned} \ddot{\lambda}_{i,j}^D(t) = & -\omega_{i,j}^2(t)\lambda_{i,j}^D(t) \\ & + \left[\frac{g_{ii}}{\lambda_{i,x}^D(t)\lambda_{i,y}^D(t)\lambda_{i,z}^D(t)} \left\{ \frac{g_{i'i'}m_i\omega_{i,j}^2(0) - g_{12}m_{i'}\omega_{i',j}^2(0)}{m_i(g_{11}g_{22} - g_{12}^2)} \lambda_{i,j}^D(t) \right\} \right] \\ & + \left[\frac{g_{12}}{\lambda_{i',x}^D(t)\lambda_{i',y}^D(t)\lambda_{i',z}^D(t)} \left\{ \frac{g_{ii}m_{i'}\omega_{i',j}^2(0) - g_{12}m_i\omega_{i,j}^2(0)}{m_i(g_{11}g_{22} - g_{12}^2)} \lambda_{i',j}^D(t) \right\} \left(\frac{\lambda_{i,j}^D(t)}{\lambda_{i',j}^D(t)} \right) \right]. \end{aligned} \quad (4.41)$$

4.4.2.2 Reminder on the single species scaling approach

In the case of a single species BEC, Eq. (4.41) simplifies to [229, 230]

$$\ddot{\lambda}_j^S(t) = -\omega_j^2(t)\lambda_j^S(t) + \frac{\omega_j^2(0)}{\lambda_x^S(t)\lambda_y^S(t)\lambda_z^S(t)\lambda_j^S(t)}, \quad (4.42)$$

where the exponent S denotes the case of a single species BEC. The atomic density is given by

$$n^S(\vec{r}, t) = \frac{n^S(\vec{r}', 0)}{\lambda_x^S(t)\lambda_y^S(t)\lambda_z^S(t)}, \quad (4.43)$$

where the initial spatial density is expressed as

$$n^S(\vec{r}, 0) = \frac{\mu - U(\vec{r}, 0)}{Ng} \times \Theta \left[\frac{\mu - U(\vec{r}, 0)}{Ng} \right]. \quad (4.44)$$

4.4.2.3 Per domain approach

The presence of different domains in BEC mixture imposes different assumptions in these different domains for the scaling approach. This is because the atomic densities of both species are described differently in each domain, depending on the presence of either one or two species in a particular domain. In the case of three domains, the density evolution in each domain is simply given by

- In domain A:

$$\begin{cases} n_1^A(\vec{r}, t) = N_1 n_1^S(\vec{r}, t), \\ n_2^A(\vec{r}, t) = 0, \end{cases} \quad (4.45)$$

- In domain B:

$$\begin{cases} n_1^B(\vec{r}, t) = N_1 n_1^D(\vec{r}, t), \\ n_2^B(\vec{r}, t) = N_2 n_2^D(\vec{r}, t), \end{cases} \quad (4.46)$$

- In domain C:

$$\begin{cases} n_1^C(\vec{r}, t) = 0, \\ n_2^C(\vec{r}, t) = N_2 n_2^S(\vec{r}, t). \end{cases} \quad (4.47)$$

Note also that, just like in the single species case where the first derivative of the TF atomic density presents a discontinuity at the edge of the condensate, the present dual-species approach does not prevent against such discontinuity of the densities at the time-dependent radii $R_A(t)$, $R_B(t)$ and $R_C(t)$. These time-dependent frontiers are defined as

$$R_A(t) = R_A(0) \lambda_1^S(t), \quad (4.48a)$$

$$R_B(t) = R_B(0) \lambda_1^D(t), \quad (4.48b)$$

$$R_C(t) = R_C(0) \lambda_2^S(t). \quad (4.48c)$$

4.5 Results

We now illustrate the results of the two-components theory by applying it to a miscible mixture of ^{87}Rb and ^{41}K atoms in the case of a pure harmonic isotropic trap. In the following, we focus on the case where the intra-species scattering length of the two species are constant but we allow the inter-species scattering length to be tuned via a Feshbach resonance from negative to positive. The paper [341] reports the discovery of two Feshbach resonances around 35 and 79 G in a mixture of ^{41}K and ^{87}Rb . Based on these results, in table 4.1 we give the values of the different scattering lengths used for the different simulations accessible with a Feshbach magnetic field below 100 G [341].

We will first show a comparison between the ground state densities predicted by the time-independent coupled Gross-Pitaevskii equations (TICGPE) and by the Thomas-Fermi (TF) approximation. We later compare the evolution of the densities of the two species calculated via the time-dependent coupled Gross-Pitaevskii equations (TDCGPE) with our generalized scaling approach in the particular case of two domains. In all cases the numerical calculations based on the Gross-Pitaevskii equation have been done following the split operator technique described in Appendix A in the case of the linear Schrödinger equation. We will finally conclude on the possibility of controlling the temperature expansion of the two species in a micro-gravity based experiment. Unless stated differently, the external traps are defined throughout the chapter by $\omega_{87\text{Rb}} = 2\pi \cdot 50 \text{ Hz}$ and $\omega_{41\text{K}} = (m_{87\text{Rb}}/m_{41\text{K}})^{1/2} \cdot \omega_{87\text{Rb}}$.

	^{87}Rb		^{41}K		$^{87}\text{Rb} - ^{41}\text{K}$		
	(a.u.)	(nm)	(a.u.)	(nm)	(a.u.)	(nm)	case
a	99.0	5.20	60.0	3.10	0	0	(i)
					-56.7	-3.00	(ii)
					-18.9	-1.00	(iii)
					+18.9	+1.00	(iv)
					+56.7	+3.00	(v)
					+70.0	+3.70	(vi)
					+163 [339]	+8.62	(vii)

Table 4.1: Intra-species and inter-species scattering lengths used in the simulations. $a_1 = a_{^{87}\text{Rb}}$, $a_2 = a_{^{41}\text{K}}$ and $a_{12} = a_{^{87}\text{Rb}-^{41}\text{K}}$. The corresponding Feshbach magnetic field can be found in [341]. Each of the scattering length proposed in the table can be achieved with a magnetic field below 100 G.

4.5.1 Ground state comparison between TF and GPE

In Fig. 4.6 and Fig. 4.7 we show how the inter-species interaction length impacts the ground state density distribution for different atoms number: $N = 10^5$ and 10^6 , in the case of two distinct domains. The left and right panels depict different representations of the wave function (see section 4.4.1.1). The representation $|\psi(r, t = 0)|^2$, left panels, and $|\chi(r, t = 0)|^2 \propto r^2 \cdot |\psi(r, t = 0)|^2$, right panels, accentuate the representation of the density distribution of each BEC respectively close to the trap minimum, $r \rightarrow 0$, or at the edges of the distributions in the different domains, $r \rightarrow R_{A,B,C}$. Both representation are interesting when comparing to the TF calculations, the left panels for the maximum amplitude and the right panels for the domains sizes.

The blue and red colors represent the density distributions of ^{87}Rb (blue) and ^{41}K (red). The solid and dashed lines depict respectively the results of the TICGPE and of the TF approximation, where the different domain sizes R_B and R_C are represented by vertical dotted-dashed and dashed lines, respectively.

As we could expect, both densities peaks at the center of the trap decrease the larger the inter-species scattering length is, varying from a negative value in the second row, where the inter-species interaction is attractive, to a positive value in the bottom row, where this interaction is repulsive. At the same time the increase of the inter-species scattering length leads to an increase of the size of each region. The radii of the two density distributions match well with the predicted radii highlighted by the vertical

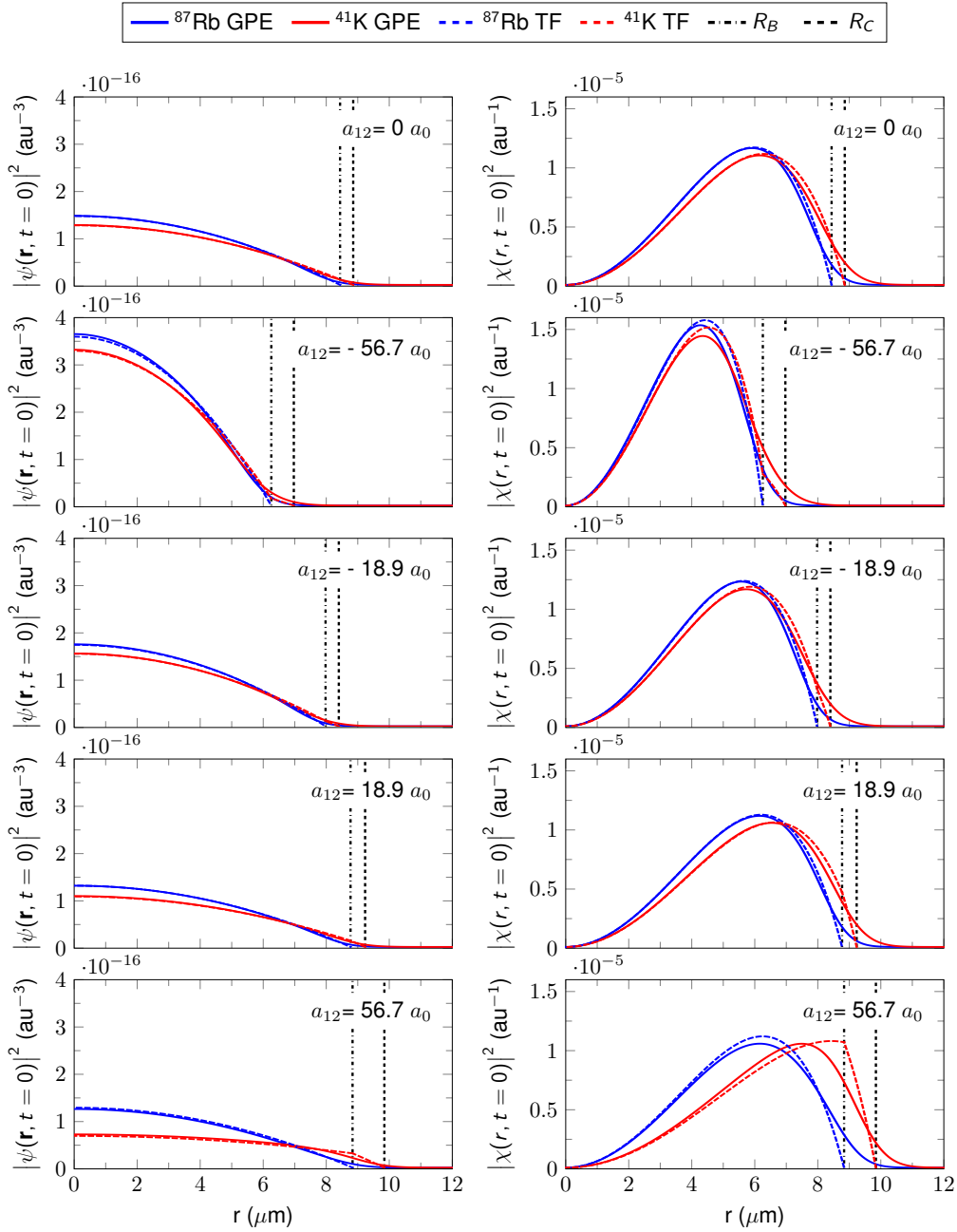


Figure 4.6: Two-domains ground state calculation. Representation of the density distributions for the cases (i): First row to (v): Last row, (see table 4.1), for 10^5 atoms of each species. The left and right panels show the density distributions in two representations. The blue and red lines represent the distribution of ^{87}Rb and ^{41}K calculated with the TICGPE (solid line) and the TF approximation (dashed line). The harmonic traps are isotropic and their frequencies are respectively $\omega_{87\text{Rb}} = 2\pi \cdot 50 \text{ Hz}$ and $\omega_{41\text{K}} = (m_{87\text{Rb}}/m_{41\text{K}})^{1/2} \cdot \omega_{87\text{Rb}}$

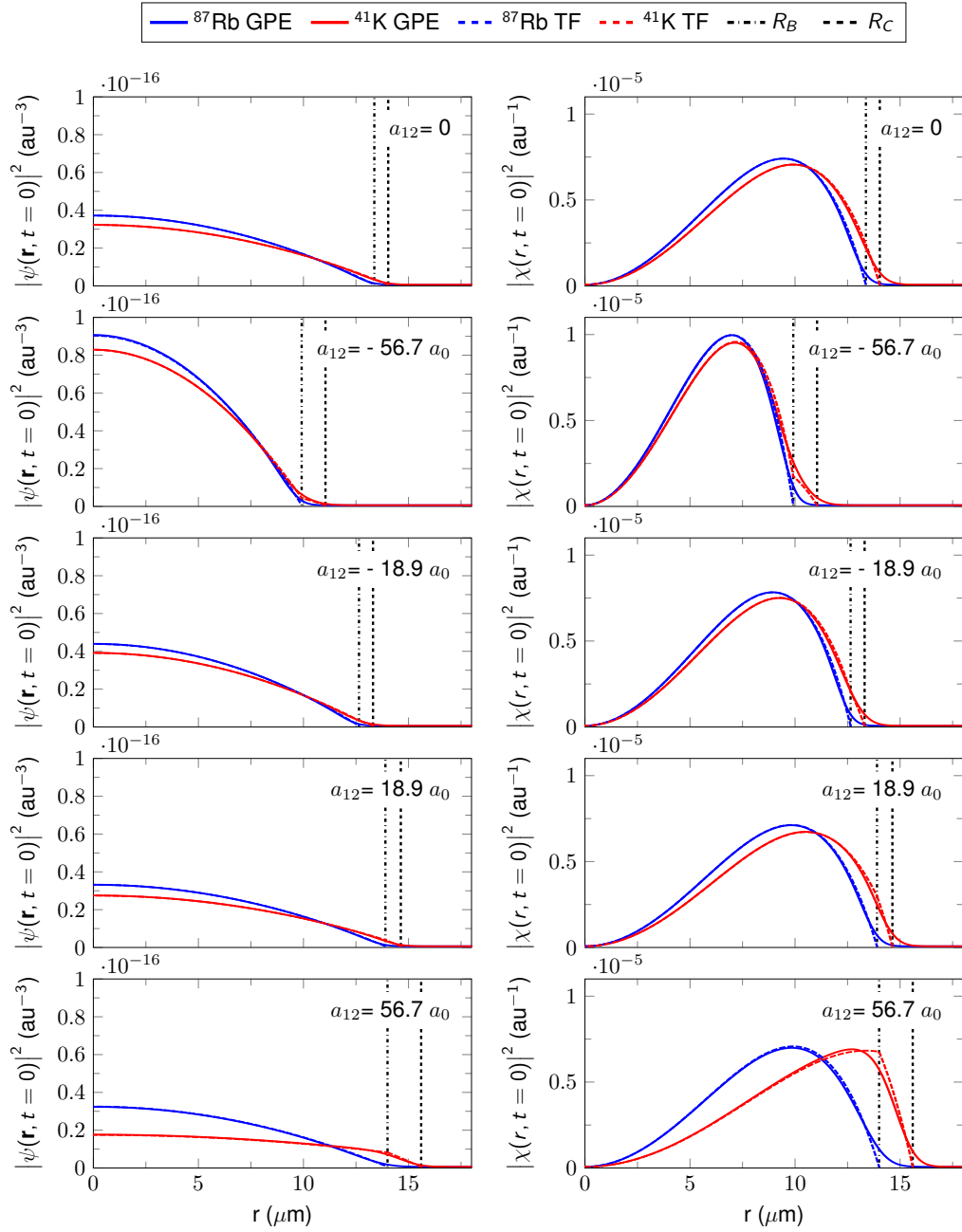


Figure 4.7: Two-domains ground state calculation. Representation of the density distributions for the cases (i): First row to (v): Last row, (see table 4.1), for 10^6 atoms of each species. The left and right panels show the density distributions in two representations. The blue and red lines represent the distribution of ^{87}Rb and ^{41}K calculated with the TICGPE (solid line) and the TF approximation (dashed line). The harmonic traps are isotropic and their frequencies are respectively $\omega_{87\text{Rb}} = 2\pi \cdot 50$ Hz and $\omega_{41\text{K}} = (m_{87\text{Rb}}/m_{41\text{K}})^{1/2} \cdot \omega_{87\text{Rb}}$

lines.

In the case where both species do not interact with each other (corresponding to $a_{12} = 0$), two independent distributions are created and the domains size, R_B and R_C , are exactly equivalent to the TF radii of the two independent species. In addition, there is no edge in the density distribution caused by a transition between one domain to another.

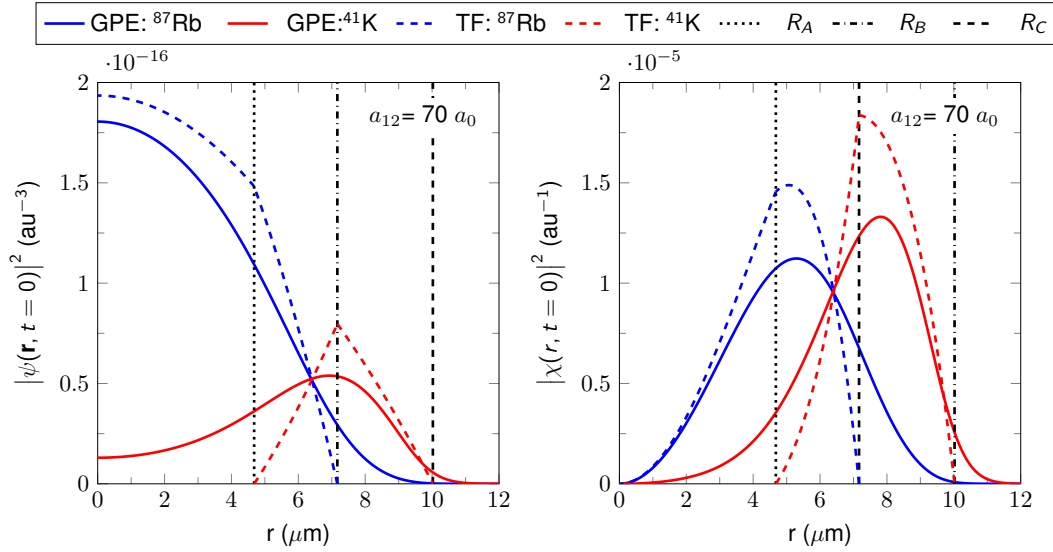


Figure 4.8: Three-domains ground state calculation. Representation of the density distributions for the case (vi), (see table 4.1), for 10^5 atoms of each species. The left and right panels show the density distributions in two representations. The blue and red lines represent the distribution of ^{87}Rb and ^{41}K calculated with the TICGPE (solid line) and the TF approximation (dashed line). The harmonic traps are isotropic and their frequencies are respectively $\omega_{87\text{Rb}} = 2\pi \cdot 50 \text{ Hz}$ and $\omega_{41\text{K}} = (m_{87\text{Rb}}/m_{41\text{K}})^{1/2} \cdot \omega_{87\text{Rb}}$

While in the case of 10^6 atoms (Fig. 4.7) the overlap between the TF approximation and the TICGPE is very convincing, in the case of 10^5 atoms (Fig. 4.6), for high values of the inter-species scattering length the model leads a small discrepancy at large distance. This can be understood at first glance in the case of a single species component problem where the TF approximation holds when the quantum pressure (kinetic energy) term $-\hbar^2 \nabla^2(\sqrt{n})/(2m\sqrt{n})$ is negligible compared to the interaction energy $gn(0)$ [231]. It thus appears that, if L is the typical length scale on which the density distribution $n(r)$ varies, the TF approximation is valid when

$$L \gg \xi_h = \sqrt{\frac{\hbar^2}{2mgn(0)}}. \quad (4.49)$$

Here ξ_h is the so-called healing length of the condensate. In the case of an harmonic potential, the validity of the TF approximation can be expressed by the ratio between the TF radius R_{TF} and ξ_h . This condition can be written as

$$\frac{R_{TF}}{\xi_h} \propto N^{2/5} \gg 1. \quad (4.50)$$

For non-zero inter-species scattering length, a similar relations should hold for the atom numbers of both species since it is for large atom numbers that the kinetic energy term is negligible compared to the interactions terms. In the expression (4.50), R_{TF} is now replaced by the domain sizes R_B and R_C .

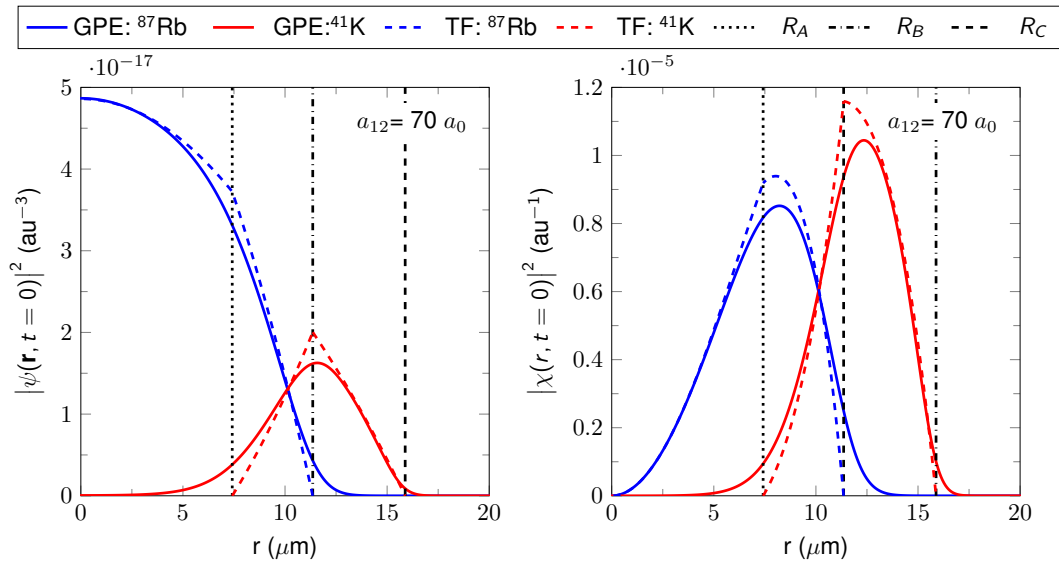


Figure 4.9: Three-domains ground state calculation. Representation of the density distributions for the case (vi), (see table 4.1), for 10^6 atoms of each species. The left and right panels show the density distributions in two representations. The blue and red lines represent the distribution of ⁸⁷Rb and ⁴¹K calculated with the TICGPE (solid line) and the TF approximation (dashed line). The harmonic traps are isotropic and their frequencies are respectively $\omega_{87\text{Rb}} = 2\pi \cdot 50 \text{ Hz}$ and $\omega_{41\text{K}} = (m_{87\text{Rb}}/m_{41\text{K}})^{1/2} \cdot \omega_{87\text{Rb}}$

The Fig. 4.8 and Fig. 4.9 show the configuration number (vi), characterized by the existence of three domains for a total number of atoms 10^5 and 10^6 , respectively. The different domain sizes R_A , R_B and R_C are respectively indicated via a dotted, dash-dotted and dashed vertical line. The density distributions calculated with the TICGPE and the TF approximation are shown in solid and dashed lines for the two species. The agreement between the two approaches is reasonable, and for the same reasons as mentioned previously the TF results improve with higher atom numbers.

4.5.2 Comparison between the TDCGPE and the generalized scaling approach

We would now like to check the accuracy of our generalized scaling approach in the case of a free expansion of the two condensates. For this, we first calculate the expansion dynamics using the time-dependent coupled Gross-Pitaevskii equations (TDCGPE) (4.34), and then calculate the same expansion dynamics using the generalized scaling equations (4.41) of the different ground state configurations, (i) to (v), shown in the Fig. 4.6 and Fig. 4.7. For simplicity, we limit our study to the case of two domains and compare two quantities of particular interest: The density profiles of the two condensates and their characteristic sizes.

The figures Fig. 4.10 and Fig. 4.11 show the density profiles after 100 ms of free expansion calculated with the TDCGPE (solid lines) and with the generalized scaling approach (dashed lines) for the cases (i) to (v) (see table 4.1) for 10^5 and 10^6 atoms in each species, respectively. In both figures, the first row depicts the case number (i) of two independent BECs, used as a reference. As already stated previously for the ground states, it can be noticed that at the domain separation the density predicted by the scaling approach may become discontinuous.

In the cases (ii) and (iii) (second and third row), where the inter-species scattering length is negative, the two species attract each other and this attraction limits the expansion velocity of the two clouds compared to the case number (i) where the inter-species interaction has been set to zero. This behavior is highlighted in Fig. 4.12, where we show the evolution of the characteristic size of the two clouds calculated with the two models.

In the case of the GPE simulation, the characteristic size evolution read as

$$\Delta R^2(t) = \langle \psi(\vec{r}, t) | r^2 | \psi(\vec{r}, t) \rangle - \langle \psi(\vec{r}, t) | r | \psi(\vec{r}, t) \rangle^2. \quad (4.51)$$

Because of the different domains the total characteristic size in the TF approximation in the case of two domains and following the notation of the section 4.3 and sec:4.4 is

given by

$$\Delta R_1^2(t) = \iiint_{r=0}^{r=\lambda_{1,r}^D(t) \cdot R_B} r^4 \sin(\theta) \frac{n_1^D(r/\lambda_{1,r}^D(t), 0)}{(\lambda_{1,r}^D(t))^3} d\theta d\phi dr, \quad (4.52a)$$

$$\begin{aligned} \Delta R_2^2(t) = & \iiint_{r=0}^{r=\lambda_{1,r}^D(t) \cdot R_B} r^4 \sin(\theta) \frac{n_2^D(r/\lambda_{2,r}^D(t), 0)}{(\lambda_{2,r}^D(t))^3} d\theta d\phi dr \\ & + \iiint_{r=\lambda_{1,r}^D(t) \cdot R_B}^{r=\lambda_{2,r}^S(t) \cdot R_C} r^4 \sin(\theta) \frac{n_1^S(r/\lambda_{1,r}^S(t), 0)}{(\lambda_{1,r}^S(t))^3} d\theta d\phi dr, \end{aligned} \quad (4.52b)$$

for the first and second species. The limits of the integral highlight only the radial component for clarity and follow the domain definition of section 4.4.

It can be noticed that the initial shape of the condensates is conserved and that the density profiles described by the scaling approach overlap relatively well with the ones predicted by the TDCGPE. During the expansion, the mean-field interaction energy decreases, and both clouds become dilute. The impact of the atom number is shown in Fig. 4.10 and Fig. 4.11, where, as expected, the increase of the atom number reduces the significance of the kinetic energy term neglected in the scaling approach.

In the cases (iv) and (v) where the inter-species scattering length is positive, the two species repel each other. The increase of the repulsion leads ^{41}K to constrain ^{87}Rb closer to $r = 0$ and the size of the overlapping domain is smaller in case (v) than in case (iv). At the same time, ^{41}K is pushed out of the overlapping domain. This phenomenon is highlighted by the decrease of the amplitude of the density probability distribution at $r = 0$ and consequently to the increase of the density probability in the outer domain, *i.e.* at $R_B < r < R_C$. The transfer of ^{41}K from the overlapping to the outer domain comes with an amplitude oscillation, recently observed in [329] in the immiscible regime. The shape of the distribution is not conserved in the overlapping domain and the scaling approach, which supposes TF parabolic shapes, fails to describe this oscillation, keeping only a kind of averaged behavior.

In each case, Fig. 4.12 shows that the characteristic sizes predicted by the scaling approach during the expansion of both clouds are in rather good agreement with the exact calculation. This is a clear indication of the interest of such scaling approaches which are numerically much less expensive than solving coupled time-dependent Gross-Pitaevskii equations, but nevertheless this approach is not always sufficient to reconstruct accurately the shape of the density profile for both species.

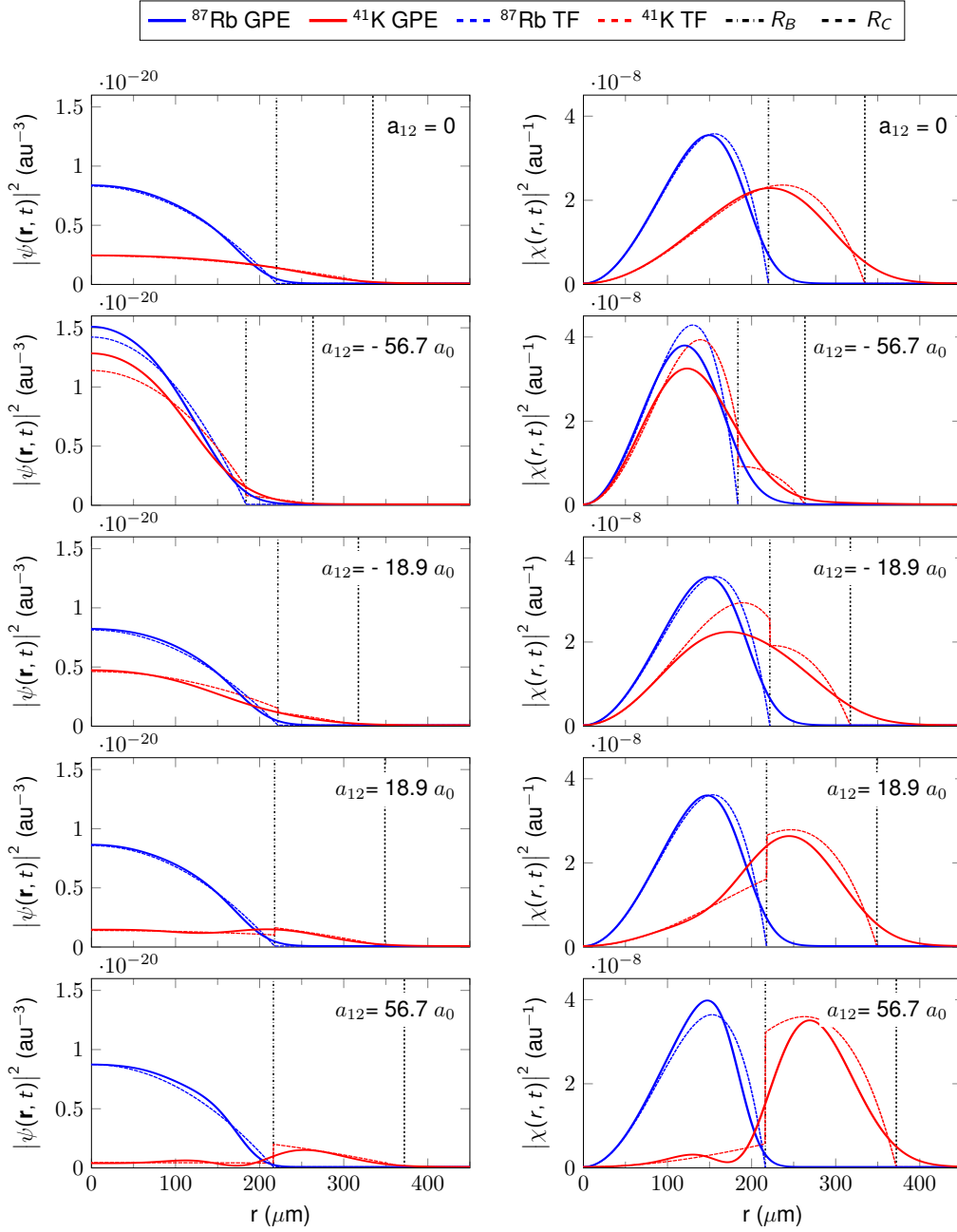


Figure 4.10: Free expansion calculation. Representation of the density distributions for the cases (i): First row to (v): Last row, (see table 4.1), for 10^5 atoms in each species after 100 ms of free expansion. The left and right panels show the density distributions in two representations. The blue and red lines represent the distribution of ^{87}Rb and ^{41}K calculated with the TDCGPE (solid line) and with the scaling approach (dashed line). The harmonic traps are isotropic and their frequencies are respectively $\omega_{87\text{Rb}} = 2\pi \cdot 50$ Hz and $\omega_{41\text{K}} = (m_{87\text{Rb}}/m_{41\text{K}})^{1/2} \cdot \omega_{87\text{Rb}}$

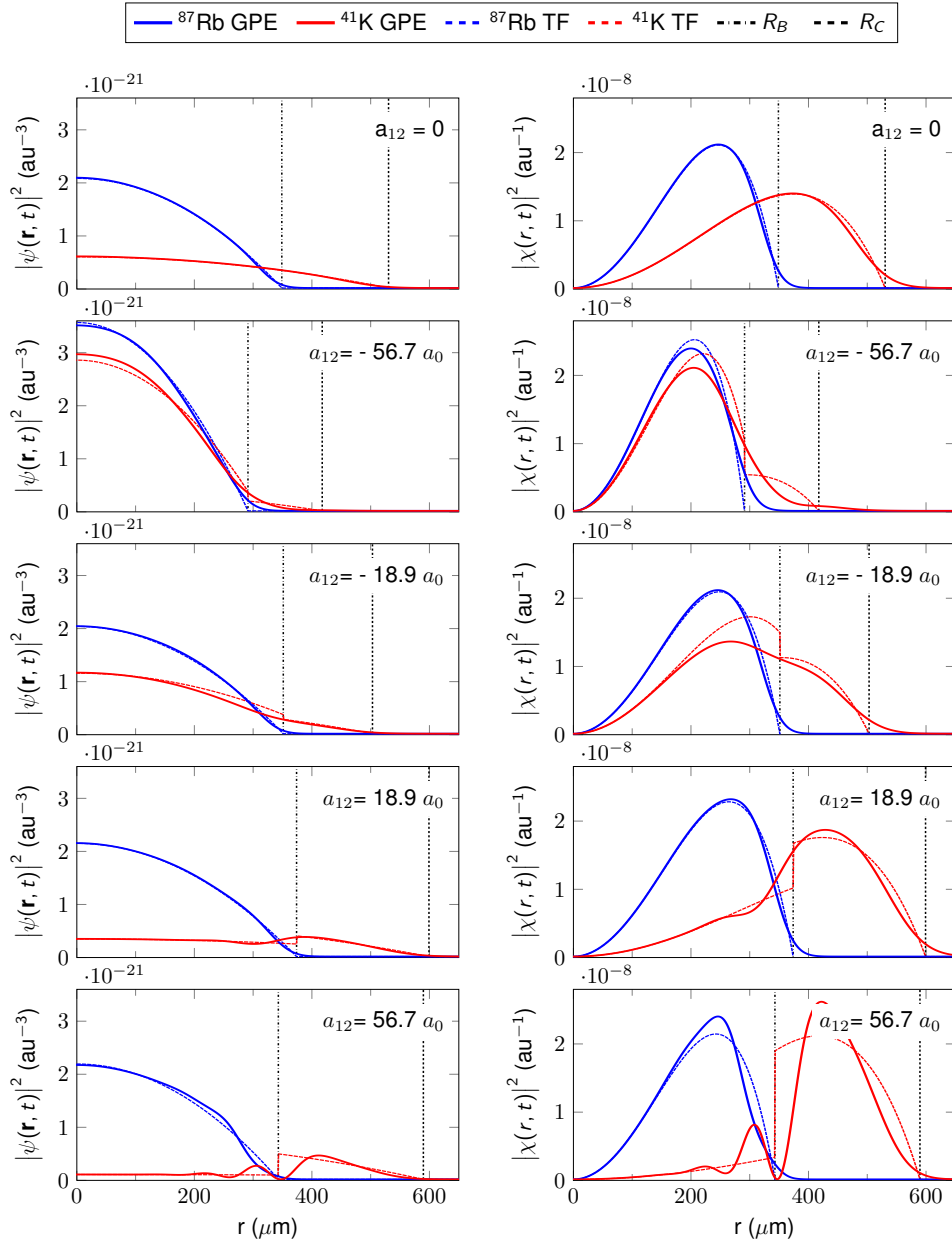


Figure 4.11: Free expansion calculation. Representation of the density distributions for the cases (i): First row to (v): Last row, (see table 4.1), for 10^6 atoms in each species after 100 ms of free expansion. The left and right panels show the density distributions in two representations. The blue and red lines represent the distribution of ^{87}Rb and ^{41}K calculated with the TDCGPE (solid line) and with the scaling approach (dashed line). The harmonic traps are isotropic and their frequencies are respectively $\omega_{87\text{Rb}} = 2\pi \cdot 50$ Hz and $\omega_{41\text{K}} = (m_{87\text{Rb}}/m_{41\text{K}})^{1/2} \cdot \omega_{87\text{Rb}}$

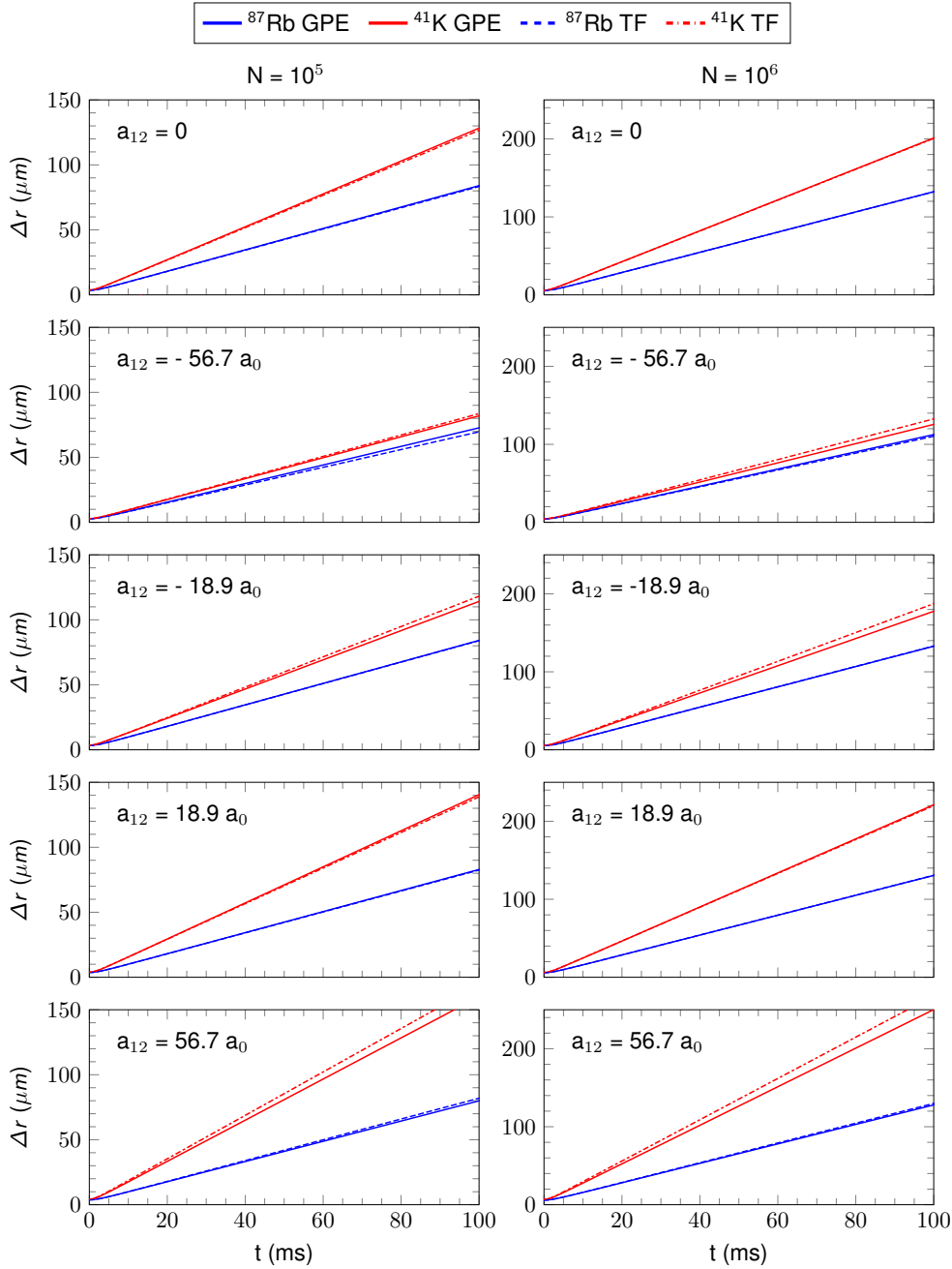


Figure 4.12: Characteristic size expansion. Evolution of the characteristic size of the two clouds during 100 ms of free expansion for the cases (i):First row to (v):Last row, (see table 4.1), for different atom numbers: 10^5 (left side) and 10^6 (right side). The blue and red lines represent the sizes of the ^{87}Rb and ^{41}K condensates calculated with the TDCGPE (solid line) and with the scaling approach (dashed line). The harmonic traps are isotropic and their frequencies are respectively $\omega_{87\text{Rb}} = 2\pi \cdot 50 \text{ Hz}$ and $\omega_{41\text{K}} = (m_{87\text{Rb}}/m_{41\text{K}})^{1/2} \cdot \omega_{87\text{Rb}}$

4.5.3 Application to dual-species twin atomic lensing to the pico-Kelvin level

We tackle now the expansion damping for two interacting species, which is instrumental for a dual atom interferometer testing the UFF. At few tens of pK expansion energy, it is possible to realize a several-second atom interferometer with exquisite phase sensitivity. We also focus on the density distributions of the two species when the different pulses are applied in order to limit detrimental effects. For this purpose and in order to stay close to experimental configurations we consider the case of 10^5 atoms in both condensates with a tunable inter-species scattering length [340, 341, 357]. Up to now the external traps are defined by $\omega_{87\text{Rb}} = 2\pi \cdot 10 \text{ Hz}$ and $\omega_{41\text{K}} = (m_{87\text{Rb}}/m_{41\text{K}})^{1/2} \cdot \omega_{87\text{Rb}}$.

We consider the case where, in presence of a Feshbach resonance, the inter-species scattering length is zero, case (i), and the case where the Feshbach magnetic field is off, the inter-species scattering length being then + 163 a.u., case (vii) [339]. In this last case, the miscibility condition is not respected anymore and both species repel each other more than they repel themselves. Such a situation leads the density oscillations that propagate during the free expansion, as discussed in the previous section and shown in Fig. 4.10 and Fig. 4.11. In the context of precision measurements, wave-front aberrations due to the quality of the optics lead to detrimental effects and important systematics in the phase measurement [86, 185, 358]. This problem is partially circumvented with techniques based on deformable mirrors to compensate the wave-front aberration [185]. It is, nevertheless, a leading systematics in precision tests, more particularly a UFF test. A distorted density profile of the atoms would similarly lead to dephasing since the atoms of the two species explore different wave-front aberrations at different times.

Following the STE-QUEST satellite mission requirements and based on the simulations of the TDCGPE, we propose a sequence of free expansion and atomic lenses for the dual-species in presence of a Feshbach magnetic field to insure a low expansion temperature for both clouds and the conservation of the shape ($a_{12} = 0$). We then study the impact of the size and shape distribution of the mixture when the Feshbach field is turned off during the last expansion step dedicated to the interferometry sequence.

The result of the study is shown in Fig. 4.13. This figure shows the impact of a sequence where the clouds are initially confined in an isotropic harmonic trap of 10 Hz and 14.56 Hz respectively for ^{87}Rb and ^{41}K in presence of the Feshbach field with $a_{12} = 0$. The sequence consists in a series of release and atomic lens to collimate the two species in presence of the Feshbach magnetic field. At $t = 0$ the trap is turned off,

and the clouds expand for 50 ms. The trap is then turned back on to its previous value during $\Delta t = 2.3$ ms (represented by the vertical dashed line in panel (e)). The sequence is repeated a second time with a free expansion of 400 ms and a second lens of duration $\Delta t = 0.3$ ms (represented by the vertical dash-dotted line). The sequence proposed in Fig. 4.13 has been optimized in the case (i), where α_{12} is fixed to zero, to limit the temperature expansion of the two BECs. This case depicts the ideal case where the two species do not interact with each other and where the density shape is conserved in time. This configuration is used as a reference to describe the impact of the inter-species interactions in the following.

The panels (a) to (d) show the density distributions 5 s after the second lens. In panel (a), the Feshbach magnetic field is never switched off, while it is switched off after 1 ms in panel (b), after 300 ms in panel (c), and after 1 s in panel (d). The different characteristic size evolution, Δr , are shown in panel (e) where the colored solid, dashed, dotted and dash-dotted lines respectively denote the cases (a) to (d). The blue and red colors respectively denote the two species, ^{87}Rb and ^{41}K . The corresponding velocities and expansion temperatures are summarized in Table 4.2. The sequence proposed here follows the expansion requirements to test the Universality of Free Fall at the 10^{-15} accuracy level [41]. Panels (b) to (d) show the impact of the strength of the inter-species interaction on the two atomic density distributions, as compared to the case (a) where this interaction disappears.

When the Feshbach field is turned off after 1 ms, the inter-species mean-field energy is not negligible and the repulsion between the two species deforms the density distribution of ^{87}Rb , as shown in panel (b). In 3D, instead of the constant filled sphere we can expect from panel (a), the density distribution of ^{87}Rb is deformed with time to approach a hollow sphere shape 5 s after the final release. This problem directly originates from the interaction between the two species and can be solved if the Feshbach magnetic field is kept on for some time after the second lens. Panels (c) and (d) show the impact of these different durations, 300 ms and 1 s respectively. Because the sequence induces a small focus of the ^{41}K cloud after the second lens (see panel (e)), the total mean-field energy is not reduced enough after 300 ms of free expansion and in this case, 5 s after the second lens the density profile is still very close to the case shown in panel (b). Due to the extremely low expansion temperature of the two species (tens of pK), even after 1 s post-lens free expansion, a small impact of the inter-species repulsion is still noticeable, as shown in panel (d).

Panel (e) highlights the impact of the mean-field energy on the characteristic sizes

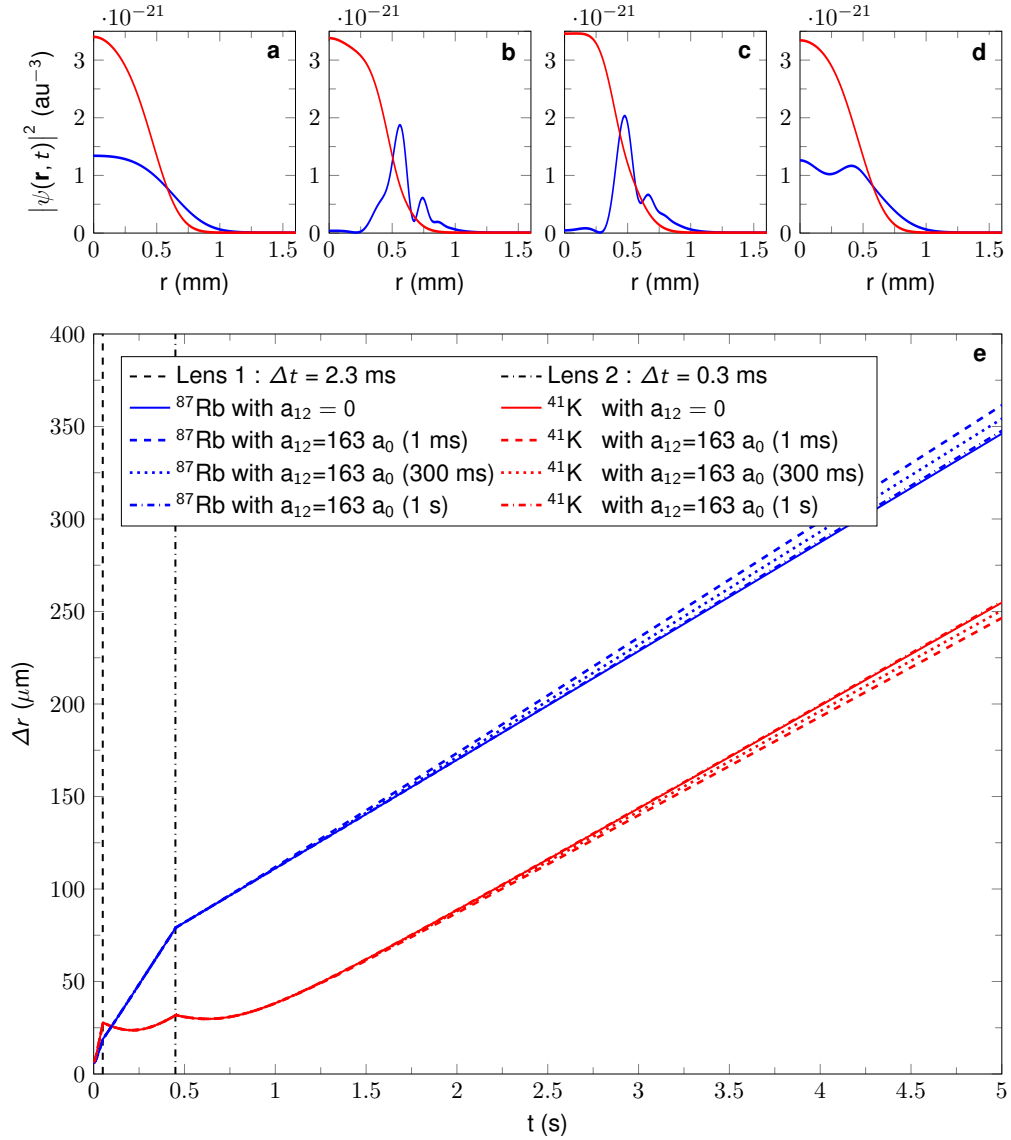


Figure 4.13: Dual species twin atomic lens. (a) to (d): Density distributions 5 s after the second lens when the Feshbach field is switched off at different times: (a) no switch-off ; (b) 1 ms after the second lens ; (c) 300 ms after the second lens ; (d) 1 s after the second lens. (e) Result of the dual-species twin atomic lens sequence in terms of density size Δr . The solid, dashed, dotted and dash-dotted lines respectively correspond to the cases (a) to (d), respectively. A first free expansion of 50 ms is followed by a first lens of duration $\Delta t = 2.3$ ms, and then by a second free expansion stage of 400 ms during which the two species expand before a final lens of duration $\Delta t = 0.3$ ms which controls the expansion rate of the two ensembles. The harmonic traps are isotropic and their frequencies are respectively $\omega_{87\text{Rb}} = 2\pi \cdot 10$ Hz and $\omega_{41\text{K}} = (m_{87\text{Rb}}/m_{41\text{K}})^{1/2} \cdot \omega_{87\text{Rb}}$

		$a_{12} = 163 a_0$ after:			Ideal case $a_{12}=0$
		1 ms	300 ms	1 s	-
^{87}Rb	Δv_{1D} ($\mu\text{m/s}$)	62.9	61.2	59.3	58.8
	T_{1D} (pK)*	41.4	39.2	36.8	36.2
^{41}K	Δv_{1D} ($\mu\text{m/s}$)	53.5	54.5	55.9	55.7
	T_{1D} (pK)*	14.1	14.6	15.4	15.3

Table 4.2: Expansion speeds and temperatures expansion of the ^{41}K and ^{87}Rb BECs after the second lens for different configuration shown in the figure Fig. 4.13. The different temperatures are calculated in 1D Cartesian following : $k_B T_{1D} = m \Delta v_{1D}^2$. The Feshbach magnetic field is switched off at different timing after the second lens, 1 ms, 300 ms and 1 s. The last column represents the case, considered ideal, where the two BECs do not interact with each other, $a_{12}=0$.

of the BECs. A direct comparison between the solid and dashed lines indicates a faster (respectively slower) expansion velocity of the ^{87}Rb cloud (respectively ^{41}K) in the case where the Feshbach magnetic field in turn off 1 ms after the final release, compared to the ideal case where a_{12} is always zero. The different expansion velocities can be found in Table 4.2. This behavior is due to the repulsive inter-species force. On one hand the outer species, here ^{87}Rb , is repelled by the inner species, here ^{41}K . The inner species thus acts as a repulsive potential for the outer species and increases its expansion speed. On the other hand, the outer species repels the inner one and acts an external repulsive potential which constrains the expansion of the inner species. For a configuration where the Feshbach field is turned off later, at 1 s for instance, the reduction of the mean-field energy reduces this effect and, as expected, the size evolution of the two species is closer to the ideal case where $a_{12} = 0$.

These different behaviors are shown in more detail in Fig. 4.14. The characteristic size 2 s after the second lens of the ^{41}K and ^{87}Rb clouds is respectively around $170 \mu\text{m}$ and $90 \mu\text{m}$ while initially being $79 \mu\text{m}$ and $32 \mu\text{m}$ at the end of the second lens. After 2 s, the mean-field interaction energy of both species is therefore reduced by more than an order of magnitude and, as a consequence, the inter-species mean-field is also approximately reduced by one order of magnitude. In Fig. 4.14 a direct comparison of the density

distributions for the cases where the Feshbach magnetic field is turned off after 1 ms (first row) and after 2 s (second row) of free expansion after the second lens is shown for different free expansion times referred as times of flight (TOF) in the different panels. In each case, just after the lens the two species have the same density distributions as seen in panels (a) and (e), which are identical. The panels (b,f), (c,g) and (d,h) show the density distribution of the two species after 2 s, 6 s and 10 s respectively. While the shape of the ^{87}Rb BEC is deformed in the first row, in the second row its shape is conserved and keeps its desired spherical filled form.

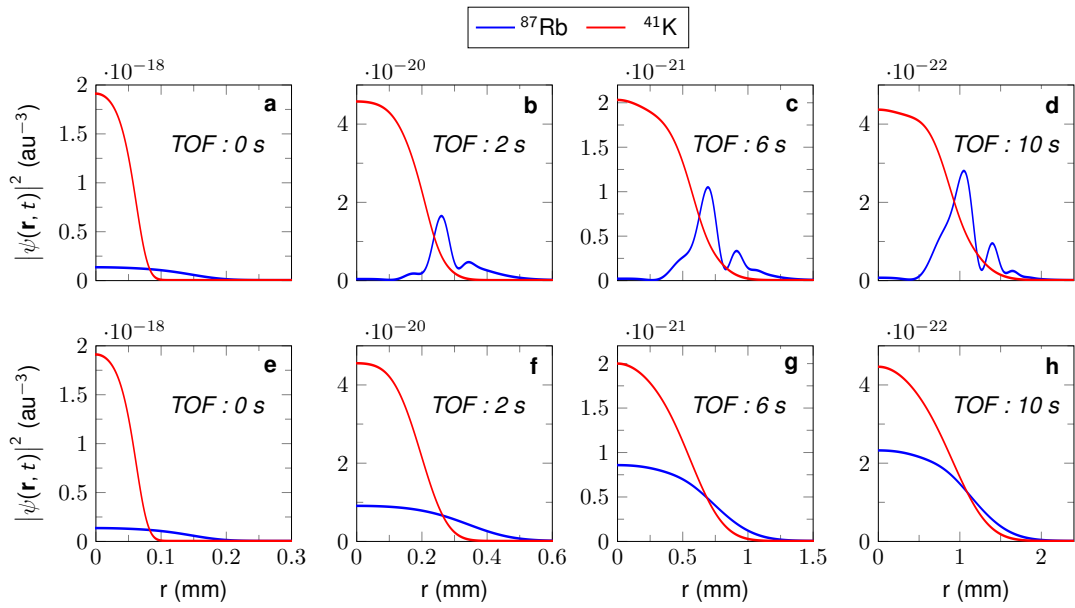


Figure 4.14: Time evolution of the density distribution of the two species when the Feshbach magnetic field is switch off 1 ms (first row) and 2 s (second row) after the second lens. Density distributions of the two species at the end of the second lens: (a,e) and 2 s: (b,f), 6 s: (c,g) and 10 s: (d,h) after the lens.

To summarize, in the same manner that non-ideal optics induce wave-front aberrations and detrimental systematics in the phase measurement of an atom interferometer, a significant change of the density profile with time will induce detrimental systematics. In this case the sensitivity of the measurement may not benefit anymore of long time interferometers. Low expansion temperatures is not the only key point of an atom interferometer. In cases where the clouds are dilute enough, with sizes here of some hundred of microns, the repulsive strength is negligible and the shape of the density distribution remains constant over seconds. Engineering sequences where the inter-species mean-field energy vanishes is then required to perform long time atom interferometers.

In the context of long time atom interferometers, atomic lenses [186] is a key tool widely used in the cold atom community [244, 291]. Until today, in each case the collimation effect is reached by the action of an electric field, of a magnetic field or even of a combination of both. A big limitation lies in the shape of the trap. To perfectly collimate an atomic ensemble, thermal or BEC, harmonic traps are required for symmetry reasons. In chapter 3, the impact of non-harmonic traps was shown in phase space. Out of the results shown in Fig. 4.13, it seems feasible to engineer a sequence to protect the shape of the inner species through its interaction with the second one. In Fig. 4.14 it can be noticed that the shape of the inner species is conserved and keeps a spherical filled density over 10 s of expansion, as shown in panels (a-d). Most of the traps, atom chip or dipole traps, can be considered harmonic at their minimum over few hundred of microns size. Nevertheless, as shown in chapter 2 and the present chapter, the collimation effect can be obtained only after the transfer of the initial mean-field energy to kinetic energy. This brings the BEC to some hundred of microns in size where the trapping potential is usually far from being harmonic.

4.6 Conclusion

While recent proposals suggest BEC mixtures as a source for dual-species matter-wave atom interferometers [41], the necessity to control both the expansion rates and the density profiles requires specific sequences of atomic lensing and tunable interactions [341]. In this chapter I compared the results of the ground state calculation with two different models and I showed a good correspondence between the simulation of the dual-species Gross-Pitaevskii equation and the Thomas-Fermi approximation in the case of two distinct and three distinct domains of existence of the condensates. In this chapter I also provided an extension of the works proposed by Y. Castin and R. Dum [229] and by Y. Kagan, E. L. Surkov and G. V. Shlyapnikov [230] to describe the expansion of a BEC mixture. The derivation was provided in the general case and then applied in the case of an isotropic trap with different atom numbers and inter-species scattering lengths. The different cases were compared to the time dependent coupled Gross-Pitaevskii equations and showed a good agreement for large atom numbers. A sequence for dual-species atom interferometers was then found and proved the possibility to limit the expansion rate of two interacting BECs of vastly different elements to few pK as required by the most challenging UFF tests. A description of the impact of the inter-species scattering length on the density profile was shown and discussed in the context of atom interferometry

CHAPTER 4. OPTIMIZED MANIPULATION OF A DEGENERATE BOSONIC MIXTURE

where the expansion rate has to be controlled through a twin lens sequence associated with tunable interactions.

CONCLUSION AND PERSPECTIVES

This thesis is dedicated to engineer quantum states required by precision matter-wave atom interferometry. Different control techniques such as Shortcut-To-Adiabaticity (STA), developed in Chapter 2, and Optimal Control Theory (OCT), developed in Chapter 3, have been presented within a clear experimental context. Both techniques show the possibility to control the position and velocity of one or two atomic clouds very precisely to the μm and $\mu\text{m.s}^{-1}$, respectively.

The theoretical study of delta-kick collimation and non-adiabatic trap decompression techniques have shown the possibility to limit the expansion energy of one species or a degenerate mixture down to the pico-Kelvin regime in Chapters 2 and 4.

In the context of optimizing the duty-cycle of atom interferometry experiments, the total required time, in each configuration, is taken into account and suggestions to improve on it were made.

As introduced at the beginning of this thesis, tests of the Universality of Free Fall (UFF) with an accuracy at the level of 10^{-15} [40, 41] rely on one hand on the possibility to precisely define the differential position and velocity of the two test masses and on the other hand on the control of the size dynamics of the two species. The sizes of the different clouds have to expand with a maximum velocity of $100 \mu\text{m.s}^{-1}$, equivalent to an expansion temperature of tens of pico-Kelvins. It is only in the configuration where a fast control of the classical and quantum motion is simultaneously present for the two species that spurious phase shifts in the differential signal (coming from residual mean-field energy, wave-front aberrations effects) can be avoided.

The aim of Chapter 2 was to engineer fast transport ramps to control the final classical degrees of freedom of Bose-Einstein condensates. This study was initiated by experimental requirements from the Quantus-2 project [244, 251, 252]. The proximity of the BEC to the atom chip surface leads to detrimental effects, such as interactions with the chip surface, atomic losses because of current fluctuations in high trap frequencies [254] and fast BEC expansion rates. All these reasons required the design of fast and controlled transport ramps. The gauging of a theoretical atom chip model developed by the Quantus-2 experimental team over the past four years gave us the possibility to design a specific ramp corresponding to the desired final classic state. This theoretical study was published in Ref. [188].

In Chapter 3, Optimal Control Theory (OCT) was applied to control the transport of two non-interacting species. This study was initiated during my internship at Stanford in the group of M. Kasevich to provide some answer to the problem of a combined input state preparation in the 10-meter long tower [37]. Due to the complexity generated by the presence of two species, the reverse engineering technique shown in Chapter 2 does not work anymore. Optimal Control Theory is then required. The evolution of the control parameter is in agreement with the requirements of the experiment. It has been designed to transport over a few millimeters the two atomic species and to bring them simultaneously at rest in a lower frequency trap configuration. In the case presented here, a smooth change of the magnetic field is required and the implementation of a smooth evolution at the starting and ending point is proposed. In the future, more elaborate techniques such as high frequency filtering could give the possibility to avoid rapid changes of the control parameter during the transport.

One of the real advantage of OCT is the possibility to design optimized and robust sequences of quantum state manipulation. The up-coming Maius-2 sounding rocket mission, with an expected launch at the end of 2020, is designed for a mixture of species on board, Potassium and Rubidium. Experimentally, during the flight the power of the batteries are expected to decrease with time. In the same way the temperature change can influence the efficiency of the different experiments foreseen. New technologies and developments are thus required [254]. A ramp optimized for a specific set of parameters and temperature is therefore subject to change and as a consequence the result of a specific input state preparation too. OCT is a very interesting tool in this context. In the same way as for the control of two species in Chapter 3, OCT can engineer a ramp to transport BECs from different initial positions in different trap configurations to given final positions. Each of these initial configurations, defined by a given set of battery

powers or other parameters subject to change with time, would then be optimized with *a single ramp*. Following this idea, the robustness of the control becomes a key point. It is therefore interesting to study the limitations of the achieved transport and their consequences for the experiment during the flight.

In the broader context of cold atom physics in microgravity, NASA’s Physical Science Research Program has selected five proposals to run experimental sequences on the multi-user facility “Cold Atom Lab” (CAL) on the International Space Station (ISS). The CAL experiment provides for the first time a persistent quantum gas platform in microgravity. The multi-user facility was developed and is currently operated by NASA’s Jet Propulsion Laboratory [359].

Within the “Consortium for Ultracold Atoms in Space” led by Nicolas Bigelow from the University of Rochester, different proposals to study cold atoms have been made. Aiming to reach the “Coldest Spot in the Universe”, Shortcut-To-Adiabaticity (STA) protocols are designed to engineer robust transport ramps in a similar way as described in Chapter 2 [360]. Different designs accounting for low expansion rates of the BECs are currently being tested. Until now, measurements have been made with the ramp we have provided both to the CAL and Quantus-2 experiments [188]. Following the research line of the Quantus-2 experiment, delta-kick collimation [165, 186, 187] is the next step to be implemented. The sequence proposed is very close to the one described in Chapter 2 and already implemented in the Quantus-2 experiment. Until now the minimum expansion temperature of the BEC observed after release is lower than 100 pK in Quantus-2 [244, 251, 252], and similar results are expected on the ISS. One of the particularities of the design of CAL is the possibility to operate with Rubidium and Potassium simultaneously. This gives the possibility to study two-components superfluids and to test the Universality of Free Fall with different atomic species. The optimal control theory tools developed in Chapter 3 are of particular interest in the context of one or two components superfluids. After a description of different two-components regimes, a generalized semi-classical approach was proposed in Chapter 4. This generalization is based on the idea of independent domains where in some regions of space the two BECs can overlap and in other regions of space only one BEC is present. The semi-classical approach describes the evolution of the two components in their respective domains as well as the evolution of the domain sizes. The proposed approach assumes the conservation of the shape of the two condensates in their respective domains.

In a recent paper, following the same goals as in Chapter 2, we have shown how OCT can engineer fast transport ramps to bring a degenerate quantum gas from one

equilibrium state to another one far from the chip surface [257]. In the case of two components in interaction, the results obtained in Chapter 3 for two non-interacting cold ensembles are not sufficient and need to be generalized. This study can be divided in different parts with, first of all the study of two classical particles with contact interactions. Then, in addition to this classical motion, the quantum motion could be described with the semi-classical approach proposed in Chapter 4. This approach, based on the definition of different domains, remains valid only if the number of domains and if the shape of the condensates are conserved. A more rigorous approach would be the numerical implementation of OCT directly on the evolution of the condensate wave functions evolving according to the time-dependent Gross-Pitaevskii equation [206, 281]. In this case, highly demanding complex numerical simulations are required and the convergence of the OCT algorithm highly depends on the initial test ramp. In each case the algorithm optimizes the evolution of the control parameter until the desired state is obtained. This initial test ramp could therefore be the one obtained using the simpler scaling approach of Chapter 4, based on the different domain definitions. The implementation of the different sub-parts thus brings the possibility to initiate the algorithm with a pre-optimized solution. Starting with a solution closer to the desired one can dramatically reduce the number of iteration steps and the calculation time of a specific sequence.

The application to dual-species twin atomic lensing developed in Chapter 4 proposed a solution to control the expansion temperature of a mixture of BECs. In this study, the trap is considered with a spherical symmetry. On one hand, the high complexity of atom chip structures gives the possibility to find specific configurations where the trap frequencies are identical in all directions. On the other hand, the low expansion rate of the two BECs after the lens require a pre-expansion sequence to release the mean-field energy [165]. The sizes of the two BECs are therefore increased at the end of these steps and the impact of the anharmonicities of the trap has to be taken into account. In a similar context, the Quantus-2 setup has experimentally demonstrated the possibility to collimate a Rubidium 87 BEC of some 10^5 atoms at an expansion temperature lower than 100 pK [244, 251, 252]. The results and the understanding of the impact of the real trap configuration are still under study at the moment in our group in Hanover. Even though after the expansion the traps are not harmonic anymore, the results obtained with the Quantus-2 experiment show high collimation capabilities but with non-symmetric density shapes [244]. The impact of the interaction between the two species discussed at the end of Chapter 4 on the shape deformation of the two BECs adds

to the non-harmonic potential effects at the DKC step used to limit the size expansion. The density distributions of the BECs are affected on one side by the inter-species mean-field energy at small sizes and on the other side by the anharmonicities of the trap for increased sizes. For each specific experiment a trade-off has therefore to be found.



NUMERICAL SIMULATION OF THE LINEAR SCHRÖDINGER EQUATION

The time evolution of an initial wave function $\psi_0(\mathbf{r})$ is described by the evolution operator defined as

$$\hat{U}(t) = \exp\left(-i\frac{\hat{H}t}{\hbar}\right), \quad (\text{A.1})$$

where \hat{H} , the Hamiltonian of the system, is a sum of the kinetic operator \hat{T} and the potential operator \hat{V} , where the wave function at time t reads as

$$\psi(\mathbf{r}, t) = \hat{U}(t) \psi_0(\mathbf{r}). \quad (\text{A.2})$$

In this thesis, the numerical results based on the GPE were obtained using the split-operator method (SOM) [361, 362] in combination with the Fourier transformation technique. At each time step Δt , since the kinetic and potential operators do not commute, the split operator method approximates the evolution operator $\hat{U}(\Delta t)$. At first order, the evolution operator for a single time step reads as follows

$$\hat{U}(\Delta t) = \exp\left(-i\frac{\hat{T}\Delta t}{\hbar}\right) \exp\left(-i\frac{\hat{V}\Delta t}{\hbar}\right) + O(\Delta t^2), \quad (\text{A.3})$$

where $O(\Delta t^2)$ represents the error made at each time step. In the work presented in this thesis, we have used the second order split-operator method, in which the evolution operator is given for a single time step propagation by

$$\hat{U}(\Delta t) = \exp\left(-i\frac{\hat{V}\Delta t}{2\hbar}\right) \exp\left(-i\frac{\hat{T}\Delta t}{\hbar}\right) \exp\left(-i\frac{\hat{V}\Delta t}{2\hbar}\right) + O(\Delta t^3), \quad (\text{A.4})$$

where the error is now proportional to Δt^3 . The separation of the kinetic operator and the potential operator is of great numerical advantage because they are respectively diagonal in momentum and in real space. To ensure a fast numerical simulation, the technique adopted consists then in applying a combination of the appropriate operator and of a Fourier transform of the wave function, where the Fourier transform is operated by using a Fast Fourier Transform (FFT) algorithm. Starting with an initial test wave function defined in real space, the time evolution is given by the sequence

$$\psi(\mathbf{r}, t + \Delta t, 1) = \exp\left(-i \frac{\hat{V} \Delta t}{2\hbar}\right) \psi(\mathbf{r}, t, 0), \quad (\text{A.5a})$$

$$\psi(\mathbf{k}, t + \Delta t, 2) = \mathcal{F} [\psi(\mathbf{r}, t + \Delta t, 1)], \quad (\text{A.5b})$$

$$\psi(\mathbf{k}, t + \Delta t, 3) = \exp\left(-i \frac{\hat{T} \Delta t}{\hbar}\right) \psi(\mathbf{k}, t + \Delta t, 2), \quad (\text{A.5c})$$

$$\psi(\mathbf{r}, t + \Delta t, 4) = \mathcal{F}^{-1} [\psi(\mathbf{k}, t + \Delta t, 3)], \quad (\text{A.5d})$$

$$\psi(\mathbf{r}, t + \Delta t, 5) = \exp\left(-i \frac{\hat{V} \Delta t}{2\hbar}\right) \psi(\mathbf{r}, t + \Delta t, 4), \quad (\text{A.5e})$$

where \mathcal{F} and \mathcal{F}^{-1} are the forward and backward Fourier transforms and the indices [0-5] in the wave function denote the different numerical steps. The total propagation of the wave function is obtained by repeating the previous sequence, *i.e.* by replacing $\psi(\mathbf{r}, t, 0)$ in Eq. (A.5a) by $\psi(\mathbf{r}, t, 5)$ of Eq. (A.5e).

Two types of propagations can be distinguished: Imaginary time propagation [363, 364] and real time propagation [361, 362]. The imaginary time propagation technique consists in changing the variable (t) to $(-it)$ in the previous set of equations. In the case of imaginary time propagation, the evolution operator is real and leads after convergence to the lowest energy state of the system [363, 364]. In the protocol, to ensure the conservation of the norm after each time step, the wave function is re-normalized to 1 at the end of each iteration described by Eq. (A.5). In the case of a real time step propagation, the evolution operator is complex and the dynamics of the wave function in a time dependent potential can be described by the steps given above in the general case, for t real.

Remark

In the case of the non-linear Schrödinger equation, one can numerically rewrite the potential term, V , as a sum of the external potential V_{ext} and the interaction potential $N g |\psi(\mathbf{r}, t)|^2$ where the density, $|\psi(\mathbf{r}, t)|^2$, is evaluated at the previous time step. In this

case the equation Eq.A.1 does not hold anymore but one can numerically follow the steps of propagation described in Eq.A.5. Another technique to propagate the solution of the non-linear Schrödinger equation can be found in [365].

BIBLIOGRAPHY

- [1] A. Einstein.
[Die Grundlage der allgemeinen Relativitätstheorie.](#)
Annalen der Physik, 354(7):769–822, 1 1916.
(page 2).
- [2] A. Einstein.
[Über Gravitationswellen.](#)
Sitzungsberichte der Königlich Preußischen Akademie der Wissenschaften (Berlin),
Seite 154-167., 1918.
(page 2).
- [3] C.W. Misner, K.S. Thorne, and J.A. Wheeler.
[Gravitation.](#)
1970.
(page 2).
- [4] W. Heisenberg.
[Über quantentheoretische Umdeutung kinematischer und mechanischer Beziehungen.](#)
Zeitschrift für Physik, 33(1):879–893, Dec 1925.
(page 2).
- [5] E. Schrödinger.
[Quantisierung als Eigenwertproblem.](#)
Annalen der Physik, 385(13):437–490, 1 1926.
(page 2).
- [6] D. Bohm.
[Quantum theory.](#)
Englewood Cliffs, N.J. : Prentice-Hall, 1959.

- (page 2).
- [7] A. Einstein.
[Über einen die Erzeugung und Verwandlung des Lichtes betreffenden heuristischen Gesichtspunkt.](#)
Annalen der Physik, 322(6):132–148, 1905.
(page 2).
- [8] A. Einstein.
[Über die von der molekularkinetischen Theorie der Wärme geforderte Bewegung von in ruhenden Flüssigkeiten suspendierten Teilchen.](#)
Annalen der Physik, 322(8):549–560, 1905.
(page 2).
- [9] A. Einstein.
[Zur Elektrodynamik bewegter Körper.](#)
Annalen der Physik, 322(10):891–921, 1905.
(page 2).
- [10] A. Einstein.
[Ist die Trägheit eines Körpers von seinem Energieinhalt abhängig?](#)
Annalen der Physik, 323(13):639–641, 1905.
(page 2).
- [11] C. Kiefer.
[Quantum Gravity.](#)
Oxford University Press, Oxford, 2007.
(pages 2, 3).
- [12] C. Lämmerzahl.
[Mass and Motion in General Relativity.](#)
Vol. 162, ed. L. Blanchet, A. Spallicci, & B. Whiting (Berlin: Springer), 2011.
(page 3).
- [13] W. M. Clifford.
[The Confrontation between General Relativity and Experiment.](#)
Living Reviews in Relativity, 17(1):4, Jun 2014.
(page 3).

- [14] A. A. Michelson and E. W. Morley.
[LVIII. On the relative motion of the earth and the luminiferous Aether.](#)
The London, Edinburgh, and Dublin Philosophical Magazine and Journal of Science, 24(151):449–463, 1887.
(page 3).
- [15] A. A. Michelson.
[The relative motion of the Earth and of the luminiferous ether.](#)
American Journal of Science, 22:120–129, 1881.
(page 3).
- [16] T. S. Jaseja, A. Javan, J. Murray, and C. H. Townes.
[Test of Special Relativity or of the Isotropy of Space by Use of Infrared Masers.](#)
Phys. Rev., 133:A1221–A1225, Mar 1964.
(page 3).
- [17] A. Brillet and J. L. Hall.
[Improved Laser Test of the Isotropy of Space.](#)
Phys. Rev. Lett., 42:549–552, Feb 1979.
(page 3).
- [18] B. Rossi and D. B. Hall.
[Variation of the Rate of Decay of Mesotrons with Momentum.](#)
Phys. Rev., 59:223–228, Feb 1941.
(page 3).
- [19] F. J. M. Farley, J. Bailey, R. C. A. Brown, M. Giesch, H. Jöstlein, S. van der Meer, E. Picasso, and M. Tannenbaum.
[The anomalous magnetic moment of the negative muon.](#)
Il Nuovo Cimento A (1965-1970), 45(1):281–286, Sep 1966.
(page 3).
- [20] D.C. Champeney, G.R. Isaak, and A.M. Khan.
[An ‘aether drift’ experiment based on the Mössbauer effect.](#)
Physics Letters, 7(4):241 – 243, 1963.
(page 3).
- [21] E. Riis, L.-U. A. Andersen, N. Bjerre, O. Poulsen, S. A. Lee, and J. L. Hall.
[Test of the Isotropy of the Speed of Light Using Fast-Beam Laser Spectroscopy.](#)

- Phys. Rev. Lett.*, 60:81–84, Jan 1988.
(page 3).
- [22] T. P. Krisher, L. Maleki, G. F. Lutes, L. E. Primas, R. T. Logan, J. D. Anderson, and C. M. Will.
[Test of the isotropy of the one-way speed of light using hydrogen-maser frequency standards.](#)
Phys. Rev. D, 42:731–734, Jul 1990.
(page 3).
- [23] S. Herrmann, A. Senger, K. Möhle, M. Nagel, E. V. Kovalchuk, and A. Peters.
[Rotating optical cavity experiment testing Lorentz invariance at the \$10^{-17}\$ level.](#)
Phys. Rev. D, 80:105011, Nov 2009.
(page 3).
- [24] R. F. C. Vessot, M. W. Levine, E. M. Mattison, E. L. Blomberg, T. E. Hoffman, G. U. Nystrom, B. F. Farrel, R. Decher, P. B. Eby, C. R. Baugher, J. W. Watts, D. L. Teuber, and F. D. Wills.
[Test of Relativistic Gravitation with a Space-Borne Hydrogen Maser.](#)
Phys. Rev. Lett., 45:2081–2084, Dec 1980.
(page 3).
- [25] M. E. Tobar, P. L. Stanwix, J. J. McFerran, J. Guéna, M. Abgrall, S. Bize, A. Clairon, Ph. Laurent, P. Rosenbusch, D. Rovera, and G. Santarelli.
[Testing local position and fundamental constant invariance due to periodic gravitational and boost using long-term comparison of the SYRTE atomic fountains and H-masers.](#)
Phys. Rev. D, 87:122004, Jun 2013.
(page 4).
- [26] R. v. Eötvös, D. Pekár, and E. Fekete.
[Beiträge zum Gesetze der Proportionalität von Trägheit und Gravität.](#)
Annalen der Physik, 373(9):11–66, 1922.
(page 4).
- [27] R.H. Dicke.
[Gravitation and the Universe.](#)
Science, 2: No. 10, 95-100(Oct. 1966)., 1 1966.

- (page 4).
- [28] V. B. Braginskii and V. I. Panov.
[Verification of equivalence of inertial and gravitational masses.](#)
Sov. Phys. JETP, 34:463–466, 1972.
(page 4).
- [29] E. G. Adelberger.
[New tests of Einstein's equivalence principle and Newton's inverse-square law.](#)
Classical and Quantum Gravity, 18(13):2397–2405, jun 2001.
(page 4).
- [30] S. Schlamminger, K. Y. Choi, T. A. Wagner, J. H. Gundlach, and E. G. Adelberger.
[Test of the Equivalence Principle Using a Rotating Torsion Balance.](#)
Phys. Rev. Lett., 100:041101, Jan 2008.
(page 4).
- [31] T. A. Wagner, S. Schlamminger, J. H. Gundlach, and E. G. Adelberger.
[Torsion-balance tests of the weak equivalence principle.](#)
Classical and Quantum Gravity, 29(18):184002, aug 2012.
(page 4).
- [32] P.G. Roll, R. Krotkov, and R.H. Dicke.
[The equivalence of inertial and passive gravitational mass.](#)
Annals of Physics, 26(3):442 – 517, 1964.
(page 4).
- [33] K. Nordtvedt.
[Equivalence Principle for Massive Bodies. I. Phenomenology.](#)
Phys. Rev., 169:1014–1016, May 1968.
(page 4).
- [34] K. Nordtvedt.
[The Relativistic Orbit Observables in Lunar Laser Ranging.](#)
Icarus, 114(1):51 – 62, 1995.
(page 4).
- [35] J. G. Williams, S. G. Turyshev, and D. H. Boggs.
[Progress in Lunar Laser Ranging Tests of Relativistic Gravity.](#)

- Phys. Rev. Lett.*, 93:261101, Dec 2004.
(page 4).
- [36] P. Touboul, G. Métris, M. Rodrigues, Y. André, Q. Baghi, J. Bergé, D. Boulanger, S. Bremer, P. Carle, R. Chhun, B. Christophe, V. Cipolla, T. Damour, P. Danto, H. Dittus, P. Fayet, B. Foulon, C. Gageant, P. Y. Guidotti, D. Hagedorn, E. Hardy, P. A. Huynh, H. Inchauspe, P. Kayser, S. Lala, C. Lämmerzahl, V. Lebat, P. Leseur, F. Liorzou, M. List, F. Löffler, I. Panet, B. Pouilloux, P. Prieur, A. Rebray, S. Reynaud, B. Rievers, A. Robert, H. Selig, L. Serron, T. Sumner, N. Tanguy, and P. Visser.
[MICROSCOPE Mission: First Results of a Space Test of the Equivalence Principle.](#)
Phys. Rev. Lett., 119:231101, Dec 2017.
(page 4).
- [37] C. Overstreet, P. Asenbaum, T. Kovachy, R. Notermans, J. M. Hogan, and M. A. Kasevich.
[Effective Inertial Frame in an Atom Interferometric Test of the Equivalence Principle.](#)
Phys. Rev. Lett., 120:183604, May 2018.
(pages 4, 5, 6, 13, 53, 63, 81, 132).
- [38] B. Barrett, L. Antoni-Micollier, L. Chichet, B. Battelier, T. Lévèque, A. Landragin, and P. Bouyer.
[Dual matter-wave inertial sensors in weightlessness.](#)
Nat. Commun., 7:13786 EP –, 12 2016.
(pages 4, 5, 6, 63).
- [39] L. Zhou, S. Long, B. Tang, X. Chen, F. Gao, W. Peng, W. Duan, J. Zhong, Z. Xiong, J. Wang, Y. Zhang, and M. Zhan.
[Test of Equivalence Principle at \$10^{-8}\$ Level by a Dual-Species Double-Diffraction Raman Atom Interferometer.](#)
Phys. Rev. Lett., 115:013004, 2015.
(pages 4, 5, 6, 12, 39).
- [40] J. Hartwig, S. Abend, C. Schubert, D. Schlippert, H. Ahlers, K. Posso-Trujillo, N. Gaaloul, W. Ertmer, and E. M. Rasel.
[Testing the universality of free fall with rubidium and ytterbium in a very large baseline atom interferometer.](#)

- New J. Phys.*, 17:035011, 2015.
(pages 4, 5, 6, 12, 13, 18, 39, 63, 131).
- [41] D. N. Aguilera, H. Ahlers, B. Battelier, A. Bawamia, A. Bertoldi, R. Bondarescu, K. Bongs, P. Bouyer, C. Braxmaier, L. Cacciapuoti, C. Chaloner, M. Chwalla, W. Ertmer, M. Franz, N. Gaaloul, M. Gehler, D. Gerardi, L. Gesa, N. Gürlebeck, J. Hartwig, M. Hauth, O. Hellmig, W. Herr, S. Herrmann, A. Heske, A. Hinton, P. Ireland, P. Jetzer, U. Johann, M. Krutzik, A. Kubelka, C. Lämmerzahl, A. Landragin, I. Lloro, D. Massonnet, I. Mateos, A. Milke, M. Nofrarias, M. Oswald, A. Peters, K. Posso-Trujillo, E. Rasel, E. Rocco, A. Roura, J. Rudolph, W. Schleich, C. Schubert, T. Schuldt, S. Seidel, K. Sengstock, C. F. Sopena, F. Sorrentino, D. Summers, G. M. Tino, C. Trenkel, N. Uzunoglu, W. von Klitzing, R. Walser, T. Wendrich, A. Wenzlawski, P. Weßels, A. Wicht, E. Wille, M. Williams, P. Windpassinger, and N. Zahzam.
[STE-QUEST-test of the universality of free fall using cold atom interferometry.](#)
Class. Quant. Grav., 31:115010, 2014.
(pages 5, 6, 12, 39, 63, 100, 125, 129, 131).
- [42] B. Altschul, Q. G. Bailey, L. Blanchet, K. Bongs, P. Bouyer, L. Cacciapuoti, S. Capozziello, N. Gaaloul, D. Giulini, J. Hartwig, L. Iess, P. Jetzer, A. Landragin, E.M. Rasel, S. Reynaud, S. Schiller, C. Schubert, F. Sorrentino, U. Sterr, J. D. Tasson, G. M. Tino, P. Tuckey, and P. Wolf.
[Quantum tests of the Einstein Equivalence Principle with the STE-QUEST space mission.](#)
Adv. Space Res., 55:501, 2015.
(pages 5, 6, 18).
- [43] A. Roura.
[Circumventing Heisenberg’s Uncertainty Principle in Atom Interferometry Tests of the Equivalence Principle.](#)
Phys. Rev. Lett., 118:160401, Apr 2017.
(pages 5, 13, 63).
- [44] G. D’Amico, G. Rosi, S. Zhan, L. Cacciapuoti, M. Fattori, and G. M. Tino.
[Canceling the Gravity Gradient Phase Shift in Atom Interferometry.](#)
Phys. Rev. Lett., 119:253201, Dec 2017.
(pages 5, 13, 63).

- [45] O. Carnal and J. Mlynek.
[Young's double-slit experiment with atoms: A simple atom interferometer.](#)
Phys. Rev. Lett., 66:2689–2692, May 1991.
(page 5).
- [46] V. P. Chebotayev, B. Ya. Dubetsky, A. P. Kasantsev, and V. P. Yakovlev.
[Interference of atoms in separated optical fields.](#)
J. Opt. Soc. Am. B, 2(11):1791–1798, Nov 1985.
(page 5).
- [47] Ch. J. Bordé.
[Atomic interferometry with internal state labelling.](#)
Physics Letters A, 140(1):10 – 12, 1989.
(page 5).
- [48] D. W. Keith, C. R. Ekstrom, Q. A. Turchette, and D. E. Pritchard.
[An interferometer for atoms.](#)
Phys. Rev. Lett., 66:2693–2696, May 1991.
(page 5).
- [49] M. Kasevich and S. Chu.
[Atomic interferometry using stimulated Raman transitions.](#)
Phys. Rev. Lett., 67:181–184, Jul 1991.
(pages 5, 6).
- [50] M. Kasevich and S. Chu.
[Measurement of the gravitational acceleration of an atom with a light-pulse atom interferometer.](#)
Appl. Phys. B, 54(5):321–332, May 1992.
(page 5).
- [51] C. Champenois, M. Büchner, R. Delhille, R. Mathevet, C. Robilliard, C. Rizzo, and J. Vigué.
[Atomic diffraction by a laser standing wave: Analysis using Bloch states.](#)
The European Physical Journal D - Atomic, Molecular, Optical and Plasma Physics,
13(2):271–278, Jan 2001.
(page 5).
- [52] A. Wicht, J. M. Hensley, E. Sarajlic, and S. Chu.

- A Preliminary Measurement of the Fine Structure Constant Based on Atom Interferometry.
Physica Scripta, T102(1):82, 2002.
(page 5).
- [53] H. Müller, S.-W. Chiow, Q. Long, C. Vo, and S. Chu.
A new photon recoil experiment: towards a determination of the fine structure constant.
Appl. Phys. B, 84(4):633–642, Sep 2006.
(page 5).
- [54] R. Bouchendira, P. Cladé, S. Guellati-Khélifa, F. Nez, and F. Biraben.
New Determination of the Fine Structure Constant and Test of the Quantum Electrodynamics.
Phys. Rev. Lett., 106:080801, Feb 2011.
(page 5).
- [55] R. H. Parker, C. Yu, W. Zhong, B. Estey, and H. Müller.
Measurement of the fine-structure constant as a test of the Standard Model.
Science, 360(6385):191–195, 2018.
(page 5).
- [56] J. B. Fixler, G. T. Foster, J. M. McGuirk, and M. A. Kasevich.
Atom Interferometer Measurement of the Newtonian Constant of Gravity.
Science, 315(5808):74–77, 2007.
(page 5).
- [57] G. Lamporesi, A. Bertoldi, L. Cacciapuoti, M. Prevedelli, and G. M. Tino.
Determination of the Newtonian Gravitational Constant Using Atom Interferometry.
Phys. Rev. Lett., 100:050801, Feb 2008.
(page 5).
- [58] G. Rosi, F. Sorrentino, L. Cacciapuoti, M. Prevedelli, and G. M. Tino.
Precision measurement of the Newtonian gravitational constant using cold atoms.
Nature, 510:518 EP –, 06 2014.
(page 5).
- [59] J. H. Müller, D. Bettermann, V. Rieger, K. Sengstock, U. Sterr, and W. Ertmer.

- [Topological phase shift in a cold-atom interferometer.](#)
Appl. Phys. B, 60(2):199–204, Feb 1995.
(page 5).
- [60] S. Lepoutre, A. Gauguet, M. Büchner, and J. Vigué.
[Test of the He-McKellar-Wilkens topological phase by atom interferometry. I. Theoretical discussion.](#)
Phys. Rev. A, 88:043627, Oct 2013.
(page 5).
- [61] S. Lepoutre, J. Gillot, A. Gauguet, M. Büchner, and J. Vigué.
[Test of the He-McKellar-Wilkens topological phase by atom interferometry. II. The experiment and its results.](#)
Phys. Rev. A, 88:043628, Oct 2013.
(page 5).
- [62] L. Pezzè, M. Gabbrielli, L. Lepori, and A. Smerzi.
[Multipartite Entanglement in Topological Quantum Phases.](#)
Phys. Rev. Lett., 119:250401, Dec 2017.
(page 5).
- [63] M. Gabbrielli, A. Smerzi, and L. Pezzè.
[Multipartite Entanglement at Finite Temperature.](#)
Sci. Rep., 8(1):15663, 2018.
(page 5).
- [64] C. R. Ekstrom, J. Schmiedmayer, M. S. Chapman, T. D. Hammond, and D. E. Pritchard.
[Measurement of the electric polarizability of sodium with an atom interferometer.](#)
Phys. Rev. A, 51:3883–3888, May 1995.
(page 5).
- [65] A. Miffre, M. Jacquy, M. Büchner, G. Tréneç, and J. Vigué.
[Atom interferometry measurement of the electric polarizability of lithium.](#)
The European Physical Journal D - Atomic, Molecular, Optical and Plasma Physics, 38(2):353–365, May 2006.
(page 5).
- [66] A. Miffre, M. Jacquy, M. Büchner, G. Tréneç, and J. Vigué.

- [Measurement of the electric polarizability of lithium by atom interferometry.](#)
Phys. Rev. A, 73:011603, Jan 2006.
(page 5).
- [67] C. Champenois, M. Büchner, R. Delhuille, R. Mathevet, C. Robilliard, C. Rizzo, and J. Vigué.
[Matter Neutrality Test Using a Mach-Zehnder Interferometer](#), pages 554–563.
Springer Berlin Heidelberg, Berlin, Heidelberg, 2001.
(page 5).
- [68] A. Arvanitaki, S. Dimopoulos, A. A. Geraci, J. Hogan, and M. Kasevich.
[How to Test Atom and Neutron Neutrality with Atom Interferometry.](#)
Phys. Rev. Lett., 100:120407, Mar 2008.
(page 5).
- [69] C. M. Caves.
[Quantum-mechanical noise in an interferometer.](#)
Phys. Rev. D, 23:1693–1708, Apr 1981.
(page 5).
- [70] S. Dimopoulos, P. W. Graham, J. M. Hogan, and M. A. Kasevich.
[General relativistic effects in atom interferometry.](#)
Phys. Rev. D, 78:042003, Aug 2008.
(page 5).
- [71] S. Dimopoulos, P. W. Graham, J. M. Hogan, M. A. Kasevich, and S. Rajendran.
[Gravitational wave detection with atom interferometry.](#)
Physics Letters B, 678(1):37 – 40, 2009.
(page 5).
- [72] R. Schnabel, N. Mavalvala, D. E. McClelland, and P. K. Lam.
[Quantum metrology for gravitational wave astronomy.](#)
Nat. Commun., 1:121 EP, 11 2010.
(page 5).
- [73] P. W. Graham, J. M. Hogan, M. A. Kasevich, and S. Rajendran.
[New Method for Gravitational Wave Detection with Atomic Sensors.](#)
Phys. Rev. Lett., 110:171102, Apr 2013.
(page 5).

- [74] Z. K. Hu, B. L. Sun, X. C. Duan, M. K. Zhou, L. L. Chen, S. Zhan, Q. Z. Zhang, and J. Luo.
[Demonstration of an ultrahigh-sensitivity atom-interferometry absolute gravimeter.](#)
Phys. Rev. A, 88:043610, Oct 2013.
(page 5).
- [75] Y. Bidel, O. Carraz, R. Charrière, M. Cadoret, N. Zahzam, and A. Bresson.
[Compact cold atom gravimeter for field applications.](#)
Appl. Phys. Lett., 102(14):144107, 2013.
(page 5).
- [76] W. Chaibi, R. Geiger, B. Canuel, A. Bertoldi, A. Landragin, and P. Bouyer.
[Low frequency gravitational wave detection with ground-based atom interferometer arrays.](#)
Phys. Rev. D, 93:021101, Jan 2016.
(page 5).
- [77] B. P. Abbott and et al.
[Observation of Gravitational Waves from a Binary Black Hole Merger.](#)
Phys. Rev. Lett., 116:061102, Feb 2016.
(page 5).
- [78] K. Y. Chung, S.-W. Chiow, S. Herrmann, S. Chu, and H. Müller.
[Atom interferometry tests of local Lorentz invariance in gravity and electrodynamics.](#)
Phys. Rev. D, 80:016002, Jul 2009.
(page 5).
- [79] S. Fray, C. A. Diez, T. W. Hänsch, and M. Weitz.
[Atomic Interferometer with Amplitude Gratings of Light and Its Applications to Atom Based Tests of the Equivalence Principle.](#)
Phys. Rev. Lett., 93:240404, Dec 2004.
(page 5).
- [80] A. Bonnin, N. Zahzam, Y. Bidel, and A. Bresson.
[Simultaneous dual-species matter-wave accelerometer.](#)
Phys. Rev. A, 88:043615, Oct 2013.

- (page 5).
- [81] D. Schlippert, J. Hartwig, H. Albers, L. L. Richardson, C. Schubert, A. Roura, W. P. Schleich, W. Ertmer, and E. M. Rasel.
[Quantum Test of the Universality of Free Fall.](#)
Phys. Rev. Lett., 112:203002, May 2014.
(pages 5, 6, 63).
- [82] M. G. Tarallo, T. Mazzoni, N. Poli, D. V. Sutyryn, X. Zhang, and G. M. Tino.
[Test of Einstein Equivalence Principle for 0-Spin and Half-Integer-Spin Atoms: Search for Spin-Gravity Coupling Effects.](#)
Phys. Rev. Lett., 113:023005, Jul 2014.
(page 5).
- [83] X.-C. Duan, X.-B. Deng, M.-K. Zhou, K. Zhang, W.-J. Xu, F. Xiong, Y.-Y. Xu, C.-G. Shao, J. Luo, and Z.-K. Hu.
[Test of the Universality of Free Fall with Atoms in Different Spin Orientations.](#)
Phys. Rev. Lett., 117:023001, Jul 2016.
(pages 5, 6, 12, 63).
- [84] S. Abend, M. Gebbe, M. Gersemann, H. Ahlers, H. Müntinga, E. Giese, N. Gaaloul, C. Schubert, C. Lämmerzahl, W. Ertmer, W. P. Schleich, and E. M. Rasel.
[Atom-Chip Fountain Gravimeter.](#)
Phys. Rev. Lett., 117:203003, Nov 2016.
(pages 5, 43).
- [85] A. Peters, K. Y. Chung, and S. Chu.
[Measurement of gravitational acceleration by dropping atoms.](#)
Nature, 400(6747):849–852, 1999.
(page 5).
- [86] A. Louchet-Chauvet, T. Farah, Q. Bodart, A. Clairon, A. Landragin, S. Merlet, and F. Pereira Dos Santos.
[The influence of transverse motion within an atomic gravimeter.](#)
New J. Phys., 13(6):065025, jun 2011.
(pages 5, 124).
- [87] J. E. Debs, P. A. Altin, T. H. Barter, D. Döring, G. R. Dennis, G. McDonald, R. P. Anderson, J. D. Close, and N. P. Robins.

- [Cold-atom gravimetry with a Bose-Einstein condensate.](#)
Phys. Rev. A, 84:033610, Sep 2011.
(page 5).
- [88] H. J. McGuinness, A. V. Rakholia, and G. W. Biedermann.
[High data-rate atom interferometer for measuring acceleration.](#)
Appl. Phys. Lett., 100(1):011106, 2012.
(page 5).
- [89] P. A. Altin, M. T. Johnsson, V. Negnevitsky, G. R. Dennis, R. P. Anderson, J. E. Debs, S. S. Szigeti, K. S. Hardman, S. Bennetts, G. D. McDonald, L. D. Turner, J. D. Close, and N. P. Robins.
[Precision atomic gravimeter based on Bragg diffraction.](#)
New J. Phys., 15(2):023009, feb 2013.
(page 5).
- [90] M. Hauth, C. Freier, V. Schkolnik, A. Senger, M. Schmidt, and A. Peters.
[First gravity measurements using the mobile atom interferometer GAIN.](#)
Appl. Phys. B, 113(1):49–55, Oct 2013.
(page 5).
- [91] O. Francis, H. Baumann, T. Volarik, C. Rothleitner, G. Klein, M. Seil, N. Dando, R. Tracey, C. Ullrich, S. Castelein, H. Hua, W. Kang, S. Chongyang, X. Songbo, T. Hongbo, L. Zhengyuan, V. Pálincás, J. Kostelecký, J. Mäkinen, J. Näränen, S. Merlet, T. Farah, C. Guerlin, F. Pereira Dos Santos, N. Le Moigne, C. Champollion, S. Deville, L. Timmen, R. Falk, H. Wilmes, D. Iacovone, F. Baccaro, A. Germak, E. Biolcati, J. Krynski, M. Sekowski, T. Olszak, A. Pachuta, J. Agren, A. Engfeldt, R. Reudink, P. Inacio, D. McLaughlin, G. Shannon, M. Eckl, T. Wilkins, D. van Westrum, and R. Billson.
[The European Comparison of Absolute Gravimeters 2011 \(ECAG-2011\) in Walferdange, Luxembourg: results and recommendations.](#)
Metrologia, 50(3):257–268, may 2013.
(page 5).
- [92] M. J. Snadden, J. M. McGuirk, P. Bouyer, K. G. Haritos, and M. A. Kasevich.
[Measurement of the Earth’s Gravity Gradient with an Atom Interferometer-Based Gravity Gradiometer.](#)
Phys. Rev. Lett., 81:971–974, Aug 1998.

- (page 5).
- [93] J. M. McGuirk, G. T. Foster, J. B. Fixler, M. J. Snadden, and M. A. Kasevich.
[Sensitive absolute-gravity gradiometry using atom interferometry.](#)
Phys. Rev. A, 65:033608, Feb 2002.
(page 5).
- [94] F. Riehle, Th. Kisters, A. Witte, J. Helmcke, and Ch. J. Bordé.
[Optical Ramsey spectroscopy in a rotating frame: Sagnac effect in a matter-wave interferometer.](#)
Phys. Rev. Lett., 67:177–180, Jul 1991.
(page 5).
- [95] T. L. Gustavson, P. Bouyer, and M. A. Kasevich.
[Precision Rotation Measurements with an Atom Interferometer Gyroscope.](#)
Phys. Rev. Lett., 78:2046–2049, Mar 1997.
(page 5).
- [96] T. L. Gustavson, A. Landragin, and M. A. Kasevich.
[Rotation sensing with a dual atom-interferometer Sagnac gyroscope.](#)
Classical and Quantum Gravity, 17(12):2385–2398, jun 2000.
(page 5).
- [97] D. S. Durfee, Y. K. Shaham, and M. A. Kasevich.
[Long-Term Stability of an Area-Reversible Atom-Interferometer Sagnac Gyroscope.](#)
Phys. Rev. Lett., 97:240801, Dec 2006.
(page 5).
- [98] J. K. Stockton, X. Wu, and M. A. Kasevich.
[Bayesian estimation of differential interferometer phase.](#)
Phys. Rev. A, 76:033613, Sep 2007.
(page 5).
- [99] A. Gauguier, B. Canuel, T. Lévêque, W. Chaibi, and A. Landragin.
[Characterization and limits of a cold-atom Sagnac interferometer.](#)
Phys. Rev. A, 80:063604, Dec 2009.
(page 5).

- [100] J. K. Stockton, K. Takase, and M. A. Kasevich.
[Absolute Geodetic Rotation Measurement Using Atom Interferometry.](#)
Phys. Rev. Lett., 107:133001, Sep 2011.
(page 5).
- [101] G. Tackmann, P. Berg, C. Schubert, S. Abend, M. Gilowski, W. Ertmer, and E.M. Rasel.
[Self-alignment of a compact large-area atomic Sagnac interferometer.](#)
New J. Phys., 14(1):015002, jan 2012.
(page 5).
- [102] H. Xue, Y. Feng, S. Chen, X. Wang, X. Yan, Z. Jiang, and Z. Zhou.
[A continuous cold atomic beam interferometer.](#)
Journal of Applied Physics, 117(9):094901, 2015.
(page 5).
- [103] Q. Bodart, S. Merlet, N. Malossi, F. P. Dos Santos, P. Bouyer, and A. Landragin.
[A cold atom pyramidal gravimeter with a single laser beam.](#)
Appl. Phys. Lett., 96(13):134101, 2010.
(page 5).
- [104] P. Gillot, O. Francis, A. Landragin, F. Pereira Dos Santos, and S. Merlet.
[Stability comparison of two absolute gravimeters: optical versus atomic interferometers.](#)
Metrologia, 51(5):L15–L17, jun 2014.
(page 5).
- [105] C. Freier, M. Hauth, V. Schkolnik, B. Leykauf, M. Schilling, H. Wziontek, H. G. Scherneck, J. Müller, and A. Peters.
[Mobile quantum gravity sensor with unprecedented stability.](#)
Journal of Physics: Conference Series, 723:012050, jun 2016.
(page 5).
- [106] R. Karcher, A. Imanaliev, S. Merlet, and F. Pereira Dos Santos.
[Improving the accuracy of atom interferometers with ultracold sources.](#)
New J. Phys., 20(11):113041, nov 2018.
(pages 5, 13).

- [107] V. Ménoret, P. Vermeulen, N. Le Moigne, S. Bonvalot, P. Bouyer, A. Landragin, and B. Desruelle.
[Gravity measurements below \$10^{-9}\$ g with a transportable absolute quantum gravimeter.](#)
Sci. Rep., 8(1):12300, 2018.
(page 5).
- [108] For details on the project, [see the url](#), accessed on July 10, 2019.
(page 5).
- [109] For details on the project, [see the url](#), accessed on July 10, 2019.
(page 5).
- [110] For details on the project, [see the url](#), accessed on July 10, 2019.
(page 5).
- [111] P. Watts, J. Vala, M. M. Müller, T. Calarco, K. B. Whaley, D. M. Reich, M. H. Goerz, and C. P. Koch.
[Optimizing for an arbitrary perfect entangler. I. Functionals.](#)
Phys. Rev. A, 91:062306, Jun 2015.
(page 5).
- [112] M. H. Goerz, G. Gualdi, D. M. Reich, C. P. Koch, F. Motzoi, K. B. Whaley, J. Vala, M. M. Müller, S. Montangero, and T. Calarco.
[Optimizing for an arbitrary perfect entangler. II. Application.](#)
Phys. Rev. A, 91:062307, Jun 2015.
(page 5).
- [113] I. Apellaniz, B. Lücke, J. Peise, C. Klempt, and T. Géza.
[Detecting metrologically useful entanglement in the vicinity of Dicke states.](#)
New J. Phys., 17(8):083027, aug 2015.
(page 5).
- [114] M. Gessner, L. Pezzè, and A. Smerzi.
[Resolution-enhanced entanglement detection.](#)
Phys. Rev. A, 95:032326, Mar 2017.
(page 5).
- [115] K. Lange, J. Peise, B. Lücke, T. Gruber, A. Sala, A. Polls, W. Ertmer, B. Juliá-Díaz, L. Santos, and C. Klempt.

- Creation of entangled atomic states by an analogue of the Dynamical Casimir effect.
New J. Phys., 20(10):103017, oct 2018.
(page 5).
- [116] F. Anders, L. Pezzè, A. Smerzi, and C. Klempt.
Phase magnification by two-axis countertwisting for detection-noise robust interferometry.
Phys. Rev. A, 97:043813, Apr 2018.
(page 5).
- [117] D. J. Wineland, J. J. Bollinger, W. M. Itano, F. L. Moore, and D. J. Heinzen.
Spin squeezing and reduced quantum noise in spectroscopy.
Phys. Rev. A, 46:R6797–R6800, Dec 1992.
(page 5).
- [118] M. Gessner, A. Smerzi, and L. Pezzè.
Metrological Nonlinear Squeezing Parameter.
Phys. Rev. Lett., 122:090503, Mar 2019.
(page 5).
- [119] O. Hosten, R. Krishnakumar, N. J. Engelsen, and M. A. Kasevich.
Quantum phase magnification.
Science, 352(6293):1552–1555, 2016.
(page 6).
- [120] L. Pezzè, A. Smerzi, M. K. Oberthaler, R. Schmied, and P. Treutlein.
Quantum metrology with nonclassical states of atomic ensembles.
Rev. Mod. Phys., 90:035005, Sep 2018.
(page 6).
- [121] M. Gessner, L. Pezzè, and A. Smerzi.
Sensitivity Limits for Multiparameter Quantum Metrology.
In *Quantum Information and Measurement (QIM) V: Quantum Technologies*, page S3B.4. Optical Society of America, 2019.
(page 6).
- [122] L. Allen and J. H. Eberly.
Optical Resonance and Two-level Atoms.

- Dover books on physics and chemistry. Dover, 1987.
(page 6).
- [123] T. Mazzoni, X. Zhang, R. Del Aguila, L. Salvi, N. Poli, and G. M. Tino.
[Large-momentum-transfer Bragg interferometer with strontium atoms.](#)
Phys. Rev. A, 92:053619, Nov 2015.
(page 6).
- [124] G. Rosi, G. D'Amico, L. Cacciapuoti, F. Sorrentino, M. Prevedelli, M. Zych, Ä. Brukner, and G.M. Tino.
[Quantum test of the equivalence principle for atoms in coherent superposition of internal energy states.](#)
Nat. Commun., 8:15529, June 2017.
(pages 6, 63).
- [125] P. Asenbaum, C. Overstreet, T. Kovachy, D. D. Brown, J. M. Hogan, and M. A. Kasevich.
[Phase Shift in an Atom Interferometer due to Spacetime Curvature across its Wave Function.](#)
Phys. Rev. Lett., 118:183602, 2017.
(pages 6, 18, 39, 53, 63).
- [126] J. Williams, S.-W. Chiow, N. Yu, and H. Müller.
[Quantum test of the equivalence principle and space-time aboard the International Space Station.](#)
New J. Phys., 18(2):025018, feb 2016.
(page 6).
- [127] C. Schubert, J. Hartwig, H. Ahlers, K. Posso-Trujillo, N. Gaaloul, U. Velte, A. Landragin, A. Bertoldi, B. Battelier, P. Bouyer, F. Sorrentino, G. M. Tino, M. Krutzik, A. Peters, S. Herrmann, C. Lämmerzahl, L. Cacciapouti, E. Rocco, K. Bongs, W. Ertmer, and E. M. Rasel.
[Differential atom interferometry with \$^{87}\text{Rb}\$ and \$^{85}\text{Rb}\$ for testing the UFF in STE-QUEST.](#)
arXiv:1312.5963, Dec 2013.
(page 6).
- [128] S. Chu.

- [Nobel Lecture: The manipulation of neutral particles.](#)
Rev. Mod. Phys., 70:685–706, Jul 1998.
(pages 7, 10).
- [129] C. N. Cohen-Tannoudji.
[Nobel Lecture: Manipulating atoms with photons.](#)
Rev. Mod. Phys., 70:707–719, Jul 1998.
(pages 7, 10).
- [130] W. D. Phillips.
[Nobel Lecture: Laser cooling and trapping of neutral atoms.](#)
Rev. Mod. Phys., 70:721–741, Jul 1998.
(pages 7, 10).
- [131] E. A. Cornell and C. E. Wieman.
[Nobel Lecture: Bose-Einstein condensation in a dilute gas, the first 70 years and some recent experiments.](#)
Rev. Mod. Phys., 74:875–893, Aug 2002.
(page 7).
- [132] W. Ketterle.
[Nobel lecture: When atoms behave as waves: Bose-Einstein condensation and the atom laser.](#)
Rev. Mod. Phys., 74:1131–1151, Nov 2002.
(pages 7, 10).
- [133] M. S. Safronova, D. Budker, D. DeMille, D. F. Jackson Kimball, A. Derevianko, and C. W. Clark.
[Search for new physics with atoms and molecules.](#)
Rev. Mod. Phys., 90:025008, Jun 2018.
(page 8).
- [134] J. P. Gordon, H. J. Zeiger, and C. H. Townes.
[The Maser—New Type of Microwave Amplifier, Frequency Standard, and Spectrometer.](#)
Phys. Rev., 99:1264–1274, Aug 1955.
(page 8).
- [135] T. H. Maiman.

- [Stimulated Optical Radiation in Ruby.](#)
Nature, 187(4736):493–494, 1960.
(page 8).
- [136] A. L. Schawlow and C. H. Townes.
[Infrared and Optical Masers.](#)
Phys. Rev., 112:1940–1949, Dec 1958.
(page 8).
- [137] T. L. Nicholson, S. L. Campbell, R. B. Hutson, G. E. Marti, B. J. Bloom, R. L. McNally, W. Zhang, M. D. Barrett, M. S. Safronova, G. F. Strouse, W. L. Tew, and J. Ye.
[Systematic evaluation of an atomic clock at \$2.10^{-18}\$ total uncertainty.](#)
Nat. Commun., 6:6896 EP –, 04 2015.
(page 8).
- [138] I. Ushijima, M. Takamoto, M. Das, T. Ohkubo, and H. Katori.
[Cryogenic optical lattice clocks.](#)
Nature Photonics, 9:185 EP –, 02 2015.
(page 8).
- [139] N. Gaaloul, A. Suzor-Weiner, L. Pruvost, M. Telmini, and E. Charron.
[Theoretical study of a cold-atom beam splitter.](#)
Phys. Rev. A, 74:023620, 2006.
(pages 8, 43, 80).
- [140] A. Ashkin.
[Acceleration and Trapping of Particles by Radiation Pressure.](#)
Phys. Rev. Lett., 24:156–159, Jan 1970.
(page 8).
- [141] A. Ashkin.
[Atomic-Beam Deflection by Resonance-Radiation Pressure.](#)
Phys. Rev. Lett., 25:1321–1324, Nov 1970.
(page 8).
- [142] A. Ashkin.
[Trapping of Atoms by Resonance Radiation Pressure.](#)
Phys. Rev. Lett., 40:729–732, Mar 1978.

- (page 8).
- [143] A. L. Migdall, J. V. Prodan, W. D. Phillips, T. H. Bergeman, and H. J. Metcalf.
[First Observation of Magnetically Trapped Neutral Atoms.](#)
Phys. Rev. Lett., 54:2596–2599, Jun 1985.
(page 8).
- [144] S. Chu, J. E. Bjorkholm, A. Ashkin, and A. Cable.
[Experimental Observation of Optically Trapped Atoms.](#)
Phys. Rev. Lett., 57:314–317, Jul 1986.
(page 8).
- [145] V. S. Bagnato, G. P. Lafyatis, A. G. Martin, E. L. Raab, R. N. Ahmad-Bitar, and
D. E. Pritchard.
[Continuous Stopping and Trapping of Neutral Atoms.](#)
Phys. Rev. Lett., 58:2194–2197, May 1987.
(page 8).
- [146] A. Ashkin.
[Applications of Laser Radiation Pressure.](#)
Science, 210(4474):1081–1088, 1980.
(page 8).
- [147] D. E. Pritchard.
[Cooling Neutral Atoms in a Magnetic Trap for Precision Spectroscopy.](#)
Phys. Rev. Lett., 51:1336–1339, Oct 1983.
(page 8).
- [148] A. Ashkin.
[Stable radiation-pressure particle traps using alternating light beams.](#)
Opt. Lett., 9(10):454–456, Oct 1984.
(page 8).
- [149] J. Dalibard, S. Reynaud, and C. Cohen-Tannoudji.
[Potentialities of a new \$\sigma_+ - \sigma_-\$ laser configuration for radiative cooling and trapping.](#)
Journal of Physics B: Atomic and Molecular Physics, 17(22):4577–4594, nov 1984.
(page 8).
- [150] S. Chu, L. Hollberg, J. E. Bjorkholm, A. Cable, and A. Ashkin.

- Three-dimensional viscous confinement and cooling of atoms by resonance radiation pressure.
Phys. Rev. Lett., 55:48–51, Jul 1985.
(page 9).
- [151] P. D. Lett, R. N. Watts, C. I. Westbrook, W. D. Phillips, P. L. Gould, and H. J. Metcalf.
Observation of Atoms Laser Cooled below the Doppler Limit.
Phys. Rev. Lett., 61:169–172, Jul 1988.
(pages 9, 84).
- [152] A. J. Kerman, V. Vuletic, C. Chin, and S. Chu.
Beyond Optical Molasses: 3D Raman Sideband Cooling of Atomic Cesium to High Phase-Space Density.
Phys. Rev. Lett., 84:439–442, Jan 2000.
(pages 9, 84, 95).
- [153] S. N. Bose.
Plancks Gesetz und Lichtquantenhypothese.
Zeitschrift für Physik, 26(1):178–181, Dec 1924.
(page 10).
- [154] M. H. Anderson, J. R. Ensher, M. R. Matthews, C. E. Wieman, and E. A. Cornell.
Observation of Bose-Einstein Condensation in a Dilute Atomic Vapor.
Science, 269(5221):198–201, 1995.
(pages 10, 64).
- [155] E. A. Cornell and C. E. Wieman.
Nobel Lecture: Bose-Einstein condensation in a dilute gas, the first 70 years and some recent experiments.
Rev. Mod. Phys., 74:875–893, Aug 2002.
(page 10).
- [156] W. Ketterle, D. S. Durfee, and D. M. Stamper-Kurn.
Making, probing and understanding Bose-Einstein condensates.
arXiv, 1999.
(pages 10, 11, 59).
- [157] K. Huang.

- Introduction to Statistical Physics.*
Taylor & Francis, 2001.
(page 11).
- [158] D. Guéry-Odelin, F. Zambelli, J. Dalibard, and S. Stringari.
[Collective oscillations of a classical gas confined in harmonic traps.](#)
Phys. Rev. A, 60:4851–4856, Dec 1999.
(page 11).
- [159] P. Pedri, D. Guéry-Odelin, and S. Stringari.
[Dynamics of a classical gas including dissipative and mean-field effects.](#)
Phys. Rev. A, 68:043608, Oct 2003.
(pages 11, 60).
- [160] I. Shvarchuck, C. Buggle, D. S. Petrov, M. Kemmann, W. von Klitzing, G. V. Shlyapnikov, and J. T. M. Walraven.
[Hydrodynamic behavior in expanding thermal clouds of \$^{87}\text{Rb}\$.](#)
Phys. Rev. A, 68:063603, Dec 2003.
(pages 11, 60).
- [161] L. de Broglie.
[A tentative theory of light quanta.](#)
The London, Edinburgh, and Dublin Philosophical Magazine and Journal of Science, 47(278):446–458, 1924.
(page 11).
- [162] H. Müller, S. W. Chiow, Q. Long, S. Herrmann, and S. Chu.
[Atom Interferometry with up to 24-Photon-Momentum-Transfer Beam Splitters.](#)
Phys. Rev. Lett., 100:180405, May 2008.
(page 12).
- [163] S.-W. Chiow, T. Kovachy, H. C. Chien, and M. A. Kasevich.
[102 \$\hbar k\$ Large Area Atom Interferometers.](#)
Phys. Rev. Lett., 107:130403, Sep 2011.
(page 12).
- [164] S. Abend.
[Atom-chip-based quantum gravimetry with Bose-Einstein condensates.](#)
PhD thesis, Leibniz University of Hanover, 2017.

- (page 12).
- [165] T. Kovachy, J. M. Hogan, A. Sugarbaker, S. M. Dickerson, C. A. Donnelly, C. Overstreet, and M. A. Kasevich.
[Matter Wave Lensing to Picokelvin Temperatures.](#)
Phys. Rev. Lett., 114:143004, 2015.
(pages 12, 19, 39, 40, 53, 80, 82, 133, 134).
- [166] H. Müller, S.-W. Chiow, S. Herrmann, S. Chu, and K.-Y. Chung.
[Atom-Interferometry Tests of the Isotropy of Post-Newtonian Gravity.](#)
Phys. Rev. Lett., 100:031101, Jan 2008.
(page 12).
- [167] H. Müntinga, H. Ahlers, M. Krutzik, A. Wenzlawski, S. Arnold, D. Becker, K. Bongs, H. Dittus, H. Duncker, N. Gaaloul, C. Gherasim, E. Giese, C. Grzeschik, T. W. Hänsch, O. Hellmig, W. Herr, S. Herrmann, E. Kajari, S. Kleinert, C. Lämmerzahl, W. Lewoczko-Adamczyk, J. Malcolm, N. Meyer, R. Nolte, A. Peters, M. Popp, J. Reichel, A. Roura, J. Rudolph, M. Schiemangk, M. Schneider, S. T. Seidel, K. Sengstock, V. Tamma, T. Valenzuela, A. Vogel, R. Walser, T. Wendrich, P. Windpassinger, W. Zeller, T. van Zoest, W. Ertmer, W. P. Schleich, and E. M. Rasel.
[Interferometry with Bose-Einstein Condensates in Microgravity.](#)
Phys. Rev. Lett., 110:093602, 2013.
(pages 12, 19, 39, 43, 52).
- [168] J. Rudolph, W. Herr, C. Grzeschik, T. Sternke, A. Grote, M. Popp, D. Becker, H. Müntinga, H. Ahlers, A. Peters, C. Lämmerzahl, K. Sengstock, N. Gaaloul, W. Ertmer, and E.M. Rasel.
[A high-flux BEC source for mobile atom interferometers.](#)
New J. Phys., 17:065001, 2015.
(pages 12, 13, 14, 18, 20, 21, 23, 43, 44, 48, 49, 52).
- [169] S. M. Dickerson, J. M. Hogan, A. Sugarbaker, D. M. S. Johnson, and M. A. Kasevich.
[Multiaxis Inertial Sensing with Long-Time Point Source Atom Interferometry.](#)
Phys. Rev. Lett., 111:083001, Aug 2013.
(page 12).
- [170] L. Zhou, Z. Y. Xiong, W. Yang, B. Tang, W. C. Peng, K. Hao, R. B. Li, M. Liu, J. Wang, and M. S. Zhan.

- Development of an atom gravimeter and status of the 10-meter atom interferometer for precision gravity measurement.
General Relativity and Gravitation, 43(7):1931–1942, Jul 2011.
(page 12).
- [171] For details on the vlbai project, [see the URL](#), accessed on July 10, 2019.
(page 12).
- [172] T. van Zoest, N. Gaaloul, Y. Singh, H. Ahlers, W. Herr, S. T. Seidel, W. Ertmer, E. Rasel, M. Eckart, E. Kajari, S. Arnold, G. Nandi, W. P. Schleich, R. Walser, A. Vogel, K. Sengstock, K. Bongs, W. Lewoczko-Adamczyk, M. Schiemangk, T. Schuldt, A. Peters, T. Könemann, H. Müntinga, C. Lämmerzahl, H. Dittus, T. Steinmetz, T. W. Hänsch, and J. Reichel.
[Bose-Einstein Condensation in Microgravity](#).
Science, 328:1540, 2010.
(pages 12, 18, 43).
- [173] R. Geiger, V. Ménotet, G. Stern, N. Zahzam, P. Cheinet, B. Battelier, A. Villing, F. Moron, M. Lours, Y. Bidel, A. Bresson, A. Landragin, and P. Bouyer.
[Detecting inertial effects with airborne matter-wave interferometry](#).
Nat. Comm., 2:474, 2011.
(pages 12, 39).
- [174] D. Becker, M. D. Lachmann, S. T. Seidel, H. Ahlers, A. N. Dinkelaker, J. Grosse, O. Hellmig, H. Müntinga, V. Schkolnik, T. Wendrich, A. Wenzlawski, B. Weps, R. Corgier, T. Franz, N. Gaaloul, W. Herr, D. Lüdtke, M. Popp, S. Amri, H. Duncker, M. Erbe, A. Kohfeldt, A. Kubelka-Lange, C. Braxmaier, E. Charron, W. Ertmer, M. Krutzik, C. Lämmerzahl, A. Peters, W. P. Schleich, K. Sengstock, R. Walser, A. Wicht, P. Windpassinger, and E. M. Rasel.
[Space-borne Bose–Einstein condensation for precision interferometry](#).
Nature, 562(7727):391–395, 2018.
(pages 12, 18, 43, 45, 46, 47, 53).
- [175] For details on the project, [see the url](#), accessed on July 10, 2019.
(pages 12, 39).
- [176] For details on the project, [see the url](#), accessed on July 10, 2019.
(page 12).

- [177] For details on the project, [see the url](#), accessed on July 10, 2019.
(page 12).
- [178] For details on the Maius project, [see the url](#), accessed on July 10, 2019.
(page 12).
- [179] [ISS picture](#), accessed on July 10, 2019.
(page 12).
- [180] For details on the CAL project, [see the url](#), accessed on July 10, 2019.
(page 12).
- [181] N. Gaaloul, J. Hartwig, C. Schubert, W. Ermtter, and E. M. Rasel.
[Precision interferometry with Bose-Einstein condensates.](#)
Proc. Int. School Phys. "Enrico Fermi", 188:657, 2014.
(pages 12, 18).
- [182] S. S. Szigeti, J. E. Debs, J. J. Hope, N. P. Robins, and J. D. Close.
[Why momentum width matters for atom interferometry with Bragg pulses.](#)
New J. Phys., 14(2):023009, feb 2012.
(page 13).
- [183] A. Louchet-Chauvet, T. Farah, Q. Bodart, A. Clairon, A. Landragin, S. Merlet, and
F. Pereira Dos Santos.
[The influence of transverse motion within an atomic gravimeter.](#)
New J. Phys., 13(6):065025, jun 2011.
(page 13).
- [184] V. Schkolnik, B. Leykauf, M. Hauth, C. Freier, and A. Peters.
[The effect of wavefront aberrations in atom interferometry.](#)
Appl. Phys. B, 120(2):311–316, Aug 2015.
(page 13).
- [185] A. Trimeche, M. Langlois, S. Merlet, and F. Pereira Dos Santos.
[Active Control of Laser Wavefronts in Atom Interferometers.](#)
Phys. Rev. Applied, 7:034016, Mar 2017.
(pages 13, 124).
- [186] S. Chu, J. E. Bjorkholm, A. Ashkin, J. P. Gordon, and L. W. Hollberg.
[Proposal for optically cooling atoms to temperatures of the order of \$10^{-6}\$ K.](#)

- Opt. Lett.*, 11:73, 1986.
(pages 13, 19, 39, 40, 129, 133).
- [187] H. Ammann and N. Christensen.
[Delta Kick Cooling: A New Method for Cooling Atoms.](#)
Phys. Rev. Lett., 78:2088, 1997.
(pages 13, 19, 39, 133).
- [188] R. Corgier, S. Amri, W. Herr, H. Ahlers, J. Rudolph, D. Guéry-Odelin, E. M. Rasel, E. Charron, and N. Gaaloul.
[Fast manipulation of Bose-Einstein condensates with an atom chip.](#)
New J. Phys., 20(5):055002, may 2018.
(pages 18, 49, 67, 132, 133).
- [189] A. Trimeche, B. Battelier, D. Becker, A. Bertoldi, P. Bouyer, C. Braxmaier, E. Charron, R. Corgier, M. Cornelius, K. Douch, N. Gaaloul, S. Herrmann, J. Müller, E. M. Rasel, C. Schubert, H. Wu, and F. Pereira Dos Santos.
[Concept study and preliminary design of a cold atom interferometer for space gravity gradiometry.](#)
working paper or preprint, April 2019.
(page 18).
- [190] E. A. Cornell and C. E. Wieman.
[Nobel Lecture: Bose-Einstein condensation in a dilute gas, the first 70 years and some recent experiments.](#)
Rev. Mod. Phys., 74:875, 2002.
(page 18).
- [191] W. Ketterle.
[Nobel lecture: When atoms behave as waves: Bose-Einstein condensation and the atom laser.](#)
Rev. Mod. Phys., 74:1131, 2002.
(page 18).
- [192] W. Hänsel, J. Reichel, P. Hommelhoff, and T. W. Hänsch.
[Magnetic Conveyor Belt for Transporting and Merging Trapped Atom Clouds.](#)
Phys. Rev. Lett., 86:608, 2001.
(pages 19, 20, 44).

- [193] M.J. Pritchard, A.S. Arnold, S.L. Cornish, D.W. Hallwood, C.V.S. Pleasant, and I.G. Hughes.
[Transport of launched cold atoms with a laser guide and pulsed magnetic fields.](#)
New J. Phys., 8:309, 2006.
(page 19).
- [194] A. Couvert, T. Kawalec, G. Reinaudi, and D. Guéry-Odelin.
[Optimal transport of ultracold atoms in the non-adiabatic regime.](#)
Europhys. Lett., 83:13001, 2008.
(page 19).
- [195] W. Hänsel, P. Hommelhoff, T. W. Hänsch, and J. Reichel.
[Bose-Einstein condensation on a microelectronic chip.](#)
Nature, 413:498, 2001.
(pages 19, 20).
- [196] A. Günther, M. Kemmler, S. Kraft, C. J. Vale, C. Zimmermann, and J. Fortágh.
[Combined chips for atom optics.](#)
Phys. Rev. A, 71:063619, 2005.
(page 19).
- [197] D. Schrader, S. Kuhr, W. Alt, M. Müller, V. Gomer, and D. Meschede.
[An optical conveyor belt for single neutral atoms.](#)
Appl. Phys. B, 73:819, 2001.
(page 19).
- [198] S. Kuhr, W. Alt, D. Schrader, I. Dotsenko, Y. Miroshnychenko, W. Rosenfeld, M. Khudaverdyan, V. Gomer, A. Rauschenbeutel, and D. Meschede.
[Coherence Properties and Quantum State Transportation in an Optical Conveyor Belt.](#)
Phys. Rev. Lett., 91:213002, 2003.
(page 19).
- [199] R. Bowler, J. Gaebler, Y. Lin, T. R. Tan, D. Hanneke, J. D. Jost, J. P. Home, D. Leibfried, and D. J. Wineland.
[Coherent Diabatic Ion Transport and Separation in a Multizone Trap Array.](#)
Phys. Rev. Lett., 109:080502, 2012.
(page 19).

- [200] A. Walther, F. Ziesel, T. Ruster, S. T. Dawkins, K. Ott, M. Hettrich, K. Singer, F. Schmidt-Kaler, and U. Poschinger.
[Controlling Fast Transport of Cold Trapped Ions.](#)
Phys. Rev. Lett., 109:080501, 2012.
(page 19).
- [201] S. Masuda and K. Nakamura.
[Fast-forward of adiabatic dynamics in quantum mechanics.](#)
Proc. R. Soc. A, 466:1135, 2010.
(page 19).
- [202] E. Torrontegui, S. Ibáñez, S. Martínez-Garaot, M. Modugno, A. del Campo, D. Guéry-Odelin, A. Ruschhaupt, X. Chen, and J. G. Muga.
[Shortcuts to Adiabaticity.](#)
Adv. At. Mol. Opt. Phys., 62(62):117, 2013.
(page 19).
- [203] M. H. S. Amin, C. J. S. Truncik, and D. V. Averin.
[Role of single-qubit decoherence time in adiabatic quantum computation.](#)
Phys. Rev. A, 80:022303, 2009.
(page 19).
- [204] R. Roy, P. C. Condylis, V. Prakash, D. Sahagun, and B. Hessmo.
[A minimalistic and optimized conveyor belt for neutral atoms.](#)
Sci. Rep., 7:13660, 2017.
(page 19).
- [205] A. Peirce, M. A. Dahleh, and H. Rabitz.
[Optimal control of quantum-mechanical systems: Existence, numerical approximation, and applications.](#)
Phys. Rev. A, 37:4950, 1988.
(pages 19, 49).
- [206] U. Hohenester, P. K. Rekdal, A. Borzi, and J. Schmiedmayer.
[Optimal quantum control of Bose-Einstein condensates in magnetic microtraps.](#)
Phys. Rev. A, 75:023602, 2007.
(pages 19, 49, 53, 58, 134).
- [207] M. Demirplak and S. A. Rice.

- [Adiabatic Population Transfer with Control Fields.](#)
J. Phys. Chem. A, 107(46):9937, 2003.
(page 19).
- [208] A. del Campo.
[Shortcuts to Adiabaticity by Counterdiabatic Driving.](#)
Phys. Rev. Lett., 111:100502, 2013.
(page 19).
- [209] E. Torrontegui, S. Ibáñez, X. Chen, A. Ruschhaupt, D. Guéry-Odelin, and J. G. Muga.
[Fast atomic transport without vibrational heating.](#)
Phys. Rev. A, 83:013415, 2011.
(page 19).
- [210] S. Masuda.
[Acceleration of adiabatic transport of interacting particles and rapid manipulations of a dilute Bose gas in the ground state.](#)
Phys. Rev. A, 86:063624, 2012.
(page 19).
- [211] S. Deffner, C. Jarzynski, and A. del Campo.
[Classical and Quantum Shortcuts to Adiabaticity for Scale-Invariant Driving.](#)
Phys. Rev. X, 4:021013, 2014.
(page 19).
- [212] M. Palmero, E. Torrontegui, D. Guéry-Odelin, and J. G. Muga.
[Fast transport of two ions in an anharmonic trap.](#)
Phys. Rev. A, 88:053423, 2013.
(page 19).
- [213] Q. Zhang, X. Chen, and D. Guéry-Odelin.
[Fast and optimal transport of atoms with nonharmonic traps.](#)
Phys. Rev. A, 92:043410, 2015.
(page 19).
- [214] Q. Zhang, J. G. Muga, D. Guéry-Odelin, and X. Chen.
[Optimal shortcuts for atomic transport in anharmonic traps.](#)
J. Phys. B, 49:125503, 2016.

- (page 19).
- [215] D. Guéry-Odelin and J. G. Muga.
[Transport in a harmonic trap: Shortcuts to adiabaticity and robust protocols.](#)
Phys. Rev. A, 90:063425, 2014.
(pages 19, 53, 58).
- [216] W. Rohringer, D. Fischer, F. Steiner, I. E. Mazets, J. Schmiedmayer, and M. Trupke.
[Non-equilibrium scale invariance and shortcuts to adiabaticity in a one-dimensional Bose gas.](#)
Sci. Rep., 5:9820, 2015.
(page 19).
- [217] S. An, D. Lv, A. del Campo, and K. Kim.
[Shortcuts to adiabaticity by counterdiabatic driving for trapped-ion displacement in phase space.](#)
Nat. Comm., 7:12999, 2016.
(page 19).
- [218] L. Pitaevskii.
[Vortex lines in an imperfect bose gas.](#)
Sov. Phys. JETP, 13:451, 1961.
(page 19).
- [219] E. P. Gross.
[Hydrodynamics of a Superfluid Condensate.](#)
J. Math. Phys., 4:195, 1963.
(page 19).
- [220] R. Folman, P. Krüger, J. Schmiedmayer, J. Denschlag, and C. Henkel.
[Microscopic Atom Optics: From Wires to an Atom Chip.](#)
Adv. At. Mol. Opt. Phys., 48:263, 2002.
(pages 20, 44).
- [221] J. Fortágh and C. Zimmermann.
[Magnetic microtraps for ultracold atoms.](#)
Rev. Mod. Phys., 79:235, Feb 2007.
(pages 20, 44).

- [222] J. Reichel and V. Vuletic.
[Atom Chips](#).
Wiley, 2011.
(page 20).
- [223] T. Nirrengarten, A. Qarry, C. Roux, A. Emmert, G. Nogues, M. Brune, J.-M. Raimond, and S. Haroche.
[Realization of a Superconducting Atom Chip](#).
Phys. Rev. Lett., 97:200405, 2006.
(page 20).
- [224] [Most of the data on rubidium atoms used here can be found in the notes by D. A. Steck](#), accessed on July 10, 2019.
(pages 21, 85).
- [225] E. Charron, M. A. Cirone, A. Negretti, J. Schmiedmayer, and T. Calarco.
[Theoretical analysis of a realistic atom-chip quantum gate](#).
Phys. Rev. A, 74:012308, Jul 2006.
(page 22).
- [226] R. A. Toupin and B. Bernstein.
Some properties of the Hessian Matrix of a Strictly Convex Function.
Journal für die reine und angewandte Mathematik (Crelles Journal), 2009.
(page 22).
- [227] Padé, H. .
An. Sc. ENS, 9:3, 1892.
(page 25).
- [228] P. Ehrenfest.
[Bemerkung über die angenäherte Gültigkeit der klassischen Mechanik innerhalb der Quantenmechanik](#).
Zeitschrift für Physik, 45:455, 1927.
(page 23).
- [229] Y. Castin and R. Dum.
[Bose-Einstein Condensates in Time Dependent Traps](#).
Phys. Rev. Lett., 77:5315, 1996.
(pages 24, 27, 99, 109, 110, 112, 129).

- [230] Y. Kagan, E. L. Surkov, and G. V. Shlyapnikov.
[Evolution of a Bose gas in anisotropic time-dependent traps.](#)
Phys. Rev. A, 55:R18, 1997.
(pages 24, 27, 99, 109, 110, 112, 129).
- [231] C.J. Pethick and H. Smith.
[Bose-Einstein Condensation in Dilute Gases.](#)
Cambridge University Press, 2002.
(pages 24, 100, 101, 117).
- [232] S. Stringari.
[Collective Excitations of a Trapped Bose-Condensed Gas.](#)
Phys. Rev. Lett., 77:2360, 1996.
(pages 27, 28, 38, 39).
- [233] M.-O. Mewes, M. R. Andrews, N. J. van Druten, D. M. Kurn, D. S. Durfee, C. G. Townsend, and W. Ketterle.
[Collective Excitations of a Bose-Einstein Condensate in a Magnetic Trap.](#)
Phys. Rev. Lett., 77:988, 1996.
(page 27).
- [234] D. Guéry-Odelin and S. Stringari.
[Scissors Mode and Superfluidity of a Trapped Bose-Einstein Condensed Gas.](#)
Phys. Rev. Lett., 83:4452, 1999.
(page 27).
- [235] F. Dalfovo, S. Giorgini, L. P. Pitaevskii, and S. Stringari.
[Theory of Bose-Einstein condensation in trapped gases.](#)
Rev. Mod. Phys., 71:463, 1999.
(page 27).
- [236] R. Dubessy, C. De Rossi, T. Badr, L. Longchambon, and H. Perrin.
[Imaging the collective excitations of an ultracold gas using statistical correlations.](#)
New J. Phys., 16(12):122001, 2014.
(page 27).
- [237] C. De Rossi, R. Dubessy, K. Merloti, M. de Goër de Herve, T. Badr, A. Perrin, L. Longchambon, and H. Perrin.

- The scissors oscillation of a quasi two-dimensional Bose gas as a local signature of superfluidity.
J. Phys. Conf. Ser., 793:012023, 2017.
(page 27).
- [238] J. F. Schaff, X. L. Song, P. Capuzzi, P. Vignolo, and G. Labeyrie.
[Shortcut to adiabaticity for an interacting Bose-Einstein condensate.](#)
Europhys. Lett., 93(2):23001, 2011.
(pages 28, 35).
- [239] J. F. Schaff, P. Capuzzi, G. Labeyrie, and P. Vignolo.
[Shortcuts to adiabaticity for trapped ultracold gases.](#)
New J. Phys., 13(11):113017, 2011.
(pages 28, 35).
- [240] G. M. Tino and M. A. Kasevich.
[Atom Interferometry.](#)
EBL-Schweitzer. IOS Press, 2014.
(page 39).
- [241] P.R. Berman.
[Atom Interferometry.](#)
Elsevier Science, 1997.
(page 39).
- [242] J. Rudolph, N. Gaaloul, Y. Singh, H. Ahlers, W. Herr, T. A. Schulze, S. T. Seidel, C. Rode, V. Schkolnik, W. Ertmer, E. M. Rasel, H. Müntinga, T. Köneemann, A. Resch, S. Herrmann, C. Lämmerzahl, T. v. Zoest, H. Dittus, A. Vogel, A. Wenzlawski, K. Sengstock, N. Meyer, K. Bongs, M. Krutzik, W. Lewoczko-Adamczyk, M. Schiemangk, A. Peters, M. Eckart, E. Kajari, S. Arnold, G. Nandi, W. P. Schleich, R. Walser, T. Steinmetz, T. W. Hänsch, and J. Reichel.
[Degenerate Quantum Gases in Microgravity.](#)
Microgravity Sci. Technol., 23:287, 2011.
(pages 39, 43, 49).
- [243] For details on the project, [see the url](#), accessed on July 10, 2019.
(pages 39, 43).
- [244] J. Rudolph.

- Matter-Wave Optics with Bose-Einstein Condensates in Microgravity*.
PhD thesis, Leibniz University of Hanover, 2016.
(pages [40](#), [43](#), [44](#), [49](#), [129](#), [132](#), [133](#), [134](#)).
- [245] For details on the quantus project, [see the url](#), accessed on July 10, 2019.
(page [43](#)).
- [246] A. Vogel, M. Schmidt, K. Sengstock, K. Bongs, W. Lewoczko, T. Schuldt, A. Peters, T. Van Zoest, W. Ertmer, E. Rasel, T. Steinmetz, J. Reichel, T. Könemann, W. Brinkmann, E. Göklü, C. Lämmerzahl, H. J. Dittus, G. Nandi, W. P. Schleich, and R. Walser.
[Bose–Einstein condensates in microgravity](#).
Appl. Phys. B, 84(4):663–671, Sep 2006.
(page [43](#)).
- [247] W. Ertmer and E. M. Rasel.
[Towards Atomic Quantum Sensors in Microgravity](#).
Nuclear Physics B - Proceedings Supplements, 166:307 – 309, 2007.
Proceedings of the Third International Conference on Particle and Fundamental Physics in Space.
(page [43](#)).
- [248] S. Herrmann, H. Dittus, and C. Lämmerzahl.
[Testing the equivalence principle with atomic interferometry](#).
Classical and Quantum Gravity, 29(18):184003, aug 2012.
(page [43](#)).
- [249] H. Ahlers, H. Müntinga, A. Wenzlawski, M. Krutzik, G. Tackmann, S. Abend, N. Gaaloul, E. Giese, A. Roura, R. Kuhl, C. Lämmerzahl, A. Peters, P. Windpassinger, K. Sengstock, W. P. Schleich, W. Ertmer, and E. M. Rasel.
[Double Bragg Interferometry](#).
Phys. Rev. Lett., 116:173601, Apr 2016.
(page [43](#)).
- [250] W. Herr.
[Eine kompakte Quelle quantenentarteter Gase hohen Flusses für die Atominterferometrie unter Schwerelosigkeit](#).
PhD thesis, Leibniz University of Hanover, 2013.

(page 43).

- [251] C. Grzeschik.
Experiments with Bose-Einstein Condensates in Microgravity.
PhD thesis, Humboldt-Universität zu Berlin, 2017.
(pages 43, 44, 132, 133, 134).
- [252] T. Sternke.
An ultracold high-flux source for matter-wave interferometry in microgravity.
PhD thesis, Carl von Ossietzky Universität Oldenburg, 2018.
(pages 43, 44, 132, 133, 134).
- [253] Private communication with W. Herr.
(page 44).
- [254] M. A. Popp.
Compact, low-noise current drivers for quantum sensors with atom chips.
PhD thesis, Leibniz University of Hanover, 2018.
(pages 44, 132).
- [255] S. T. Seidel.
Eine Quelle für die Interferometrie mit Bose-Einstein-Kondensaten auf Höhenforschungsraketen.
PhD thesis, Leibniz University of Hanover, 2014.
(page 45).
- [256] S. Abend, M. Gebbe, M. Gersemann, H. Ahlers, H. Müntinga, E. Giese, N. Gaaloul, C. Schubert, C. Lämmerzahl, W. Ertmer, W. P. Schleich, and E. M. Rasel.
Atom-Chip Fountain Gravimeter.
Phys. Rev. Lett., 117:203003, 2016.
(page 49).
- [257] S. Amri, R. Corgier, D. Sugny, E. M. Rasel, N. Gaaloul, and E. Charron.
Optimal control of the transport of Bose-Einstein condensates with atom chips.
Sci. Rep., 9(1):5346, 2019.
(pages 49, 58, 82, 134).
- [258] K. Henderson, C. Ryu, C. MacCormick, and M. G. Boshier.

- [Experimental demonstration of painting arbitrary and dynamic potentials for Bose-Einstein condensates.](#)
New J. Phys., 11(4):043030, 2009.
(page 49).
- [259] A. del Campo and M. G. Boshier.
[Shortcuts to adiabaticity in a time-dependent box.](#)
Sci. Rep., 2:648, 2012.
(page 49).
- [260] D. Johnson.
[Long baseline atom interferometry.](#)
PhD thesis, Stanford, 2011.
(page 52).
- [261] A. Sugarbaker.
[Atom interferometry in a 10 m fountain.](#)
PhD thesis, Stanford, 2014.
(pages 52, 63).
- [262] S. Dickerson.
[Long-time atom interferometry for precision tests of fundamental physics.](#)
PhD thesis, Stanford, 2014.
(pages 52, 63, 65).
- [263] V. Giovannetti, S. Lloyd, and L. Maccone.
[Quantum Metrology.](#)
Phys. Rev. Lett., 96:010401, Jan 2006.
(page 52).
- [264] L. S. Pontryagin, V. G. Bol'tanskii, R. S. Gamkrelidze, and E. F. Mischenko.
[The Mathematical Theory of Optimal Processes.](#)
Proceedings of the Edinburgh Mathematical Society, 15(2):157–158, 1966.
(pages 52, 56).
- [265] E. B. Lee and L. Markus.
Foundations of optimal control theory.
Wiley, 1967.
(pages 52, 55, 56).

- [266] D. E. Kirk and L. Markus.
Foundations of optimal control theory.
Dover Publications, 2004.
(pages 52, 53, 55).
- [267] A. E. Bryson and Y. C. Ho.
Applied optimal control : optimization, estimation, and control.
New York, ; Abingdon, Oxon: Taylor and Francis, 1975.
(page 52).
- [268] D. D'Alessandro.
Introduction to Quantum Control and Dynamics.
Chapman & Hall: Applied Mathematics & Nonlinear Science. CRC Press, 2007.
(page 52).
- [269] B. Bonnard and D. Sugny.
Optimal Control with Applications in Space and Quantum Dynamics.
Aims Series on Applied Mathematics. American Institute of Mathematical Sciences, 2012.
(page 52).
- [270] H. A. Fürst, M.H. Goerz, U. G. Poschinger, M. Murphy, S. Montangero, T. Calarco, F. Schmidt-Kaler, K. Singer, and C. P. Koch.
Controlling the transport of an ion: classical and quantum mechanical solutions.
New J. Phys., 16(7):075007, jul 2014.
(page 52).
- [271] S. J. Glaser, U. Boscain, T. Calarco, C. P. Koch, W. Köckenberger, R. Kosloff, I. Kuprov, B. Luy, S. Schirmer, T. Schulte-Herbrüggen, D. Sugny, and F. K. Wilhelm.
Training Schrödinger's cat: quantum optimal control.
The European Physical Journal D, 69(12):279, Dec 2015.
(pages 52, 53).
- [272] V. Krotov.
Global Methods in Optimal Control Theory.
Chapman & Hall/CRC Pure and Applied Mathematics. Taylor & Francis, 1995.
(page 53).

- [273] N. Khaneja, T. Reiss, C. Kehlet, T. Schulte-Herbrüggen, and S. J. Glaser.
[Optimal control of coupled spin dynamics: design of NMR pulse sequences by gradient ascent algorithms.](#)
Journal of Magnetic Resonance, 172(2):296 – 305, 2005.
(page 53).
- [274] J. Werschnik and E. K. U. Gross.
[Quantum optimal control theory.](#)
Journal of Physics B: Atomic, Molecular and Optical Physics, 40(18):R175–R211,
sep 2007.
(page 53).
- [275] C. Brif, R. Chakrabarti, and H. Rabitz.
[Control of quantum phenomena: past, present and future.](#)
New J. Phys., 12(7):075008, jul 2010.
(page 53).
- [276] S. Deffner and E. Lutz.
[Quantum Speed Limit for Non-Markovian Dynamics.](#)
Phys. Rev. Lett., 111:010402, Jul 2013.
(page 53).
- [277] D. M. Reich, N. Katz, and C. P. Koch.
[Exploiting Non-Markovianity for Quantum Control.](#)
Sci. Rep., 5:12430 EP –, 07 2015.
(page 53).
- [278] E. Mangaud, R. Puthumpally-Joseph, D. Sugny, C. Meier, O. Atabek, and
M. Desouter-Lecomte.
[Non-Markovianity in the optimal control of an open quantum system described by hierarchical equations of motion.](#)
New J. Phys., 20(4):043050, apr 2018.
(page 53).
- [279] J. Fischer, D. Basilewitsch, C. P. Koch, and D. Sugny.
[Time-optimal control of the purification of a qubit in contact with a structured environment.](#)
Phys. Rev. A, 99:033410, Mar 2019.

- (page 53).
- [280] C. A. Weidner and D. Z. Anderson.
[Experimental Demonstration of Shaken-Lattice Interferometry.](#)
Phys. Rev. Lett., 120:263201, Jun 2018.
(page 53).
- [281] G. Jäger, D. M. Reich, M. H. Goerz, C. P. Koch, and U. Hohenester.
[Optimal quantum control of Bose-Einstein condensates in magnetic microtraps: Comparison of gradient-ascent-pulse-engineering and Krotov optimization schemes.](#)
Phys. Rev. A, 90:033628, Sep 2014.
(pages 53, 134).
- [282] J.-F. Mennemann, D. Matthes, R. M. Weishäupl, and T. Langen.
[Optimal control of Bose-Einstein condensates in three dimensions.](#)
New J. Phys., 17(11):113027, nov 2015.
(page 53).
- [283] S. van Frank, M. Bonneau, J. Schmiedmayer, S. Hild, C. Gross, M. Cheneau, I. Bloch, T. Pichler, A. Negretti, T. Calarco, and S. Montangero.
[Optimal control of complex atomic quantum systems.](#)
Sci. Rep., 6:34187 EP –, 10 2016.
(page 53).
- [284] D. Hocker, J. Yan, and H. Rabitz.
[Optimal nonlinear coherent mode transitions in Bose-Einstein condensates utilizing spatiotemporal controls.](#)
Phys. Rev. A, 93:053612, May 2016.
(page 53).
- [285] E. Torrontegui, S. Martínez-Garaot, M. Modugno, X. Chen, and J. G. Muga.
[Engineering fast and stable splitting of matter waves.](#)
Phys. Rev. A, 87:033630, Mar 2013.
(page 53).
- [286] X. J. Lu, X. Chen, J. Alonso, and J. G. Muga.
[Fast transitionless expansions of Gaussian anharmonic traps for cold atoms: Bang-singular-bang control.](#)

BIBLIOGRAPHY

- Phys. Rev. A*, 89:023627, Feb 2014.
(page 53).
- [287] For details on the stanford project, [see the URL](#), accessed on July 10, 2019.
(page 53).
- [288] A. Sugarbaker, S. M. Dickerson, J. M. Hogan, D. M. S. Johnson, and M. A. Kasevich.
[Enhanced Atom Interferometer Readout through the Application of Phase Shear.](#)
Phys. Rev. Lett., 111:113002, Sep 2013.
(page 53).
- [289] G. Ness, C. Shkedrov, Y. Florshaim, and Y. Sagi.
[Realistic shortcuts to adiabaticity in optical transfer.](#)
New J. Phys., 20(9):095002, sep 2018.
(page 57).
- [290] D. Guéry-Odelin.
[Mean-field effects in a trapped gas.](#)
Phys. Rev. A, 66:033613, Sep 2002.
(page 60).
- [291] T. Kovachy.
[New techniques for precision atom interferometry and applications to fundamental tests of gravity and of quantum mechanics.](#)
PhD thesis, Stanford, 2016.
(pages 63, 67, 129).
- [292] W. Petrich, M. H. Anderson, J. R. Ensher, and E. A. Cornell.
[Stable, Tightly Confining Magnetic Trap for Evaporative Cooling of Neutral Atoms.](#)
Phys. Rev. Lett., 74:3352–3355, Apr 1995.
(pages 63, 65).
- [293] E. Majorana.
[Atomi orientati in campo magnetico variabile.](#)
Il Nuovo Cimento (1924-1942), 9(2):43–50, Feb 1932.
(page 64).
- [294] M. Abramowitz and I. A. Stegun.

Handbook of Mathematical Functions: With Formulas, Graphs, and Mathematical Tables.

Applied mathematics series. Dover Publications, 1965.

(page 65).

- [295] V. G. Minogin, J. A. Richmond, and G. I. Opat.
[Time-orbiting-potential quadrupole magnetic trap for cold atoms.](#)
Phys. Rev. A, 58:3138–3145, Oct 1998.
(page 65).
- [296] X. Chen, E. Torrontegui, D. Stefanatos, J. S. Li, and J. G. Muga.
[Optimal trajectories for efficient atomic transport without final excitation.](#)
Phys. Rev. A, 84:043415, Oct 2011.
(page 72).
- [297] T. L Ho and V. B. Shenoy.
[Binary Mixtures of Bose Condensates of Alkali Atoms.](#)
Phys. Rev. Lett., 77:3276–3279, Oct 1996.
(pages 98, 99).
- [298] B. D. Esry, C. H. Greene, J. P. Burke Jr., and J. L. Bohn.
[Hartree-Fock Theory for Double Condensates.](#)
Phys. Rev. Lett., 78:3594–3597, May 1997.
(pages 98, 99).
- [299] H. Pu and N. P. Bigelow.
[Properties of Two-Species Bose Condensates.](#)
Phys. Rev. Lett., 80:1130–1133, Feb 1998.
(page 98).
- [300] P. Öhberg.
[Stability properties of the two-component Bose-Einstein condensate.](#)
Phys. Rev. A, 59:634–638, Jan 1999.
(page 98).
- [301] B. D. Esry.
[Impact of spontaneous spatial symmetry breaking on the critical atom number for two-component Bose-Einstein condensates.](#)
Phys. Rev. A, 58:R3399–R3402, Nov 1998.

- (page 98).
- [302] B. D. Esry and C. H. Greene.
[Spontaneous spatial symmetry breaking in two-component Bose-Einstein condensates.](#)
Phys. Rev. A, 59:1457–1460, Feb 1999.
(page 98).
- [303] E. Timmermans.
[Phase Separation of Bose-Einstein Condensates.](#)
Phys. Rev. Lett., 81:5718–5721, Dec 1998.
(page 98).
- [304] S. T. Chui and P. Ao.
[Broken cylindrical symmetry in binary mixtures of Bose-Einstein condensates.](#)
Phys. Rev. A, 59:1473–1476, Feb 1999.
(page 98).
- [305] C. K. Law, H. Pu, N. P. Bigelow, and J. H. Eberly.
[Quantum phase diffusion of a two-component dilute Bose-Einstein condensate.](#)
Phys. Rev. A, 58:531–535, Jul 1998.
(page 98).
- [306] C. K. Law, H. Pu, N. P. Bigelow, and J. H. Eberly.
[“Stability Signature” in Two-Species Dilute Bose-Einstein Condensates.](#)
Phys. Rev. Lett., 79:3105–3108, Oct 1997.
(page 98).
- [307] J. Williams, R. Walser, J. Cooper, E. Cornell, and M. Holland.
[Nonlinear Josephson-type oscillations of a driven, two-component Bose-Einstein condensate.](#)
Phys. Rev. A, 59:R31–R34, Jan 1999.
(page 98).
- [308] P. Ao and S. T. Chui.
[Binary Bose-Einstein condensate mixtures in weakly and strongly segregated phases.](#)
Phys. Rev. A, 58:4836–4840, Dec 1998.
(pages 98, 101).

- [309] P. Öhberg and S. Stenholm.
[Hartree-Fock treatment of the two-component Bose-Einstein condensate.](#)
Phys. Rev. A, 57:1272–1279, Feb 1998.
(page 98).
- [310] C. J. Myatt, E. A. Burt, R. W. Ghrist, E. A. Cornell, and C. E. Wieman.
[Production of Two Overlapping Bose-Einstein Condensates by Sympathetic Cooling.](#)
Phys. Rev. Lett., 78:586–589, Jan 1997.
(page 98).
- [311] D. S. Hall, M. R. Matthews, J. R. Ensher, C. E. Wieman, and E. A. Cornell.
[Dynamics of Component Separation in a Binary Mixture of Bose-Einstein Condensates.](#)
Phys. Rev. Lett., 81:1539–1542, Aug 1998.
(page 98).
- [312] D. M. Stamper-Kurn, M. R. Andrews, A. P. Chikkatur, S. Inouye, H. J. Miesner, J. Stenger, and W. Ketterle.
[Optical Confinement of a Bose-Einstein Condensate.](#)
Phys. Rev. Lett., 80:2027–2030, Mar 1998.
(page 98).
- [313] V. Schweikhard, I. Coddington, P. Engels, S. Tung, and E. A. Cornell.
[Vortex-Lattice Dynamics in Rotating Spinor Bose-Einstein Condensates.](#)
Phys. Rev. Lett., 93:210403, Nov 2004.
(page 98).
- [314] C. Hamner, J. J. Chang, P. Engels, and M. A. Hoefer.
[Generation of Dark-Bright Soliton Trains in Superfluid-Superfluid Counterflow.](#)
Phys. Rev. Lett., 106:065302, Feb 2011.
(page 98).
- [315] X. C. Yao, H. Z. Chen, Y. P. Wu, X. P. Liu, X. Q. Wang, X. Jiang, Y. Deng, Y. A. Chen, and J. W. Pan.
[Observation of Coupled Vortex Lattices in a Mass-Imbalance Bose and Fermi Superfluid Mixture.](#)
Phys. Rev. Lett., 117:145301, Sep 2016.

- (page 98).
- [316] M. Trippenbach, K. Góral, K. Rzazewski, B. Malomed, and Y. B. Band.
[Structure of binary Bose-Einstein condensates.](#)
Journal of Physics B: Atomic, Molecular and Optical Physics, 33(19):4017–4031,
sep 2000.
(pages 98, 99).
- [317] M. J. Edmonds, K. L. Lee, and N. P. Proukakis.
[Kinetic model of trapped finite-temperature binary condensates.](#)
Phys. Rev. A, 91:011602, Jan 2015.
(page 98).
- [318] K. L. Lee, N. B. Jørgensen, I. K. Liu, L. Wacker, J. J. Arlt, and N. P. Proukakis.
[Phase separation and dynamics of two-component Bose-Einstein condensates.](#)
Phys. Rev. A, 94:013602, Jul 2016.
(page 98).
- [319] K. L. Lee, N. B. Jørgensen, L. J. Wacker, M. G. Skou, K. T. Skalmstang, J. J. Arlt,
and N. P. Proukakis.
[Time-of-flight expansion of binary Bose–Einstein condensates at finite tempera-
ture.](#)
New J. Phys., 20(5):053004, may 2018.
(page 98).
- [320] P. Maddaloni, M. Modugno, C. Fort, F. Minardi, and M. Inguscio.
[Collective Oscillations of Two Colliding Bose-Einstein Condensates.](#)
Phys. Rev. Lett., 85:2413–2417, Sep 2000.
(page 98).
- [321] I. Ferrier-Barbut, M. Delehaye, S. Laurent, A. T. Grier, M. Pierce, B. S. Rem,
F. Chevy, and C. Salomon.
[A mixture of Bose and Fermi superfluids.](#)
Science, 345(6200):1035–1038, 2014.
(page 98).
- [322] G. Sorelli, M. Gessner, A. Smerzi, and L. Pezzè.
[Fast and optimal generation of entanglement in bosonic Josephson junctions.](#)
Phys. Rev. A, 99:022329, Feb 2019.

(page 98).

- [323] D. M. Stamper-Kurn and M. Ueda.
[Spinor Bose gases: Symmetries, magnetism, and quantum dynamics.](#)
Rev. Mod. Phys., 85:1191–1244, Jul 2013.
(page 98).
- [324] M. G. Hu, M. J. Van de Graaff, D. Kedar, J. P. Corson, E. A. Cornell, and D. S. Jin.
[Bose Polarons in the Strongly Interacting Regime.](#)
Phys. Rev. Lett., 117:055301, Jul 2016.
(page 98).
- [325] N. B. Jørgensen, L. Wacker, K. T. Skalmstang, M. M. Parish, J. Levinsen, R. S. Christensen, G. M. Bruun, and J. J. Arlt.
[Observation of Attractive and Repulsive Polarons in a Bose-Einstein Condensate.](#)
Phys. Rev. Lett., 117:055302, Jul 2016.
(page 98).
- [326] C. R. Cabrera, L. Tanzi, J. Sanz, B. Naylor, P. Thomas, P. Cheiney, and L. Tarruell.
[Quantum liquid droplets in a mixture of Bose-Einstein condensates.](#)
Science, 359(6373):301–304, 2018.
(page 98).
- [327] G. Semeghini, G. Ferioli, L. Masi, C. Mazzinghi, L. Wolswijk, F. Minardi, M. Modugno, G. Modugno, M. Inguscio, and M. Fattori.
[Self-Bound Quantum Droplets of Atomic Mixtures in Free Space.](#)
Phys. Rev. Lett., 120:235301, Jun 2018.
(page 98).
- [328] E. Fava, T. Bienaimé, C. Mordini, G. Colzi, C. Qu, S. Stringari, G. Lamporesi, and G. Ferrari.
[Observation of Spin Superfluidity in a Bose Gas Mixture.](#)
Phys. Rev. Lett., 120:170401, Apr 2018.
(page 98).
- [329] A. Burchianti, C. D’Errico, S. Rosi, A. Simoni, M. Modugno, C. Fort, and F. Minardi.
[Dual-species Bose-Einstein condensate of \$^{41}\text{K}\$ and \$^{87}\text{Rb}\$ in a hybrid trap.](#)
Phys. Rev. A, 98:063616, Dec 2018.
(pages 98, 120).

- [330] S. Beattie, S. Moulder, R. J. Fletcher, and Z. Hadzibabic.
[Persistent Currents in Spinor Condensates.](#)
Phys. Rev. Lett., 110:025301, Jan 2013.
(page 98).
- [331] M. Abad, A. Sartori, S. Finazzi, and A. Recati.
[Persistent currents in two-component condensates in a toroidal trap.](#)
Phys. Rev. A, 89:053602, May 2014.
(page 98).
- [332] J. M. McNamara, T. Jeltsov, A. S. Tychkov, W. Hogervorst, and W. Vassen.
[Degenerate Bose-Fermi Mixture of Metastable Atoms.](#)
Phys. Rev. Lett., 97:080404, Aug 2006.
(page 98).
- [333] A. G. Truscott, K. E. Strecker, W. I. McAlexander, G. B. Partridge, and R. G. Hulet.
[Observation of Fermi Pressure in a Gas of Trapped Atoms.](#)
Science, 291(5513):2570–2572, 2001.
(page 98).
- [334] F. Schreck, L. Khaykovich, K. L. Corwin, G. Ferrari, T. Bourdel, J. Cubizolles, and C. Salomon.
[Quasipure Bose-Einstein Condensate Immersed in a Fermi Sea.](#)
Phys. Rev. Lett., 87:080403, Aug 2001.
(page 98).
- [335] S. B. Papp, J. M. Pino, and C. E. Wieman.
[Tunable Miscibility in a Dual-Species Bose-Einstein Condensate.](#)
Phys. Rev. Lett., 101:040402, Jul 2008.
(pages 98, 99, 101).
- [336] M. K. Tey, S. Stellmer, R. Grimm, and F. Schreck.
[Double-degenerate Bose-Fermi mixture of strontium.](#)
Phys. Rev. A, 82:011608, Jul 2010.
(page 98).
- [337] S. Sugawa, R. Yamazaki, S. Taie, and Y. Takahashi.
[Bose-Einstein condensate in gases of rare atomic species.](#)
Phys. Rev. A, 84:011610, Jul 2011.

(page 98).

- [338] S. Stellmer, R. Grimm, and F. Schreck.
[Production of quantum-degenerate strontium gases.](#)
Phys. Rev. A, 87:013611, Jan 2013.
(page 98).
- [339] G. Ferrari, M. Inguscio, W. Jastrzebski, G. Modugno, G. Roati, and A. Simoni.
[Collisional Properties of Ultracold K-Rb Mixtures.](#)
Phys. Rev. Lett., 89:053202, Jul 2002.
(pages 99, 114, 124).
- [340] G. Modugno, M. Modugno, F. Riboli, G. Roati, and M. Inguscio.
[Two Atomic Species Superfluid.](#)
Phys. Rev. Lett., 89:190404, Oct 2002.
(pages 99, 124).
- [341] G. Thalhammer, G. Barontini, L. De Sarlo, J. Catani, F. Minardi, and M. Inguscio.
[Double Species Bose-Einstein Condensate with Tunable Interspecies Interactions.](#)
Phys. Rev. Lett., 100:210402, May 2008.
(pages 99, 113, 114, 124, 129).
- [342] J. W. Park, C. H. Wu, I. Santiago, T. G. Tiecke, S. Will, P. Ahmadi, and M. W. Zwierlein.
[Quantum degenerate Bose-Fermi mixture of chemically different atomic species with widely tunable interactions.](#)
Phys. Rev. A, 85:051602, May 2012.
(page 99).
- [343] G. Roati, F. Riboli, G. Modugno, and M. Inguscio.
[Fermi-Bose Quantum Degenerate \$^{40}\text{K}\$ - \$^{87}\text{Rb}\$ Mixture with Attractive Interaction.](#)
Phys. Rev. Lett., 89:150403, Sep 2002.
(page 99).
- [344] Z. Hadzibabic, C. A. Stan, K. Dieckmann, S. Gupta, M. W. Zwierlein, A. Görlitz, and W. Ketterle.
[Two-Species Mixture of Quantum Degenerate Bose and Fermi Gases.](#)
Phys. Rev. Lett., 88:160401, Apr 2002.
(page 99).

- [345] C. Silber, S. Günther, C. Marzok, B. Deh, P. W. Courteille, and C. Zimmermann.
[Quantum-Degenerate Mixture of Fermionic Lithium and Bosonic Rubidium Gases.](#)
Phys. Rev. Lett., 95:170408, Oct 2005.
(page 99).
- [346] M. Taglieber, A.-C. Voigt, T. Aoki, T. W. Hänsch, and K. Dieckmann.
[Quantum Degenerate Two-Species Fermi-Fermi Mixture Coexisting with a Bose-Einstein Condensate.](#)
Phys. Rev. Lett., 100:010401, Jan 2008.
(page 99).
- [347] A. D. Lercher, T. Takekoshi, M. Debatin, B. Schuster, R. Rameshan, F. Ferlaino, R. Grimm, and H. C. Nägerl.
[Production of a dual-species Bose-Einstein condensate of Rb and Cs atoms.](#)
The European Physical Journal D, 65(1):3–9, Nov 2011.
(page 99).
- [348] D. J. McCarron, H. W. Cho, D. L. Jenkin, M. P. Köppinger, and S. L. Cornish.
[Dual-species Bose-Einstein condensate of \$^{87}\text{Rb}\$ and \$^{133}\text{Cs}\$.](#)
Phys. Rev. A, 84:011603, Jul 2011.
(page 99).
- [349] M. Repp, R. Pires, J. Ulmanis, R. Heck, E. D. Kuhnle, M. Weidemüller, and E. Tiemann.
[Observation of interspecies \$^6\text{Li}\$ - \$^{133}\text{Cs}\$ Feshbach resonances.](#)
Phys. Rev. A, 87:010701, Jan 2013.
(page 99).
- [350] B. Pasquiou, A. Bayerle, S. M. Tzanova, S. Stellmer, J. Szczepkowski, M. Parigger, R. Grimm, and F. Schreck.
[Quantum degenerate mixtures of strontium and rubidium atoms.](#)
Phys. Rev. A, 88:023601, Aug 2013.
(page 99).
- [351] L. Wacker, N. B. Jørgensen, D. Birkmose, R. Horchani, W. Ertmer, C. Klempt, N. Winter, J. Sherson, and J. J. Arlt.
[Tunable dual-species Bose-Einstein condensates of \$^{39}\text{K}\$ and \$^{87}\text{Rb}\$.](#)
Phys. Rev. A, 92:053602, Nov 2015.

(page 99).

- [352] F. Wang, X. Li, D. Xiong, and D. Wang.
[A double species \$^{23}\text{Na}\$ and \$^{87}\text{Rb}\$ Bose–Einstein condensate with tunable miscibility via an interspecies Feshbach resonance.](#)
Journal of Physics B: Atomic, Molecular and Optical Physics, 49(1):015302, nov 2015.
(page 99).
- [353] R. Roy, A. Green, R. Bowler, and S. Gupta.
[Two-Element Mixture of Bose and Fermi Superfluids.](#)
Phys. Rev. Lett., 118:055301, Feb 2017.
(page 99).
- [354] T. A. Schulze, T. Hartmann, K. K. Voges, M. W. Gempel, E. Tiemann, A. Zenesini, and S. Ospelkaus.
[Feshbach spectroscopy and dual-species Bose-Einstein condensation of \$^{23}\text{Na}\$ – \$^{39}\text{K}\$ mixtures.](#)
Phys. Rev. A, 97:023623, Feb 2018.
(page 99).
- [355] A. Trautmann, P. Ilzhöfer, G. Durastante, C. Politi, M. Sohmen, M. J. Mark, and F. Ferlaino.
[Dipolar Quantum Mixtures of Erbium and Dysprosium Atoms.](#)
Phys. Rev. Lett., 121:213601, Nov 2018.
(page 99).
- [356] A. Simoni, F. Ferlaino, G. Roati, G. Modugno, and M. Inguscio.
[Magnetic Control of the Interaction in Ultracold K-Rb Mixtures.](#)
Phys. Rev. Lett., 90:163202, Apr 2003.
(page 99).
- [357] G. Barontini.
[Ultracold Bose-Bose mixtures with tunable interspecies interactions.](#)
PhD thesis, University of Firenze, 2009.
(page 124).
- [358] J. Y. Wang and D. E. Silva.
[Wave-front interpretation with Zernike polynomials.](#)

- Appl. Opt.*, 19(9):1510–1518, May 1980.
(page 124).
- [359] E. R. Elliott, M. C. Krutzik, J. R. Williams, R. J. Thompson, and D. C. Aveline.
[NASA’s Cold Atom Lab \(CAL\): system development and ground test status.](#)
npj Microgravity, 4(1):16, 2018.
(page 133).
- [360] For details on the CAL project, [see the url](#), accessed on July 10, 2019.
(page 133).
- [361] M. D. Feit, J. A. Fleck, Jr., and A. Steiger.
[Solution of the Schroedinger equation by a spectral method.](#)
J. Comput. Phys., 47:412, 1982.
(pages 137, 138).
- [362] S. Takagi.
[Quantum Dynamics and Non-Inertial Frames of Reference. IGenerality.](#)
Prog. Theor. Phys., 85:463, 1991.
(pages 137, 138).
- [363] R. Kosloff and H. Tal-Ezer.
[A direct relaxation method for calculating eigenfunctions and eigenvalues of the schrödinger equation on a grid.](#)
Chemical Physics Letters, 127(3):223 – 230, 1986.
(page 138).
- [364] L. Lehtovaara, J. Toivanen, and J. Eloranta.
[Solution of time-independent Schrödinger equation by the imaginary time propagation method.](#)
Journal of Computational Physics, 221(1):148 – 157, 2007.
(page 138).
- [365] I. Schaefer, H. Tal-Ezer, and R. Kosloff.
[Semi-global approach for propagation of the time-dependent Schrödinger equation for time-dependent and nonlinear problems.](#)
Journal of Computational Physics, 343:368 – 413, 2017.
(page 139).

Titre : Ingénierie d'états atomiques pour l'interférométrie de précision

Mots clés : Raccourcis Adiabatiques, Théorie du Contrôle Optimal, Ensemble thermique, Condensats de Bose-Einstein (CBE), Mélanges de CBE, Puce atomique

Résumé : La physique moderne repose sur deux théories fondamentales distinctes, la relativité générale et la mécanique quantique. Toutes les deux décrivent d'une part les phénomènes macroscopiques et cosmologiques tels que les ondes gravitationnelles et les trous noirs et d'autre part les phénomènes microscopiques comme la superfluidité ou le spin des particules. L'unification de ces deux théories reste, jusqu'à présent, un problème non résolu. Il est intéressant de noter que les différentes théories de gravité quantique prédisent une violation des principes de la relativité générale à différents niveaux. Il est donc hautement intéressant de détecter les violations de ces principes et de déterminer à quel niveau elles se produisent.

De récentes propositions pour effectuer des tests du principe d'équivalence d'Einstein suggèrent une amélioration spectaculaire des performances en utilisant des capteurs atomiques à ondes de matière. Dans ce contexte, il est nécessaire de concevoir

des états d'entrée de l'interféromètre avec des conditions initiales bien définies. Un test de pointe de l'universalité de la chute libre (Universality of Free Fall en anglais (UFF)) nécessiterait, par exemple, un contrôle des positions et des vitesses avec une précision de l'ordre de $1 \mu\text{m}$ et $1 \mu\text{m}\cdot\text{s}^{-1}$, respectivement. De plus, les systématiques liées à la taille du paquet d'ondes limitent le taux d'expansion maximum possible à $100 \mu\text{m}\cdot\text{s}^{-1}$. La création initiale des états d'entrée de l'interféromètre doit être assez rapide, de l'ordre de quelques centaines de ms au maximum, pour que le temps de cycle de l'expérience soit pertinent d'un point de vue métrologique. Dans cette thèse j'ai développé des séquences optimisées s'appuyant sur l'excitation du centre de masse et la de la taille d'un ou plusieurs ensembles d'atomes refroidis ainsi que dégénérés. Certaines séquences proposé dans cette thèse ont déjà été implémenté dans des expériences augmentant de manière significative le controle des ensembles atomiques.

Title : Engineered atomic states for precision interferometry

Keywords : Shortcut-to-Adiabaticity (STA), Optimal Control Theory (OCT), Thermal ensemble, Bose-Einstein Condensates (BEC), BEC Mixtures, Atom chip

Abstract : Modern physics relies on two distinct fundamental theories, General Relativity and Quantum Mechanics. Both describe on one hand macroscopic and cosmological phenomena such as gravitational waves and black holes and on the other hand microscopic phenomena as superfluidity or the spin of particles. The unification of these two theories remains, so far, an unsolved problem. Interestingly, candidate Quantum Gravity theories predict a violation of the principles of General Relativity at different levels. It is, therefore, of a timely interest to detect violations of these principles and determine at which level they occur.

Recent proposals to perform Einstein Equivalence Principle tests suggest a dramatic performance improvement using matter-wave atomic sensors. In this context, the design of the input states with well defined

initial conditions is required. A state-of-the-art test of the universality of free fall (UFF) would, for example, require a control of positions and velocities at the level of $1 \mu\text{m}$ and $1 \mu\text{m}\cdot\text{s}^{-1}$, respectively. Moreover, size-related systematics constrain the maximum expansion rate possible to the $100 \mu\text{m}\cdot\text{s}^{-1}$ level. This initial engineering of the input states has to be quite fast, of the order of few hundred ms at maximum, for the experiment's duty cycle to be metrologically-relevant. In this thesis I developed optimized sequences based on the excitation of the center of mass and the size excitation of one or two cooled atomic sample as well as degenerated gases. Some sequences proposed in this thesis have already been implemented in experiments and significantly increase the control of atomic ensembles.

